

An Early Separation Scheme for the LHC Luminosity Upgrade

THÈSE N° 4574 (2010)

PRÉSENTÉE LE 18 FÉVRIER 2010

À LA FACULTÉ SCIENCES DE BASE

LABORATOIRE DE PHYSIQUE DES ACCÉLÉRATEURS DE PARTICULES

PROGRAMME DOCTORAL EN PHYSIQUE

ÉCOLE POLYTECHNIQUE FÉDÉRALE DE LAUSANNE

POUR L'OBTENTION DU GRADE DE DOCTEUR ÈS SCIENCES

PAR

Guido STERBINI

acceptée sur proposition du jury:

Prof. G. Gremaud, président du jury

Prof. L. Rivkin, directeur de thèse

Prof. A. Blondel, rapporteur

Dr J.-P. Koutchouk, rapporteur

Prof. M. Q. Tran, rapporteur



ÉCOLE POLYTECHNIQUE
FÉDÉRALE DE LAUSANNE

Suisse
2010

Résumé

Dans cette thèse, nous examinons les possibilités d'amélioration de la luminosité du Grand Collisionneur de Hadrons (LHC) grâce à l'utilisation d'une insertion ESS, « Early Separation Scheme ». Cette insertion permet d'augmenter la luminosité de la machine en réduisant l'angle de croisement des deux faisceaux aux points de collisions, tout en minimisant les effets préjudiciables de l'interaction entre faisceaux.

Composée de quatre dipôles, chacune des insertion ESS est située au niveau d'un point d'interaction de haute luminosité du LHC. Il en existe deux correspondant aux détecteurs ATLAS et CMS. Deux des quatre dipôles composant l'insertion ESS, les dipôles D0, doivent être intégrés dans la caverne du détecteur.

Tout d'abord, nous montrons que combinée à une augmentation du courant du faisceau et à un système de focalisation plus puissant, l'insertion ESS peut fournir une luminosité intégrée de 3000 fb^{-1} sur une période d'environ 6,5 à 7 années avec une luminosité nivelée à $5,5 \cdot 10^{34} \text{ cm}^{-2} \text{ s}^{-1}$. Ceci est rendu possible grâce au contrôle de luminosité par variation de l'angle de croisement des faisceaux.

Ensuite l'impact de l'insertion ESS est étudié du point de vue de la dynamique du faisceau par évaluation de ses effets linéaires et non-linéaires. Nous démontrons, en utilisant une approche analytique, que tous les effets linéaires sont négligeables. Puis, l'interaction électromagnétique entre faisceaux, effet non-linéaire, est évaluée au moyen de simulations numériques et d'expériences. Les résultats obtenus donnent de solides indications sur l'angle de croisement minimum compatible avec la stabilité des faisceaux.

À partir de ces indications et en considérant les différentes limites liées à l'intégration de l'insertion ESS dans les détecteurs, nous proposons de placer le dipôle D0 à 14 m du point d'interaction. Le champ magnétique intégré exigé et les contraintes spatiales à l'intérieur des détecteurs impliquent l'utilisation de dipôles supraconducteurs : nous avons alors optimisé leurs ouvertures pour réduire la puissance déposée sur la bobine de l'aimant par les débris des collisions. En raison à la fois de la forte densité de puissance déposée sur la bobine et du champ magnétique de 9 T nécessaire, nous proposons une coupe transversale de l'aimant devant être réalisé avec un câble supraconducteur Nb_3Sn refroidi à 4,2 K.

MOTS CLÉS : Early Separation Scheme, Phase II d'augmentation de luminosité du LHC, sLHC, effet faisceau-faisceau, expériences avec les fils dans l'SPS, dipôle D0.

Abstract

In this thesis we evaluate the potential of the Early Separation Scheme for the Luminosity Upgrade of the Large Hadron Collider (LHC). The main goal of the Early Separation Scheme is to reduce the crossing angle between the proton beams at the collision point in order to increase the luminosity performance of the machine and to alleviate, at the same time, the detrimental effects due to the electromagnetic interaction between the beams.

The Early Separation Scheme consists of four dipoles for each of the two high luminosity Interaction Points of the LHC, corresponding to the ATLAS and CMS detectors. Two dipoles out of the four, the so-called D0 dipoles, have to be integrated in the experimental cavern.

We show that, working in synergy with an increased beam current and with a stronger final focusing system, the Early Separation Scheme can provide an integrated luminosity of 3000 fb^{-1} over a period of $6.5 - 7$ years with a leveled luminosity of $5.5 \cdot 10^{34} \text{ cm}^{-2} \text{ s}^{-1}$. These figures are possible thanks to the luminosity leveling by using the crossing angle.

We study the impact of the Early Separation Scheme from the beam dynamics point of view by evaluating its linear and non-linear effects. We show, using an analytical approach, that all induced linear effects are negligible. The non-linear effects, namely the electromagnetic interaction between the beams, are considered by means of numerical simulations and dedicated experiments. From the simulation and the experimental results, we have indications about the minimum beam crossing angle that is still compatible with the beam dynamics constraints.

From these indications and by considering the different issues related to the integration of the scheme in the detectors, we propose to position the D0 dipole at 14 m from the Interaction Point. The integrated magnetic field required and the space constraints in the detectors imply the use of a superconducting D0 dipole: we optimize its aperture to reduce the power deposited on the magnet's coil by the collision debris. Due to the high power density impinging on the coil and to the 9 T magnetic field required, we propose a magnet cross-section using a Nb_3Sn superconducting cable at the temperature of 4.2 K.

KEYWORDS: Early Separation Scheme, Phase II LHC Luminosity Upgrade, sLHC, beam-beam effect, SPS wire experiments, D0 dipole.

Contents

Introduction	1
1 The Concept of Early Separation	3
1.1 Motivations and goals for the LHC Luminosity Upgrade	3
1.2 The luminosity challenge in the sLHC	5
1.2.1 Luminosity for head-on collisions	5
1.2.2 The crossing scheme in the LHC	7
1.2.3 Other parameters influencing the luminosity	15
1.3 The Early Separation concept for the sLHC	18
1.3.1 Strategies for the luminosity increase	18
1.3.2 Principle and layout	19
1.3.3 The integrated magnetic field requested in the magnets	20
2 Luminosity leveling and performance	23
2.1 Motivation and principle of the luminosity leveling via the crossing angle	23
2.2 Sources of luminosity decay	25
2.3 An analytical model for the luminosity leveling	26
2.3.1 The luminosity evolution without luminosity leveling	26
2.3.2 The luminosity leveling with the crossing angle	27
2.3.3 Luminosity leveling strategies	29
2.4 A numerical model for the luminosity leveling	35
2.5 Luminosity performance of the Early Separation Scheme	37
2.5.1 Scenarios and performance	37
2.5.2 General remarks on the luminosity leveling	39
3 The induced beam dynamics effect	43
3.1 Linear beam dynamics effects	43
3.1.1 The dispersion induced by the scheme	43
3.1.2 The on-momentum β -beating induced by the scheme	44
3.1.3 The impact of the scheme on the beam-beam tune shift	47
3.2 Non-linear beam dynamics effects	48
3.2.1 Diffusion due to the machine non-linearities	49
3.2.2 Analytic expression of the beam-beam interaction	52
3.2.3 Scaling laws for the beam-beam interaction	57
4 Simulations and experiments	63
4.1 The simulations for the Early Separation Scheme	63
4.1.1 The choice for the indicator of the dynamic aperture	63
4.1.2 The simulation code written in CUDA TM	66
4.1.3 The simulations results	72
4.2 The wire experiment in the SPS	78
4.2.1 The experimental setup	78
4.2.2 Experiments at 37 GeV/c	86
4.2.3 Experiments at 55 GeV/c	92
4.2.4 Experiments at 120 GeV/c	96
4.3 Summary and interpretation of the experiments	99

5	The integration and the preliminary design	101
5.1	The integration in the detectors of the Early Separation Scheme	101
5.2	The power deposited on the D0 dipole by the collision debris	110
5.2.1	The debris from the Interaction Point	111
5.2.2	The simulations of the power deposition on the D0 dipole	113
5.3	The magnet preliminary design	116
5.3.1	The mechanical stresses on the D0 dipole's coils	117
5.3.2	A preliminary cross-section for the D0 dipole	118
	Conclusions	123
	Acknowledgments	125
	Bibliography	129

List of Figures

1.1	The Tevatron Run II experience.	4
1.2	The evolution of the peak and integrated luminosity for the LHC and sLHC	5
1.3	The pp cross-section.	6
1.4	The geometric reference frames at the Interaction Point.	7
1.5	A simplified representation of the nominal crossing angle in the LHC.	8
1.6	The physical beam trajectories of the nominal LHC crossing.	8
1.7	The beam separation pattern of the nominal LHC.	9
1.8	The geometric factor, F_G , as function of the Piwinski angle.	11
1.9	The Interaction Region layout of ATLAS and CMS in the LSS.	12
1.10	The β_x -function at the Interaction Regions 1 and 5.	13
1.11	The β_y -function at the Interaction Regions 1 and 5.	13
1.12	The horizontal reference orbit at the Interaction Regions 1 and 5.	14
1.13	The closed orbit in Interaction Region 1.	14
1.14	The cross-section of the LHC correctors for the beam crossing.	15
1.15	The hourglass factor F_{HG}	16
1.16	Comparison between F and F_G factors.	17
1.17	The F and F_G factors as function of the inner normalized separation, Δ_{in}	17
1.18	Comparison between the nominal crossing and the Early Separation Scheme.	20
1.19	Layout of the Early Separation Scheme.	20
1.20	The relative polarity of the D0 and the OC dipoles.	21
1.21	An example of the closed orbit for the Early Separation Scheme.	22
1.22	An example of the integrated field required for the D0 and the OC dipoles.	22
2.1	The F factor as function of β^* for different values of Δ_{in}	24
2.2	Comparison between the $N_b(t)$ evolution with and without leveling.	27
2.3	The T_l value as function of the bunch population, N_{b0} , and for different β^*	28
2.4	The luminosity and total beam-beam tune shift for a $\beta^* = 0.15$ m.	30
2.5	A parametric studies of the luminosity with leveling.	31
2.6	A parametric studies of ΔQ_{bb} with leveling.	32
2.7	The meaning of the average turn-around time.	33
2.8	The different load lines in the luminosity plane.	34
2.9	Simulink TM model used for the luminosity leveling	35
2.10	Analytical and numerical results for the luminosity.	36
2.11	Analytical and numerical results on the beam-beam tune shift.	37
2.12	The integrated luminosity versus the total beam-beam tune shift.	39
2.13	The integrated luminosity versus the bunch population.	40
2.14	The integrated luminosity gain provided by the Early Separation Scheme	40
2.15	The bunch population, N_b , as function of the inner separation.	41
2.16	The luminous region size (RMS) during the run time.	41
3.1	The Early Separation Scheme closed orbit and induced dispersion.	45
3.2	The total dispersion of the machine.	45
3.3	The phase advance in the drift space of the Interaction Region.	46
3.4	The induced on-momentum β -beating for $Q=0.31$	47
3.5	The total tune shifts with respect to Δ_{in}	48
3.6	The tune diagram.	49

3.7	The similarity transformation \mathcal{C} .	51
3.8	The electric potential for a Gaussian charge distribution.	54
3.9	The ratio between σ_x and σ_y for the Beam 1 and the Beam 2 at IP1 and IP5.	55
3.10	The beam-wire approximation.	56
3.11	From the natural to the normalized phase space in a linear machine.	58
3.12	From natural to the normalized phase space in a non-linear machine.	58
3.13	The equivalence between the Ring A and the Ring B.	59
4.1	A linear machine in the phase space and in the frequency domain.	64
4.2	A non-linear machine in the phase space and in the frequency domain.	65
4.3	A “stable” particle in a non-linear machine.	66
4.4	An “unstable” particle in a non-linear machine.	67
4.5	The nominal LHC tune footprint.	68
4.6	A Gaussian beam in the physical plane and in the amplitude plane.	69
4.7	The meaning of the color coding in the amplitudes plane.	69
4.8	The color codes used in all the following amplitudes plots.	70
4.9	Particle initial conditions used in the tracking studies.	70
4.10	Final conditions after $3 \cdot 10^5$ turns in the tracking studies (single precision).	71
4.11	Nominal LHC tracking results.	72
4.12	Nominal LHC with ultimate current tracking results.	72
4.13	An example of beam-beam excitation.	73
4.14	An example of beam-beam compensation using a wire.	73
4.15	The beam separation with the D0 dipole at different distances from the IP.	74
4.16	Comparison of the (sorted) beam separation patterns.	76
4.17	The beam DA of the Early Separation Scheme at nominal tunes.	77
4.18	The beam DA of the Early Separation Scheme with optimized tunes.	78
4.19	The tune footprint with the Early Separation Scheme.	79
4.20	The SPS wires in the Straight Section 5 of the SPS tunnel.	80
4.21	The wires of the BBLR1 and the of the BBLR2 equipments.	80
4.22	The β -functions at the SPS wire positions.	81
4.23	The phase advances at the SPS wire positions.	81
4.24	The three SPS cycles used during the 2008-09 wire experiments at the SPS.	82
4.25	The orbit correction at 55 GeV/c.	83
4.26	The minimum normalized beam-wire separation in SPS.	84
4.27	The beam structure used in the SPS experiment.	85
4.28	An example of beam current behavior during the SPS experiments.	85
4.29	The dependence of $\Delta Q_{x,y}$ with respect to d at $p = 55$ GeV/c.	86
4.30	The beam losses induced by the wire versus wire current.	88
4.31	The Sp̄pS beam separation pattern.	88
4.32	The dynamic aperture simulated at (0.31, 0.32)	89
4.33	The losses due to the wire changing the vertical tune.	90
4.34	The compensation experiment in SPS at 9σ separation.	91
4.35	Distance scan at different tunes.	91
4.36	The losses induced by the wire with the optimized vertical tune (37 GeV/c).	92
4.37	The simulation of the dynamic aperture for the SPS distance scans.	93
4.38	The losses induced by the wire with the optimized vertical tune (55 GeV/c).	94
4.39	A current scan with the optimized vertical tune (55 GeV/c).	95
4.40	The difference in the tail of the beam profiles.	96
4.41	Coast at 120 GeV/c with a beam-wire separation of 8σ .	97
4.42	The different tune shift directions due to the BBLR1 and the BBLR2 polarity.	98
4.43	Coast at 120 GeV/c with a beam-wire separation of 9σ .	99
5.1	The logic flow used to dimension the Early Separation Scheme.	102
5.2	An artistic view of ATLAS and CMS detectors.	103
5.3	Artistic and simplified view of the longitudinal section of ATLAS and CMS.	104
5.4	Details of the possible position for the D0 dipole in ATLAS.	105
5.5	The magnetic field in ATLAS and CMS detectors.	106

5.6	A simplified FE model to compute the force on the yoke of the D0 dipole.	107
5.7	The beam normalized separation for one side of the Interaction Point.	108
5.8	The luminosity performance with the D0 dipole at 14 m from the IP.	109
5.9	The proposed position of the D0 dipole in the experiment.	110
5.10	The debris particles emerging from the Interaction Point.	112
5.11	The distribution of the energy of the collision debris.	113
5.12	The polar angle ϕ_s	113
5.13	The simplified model of the D0 magnet used in the simulation.	114
5.14	The average and peak power deposition along the D0 dipole.	115
5.15	The peak deposition on the D0 magnet as function of its aperture.	115
5.16	The average power deposition on the D0 dipole inner and outer layer.	116
5.17	The D0 magnetic field for different coil thickness.	118
5.18	The preliminary cross-section of the D0 dipole considered.	120
5.19	The magnetic load line of the D0 dipole.	121

Introduction

The Large Hadron Collider (LHC) is a 7 TeV proton-proton collider presently under commissioning at CERN, the European Organization for Nuclear Research. Since 2002, studies are on going with the goal of increasing its performance beyond the nominal one. The feasibility of an upgrade of the collider's luminosity and energy was initially explored. Presently, a great part of the efforts and studies are dedicated to the LHC Luminosity Upgrade: the technology that will be adopted in the Luminosity Upgrade could, later on, pave the way for the even more challenging Energy Upgrade.

The physics motivation behind the LHC Luminosity Upgrade is two-fold: it would allow to do precision physics of rare interactions at LHC and to expand, in practice, the energy reach of the machine. There is, in addition, a technical and practical motivation: after about 8 years of operations, some components of the machine and of the detectors will be damaged by the high radiation dose and they will need to be replaced. It appears natural to substitute them with increased performance components and systems, taking advantage of the experience acquired during the machine operations and of the latest technology advances in the accelerator field.

Due to complexity of the project, a staged approach is followed involving two phases. The framework of this study is the very ambitious luminosity upgrade of Phase II: its target is to gain an order of magnitude on the nominal LHC luminosity. Several proposals for the Phase II upgrade are under evaluation: one of these is the Early Separation Scheme, the topic of this thesis.

In the nominal LHC, the beams cross at an angle in the interaction points. This allows a single beam collision in the detector and minimizes the detrimental electromagnetic interactions between the beams on either side of the crossing point (parasitic beam-beam interactions). The crossing angle reduces however the geometric overlap between the beams and, consequently, the machine luminosity. The primary goal of the Early Separation Scheme is to decrease the crossing angle at the interaction point while maintaining a sufficient separation at the parasitic beam-beam encounters. It opens the possibility of a further reduction of the value of the β -function at the Interaction Point and of luminosity leveling.

A major issue of this scheme is the introduction of new dipoles inside the detectors and their integration. A compromise has to be found between minimum impact on the detector and efficiency of the scheme to increase the luminosity. This study is intended to explore the potential the Early Separation Scheme and the terms of compromise for a possible implementation. The results will be pursued by means of analytical and numerical approaches, using existing software and/or implementing specific code for addressing more peculiar tasks. Experimental studies will be conducted and compared to the simulations.

The major questions to address in the present thesis will be the followings:

- to identify the parameter space of the Early Separation Scheme. Starting from there, to define its hardware requirements in terms of dipoles and to choose the most adequate magnet technology to be adopted in the scheme,
- to describe, for the different scenarios of the upgrade, the potential of the scheme evaluating its flexibility and its gain in terms of integrated luminosity,
- to address in details the linear and non-linear beam dynamics effects by means of analytical approach and numerical tools,
- to investigate to what degree the non-linear dynamics effect of sLHC can be reproduced in other machines and to perform experiments at the CERN Super Proton Synchrotron in order to extrapolate the sLHC beam dynamics,
- to identify for the LHC high luminosity experiments the specific integration problems in terms of position and magnetic field compatibility,
- to perform an energy deposition study for the dipole closer to the interaction point and consider, if needed, adequate shielding strategy,
- to propose a preliminary cross-section of the dipole closer to the interaction point paying particular attention to the mechanical stress of the magnet's coil.

All the previous points will finally converge in a realistic proposal, common to the two experiments, featuring the best compromise between hardware integration difficulties and beam dynamics stability.

The present document is organized in five chapters.

In the first chapter the framework of the study is described, developing the motivations, the goals and the requirements for the LHC Luminosity Upgrade. We analyze the need for the crossing angle and its impact on the peak luminosity of the collider. After having introduced the Early Separation Scheme, we explain how it may overcome some limitations of the present machine. We compare the nominal LHC crossing scheme with the proposed one underlining its potential in terms of performance and its issues with respect to the integration in the detectors. An analysis of the integrated magnetic field required is given.

In the second chapter we introduce one of the most powerful aspect of the scheme: the luminosity leveling. After the description of the physical model adopted, we compare the results of its analytical and numerical solutions. All the potential improvement due to the Early Separation Scheme are shown on the luminosity plane (peak luminosity versus integrated luminosity).

In the third chapter the linear and non-linear beam dynamics effects induced by the Early Separation Scheme are discussed. The linear effects are analytically developed and verified using the MAD-X code. The scaling laws needed to compare the non-linear dynamics of different machines are investigated: this is a fundamental introduction and justification to the following chapter.

In the fourth chapter we present the simulations and the experiments performed in order to evaluate the non-linear effect of the proposed scheme. The simulation code is written and compiled for a multi-processors graphics card. The simulations outcome is compared with the results collected during about 100 hours of experiments in the Super Proton Synchrotron at CERN.

The fifth and last chapter is dedicated to the integration studies of the Early Separation Scheme with particular emphasis on the dipole closer to the interaction region. The specific integration difficulties in the ATLAS and CMS experiments are described. The power deposited on the dipoles from the non-elastic collision at the interaction point is computed using the FLUKA code. Technical solutions of Nb-Ti and Nb₃Sn superconductors are considered and compared with particular emphasis to their mechanical stress limitation. A cross-section for the magnet is proposed and optimized using the ROXIE code.

Finally, the results achieved in the present work are summarized in the Conclusions.

Chapter 1

The Concept of Early Separation

Contents

1.1	Motivations and goals for the LHC Luminosity Upgrade	3
1.2	The luminosity challenge in the sLHC	5
1.2.1	Luminosity for head-on collisions	5
1.2.2	The crossing scheme in the LHC	7
1.2.3	Other parameters influencing the luminosity	15
1.3	The Early Separation concept for the sLHC	18
1.3.1	Strategies for the luminosity increase	18
1.3.2	Principle and layout	19
1.3.3	The integrated magnetic field requested in the magnets	20

In this chapter the Early Separation Scheme concept is presented: it can contribute in a significant way to the Luminosity Upgrade of the Large Hadron Collider (LHC). In order to have the adequate context to introduce this work, the motivations, the goals and requirements for the Luminosity Upgrade are described (Section 1.1). A detailed explanation of the important parameters for the sLHC luminosity is given (Section 1.2). In addition to that, the crossing scheme in the nominal LHC is presented: the goal is to emphasize the differences and the analogies between the Early Separation Scheme and the present scheme (Section 1.3).

1.1 Motivations, goals and requirements for the LHC Luminosity Upgrade

The Large Hadron Collider (LHC, [1]) is the collider presently (2009) being commissioned at CERN (European Organization for Nuclear Research, [2]). Its mission is to push forward our knowledge in High Energy Physics and to test in a new energy domain the Standard Model, the current state of the classification of elementary particles. The LHC is set to explore with its six experiments (ALICE, ATLAS, CMS, LHCb, LHCf, TOTEM) an extremely rich physics landscape that spans from the Higgs particle physics, to the supersymmetry, extra dimensions, precision measurements of the top quark and quark-gluon plasma physics.

Starting from 2002, investigations on possible LHC upgrade paths have been addressed at CERN [3]. The major motivations of the sLHC are related both to physics [4] and technology considerations:

- with the expected LHC luminosity evolution, the discovery potential of the machine may saturate after 4 – 5 years of operations: several years may be required to halve the statistical error of the measurements. With the Luminosity Upgrade it would be possible to overcome this limit and perform precision physics at sLHC.
- a boost of the luminosity increases the discovery range of the machine itself. With sLHC it would be possible to observe the very rare processes in the LHC energy range that cannot be, in practice, investigated in the present machine pushing, de facto, the energy frontier even further.
- the final focusing quadrupoles due the high radiation dose may not survive for more than 8 – 10 years and their replacement has to be considered. For the new quadrupoles it is reasonable to exploit the experience that will be acquired during the first years of LHC operation together with the technology progress in the field. For similar reasons the ATLAS and CMS detectors plan a major maintenance intervention to replace their inner detectors.

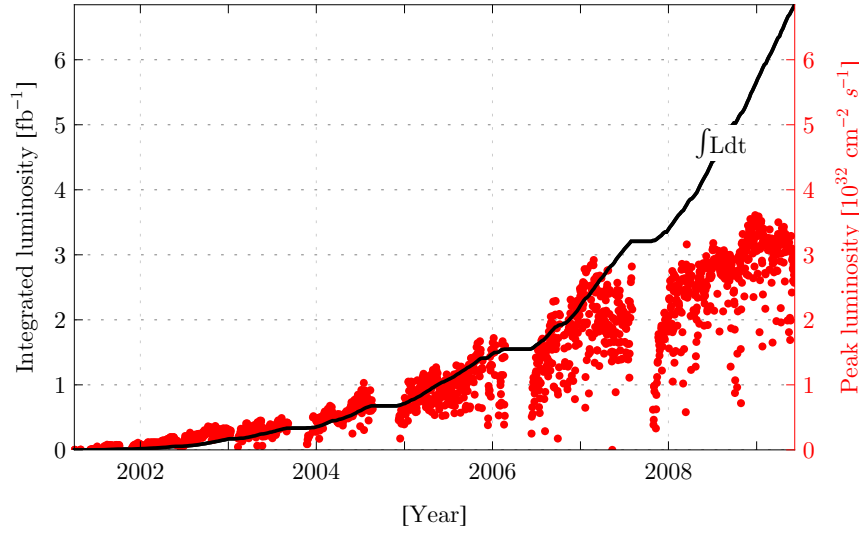


Figure 1.1: The Tevatron Run II experience. The performance of the collider increases year by year. The Run II provided, until now (2009), ≈ 50 times larger integrated luminosity with respect to the Run I. Courtesy of Dr. Vaia Papadimitriou.

To push the LHC beyond its nominal limits appears to be a very challenging and ambitious target both from the collider and the detectors side. The experience with the real machine, through a natural learning process, will most likely give important feedback for potential of performance improvements. Significant increase over the initial luminosity performance has been observed in other colliders, e.g., in the Tevatron at Fermi National Accelerator Laboratory ([5], Fig. 1.1). Because of the long development times, it is however necessary to anticipate possible solutions.

Due the technological complexity and financial cost of the an LHC upgrade, a staged approach has been preferred (Fig. 1.2 from [6]): a Phase I [7] and Phase II [8] Luminosity Upgrade have been foreseen. The Phase I will profit from the new LINAC4 and a new final focusing system to increase the peak luminosity by a factor 2 – 3. The Phase II, on the other hand, should push the machine performance to the limit of the LHC systems that are not planned to be upgraded, e.g., the LHC arcs. During the Phase II only the ATLAS and the CMS experiments (the two high luminosity experiments) are supposed to acquire data. The goal for the Phase II sLHC (later on simply referred to as sLHC) is to collect 3000 fb^{-1} of integrated luminosity per experiment in a reasonable period of time (3 – 4 years, [8]). This requires increasing the luminosity by a factor of ten to about $10^{35} \text{ cm}^{-2} \text{ s}^{-1}$. However, the proton-proton collisions for bunch crossing, the so-called multiplicity or pile-up, should be less than 400 (to compare to ≈ 22 in the nominal LHC).

For the LHC Luminosity Upgrade, the hardware of the collider’s arc and the detectors magnet system are not planned to be upgraded. A complete renewal on the Super Proton Synchrotron (SPS) Injectors [9] (e.g., LINAC4, already under construction [10], SPL, PS2) can be envisaged for sLHC with a partial upgrade of the SPS itself [11, 12].

All the proposed hardware solutions should be installed in a reasonable time (≈ 1 year) to minimize the shut-down period and to limit the consequent loss of integrated luminosity. In addition to that, they should be commissioned in the shortest amount of time and should not increase the complexity of the operations. Moreover, the collider’s subsystem possibly installed in the experimental caverns should allow an easy access to the detectors for the needed maintenance interventions.

The framework of this thesis is the Phase II LHC Luminosity Upgrade.

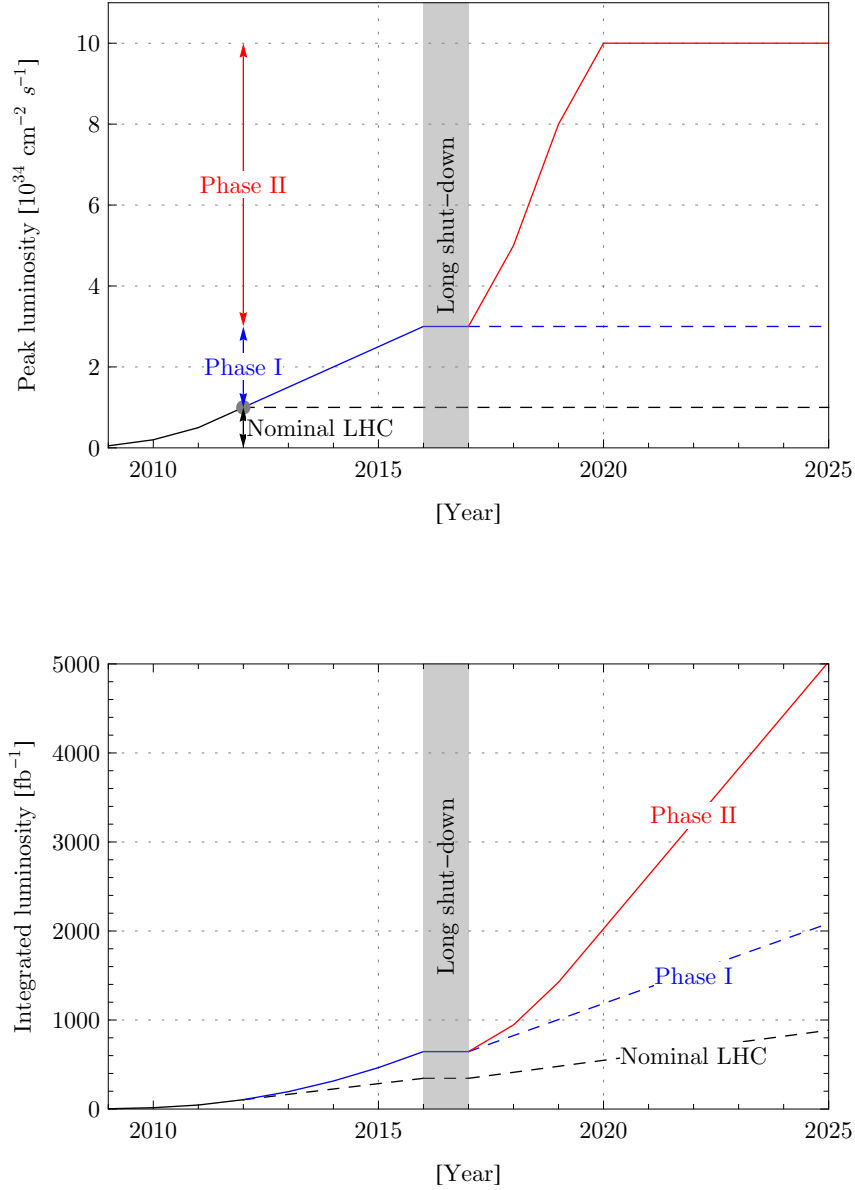


Figure 1.2: The reference evolution of the peak and integrated luminosity for the LHC and sLHC for each of the two high luminosity experiments. Data from the LHC Committee of July 2008.

1.2 The luminosity challenge in the sLHC

1.2.1 Luminosity for head-on collisions

In High Energy Physics, colliders are machines intended to collide two opposite beams of charged particle. Their aim is to reproduce and to investigate energetic particles interactions (events). LHC will be the sixth hadron collider ever built (after ISR [13] at CERN, Sp \bar{p} S [14] at CERN, Tevatron [15] at Fermi National Accelerator Laboratory, HERA [16] at the Deutsches Elektronen Synchrotron (a hadron-lepton collider) and RHIC [17] at Brookhaven National Laboratory).

Together with its center of mass energy, the collider luminosity L is the most important figure of merit

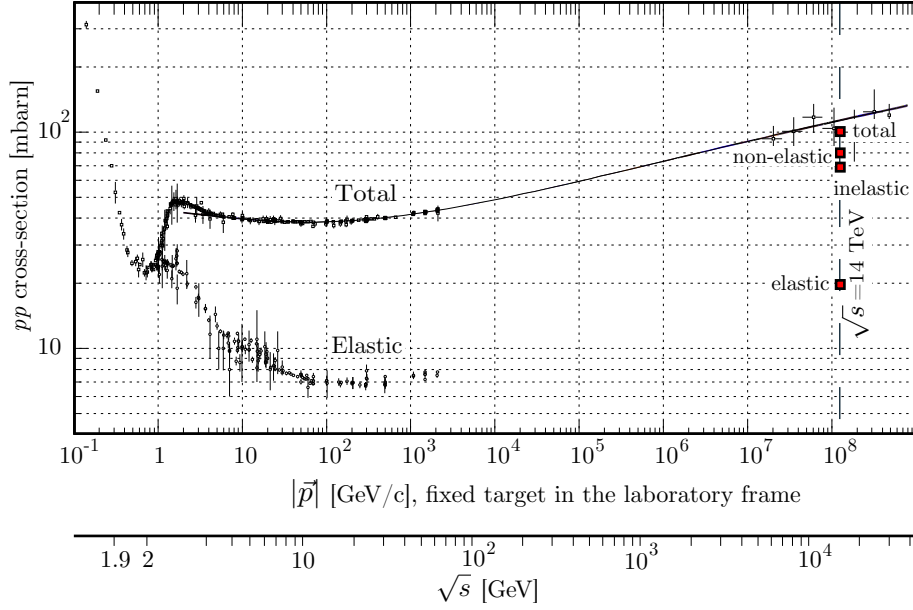


Figure 1.3: The pp cross-section. The assumptions for LHC at nominal collision energy are: a total pp cross-section of ≈ 100 mbarn, a non-elastic cross-section of ≈ 80 mbarn, an inelastic cross-section of ≈ 70 mbarn and, therefore, an elastic cross-section of ≈ 20 mbarn. Courtesy of the Particle Data Group [20].

of the machine. It is proportional to the events' time rate

$$\frac{dN_{event}}{dt} = L \sigma_{event}$$

where σ_{event} represents the cross-section of the event we are interesting in: it depends on the energy at the center of mass of the collision and it is a relativistic invariant [18].

The LHC nominal luminosity is $10^{34} \text{ cm}^{-2} \text{ s}^{-1}$ [1]. Assuming a non-elastic cross-section (the sum of the inelastic and the diffractive cross-sections) for the proton-proton interaction of 80 mbarn [19] [20] (see Fig. 1.3, 1 barn = 10^{-28} m^2), it yields a total of $8 \cdot 10^8$ collisions per second, that is ≈ 25 non-elastic collisions per crossing. For beams that have more than one bunch, the so-called multi-bunched beams, the luminosity can be expressed as

$$L = n_b f_b L_{SC} \quad (1.1)$$

where n_b is the number of the bunches per beam, f_b the beam revolution frequency and the L_{SC} is the single crossing luminosity, proportional to the number of events for a single bunch crossing. In the LHC there are 2808 bunches that travel with $f_b = 11.245 \text{ kHz}$, therefore, the single crossing luminosity is $3.56 \cdot 10^{30} \text{ cm}^{-2}$ [1].

The number of events per bunch crossing is the same in all the reference frames therefore the single crossing luminosity is a relativistic invariant. It can be expressed as [18, 21]

$$L_{SC} = R(\vec{v}_1, \vec{v}_2) \int_{-\infty}^{\infty} \int_{-\infty}^{\infty} \int_{-\infty}^{\infty} \int_{-\infty}^{\infty} N_1 N_2 \rho_1(x, y, s, t) \rho_2(x, y, s, t) dx dy ds dt \quad (1.2)$$

where

$$R(\vec{v}_1, \vec{v}_2) = \frac{\sqrt{c^2 \left\| \vec{v}_1 - \vec{v}_2 \right\|^2 - \left\| \vec{v}_1 \times \vec{v}_2 \right\|^2}}{c}.$$

The subscripts refer to the two colliding beams, c is the speed of light, $\rho_{1,2}$ and $\vec{v}_{1,2}$ are respectively the beam distribution and the beam velocity in the reference frame adopted (since L_{SC} is a relativistic invariant its value does not depend on the reference frame used for its computation), $N_{1,2}$ is the number of particles in the colliding bunches, x, y, s and t are the space-time coordinates.

Usually, in the surrounding of the beam Interaction Point (IP) of the collider, the colliding beam trajectories lie in the same plane. In the following we consider the reference systems shown in Fig. 1.4: we assume a vertical crossing, i.e., the beams move in the plane $\{y, s\}$. The $\{x, y, s\}$ represent the machine reference frame while the $\{x_{1,2}, y_{1,2}, s_{1,2}\}$ are, respectively, the reference frame of the two colliding beams. We use z to refer to a generic transverse coordinate (x or y). The θ_c represents the full crossing angle between the two beams. The general approach considered is to define the bunch distributions in the $\{x_{1,2}, y_{1,2}, s_{1,2}\}$ and express them, by means of a transformation, in the $\{x, y, s\}$ before computing the convolution of Eq. 1.2. The first and the second beam travels along the s_1 and $-s_2$ directions respectively.

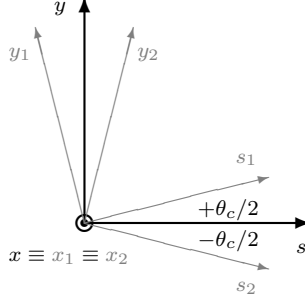


Figure 1.4: The geometric reference frames. The $\{x, y, s\}$ represent the machine reference frame while the $\{x_{1,2}, y_{1,2}, s_{1,2}\}$ are, respectively, the reference frame of the two colliding beams.

We assume no crossing angle between the beams ($\theta_c = 0$, i.e., head-on crossing), a constant β -function all along the luminous region and Gaussian beams, that is

$$\rho_{1,2}(x, y, s, t) = \frac{1}{2\sqrt{2}\pi^{3/2}\sigma_{x_{1,2}}\sigma_{y_{1,2}}\sigma_{s_{1,2}}} \exp\left(-\frac{x^2}{2\sigma_{x_{1,2}}^2} - \frac{y^2}{2\sigma_{y_{1,2}}^2} - \frac{(s \mp v_{1,2}t)^2}{2\sigma_{s_{1,2}}^2}\right)$$

where the σ 's represent the standard deviation of the distribution for the beam in the direction indicated by the subscripts. The transverse standard deviation of the distribution, σ_z , is given by

$$\sigma_z = \sqrt{\epsilon_z \beta_z}$$

where ϵ_z and β_z represent, respectively, the beam emittance and the betatron function along the z -direction [22]. From Eq. 1.2 we have

$$L_{SC} = \frac{N_1 N_2}{2\pi \sqrt{(\sigma_{x_1}^2 + \sigma_{x_2}^2)(\sigma_{y_1}^2 + \sigma_{y_2}^2)}}. \quad (1.3)$$

Considering symmetric and equal beams, $\sigma_{x_1} = \sigma_{x_2} = \sigma_{y_1} = \sigma_{y_2} = \sigma$ and $N_1 = N_2 = N_b$, from Eqs. 1.1-1.3, we get the well known formula

$$L = \frac{n_b f_b N_b^2}{4\pi \sigma^2}. \quad (1.4)$$

In the following Gaussian bunches are always assumed.

1.2.2 The crossing scheme in the LHC

The need for a beam crossing angle

In LHC the nominal peak luminosity will be reached with an unprecedented large number of bunches ($n_b = 2808$). To increase the number of bunches (keeping constant the machine circumference) the inter-bunch separation has to decrease: the LHC bunches are separated by 25 ns in time that, in the ultra-relativistic approximation ($v \approx c$), corresponds to a longitudinal separation of ≈ 7.5 m.

This separation is much shorter than the region where the two beams share the same vacuum pipe (~ 120 m), that is where they have the same reference orbit: in order to have a single beam collision in the detector they have to collide with an angle (Fig. 1.5) and travel on different paths (different closed orbits) until they are physically separated in two independent vacuum chambers. There is a second important reason for having a crossing angle and it is related to the collider and not to the detector: it is important to

limit as much as possible the electromagnetic interactions between the two beams (the so-called beam-beam effect). A strong beam-beam interaction can, in fact, rapidly degrade the beam lifetime, increasing the background in the experiment and decreasing the integrated luminosity of the collider (see Section 3.2). The collision (and the so-called head-on beam-beam effect) cannot be avoided since it is the essential feature of the collider, on the other hand all the parasitic interactions between the beams that occurs while the bunches are close to the Interaction Point but not colliding have to be minimized. They are referred to as long-range beam-beam encounters (LRBB).

In Fig. 1.6 the nominal crossing bumps are shown (the ring alignment orbit and the beam closed orbit). The 19 bunches represented are in the domain where the paraxial hypothesis can be considered still valid: in this hypothesis we assume that the transverse momentum of the particle is negligible with respect to the longitudinal one (see Chapter 3). This implies that the distance, along the beam closed orbit, of two points, A and B, is assumed equal to the distance, along the reference orbit, of the points A' and B', where A' and B' are the projections of A and B on the reference orbit (see Fig. 1.6, not to scale). This approximation allows us to evaluate the distance of two consecutive bunches on the ring alignment orbit even if they are traveling on the beam closed orbit. In Fig. 1.6 we represent plane curves (the crossing is in the plane of the machine, i.e., horizontal, like in the Interaction Point 5) but they can be skew (the crossing is vertical, like in the Interaction Point 1).

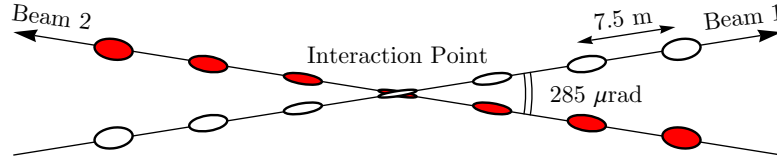


Figure 1.5: A simplified representation of the nominal crossing angle in LHC: when the bunch approaches the Interaction Point its transversal size reduces.

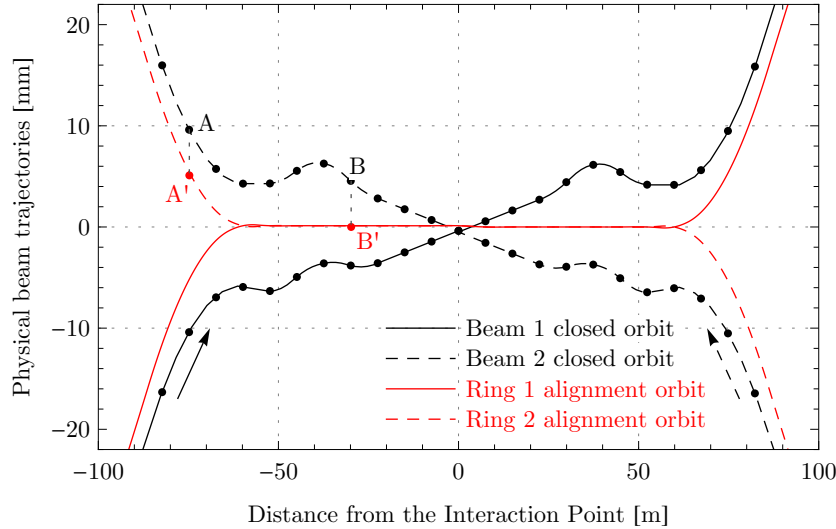


Figure 1.6: The physical beam trajectories of the nominal LHC crossing assuming horizontal crossing: the closed orbit bumps are horizontal and therefore in the same plane of the reference orbit. The black points on the orbits represents the equally spaced beam bunches (for the paraxial approximation, their projections in the s -direction are assumed to be also equally spaced): in the plot they do not appear equally spaced because the two axes are not to scale.

Though necessary, the presence of the crossing angle has a negative effect on the peak luminosity of the collider since it reduces the geometrical overlap between the two bunches with a negative effect on the single bunch luminosity (see Eq. 1.2). The crossing angle between the two beams, θ_c is the fundamental parameter of the present study.

It has an impact on the overall performance of the machine:

- a large crossing angle reduces the peak luminosity (see Section 1.2.2)
- a small crossing angle may reduce the beam lifetime, decreasing the integrated luminosity, and it may increase the detector background, thus reducing the detector efficiency (see Chapters 3 and 4).

As we discuss in Section 3.2.3, the beam-beam effect is dominated by the distance between the beams normalized by the beam transverse size (see Fig. 1.7). The Fig. 1.7 represents the so-called *beam separation pattern*: it shows, in the proximity of the Interaction Point, the normalized beam separation. Since the two beams move in opposite directions with the same speed they interact each ≈ 3.74 m in nominal LHC (half the bunch spacing). In the experimental drift space the separation is ≈ 9.5 σ .

It is useful to introduce here the *inner normalized separation*, Δ_{in} , proportional to the θ_c and to the inverse of the beam divergence at the Interaction Point:

$$\Delta_{in} = \theta_c \sqrt{\frac{\beta^*}{\epsilon}} \quad (1.5)$$

and therefore

$$\theta_c = \Delta_{in} \sqrt{\frac{\epsilon}{\beta^*}}. \quad (1.6)$$

The normalized inner separation of the nominal LHC is 9.5.

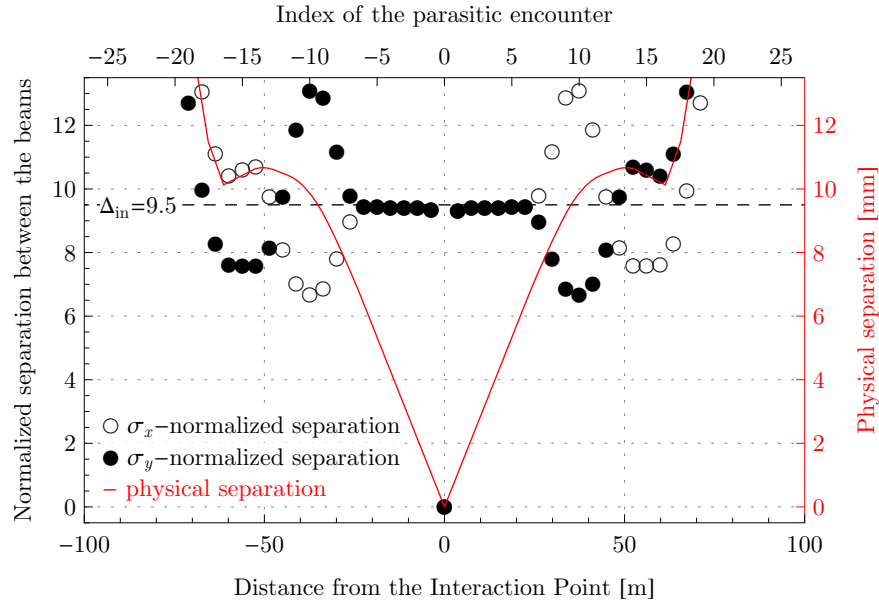


Figure 1.7: The beam separation pattern of the nominal LHC. In the plot we show the normalized beam separation of the nominal LHC assuming horizontal crossing angle. The normalization is done with respect to σ_x and σ_y of the Beam 1. It can be shown that all possible normalizations ($\sigma_{xB1}, \sigma_{xB2}, \sigma_{yB1}, \sigma_{yB2}$) are equivalent due to the phase advance at the Interaction Region (see Chapter 3). As reference, we show also the physical separation between the beams (right scale).

The luminosity loss factor due to the crossing angle

In the following the effect of θ_c on the peak luminosity is computed. Assuming that $\sigma_{x_1} = \sigma_{x_2} = \sigma_x$, $\sigma_{y_1} = \sigma_{y_2} = \sigma_y$, $\sigma_{s_1} = \sigma_{s_2} = \sigma_s$, $v_1 = v_2 = v$ we have, in the machine reference frame,

$$\rho_{1,2} = \frac{1}{2\sqrt{2}\pi^{3/2}\sigma_x\sigma_y\sigma_s} \exp\left(-\frac{(\mp v \sin(\theta_c/2)t + y \cos(\theta_c/2) - s \sin(\theta_c/2))^2}{2\sigma_y^2}\right) \times \exp\left(-\frac{(\mp v \cos(\theta_c/2)t + y \sin(\theta_c/2) + s \cos(\theta_c/2))^2}{2\sigma_s^2} - \frac{x^2}{2\sigma_x^2}\right)$$

and

$$\vec{v}_{1,2} = \{0, v \sin(\theta_c/2), \pm v \cos(\theta_c/2)\}. \quad (1.7)$$

From Eq. 1.2

$$L_{SC} = \frac{N_1 N_2 (\cos(\theta_c) + 1)}{4\sqrt{2}\pi\sigma_x \sqrt{\cos^2(\theta_c) (\sigma_y^2 (\cos(\theta_c) + 1) - \sigma_s^2 (\cos(\theta_c) - 1))}}.$$

Assuming $N_1 = N_2 = N_b$, from Eq. 1.1, we have

$$L = \frac{n_b f_b N_b^2}{4\pi \sigma_x \sigma_y} \tilde{F}_G(\theta_c, \sigma_y, \sigma_s), \quad (1.8)$$

where

$$\tilde{F}_G(\theta_c, \sigma_y, \sigma_s) = \frac{\sigma_y (\sec(\theta_c) + 1)}{\sqrt{2} \sqrt{\cos(\theta_c) (\sigma_y^2 - \sigma_s^2) + \sigma_y^2 + \sigma_s^2}}.$$

Expanding the trigonometric functions to the second order in θ_c with initial point $\theta_c = 0$ and, after simplifying ($\theta_c \ll 1$) we have

$$\tilde{F}_G(\theta_c, \sigma_y, \sigma_s) \approx F_G(\theta_c, \sigma_y, \sigma_s) = \frac{1}{\sqrt{1 + \theta_{PA}^2}} \quad \text{where} \quad \theta_{PA} = \frac{\theta_c \sigma_s}{2\sigma_y}.$$

The quantity indicated with θ_{PA} is the so-called Piwinski angle [23]. It is sometime useful to express the θ_{PA} as function of β^* and of Δ_{in} (from Eq. 1.6)

$$\theta_{PA} = \frac{\theta_c \sigma_s}{2\sqrt{\beta_y^* \epsilon_y}} = \frac{\Delta_{in} \sigma_s}{2\beta_y^*}. \quad (1.9)$$

In Fig. 1.8, the geometrical loss factor, F_G , is shown as function of the Piwinski angle: in the nominal LHC it introduces a loss of peak luminosity of more than 15%. It is worth noting that increasing the Piwinski angle the geometrical loss factor decreases rapidly.

For completeness we report in Fig. 1.8, right scale, the relative error between the function \tilde{F}_G and the geometrical loss factor: it is negligible (in the 10^{-7} range in a large space of the parameters) that is why in the rest of the present study we will always refer to the geometrical loss factor, F_G .

Implementation of the nominal LHC crossing scheme

In the Long Straight Section (LSS), the straight region (i.e., without arc dipoles) in the tunnel that hosts the Interaction Region (Fig. 1.9), the alignment orbit of the machine is set by the dipoles D1 and D2. Differently from arc dipoles, they are used for the separation and recombination of the two beams. The alignment orbit is the path along which the magnetic center of the machine elements is aligned. The two alignment orbits lie in the horizontal plane like everywhere else in the machine (Figs. 1.12). In Fig. 1.9 the magnets of the LSS are shown: together with the dipole magnets D1 and D2 there are nine quadrupole units for each side of the Interaction Region: Q1, Q2a, Q2b, Q3, Q4, Q5, Q6, Q7 and Q7b. The first four quadrupoles units (Q1, Q2a, Q2b, Q3) belong to the so-called *triplet* (since they are equivalent to three lens: Q2a and Q2b, in fact, have the same polarity and correspond therefore to a single lens), the others are the *matching section* quadrupoles.

For sake of completeness the horizontal and vertical β -functions in the Interaction Region are, respectively, reported in Figs. 1.10 and 1.11.

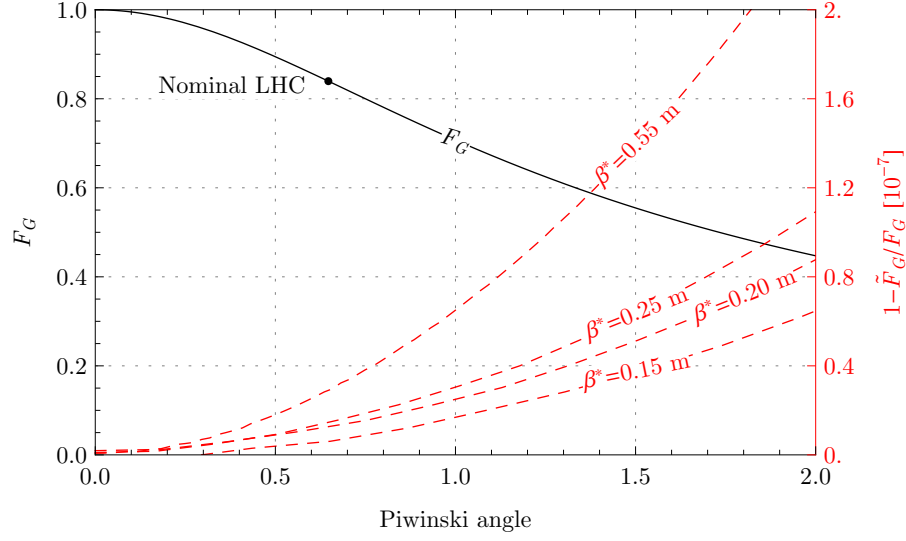


Figure 1.8: The geometric factor F_G as function of the Piwinski angle. The relative error between \tilde{F}_G and F_G is also shown, in units of 10^{-7} : we can conclude that, in the domain of interest, the F_G and \tilde{F}_G differ by less than 10^{-6} units.

In the nominal LHC the beams collide in Interaction Point 1, IP1, and Interaction Point 5, IP5, with a full crossing angle, θ_c , of $285 \mu\text{rad}$. In the region enclosed between the D1's the closed orbits of the two beams lie in the same plane: this plane is vertical in IP1 (Fig. 1.13) and horizontal in IP5. The trajectory of the beams in the laboratory reference frame is the sum of the ring alignment orbits and of the separation bumps (beam closed orbits).

During the LHC injection, ramp and squeeze the two beams are not colliding: nevertheless all crossing bump magnets are switched on and ramp together with the beam momentum. The collisions do not occur because the beams are separated in the other plane of the crossing angle by separation bumps (therefore the separation is horizontal in IP1 and vertical in IP5). To put the beams into collision these separation bumps are rapidly switched off. The present crossing scheme is quite complex: it extends until the quadrupole Q6 (for a total length larger than 350 m). The orbit bumps go through many quadrupoles from Q1 to Q6. For each Interaction Point, six dipoles per beam steer the closed orbit [1][25]: they can be single-aperture combined horizontal and vertical correctors (MCBX, Fig. 1.14, *left*) or twin-aperture dipoles individually powered and arranged so that the field in one aperture is vertical and the other horizontal (MCBC and MCBY, Fig. 1.14, *center* and *right*). This introduces an additional complexity due to the magnetic cross talk between the two planes (MCBX) or the two apertures (MCBC and MCBY) that can give rise to a coupling between the vertical and horizontal closed orbits of the same beam and between the closed orbits of the two beams.

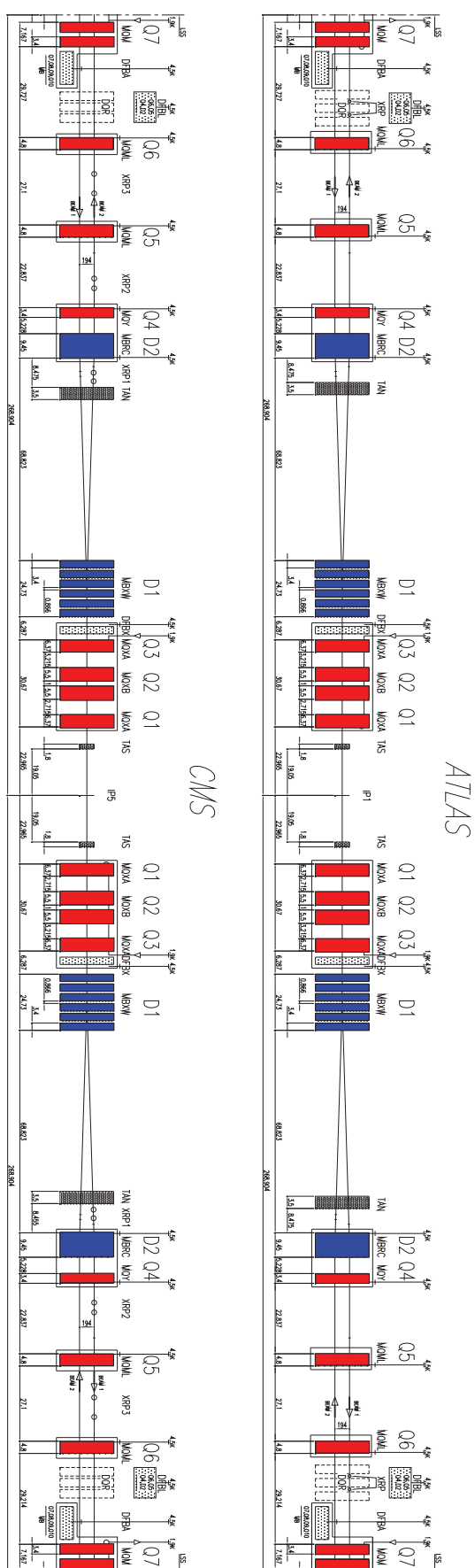
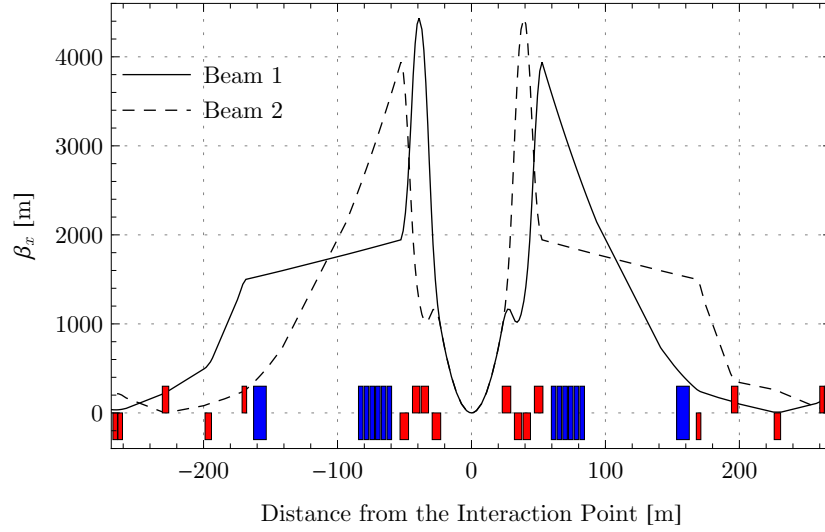
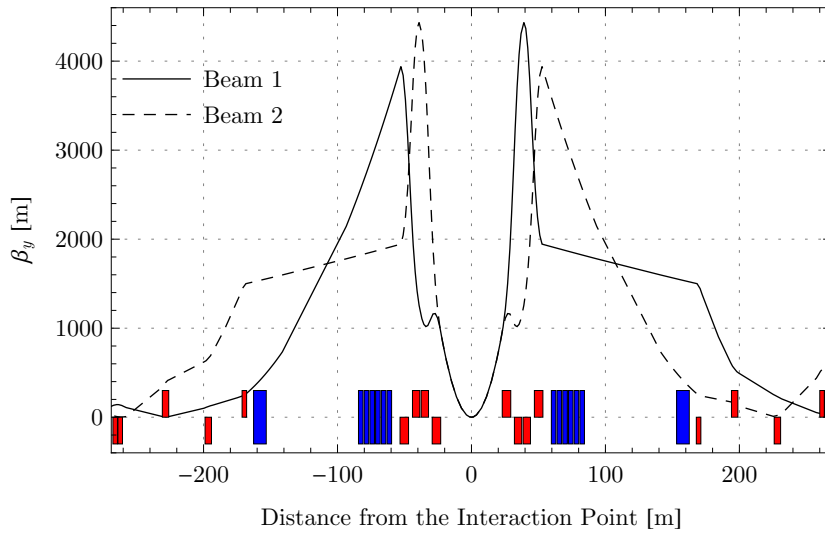


Figure 1.9: The Interaction Region layout of ATLAS and CMS in the Long Straight Section (LSS) [24]. They are almost identical apart from the detectors of the LHCf experiment in IR1 and the TOTEM experiment in IR5.

Figure 1.10: The β_x -function at the Interaction Regions 1 and 5.Figure 1.11: The β_y -function at the Interaction Regions 1 and 5.

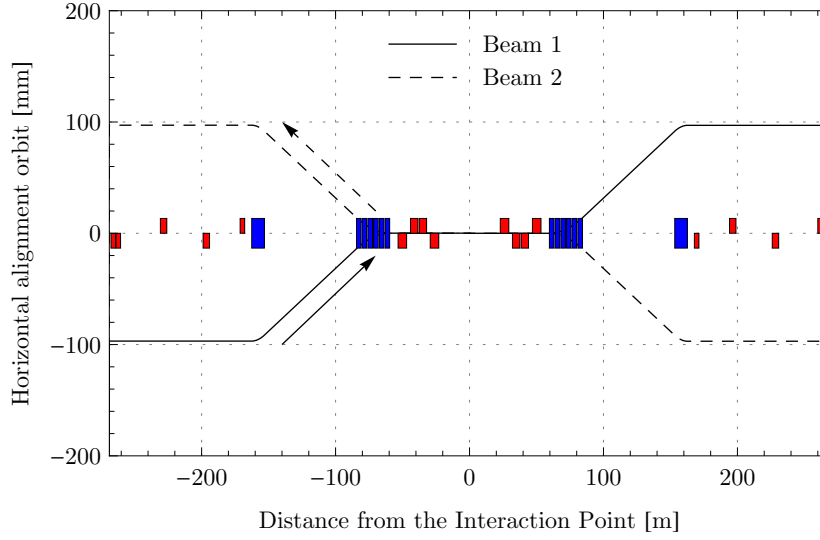


Figure 1.12: The horizontal reference orbit at the Interaction Regions 1 and 5. In the vertical plane the reference orbit is always equal to zero.

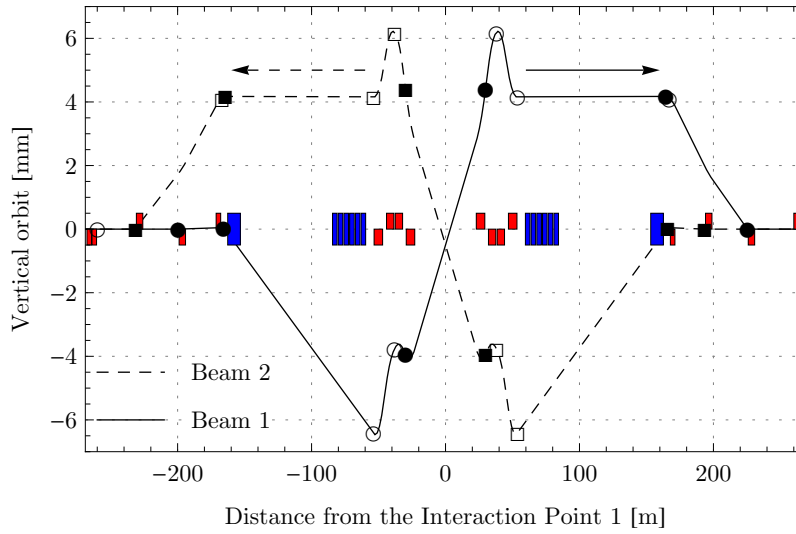


Figure 1.13: The closed orbit in the Interaction Region 1. The Beam 1 and Beam 2 orbit correctors are marked, respectively, with \circ and \square (we use the full marker if the magnet is switched on, the empty marker if it is switched off). The horizontal closed orbit is equal to zero in the Interaction Region 1.

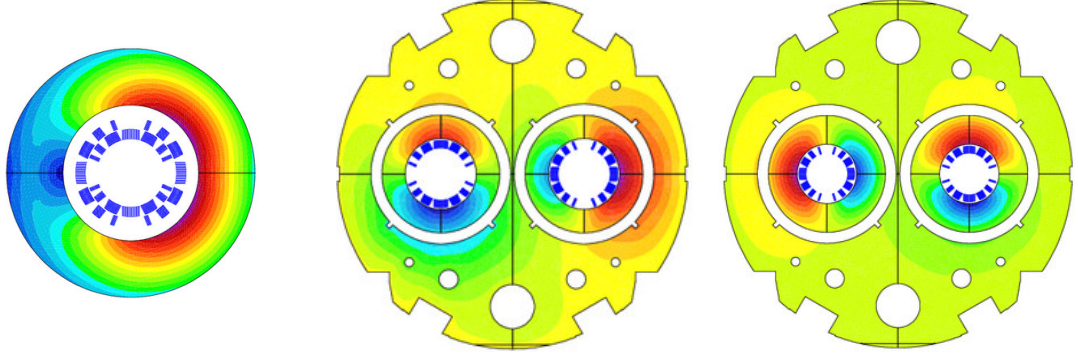


Figure 1.14: The cross-section of the single-aperture nested orbit corrector MCBX (*left*, it combines horizontal and vertical magnetic field), and of double-aperture orbit corrector MCBY (*center*) and MCBC (*right*). The drawings are not to scale. The colors represent the intensity of the magnetic vector potential. Courtesy of S. Russenschuck [26].

1.2.3 Other parameters influencing the luminosity

In this section other potential source of luminosity losses are investigated. The following analysis shows that their effect is negligible in the assumed parameter space for the sLHC.

The hourglass effect in sLHC

For the luminosity upgrade, it is foreseen to reduce the β -function at the Interaction Point, IP, by a significant amount. This could give rise to a relevant loss of performance due to the so-called hourglass effect [18].

Considering that the β -function is varying along the s -coordinate and that the IP, $s = 0$, is in a drift space where the β -function is minimized ($\beta_{IP} = \beta(0) = \beta^*$, $d\beta/ds = 0$ at the IP), we have, in the machine reference frame,

$$\beta(s) = \beta^* + \frac{s^2}{\beta^*} \quad (1.10)$$

therefore, assuming that the β -functions are equal in the two planes and for the two beams, no crossing angle between the beams and $v_1 = v_2 = v$, we have

$$\rho_{1,2} = \frac{1}{2\sqrt{2}\pi^{3/2}\sigma_{s1,2}^2\sqrt{\epsilon_{x1,2}(s^2/\beta^* + \beta^*)}\sqrt{\epsilon_{y1,2}(s^2/\beta^* + \beta^*)}} \times \exp\left(-\frac{(s \mp vt)^2}{2\sigma_{s1,2}^2} - \frac{x^2}{2\epsilon_{x1,2}(s^2/\beta^* + \beta^*)} - \frac{y^2}{2\epsilon_{y1,2}(s^2/\beta^* + \beta^*)}\right) \quad (1.11)$$

where $\epsilon_{x1,2}$ and $\epsilon_{y1,2}$ are the horizontal and vertical emittances of the two beams. Replacing the Eq. 1.11 in the Eq. 1.2, we have

$$L_{SC} = \frac{N_1 N_2}{\sqrt{2\pi(\epsilon_{x1} + \epsilon_{x2})(\epsilon_{y1} + \epsilon_{y2})(\sigma_{s1}^2 + \sigma_{s2}^2)}} \exp\left(\frac{2\beta^{*2}}{\sigma_{s1}^2 + \sigma_{s2}^2}\right) \text{erfc}\left(\frac{\sqrt{2}\beta^*}{\sqrt{\sigma_{s1}^2 + \sigma_{s2}^2}}\right). \quad (1.12)$$

If we assume symmetric beams ($\epsilon_{x1} = \epsilon_{x2} = \epsilon_{y1} = \epsilon_{y2} = \epsilon$, $\sigma_{s1} = \sigma_{s2} = \sigma_s$ and $N_1 = N_2 = N_b$) and replace the Eq. 1.12 in the Eq. 1.1,

$$L = \frac{n_b f_b N_b^2}{4\pi \sigma^2} F_{HG}\left(\frac{\beta^*}{\sigma_s}\right)$$

where the F_{HG}

$$F_{HG}\left(\frac{\beta^*}{\sigma_s}\right) = \frac{\sqrt{\pi}\beta^*}{\sigma_s} \exp\left(\frac{\beta^{*2}}{\sigma_s^2}\right) \text{erfc}\left(\frac{\beta^*}{\sigma_s}\right).$$

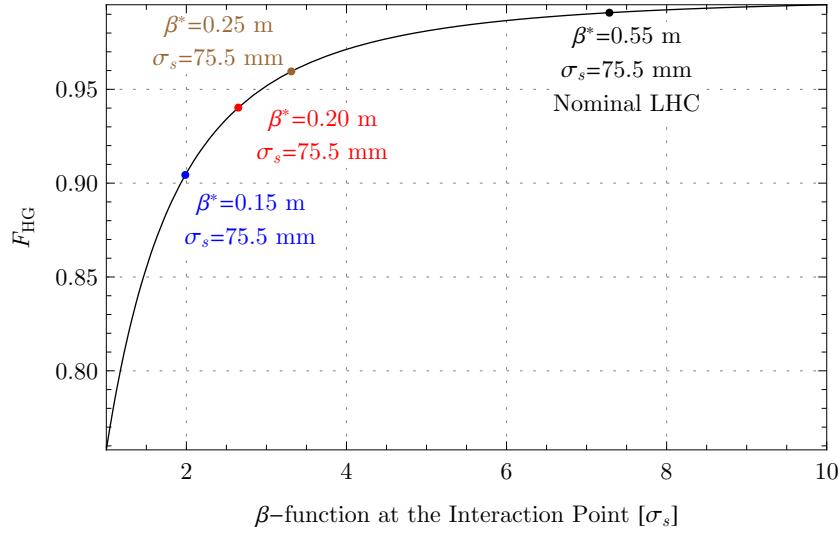


Figure 1.15: The hourglass factor F_{HG} (vanishing crossing angle).

The F_{HG} represents the so-called *hourglass factor* [27] .

In Fig. 1.15 the hourglass factor is shown for different β^*/σ_s values ($\theta_c = 0$): it is negligible for the nominal LHC and causes a loss in peak luminosity smaller than the 10% for $\beta^* = 0.15$ m (as we discuss in Chapter 2 this seems to be the lower reachable value of β^* with the present LHC arc constraints and the present magnet technology). In the following paragraphs the coupling between the hourglass effect and a non vanishing crossing angle will be discussed.

The combination of the hourglass effect and the geometrical loss factor

It is interesting to analyze the coupling between the luminosity loss due to the hourglass effect and the one due to the beam crossing angle (θ_c). In that case, due to the increased complexity, it is not possible to solve in a closed form the integral of Eq. 1.2.

The charge density of the two bunches can be expressed as

$$\rho_{1,2} = \frac{1}{(2\pi)^{3/2}\epsilon(s^2/\beta^* + \beta^*)\sigma_s} \exp\left(\frac{(-vt\sin(\theta_c/2) + y\cos(\theta_c/2) \mp s\sin(\theta_c/2))^2}{-2\epsilon(s^2/\beta^* + \beta^*)}\right) \times \exp\left(-\frac{(\mp vt\cos(\theta_c/2) \pm y\sin(\theta_c/2) + s\cos(\theta_c/2))^2}{2\sigma_s^2} - \frac{x^2}{2\epsilon(s^2/\beta^* + \beta^*)}\right)$$

and Eq. 1.7 still holds. Replacing the previous equations in Eq. 1.2 yields

$$L_{SC} = \frac{N_1 N_2}{4\pi\sigma_x\sigma_y} F(\theta_c, \beta^*, \epsilon, \sigma_s),$$

where F is

$$\int_{-\infty}^{\infty} \frac{\beta^{*2} \cos^2(\frac{\theta_c}{2}) \sec(\theta_c)}{\sqrt{\pi}(s^2 + \beta^{*2})\sigma_s} \exp\left(\frac{s^2(\cos(\theta_c)(s^2\epsilon + \beta^{*2}\epsilon - \beta^*\sigma_s^2) + s^2\epsilon + \beta^*\sigma_s^2 + \beta^{*2}\epsilon)}{-2\epsilon(s^2 + \beta^{*2})\sigma_s^2}\right) ds.$$

In Fig. 1.16, the comparison between the F and the F_G is illustrated. For normalized inner separation, Δ_{in} , greater or equal than 4 (and in the range of the nominal σ_s and ϵ), it is possible to observe that F and F_G differ by less than 2%. The dominant effect is therefore related to the crossing angle and not to the hourglass effect. Finally we have

$$L = \frac{n_b f_c N_1 N_2}{4\pi\sigma_x\sigma_y} F(\theta_c, \sigma_y, \sigma_s) \quad (1.13)$$

where

$$F(\theta_c, \sigma_y, \sigma_s) \simeq \frac{1}{\sqrt{1 + (\theta_c \sigma_s / (2\sigma_y))^2}} \quad \text{if } \Delta_{in} \gtrsim 4. \quad (1.14)$$

In Fig. 1.17, the F and the F_G factors are shown as function of the normalized inner separation for different

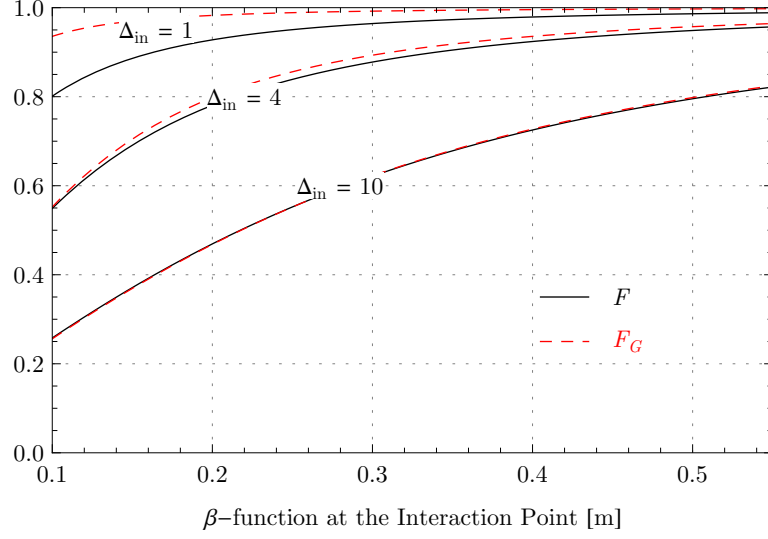


Figure 1.16: Comparison between F and F_G factors ($\sigma_s = 75.5$ mm, $\epsilon = 5 \cdot 10^{-10}$ m·rad).

β^* : the plot confirms the validity of the approximation presented in Eq. 1.14.

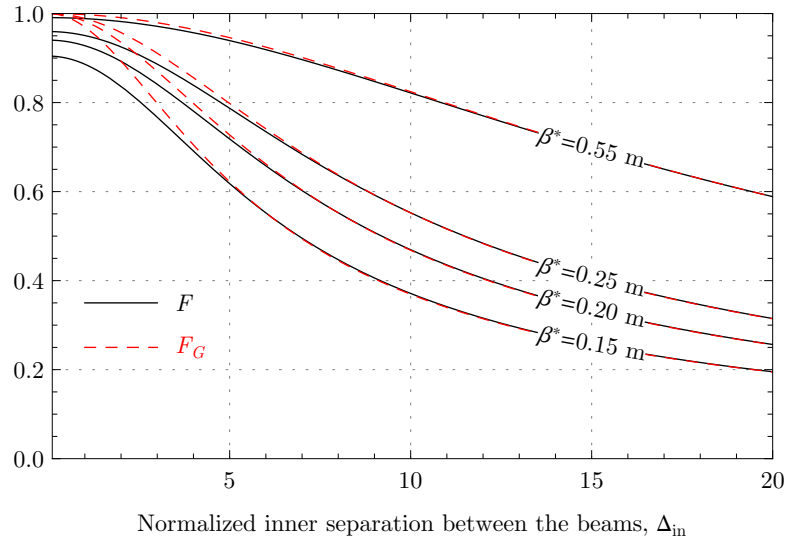


Figure 1.17: The F and F_G factors as function of the inner normalized separation Δ_{in} ($\sigma_s = 75.5$ mm, $\epsilon = 5 \cdot 10^{-10}$ m·rad). It is possible to observe that for $\Delta_{in} \gtrsim 4$, the two curves differ by less than 2%.

The Crab Crossing Scheme and its luminosity reduction factor

The Crab Crossing Scheme is a beam crossing scheme [28] where, differently from the nominal and the Early Separation Scheme, the bunches rotate longitudinally with respect to the beam closed orbit. This allows to have a perfect head-on collision even with a non-vanishing crossing angle between the beams, making possible, at the same time, an increase of the peak luminosity (due to the head-on crab-crossing) and a decrease of the strength of the beam-beam interaction (due to the beam separation provided by crossing angle).

The longitudinal bunch rotation is carried out by a radio-frequency cavity, the so-called RF crab cavity, that gives a variable kick to the bunch: the kick is proportional to the longitudinal distance from the bunch center, therefore, each “slice” of the bunch has its proper closed orbit. The RF crab cavities have been tested with success in lepton machines but they have never been used in hadron machines. Differently from the Early Separation Scheme (see Chapters 4 and 5), they can make perfect head-on collisions without requiring the installation of additional hardware in the detectors. Similarly to the Early Separation Scheme, they can level the peak luminosity via the crossing angle by changing the voltage of the RF cavities. Therefore their potential for the machine and the detectors is very large. Studies on their technological feasibility for the LHC upgrade are on going. The outcome of this research will define the maximum angle of the crab rotation that is compatible with a safe operation of the sLHC. On one hand, if this angle is sufficiently large to compensate the sLHC crossing angle then the crab-crossing are a much better solution for the upgrade than the Early Separation Scheme. On the other hand, if this angle is only a fraction of the needed one, the crab crossing can be used together with the Early Separation Scheme to reduce as much as possible the geometrical loss due to the crossing angle.

In the following the luminosity effect of the ideal head-on crab crossing is shown. In the computation we neglect the hourglass effect and the crab rotation of the bunch is assumed to be negligible in the luminous region. For the Crab Crossing Scheme, assuming the ys -plane as crossing plane, we have

$$\rho_{1,2} = \frac{1}{2\sqrt{2}\pi^{3/2}\sigma_x\sigma_y\sigma_s} \exp\left(-\frac{(y - vt \sin(\theta_c/2))^2}{2\sigma_y^2} - \frac{(s \mp vt \cos(\theta_c/2))^2}{2\sigma_s^2} - \frac{x^2}{2\sigma_x^2}\right)$$

and Eq. 1.7 still holds. After replacing the previous equation in Eq. 1.2, we have

$$L_{SC} = \frac{N_1 N_2 \cos(\theta_c/2)}{4\pi\sigma_x\sigma_y}.$$

It is possible to conclude that the luminosity loss factor due to the crab crossing, $F_{CC} = \cos(\theta_c/2)$, can be neglected ($F_{CC} \approx 1$) for $\theta_c < 10^{-2}$ rad, i.e., in the expected range for the LHC upgrade [29].

1.3 The Early Separation concept for the sLHC

1.3.1 Strategies for the luminosity increase

Recalling the Eqs. 1.9, 1.13, 1.14, assuming round beams (i.e., $\sigma_x = \sigma_y = \sigma = \sqrt{\epsilon \beta^*}$) and $N_1 = N_2 = N_b$, we have

$$L = \frac{f_c n_b N_b^2}{4\pi \epsilon \beta^*} F$$

$$F \simeq \frac{1}{\sqrt{1 + (\Delta_{in}\sigma_s / (2\beta^*))^2}} \quad \text{if } \Delta_{in} \gtrsim 4,$$

where ϵ is a property of the beam (its emittance) and β^* is a property of the collider (the value of the betatron function at the Interaction Point). In the previous formulas we consider N_b and ϵ at the start of the physical run therefore L , the generic instantaneous luminosity, represents in this particular case the peak luminosity of the machine. Two strategies appear possible to increasing the peak luminosity L :

- increase the beam current $f_c \cdot n_b \cdot N_b$: for the same total beam current variation, an increase of bunch current (N_b) produces a higher gain in peak luminosity since $L \propto N_b^2$. In a superconducting machine like the LHC a beam current increase can make the machine operation difficult and possibly risky: all the machine subsystems are affected by that choice since it is not a local modification and the stored beam energy in the machine is increased. Due to the fixed length of the collider and its ultra-relativistic beams, f_c is almost constant. For that reason it is usual to designate as beam current the

beam charge itself ($n_b \cdot N_b$). Moreover, a current increase will strengthen the beam-beam interaction (see Section 3.2.2) therefore, in order to preserve a reasonable beam lifetime, an increase of the crossing angle (i.e., of the normalized inner separation Δ_{in}) has to be foreseen, decreasing the peak luminosity (see Fig. 1.17).

- decrease the beam r.m.s. transversal size at the Interaction Point, $\sigma = \sqrt{\epsilon \beta^*}$. Reducing the ϵ requires an important intervention on the injection chain of the collider and increase the energy density of the beam all along the ring. On the other hand, reducing β^* can be almost transparent for the rest of the machine and therefore easier. A reduction of the beam size has an impact of the beam-beam interaction too: we need to operate at constant Δ_{in} (see Section 3.2.3). If we reduce β^* we have to increase the crossing angle to keep constant the normalized inner separation (see Eq. 1.5 and Fig. 1.16), while reducing the beam emittance will have no direct effect on Δ_{in} (see Eq. 1.9). Nevertheless, in analogy to the case of an increase of the beam current, a reduction of the beam emittance makes the beam-beam interaction stronger. Therefore, also in this case, an increase of the crossing angle is required since we have to increase Δ_{in} to decrease the beam-beam effect (see Section 3.2.3).

We can conclude that, for the nominal LHC crossing scheme, an increase of peak luminosity implies an increase of the beam crossing angle. In the following section we explain how this conclusion is modified with an Early Separation Scheme.

The goal of the upgrade is however not to increase the peak luminosity alone but to maximize the integrated luminosity. In Chapter 2, the relation between these two quantities is analyzed in details and it is shown that in the expected sLHC regime an increase of beam current cannot be avoided to reach the Phase II targets (3000 fb^{-1} in a reasonable time). Moreover it is shown that the Early Separation Scheme, through the luminosity leveling, can give a significant contribution to the machine integrated luminosity.

1.3.2 Principle and layout

The Early Separation scheme is one possible solution for achieving the integrated sLHC luminosity target and, as already mentioned, it is being considered for the LHC Luminosity Upgrade Phase II.

Its main goals are

- to reduce the crossing angle in order to increase the geometric loss factor F and therefore the integrated luminosity
- to allow a dynamic adjustment of the luminosity (leveling) through the control of the crossing angle (therefore the control of F) in order to reduce the peak luminosity of the machine.

This is possible by decoupling the crossing angle θ_c , from the beam separation in the rest of Interaction Region: this offers a great flexibility during the sLHC operations and, as will be shown, significant gain in integrated luminosity. A complete analysis of the performance of the scheme is given in Chapter 2: the expected gain in integrated luminosity is within the 25–30% range and it can be delivered without increasing the peak luminosity and keeping the detector multiplicity pile-up relatively low (≈ 150 events per crossing at 25 ns bunch separation). If the number of protons per bunch can be increased up to $2.3 \cdot 10^{11}$, it would be possible to collect 3000 fb^{-1} over a period of 6.5–7 years.

The Early Separation Scheme (Fig. 1.18, *bottom*) consists of two dipoles (designated as D0, since it comes before the D1, and the OC, acronym of orbit corrector) on each side of each high luminosity Interaction Point, IP1 (ATLAS, [30]) and IP5 (CMS, [31]). All dipoles are single-aperture magnets and are positioned in the drift space between the final focusing quadrupoles (the triplet, Fig. 1.18). The D0 is closer to the Interaction Point than the OC (see Fig. 1.18).

In the nominal LHC the front face of the triplet is at 22.95 m from the Interaction Point (IP) and, between the triplet and the IP, a copper absorber (TAS) is installed. Its entry face is at 19.05 m from the IP: this position can be considered as the interface between the LHC tunnel and the experimental cavern.

In the present machine, all the active elements of the collider are in the tunnel: with the Early Separation Scheme an integration of relatively large orbit correctors in the detectors is required. In this study a proposal of an identical Early Separation Scheme layout in the two IPs is preferred: in spite of the differences between ATLAS and CMS structures, the priority is to give to the two detectors identical performance in term of luminosity. On top of that it seems a reasonable choice to reduce the complexity in the machine during the commissioning, the operation and the maintenance.

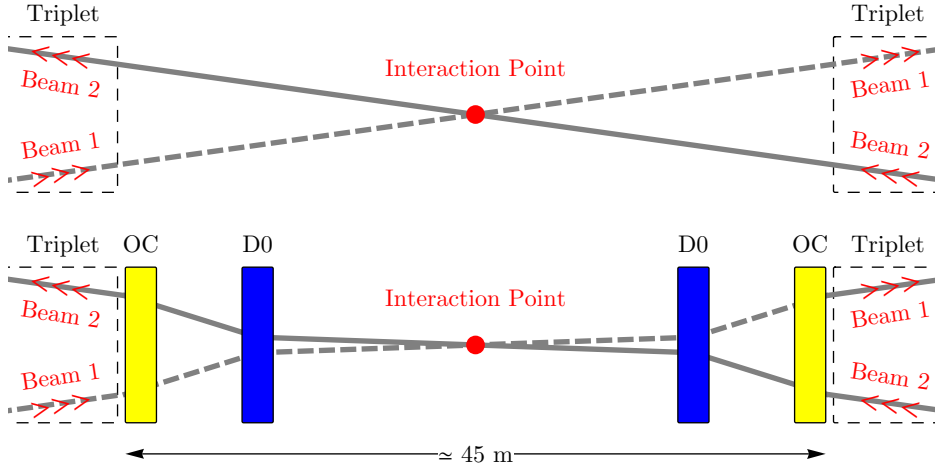


Figure 1.18: Comparison between the nominal crossing scheme (*top*) and the Early Separation Scheme (*bottom*). Not to scale. The Early Separation Scheme can reduce the crossing angle keeping the same beam closed orbits in the triplets.

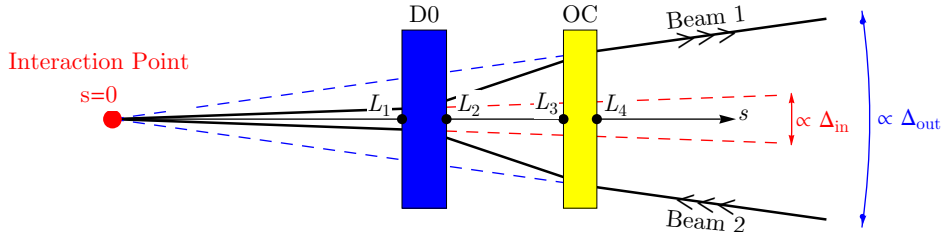


Figure 1.19: Layout of the Early Separation Scheme. The meaning of the symbols used in this section is indicated. In particular we can observe that in the Early Separation Scheme two angles are defined and they are proportional to the Δ_{in} and the Δ_{out} . In the nominal crossing scheme we have instead $\Delta_{in} \equiv \Delta_{out}$.

1.3.3 The integrated magnetic field requested in the magnets

The integrated magnetic field requested in the D0 and in the OC dipoles depends on several parameters related to the Early Separation layout (position of the D0 and of the OC), to the final focusing (β^* , Δ_{in} , beam separation in the triplet) and to the beam itself (ϵ , magnetic rigidity). Since the bump provided by the Early Separation Scheme is confined in the drift region between the triplets, it is possible to have a simple analytical formula for the closed orbit matching.

The actual machine closed orbit will be given, due to the linearity, by the sum of the closed orbit without the Early Separation Scheme (considering all other LHC orbit correctors, Section 1.2.2) and the one provided by the scheme itself. It modifies the closed orbit only in the plane of the beam crossing, its bump is antisymmetric with respect to the Interaction Point and will close after the OC dipole (to be totally decoupled from the rest of the machine, in particular to the closed orbit in the triplets): this implies that the field direction of the four dipoles is perpendicular to the plane of the bump, the field direction of the OC dipole is opposite to that of the D0 dipole. The polarity of the D0 dipoles (and of the OC dipoles) in the two sides of the Interaction Point is opposite (Fig. 1.20).

In the following, due to symmetry, only half of the Interaction Region is considered ($s > 0$). It is possible to express the bump propagated by the Early Separation Scheme, $z(s)$, with the following general function (thick element approach)

$$z(s) = \begin{cases} z'_0 s & 0 \leq s < L_1 \\ \frac{1}{2B\rho} B_{D0} (s - L_1)^2 + z'_0 s & L_1 \leq s < L_2 \\ \frac{1}{2B\rho} B_{D0} (-2L_1 s + L_2 (2s - L_2) + L_1^2) + z'_0 s & L_2 \leq s < L_3 \\ \frac{1}{2B\rho} (B_{D0} (-2L_1 s + 2L_2 s + L_1^2 - L_2^2) + B_{OC} (s - L_3)^2) + z'_0 s & L_3 \leq s < L_4 \end{cases} \quad (1.15)$$

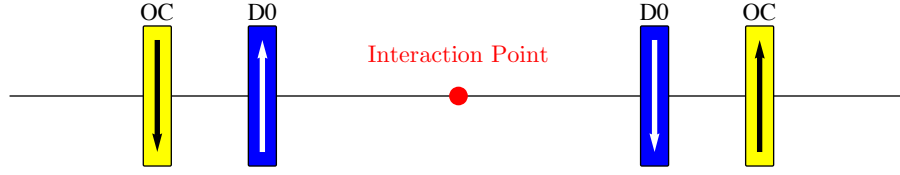


Figure 1.20: The relative polarity of the D0 and the OC dipoles.

Parameter	Unit	Value
Δ_{in}	—	5
Δ_{out}	—	12
s_{D0}	[m]	14
s_{OC}	[m]	21
β^*	[m]	0.15
ϵ	[m·rad]	$5 \cdot 10^{-10}$
l_{D0}	[m]	2
l_{OC}	[m]	1.5
γ_r	—	7461

Table 1.1: Parameters used in the Early Separation Scheme (if not differently stated).

where z'_0 is the $\frac{dz(s)}{ds}|_{s=0}$ (due to the bump anti-symmetry $z(0) = 0$). The meaning of L_1 , L_2 , L_3 and L_4 used in the previous equation are shown in Fig. 1.19, $B\rho$ is the beam magnetic rigidity, B_{D0} and B_{OC} are the magnetic fields in the respective magnets. It is worth noting that Eq. 1.15 does not refer to the closed bump: it is the propagation of an initial condition problem. If this propagation is correctly closed (matched), $z(L_4) = 0$, the propagative solution becomes equivalent to the periodic solution (closed orbit). From the Eq. 1.15, it is possible to derive a thin element approximation, assuming that the thin dipole are centered in middle of the thick ones. It yields

$$z(s) = \begin{cases} z'_0 s & 0 \leq s < \frac{L_1+L_2}{2} \\ \frac{1}{2B\rho} B_{D0}(L_2 - L_1) (-L_1 - L_2 + 2s) + z'_0 s & \frac{L_1+L_2}{2} \leq s \leq \frac{L_3+L_4}{2} \end{cases} \quad (1.16)$$

If we impose in the Eq. 1.16 the closed bump condition, we obtain the value of the integrated magnetic field requested in the D0 and in the OC:

$$\left| \int_{D0} B dl \right| = \frac{B\rho}{2} \frac{|\Delta_{in} - \Delta_{out}|}{(s_{OC} - s_{D0})} \sqrt{\frac{\epsilon}{\beta^*}} s_{OC} \quad \text{and} \quad \left| \int_{OC} B dl \right| = \frac{B\rho}{2} \frac{|\Delta_{in} - \Delta_{out}|}{(s_{OC} - s_{D0})} \sqrt{\frac{\epsilon}{\beta^*}} s_{D0} \quad (1.17)$$

where $s_{D0} = \frac{L_1+L_2}{2}$, $s_{OC} = \frac{L_3+L_4}{2}$ (the geometrical center of the two dipoles), therefore $s_{D0} < s_{OC}$. The Δ_{in} is the already introduces normalized inner separation (the beam normalized separation between the Interaction Point and the entry face of the D0 dipole, Eq. 1.5): it is directly connected to θ_c by the Eq. 1.6. The Δ_{out} is that is the normalized beam separation at the exit face of the OC dipole (normalized outer separation, see Fig. 1.19). With the Early Separation magnets switched off we have $\Delta_{in} \equiv \Delta_{out}$.

From Eq. 1.17 the D0's integrated field is a factor s_{OC}/s_{D0} stronger than the OC's one (lever arm effect). The magnet strength has to be increased proportionally to the beam divergence at the Interaction Point and to the difference between the Δ_{out} and the Δ_{in} . It decreases by increasing the D0-OC distance and/or by reducing the D0's distance from the Interaction Point.

In Fig. 1.21 the Eqs. 1.15-1.16 are compared to the machine closed orbit. We can observe that the thin approximation, as expected, is equivalent to the thick dipoles closed orbit outside the magnets and describes, inside the magnets, the beam orbits with good accuracy (few per cent level).

In Fig. 1.22 the integrated field required is shown assuming the value of Table 1.1: this corresponds, for $\beta^* = 0.15$ m, to an integrated field for the D0 and the OC of, respectively, ≈ 15 T·m and ≈ 10 T·m. The implications on the choice of the magnet technology will be developed in Chapter 5.

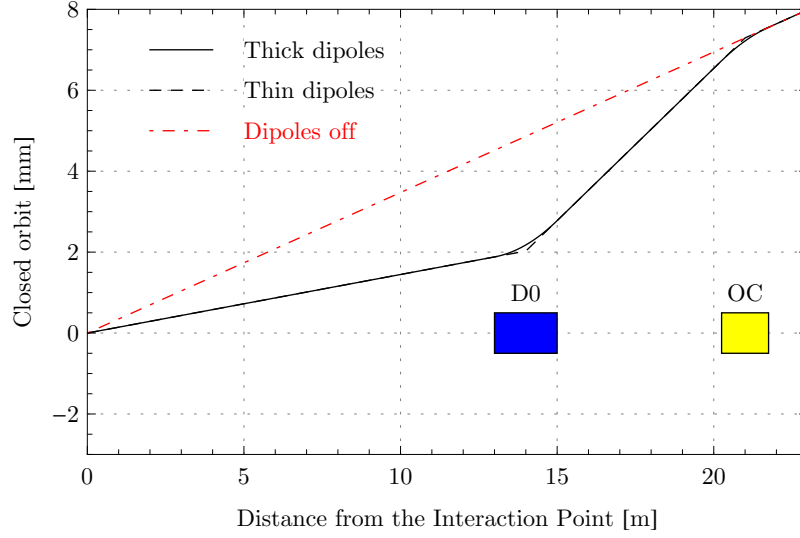


Figure 1.21: An example of the closed orbit for the Early Separation Scheme (parameters taken from Table 1.1).

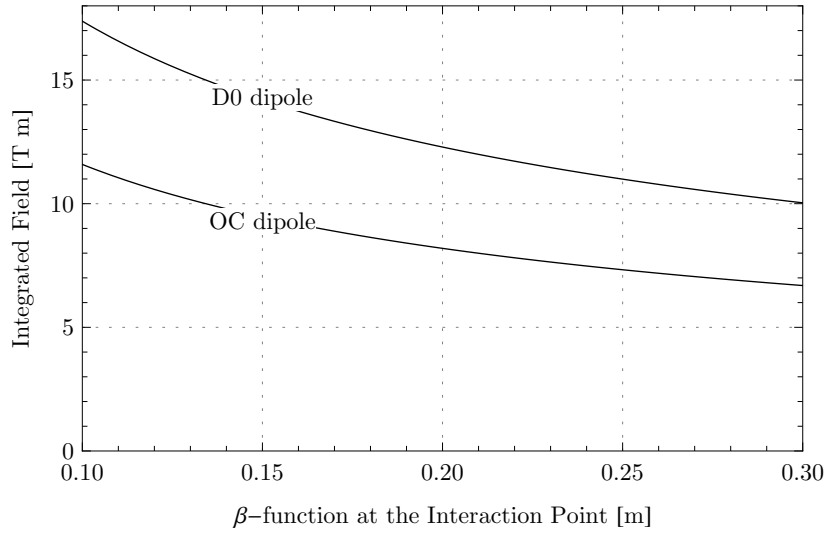


Figure 1.22: An example of the integrated field required for the D0 and the OC dipoles (β^* is varying, the other parameters are taken from Table 1.1).

Chapter 2

Luminosity leveling and performance with the Early Separation Scheme

Contents

2.1	Motivation and principle of the luminosity leveling via the crossing angle . .	23
2.2	Sources of luminosity decay	25
2.3	An analytical model for the luminosity leveling	26
2.3.1	The luminosity evolution without luminosity leveling	26
2.3.2	The luminosity leveling with the crossing angle	27
2.3.3	Luminosity leveling strategies	29
2.4	A numerical model for the luminosity leveling	35
2.5	Luminosity performance of the Early Separation Scheme	37
2.5.1	Scenarios and performance	37
2.5.2	General remarks on the luminosity leveling	39

In this Chapter the concept and the performance of a leveling scheme for the LHC luminosity upgrade using the crossing angle is presented. With the Early Separation Scheme it is possible to vary the crossing angle between the beams during the physics run with a local modification of the beam closed orbit. Differently from a luminosity leveling done varying the focusing strength of the machine, the one we present minimizes the impact on the other systems of the collider. In general, limiting the peak luminosity thanks to the leveling, introduces an additional flexibility in the operations that can be exploited to fulfill the collider's and the experiments' needs.

2.1 Motivation and principle of the luminosity leveling via the crossing angle

In sLHC the decay of the luminosity due to the beam collision (proton-proton burning off) is expected to become dominant over the other beam loss mechanisms and very significant as compared to the nominal LHC parameters. This is particularly true for scenarios where the luminosity increase is obtained mostly by means other than a beam current increase. A large variation of the luminosity over a few hours run shows many drawbacks, both for the detectors and the machine components.

From the machine point of view the main issues are related to the peak and the average power deposition in the superconducting triplets and in the ancillary magnets. To prevent a quench (a transition from the superconducting state of the magnet to the normal conducting one), the interaction region of the collider has to be designed for the maximum instantaneous luminosity. The present knowledge shows that the capability of Nb-Ti appears significantly exceeded while the Nb₃Sn technology could face it though with additional improvements of the shielding efficiency (see Chapter 5).

For the experiment itself, the high initial peak luminosity produces a higher multiplicity (number of pp interactions per bunch crossing) and a stronger background signal. To cope with it, either the detector has to be designed for the peak multiplicity that is significantly above the design goals of the present detectors or a fraction of the running time will not be used efficiently for data taking.

A possible answer to this challenge is luminosity leveling, that is a method to operate the machine in such a way as to keep constant the luminosity over a period of several hours. It is usually proposed to adjust in real time the beam size at the crossing point to obtain this result (slow reduction of β -function at the Interaction Point, β^* , while the beams are colliding). This is the way to do leveling if the beams interact perfectly head-on. This was never made operational in practice since in present colliders the luminosity decays range within acceptable levels and, at the same time, energy deposition is not a critical issue. While a modulation of the focusing is indeed a priori simple, it has a large number of side effects that are bound to make it delicate in practice: when the focusing is modified, its chromatic correction has to be adjusted. As it is not locally corrected, all the arc sextupoles have to be ramped, with unwanted feed-down effects on the betatron tunes and closed orbit all around the machine, including in the collimation sections. Likewise, the modification of the β -function at the place where it reaches its maximum requires strictly local correction of alignment or tilt imperfections, rarely obtained in practice, resulting, e.g., in closed orbit distortions propagating to the whole machine. In the LHC the situation is further complicated by the presence of a crossing angle that extends up to Q5/Q6 (Fig. 1.13) and that creates feed-down effects depending on the detail of the optics, of the imperfections and of their correction strategy or capability. While this method is certainly not impossible, its complexity may require a long time, i.e., integrated luminosity, to make it operational and due to its complexity it increases the risks during the machine operations (quench induced by the beam losses, beam dump induced by the interlock system, etc.) resulting in a significant loss of integrated luminosity.

The Early Separation Scheme allows a different and original approach to luminosity leveling that appears less difficult to implement. The principle is to modify the crossing angle, θ_c , in real-time with an adjustment of the beam trajectories only in the experimental straight section between the left and right Q1 quadrupoles. In this way advantage is made of the significant influence of the crossing angle or rather of the geometrical loss factor F on the luminosity, as shown on Figure 2.1 and, only for normalized beam inner separation (Δ_{in}) greater than four, in Eq. 1.14, here recalled for the convenience of the reader

$$F(\theta_c, \sigma_y, \sigma_s) \simeq \frac{1}{\sqrt{1 + (\theta_c \sigma_s / (2\sigma_y))^2}} \quad \text{if } \Delta_{in} \gtrsim 4. \quad (2.1)$$

where symbols are used with their usual meaning.

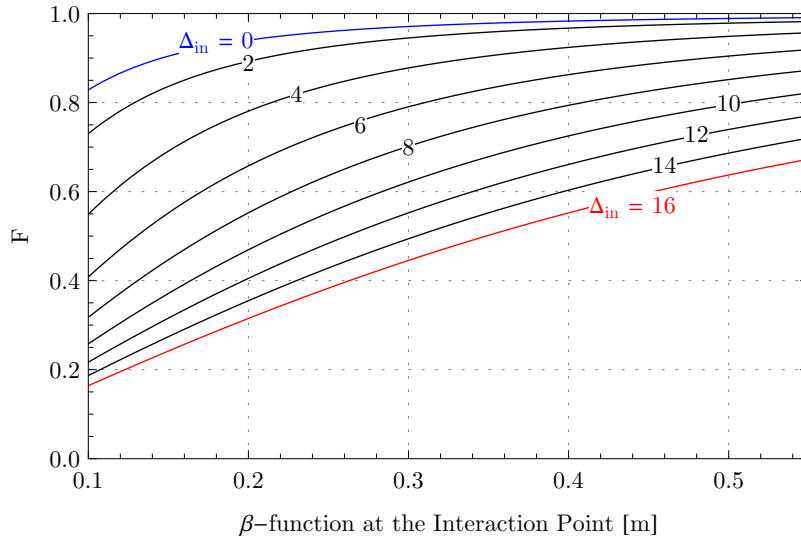


Figure 2.1: The F factor as function of β^* for different values of Δ_{in} ($\sigma_s = 75.5$ mm, $\epsilon = 5 \cdot 10^{-10}$ m·rad).

All the side-effects met when modulating the focusing and introduced before are suppressed. Other side effects are nevertheless present:

- a modulation of the length of the luminous region,
- a modulation of the beam-beam tune shift and tune spread,
- a modulation of the coupling between synchrotron motion and betatron motion.

The two first issues are discussed in this chapter while the latter is a general issue for the luminosity upgrade that goes beyond the goal of this study.

While the side-effects are anticipated to be small or negligible, the range within which the θ_c is nevertheless limited by the hardware capabilities of the Early Separation Scheme (Eq. 1.17) and by the beam-beam effect:

- at the bottom (minimum θ_c), by the number of parasitic encounters at reduced distance that can be afforded (see Fig. 1.7),
- at the top (maximum θ_c), by possible synchro-betatron resonances. From the analysis in [32] this does not seem a limiting factor.

In the following the simplified law of luminosity decay is established and used to build analytical and numerical model of luminosity leveling. Finally, using these models, the luminosity performance of the scheme are presented and discussed.

2.2 Sources of luminosity decay

In order to describe the evolution of the luminosity versus time, a model of luminosity decay has been considered. It has been assumed that the luminosity is dominated by the following three mechanisms:

- the protons burning,
- the intra-beam scattering,
- the rest gas scattering.

All these phenomena are coupled. It has been assumed that the emittance growth due to resonance excitation or to non-linearities is compensated, at 7 TeV/c, by the synchrotron radiation damping and therefore neglected. In the following the function with the subscript “0” refers to their initial value (i.e., for $t = 0$).

The protons burning

The equation that describes the proton burning due to the luminosity itself is [1]

$$\dot{N}_b(t) = -\frac{\sigma}{n_b} n_{exp} L(t) \quad (2.2)$$

where $N_b(t)$ is the number of protons per bunch, n_b is the number of the bunches, n_{exp} the number of experiments, the $L(t)$ the single experiment luminosity and σ is the pp total cross-section. In the following we assume $n_{exp} = 2$ and $\sigma = 100$ mbarn [3] (see Fig. 1.3 from [20]). The time required to reach $1/e$ of the initial luminosity, τ_{pp} , is given by [3]

$$\tau_{pp} = (\sqrt{e} - 1) \frac{N_{b0} n_b}{\sigma L_0 n_{exp}}.$$

The intra-beam scattering

The equation that describes the emittance growth due to the intra-beam scattering is [3] [18]

$$\dot{\epsilon}(t) = \frac{1}{\tau_{IBS}} \epsilon(t), \quad \tau_{IBS} = 91.3 \frac{1.15 \cdot 10^{11}}{N_b(t)} \text{ [h]}$$

where $\epsilon(t)$ is the beam emittance, τ_{IBS} is the time constant for intra beam scattering and $N_b(t)$ is the number of protons per bunch considered.

The rest gas scattering

The equation that describes the loss of protons due to the scattering on the rest gas [3] [18]

$$\dot{N}_b(t) = -\frac{1}{\tau_{RGS}} N_b, \quad \tau_{RGS} = 78.35 \frac{1.15 \cdot 10^{11} \times 2808}{n_b N_b(t)} \text{ [h]}$$

where τ_{RGS} is the time constant for rest gas scattering, $N_b(t)$ and n_b is respectively the number of protons per bunch and the number of bunches considered.

The relative importance of the decay sources

In the approximation that the three loss mechanisms sum up with a negligible coupling, the luminosity lifetime, τ_{lum} , can be expressed as [3]

$$\frac{1}{\tau_{lum}} = \frac{1}{\tau_{IBS}} + \frac{2}{\tau_{RGS}} + \frac{1}{\tau_{pp}}. \quad (2.3)$$

In Table 2.1, we report the time constants relative to the LHC and sLHC for each of the three physical processes we discussed: the time constants are evaluated at the beginning of the physical run assuming, for the sLHC, a $L(t=0) = 10^{35} \text{ cm}^{-2}\text{s}^{-1}$, $N_b(t=0) = N_{b0} = 2.3 \cdot 10^{11}$ ppb and $n_b = 2808$. The values relative to the LHC are the nominal ones [1]. It is possible to conclude that the dominant mechanism is

Table 2.1: The relative importance of the decay sources.

Time constant	in LHC [h]	in sLHC [h]
τ_{pp}	29.10	5.82
τ_{IBS}	91.3	45.65
τ_{RGS}	78.35	39.17
τ_{lum}	14.12	4.09

the pp burning: this is especially true for the sLHC case. Hence, the analytical model will only include the dominant source while we will consider all three effects in the numerical approach.

2.3 An analytical model for the luminosity leveling

2.3.1 The luminosity evolution without luminosity leveling

Solving the Eq. 2.2 with

$$L(t) = L_0 \frac{N_b(t)^2}{N_{b0}^2},$$

it yields

$$N_b(t) = N_{b0} \frac{1}{1 + t/\tau} \quad (2.4)$$

where

$$\tau = \frac{N_{b0} n_b}{\sigma L_0 n_{exp}}. \quad (2.5)$$

From Eq. 2.5 is possible to conclude that, gaining a factor G on the starting luminosity (L_0), the luminosity decay rate, $1/\tau$

- remains unchanged if the luminosity gain is obtained by increasing the bunches number (n_b)
- is increased by a factor \sqrt{G} if the luminosity gain is obtained by increasing the N_{b0} by a factor \sqrt{G}
- is increased by a factor G if the luminosity gain is obtained by means other than the beam current (n_b , N_{b0}).

This consideration is important to evaluate the impact of the peak luminosity has on the integrated luminosity in the case of a natural decay: assuming a gain G on the peak luminosity the corresponding increase of integrated luminosity will be larger if we increase the n_b instead of the N_{b0} . The reduction of the β^* gives the smaller improvement of integrated luminosity for a given gain in peak luminosity.

Quantitatively, the integrated luminosity, for the physical run of duration T_{run} , is given by:

$$\int_0^{+T_{run}} L(t)dt = \int_0^{+T_{run}} L_0 \frac{1}{(1 + t/\tau)^2} dt = \frac{T_{run}\tau}{T_{run} + \tau} L_0. \quad (2.6)$$

As limit scenarios, two opposite regimes can be considered from the Eq. 2.6:

- a slow luminosity decay compared to the run duration,
- fast decay luminosity decay compared to the run duration.

For slow decay the Eq. 2.6 yields

$$\int_0^{+T_{run}} L(t) dt \approx T_{run} L_0 \quad (2.7)$$

i.e., in this regime, the integrated luminosity is proportional to the peak luminosity (L_0). While for fast decay, the Eq. 2.6 yields

$$\int_0^{+T_{run}} L(t) dt \approx \tau L_0 = \frac{N_{b0} n_b}{\sigma n_{exp}}, \quad (2.8)$$

that is the integrated luminosity does not depend on the peak luminosity (or the β^* , or the ϵ) in this regime but only on the total beam current (more properly beam charge, $n_b N_b$).

The expected luminosity decay time for the nominal LHC is 14.1 h (see Table 2.1). From the previous considerations, if the number of bunches is not increased, the sLHC will have a shorter decay time with respect to the LHC. This means that the sLHC will be closer than the LHC to the fast decay regime: to increase the integrated luminosity the beam current is an essential component while an increase in the peak luminosity will not translate into an equal increase on the integrated luminosity. As explained in this chapter luminosity leveling can allow a higher beam current and, at the same time, a lower peak luminosity with a significant gain in the overall performance.

2.3.2 The luminosity leveling with the crossing angle

The beam current evolution during the luminosity leveling

During the leveling the luminosity is constant ($L(t) = L_0$). From the Eq. 2.2

$$N_b(t) = N_{b0} (1 - t/\tau). \quad (2.9)$$

where τ is still defined as Eq. 2.5. The proton burning therefore causes a linear and faster, in relation to the free evolution (Eq. 2.4), decay of the current. In Fig. 2.2, the comparison of the $N_b(t)$ evolution for leveled

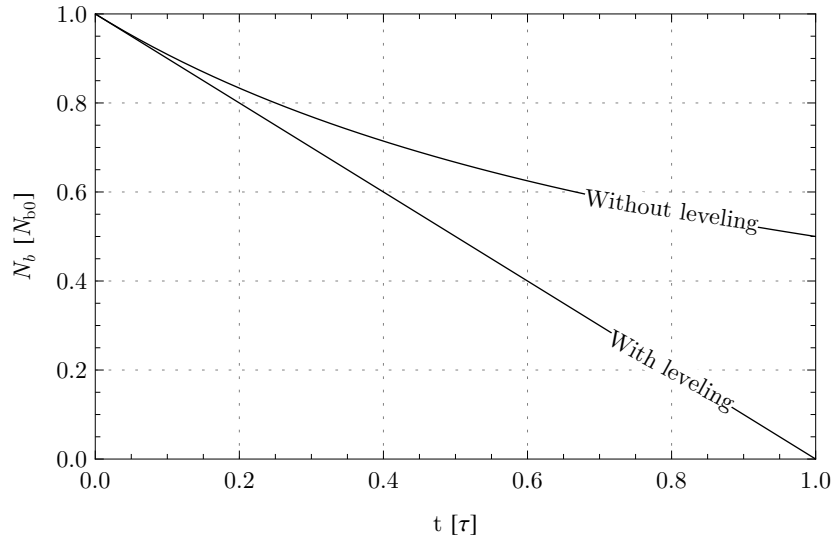


Figure 2.2: Comparison between the $N_b(t)$ evolution with and without leveling.

and not leveled case is shown. After a time t equal to τ all protons are burnt. In a real case, as we show in the following section, the leveling cannot be maintained until $t = \tau$ but has to be stopped before. When the leveling is interrupted the luminosity evolution behaves like in the free evolution (with initial condition corresponding to the final condition of the leveling).

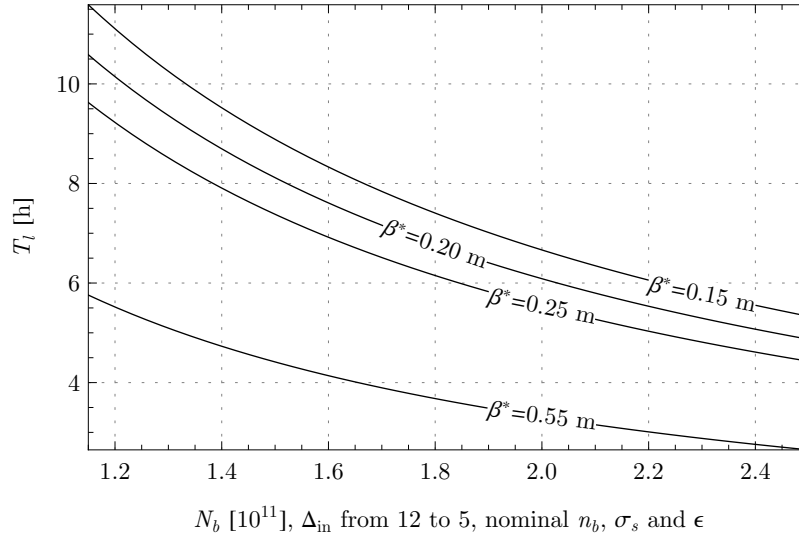


Figure 2.3: The T_l value as function of the bunch population, N_b , and for different β^* (leveling with Δ_{in} from 12 to 5). It is worth noting that the T_l decreases increasing the N_b and increases reducing the β^* .

Practical duration of the leveling plateau

In the case of leveling with angle, the actual duration of the leveling period, T_l , can be computed from the maximum and minimum of the beam separation. In order to level the luminosity, i.e., to compensate for the beam current loss, the geometrical factor F has to behave like

$$F(t) = F_0 \frac{1}{(1 - t/\tau)^2} \quad (2.10)$$

and this implies, assuming $F(t) \leq F_{max} \leq 1$, that

$$T_l = \tau \left(1 - \sqrt{\frac{F_0}{F_{max}}} \right) \leq \tau. \quad (2.11)$$

The values of F_0 and F_{max} will depend on the initial Δ_{in} , $\Delta_{in}(t=0)$, and the final Δ_{in} , $\Delta_{in}(t=T_l)$. In Fig. 2.3 some examples of duration of the leveling are given as function of the N_b and for different value of β^* (the value of the β -function at the Interaction Point): increasing the mean current or the β^* reduces, for a given range of Δ_{in} , the duration of the leveling plateau.

The evolution of luminosity related function after the leveling plateau

In the following we report during all the duration of the physics run, that is before and after the leveling plateau, the following functions:

- luminosity $L(t)$,
- bunch population $N_b(t)$,
- geometrical loss factor $F(t)$,
- integrated luminosity,
- total beam-beam tune shift $\Delta Q_{bb}(t)$.

In case of luminosity leveling (assuming the same leveling strategy in all the Interaction Points) we have

$$L(t) = \begin{cases} L_0 & \text{for } 0 \leq t \leq T_l \\ L_0 (1 + (t - T_l)(\tau - T_l)^{-1})^{-2} & \text{for } t > T_l \end{cases} \quad (2.12)$$

where

$$L_0 = \frac{n_b f_r N_{b0}^2}{4\pi \beta^* \epsilon} F_0$$

and τ and T_l are defined, respectively, in Eqs. 2.5 and 2.11.

We can generalize the Eqs. 2.9 and 2.10 with the following

$$N_b(t) = \begin{cases} N_{b0} (1 - t/\tau) & \text{for } 0 \leq t \leq T_l \\ N_{b0} (\tau - T_l)^2 (\tau (t + \tau - 2T_l))^{-1} & \text{for } t > T_l \end{cases} \quad (2.13)$$

and

$$F(t) = \begin{cases} F_0(1 - t/\tau)^{-2} & \text{for } 0 \leq t \leq T_l \\ F_{max} & \text{for } t > T_l. \end{cases} \quad (2.14)$$

Regarding the integrated luminosity, from the Eq. 2.12 it yields

$$\int_0^{+t} L(\bar{t}) d\bar{t} = \begin{cases} L_0 t & \text{for } 0 \leq t \leq T_l \\ L_0 (\tau - T_l)^2 (\tau (t + \tau - 2T_l))^{-1} & \text{for } t > T_l. \end{cases} \quad (2.15)$$

The total beam-beam tune shift, ΔQ_{bb} , in the approximation discussed in Section 3.1.3 (two crossing points with alternating crossing, one horizontal the other vertical, Fig. 3.5) is

$$\Delta Q_{bb}(t) = \begin{cases} 2 \xi_0 (1 - t/\tau)^{-1} & \text{for } 0 \leq t \leq T_l \\ 2 \xi_0 \frac{F_{max}}{F_0} (\tau - T_l)^2 (\tau (t + \tau - 2T_l))^{-1} & \text{for } t > T_l \end{cases} \quad (2.16)$$

where

$$\xi_0 = \xi F_0$$

and ξ is defined in the Eq. 3.10.

The maximum value of the beam-beam tune shift during the physics run

From Eq. 2.16 it is possible to compute the maximum total beam-beam tune shift, $\Delta Q_{bb}|_{max}$: during the leveling the module of ΔQ_{bb} increases and is maximized at the end of the leveling (i.e., for $t = T_l$), therefore

$$\Delta Q_{bb}|_{max} = 2\xi_0 \frac{1}{1 - T_l/\tau} = 2\xi \sqrt{F_0 F_{max}}.$$

This means that the maximum beam-beam tune shift with leveling is smaller than the one without leveling (assuming a fixed $F = F_{max}$). Therefore, with leveling, it is possible to have for a given $\Delta Q_{bb}|_{max}$ more beam current in the machine with a significant improvement of the integrated luminosity. On the other hand, it is worth noting that the total beam-beam tune shift is only one of the possible limitations on increasing of the beam current: the leveling can alleviate it but there still are others to overcome for a successful exploitation of the scheme (injectors, collective effects, collimation...).

2.3.3 Luminosity leveling strategies

In Fig. 2.4, *top*, we compare the two scenarios with fixed crossing angle ($\Delta_{in} = 5$ and 12) with a leveling with Δ_{in} that goes from 12 to 5. The duration of the leveled luminosity interval (T_l) is ≈ 5 hours. We assumed a $\beta^* = 0.15$ m, $N_b = 2.3 \cdot 10^{11}$, $n_b = 2808$. We can observe that the non-leveled luminosity curves of the sLHC decay much faster than in the nominal LHC. With the leveling strategy we are considering we can halve the peak luminosity with respect to the curve $\Delta_{in} = 5$ and, at the same time, gain in term of integrated luminosity with respect to the curve $\Delta_{in} = 12$. In Fig. 2.4, *bottom*, we show the corresponding ΔQ_{bb} of the four luminosity curves of Fig. 2.4, *top*: in free evolution the ΔQ_{bb} is decreasing while increases during the leveling. The ΔQ_{bb} should be as low as possible in the collider: we can observe that the curve $\Delta_{in} = 5$ has the higher ΔQ_{bb} while the curve of luminosity leveling scenario has a ΔQ_{bb} higher than the curve $\Delta_{in} = 12$ but its values are similar to those of the nominal LHC case.

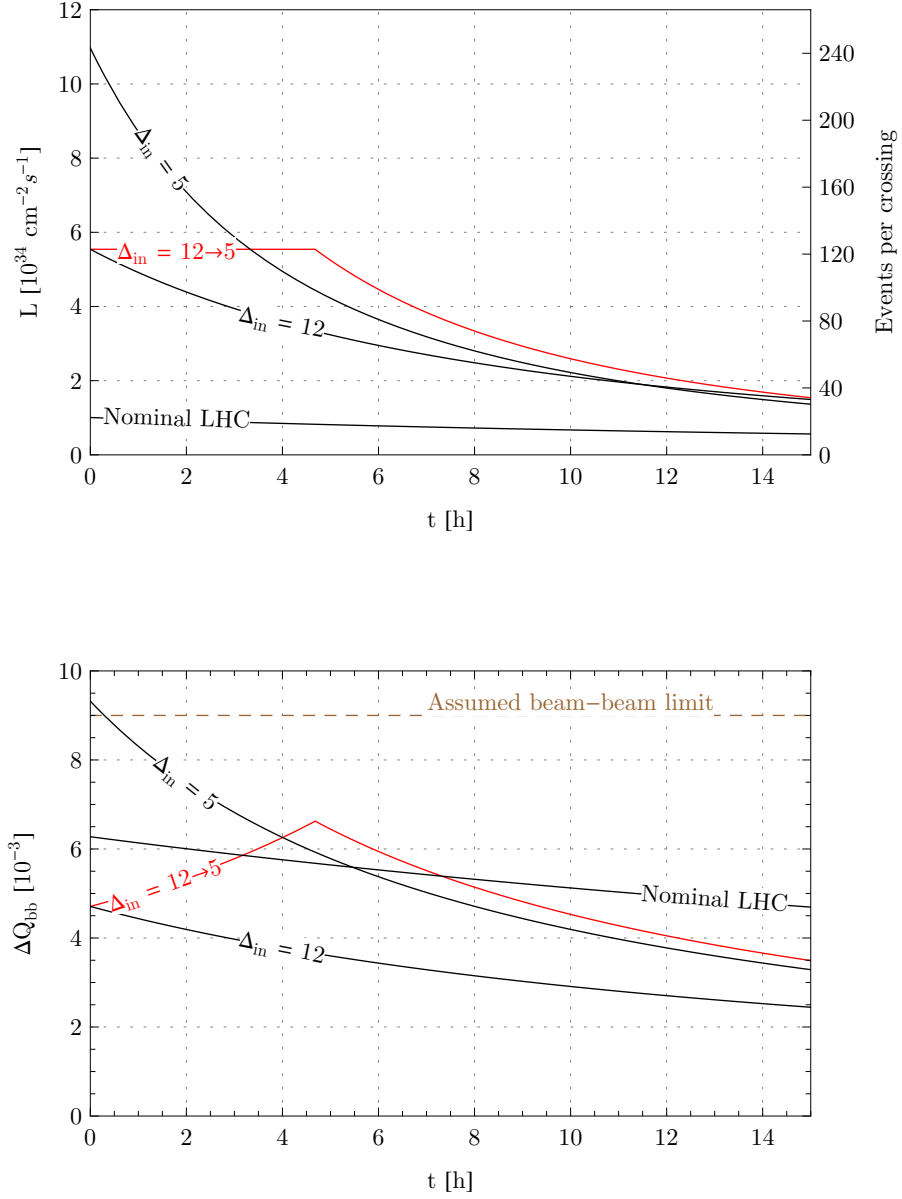


Figure 2.4: The luminosity and total beam-beam tune shift for a $\beta^* = 0.15$ m, $N_b = 2.3 \cdot 10^{11}$, $n_b = 2808$. The nominal LHC luminosity behavior has been displayed for reference. We compare the two scenarios with fixed crossing angle ($\Delta_{in} = 5$ and 12) with a leveling with Δ_{in} that goes from 12 to 5. The duration of the leveled luminosity interval (T_l) is ≈ 5 hours.

For the reasons we discuss in the following three chapters, we design the Early Separation Scheme to do exactly this kind of leveling, that is starting the physics run with a large crossing angle, $\Delta_{in} = 12$, and slowly reducing it until $\Delta_{in} = 5$.

In Fig. 2.5 a parametric studies of the luminosity varying the minimum Δ_{in} (with Δ_{in} at the start equal to 12) and varying the Δ_{in} at the start (with Δ_{in} at the end of the physics run equal to 5). From these plots the flexibility of the Early Separation Scheme is put in evidence. Varying the leveling strategy (with the same hardware) it is possible to lower the peak luminosity (extending, in doing so, the T_l) and to face the possible limitations of the machine or of the experiments (ΔQ_{bb} , beam-beam effect, pile-up, background

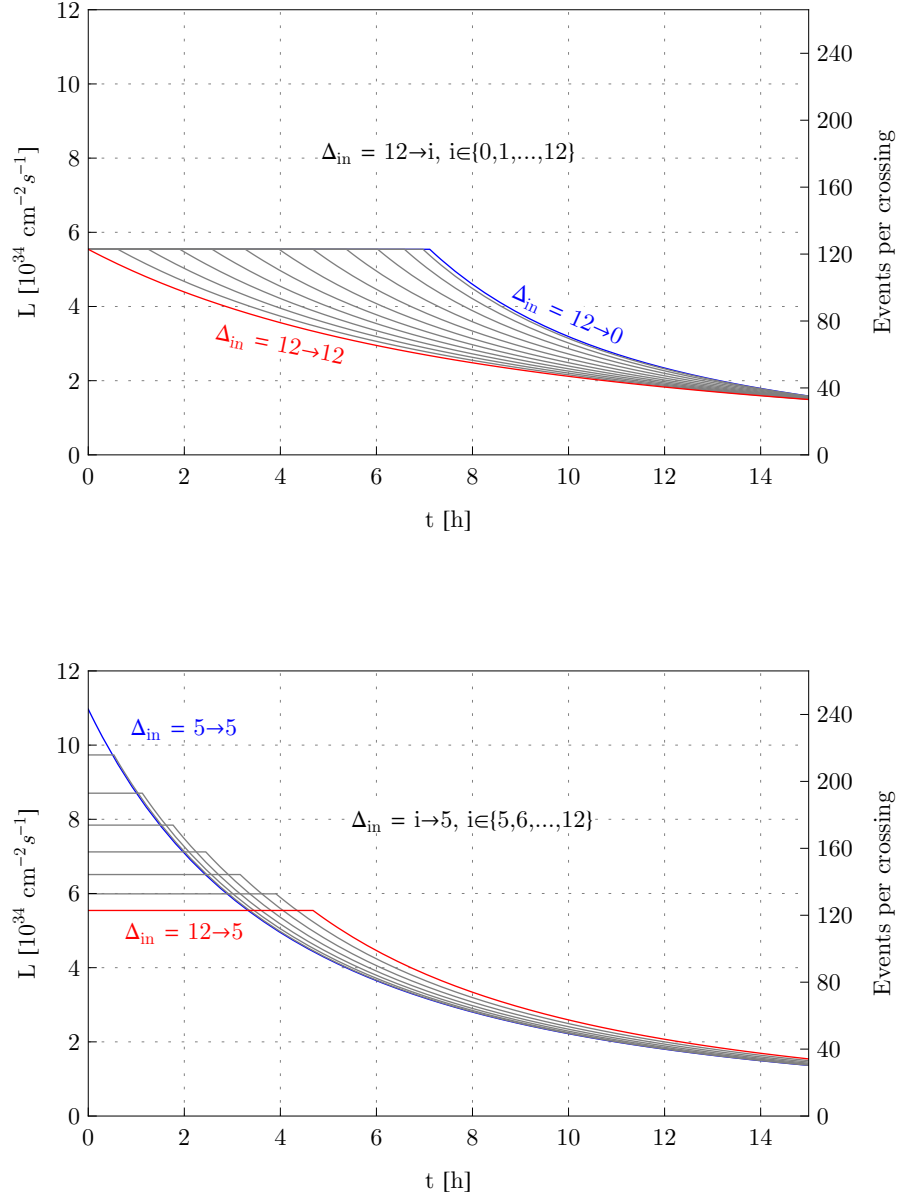


Figure 2.5: A parametric studies of the luminosity varying the minimum Δ_{in} (Δ_{in} at the start equal to 12), *top*, and varying the Δ_{in} at the start (Δ_{in} at the end equal to 5), *bottom*. From the previous plots the flexibility of the Early Separation Scheme is put in evidence. Varying the leveling strategy (with the same hardware) it is possible to lower the peak luminosity (extending the T_l) and to face the possible limitations of the machine or of the experiments (ΔQ_{bb} , beam-beam effect, pile-up, background noise...) with a convenient choice of the leveling parameters. The values assumed are $\beta^* = 0.15$ m, $N_b = 2.3 \cdot 10^{11}$, $n_b = 2808$.

noise...) with a convenient choice of the leveling parameters. It is worth noting that the minimum Δ_{in} for which we are designing the Early Separation Scheme is 5 (see Chapter 5). To go beyond this value, additional or different solutions are needed: in our opinion the best candidate in that respect is the Crab Crossing Scheme (see Section 1.2.3).

In Fig. 2.6 the behavior during the leveling of the ΔQ_{bb} is shown: reducing the minimum Δ_{in} or reducing the initial Δ_{in} implies a larger head-on tune shift.

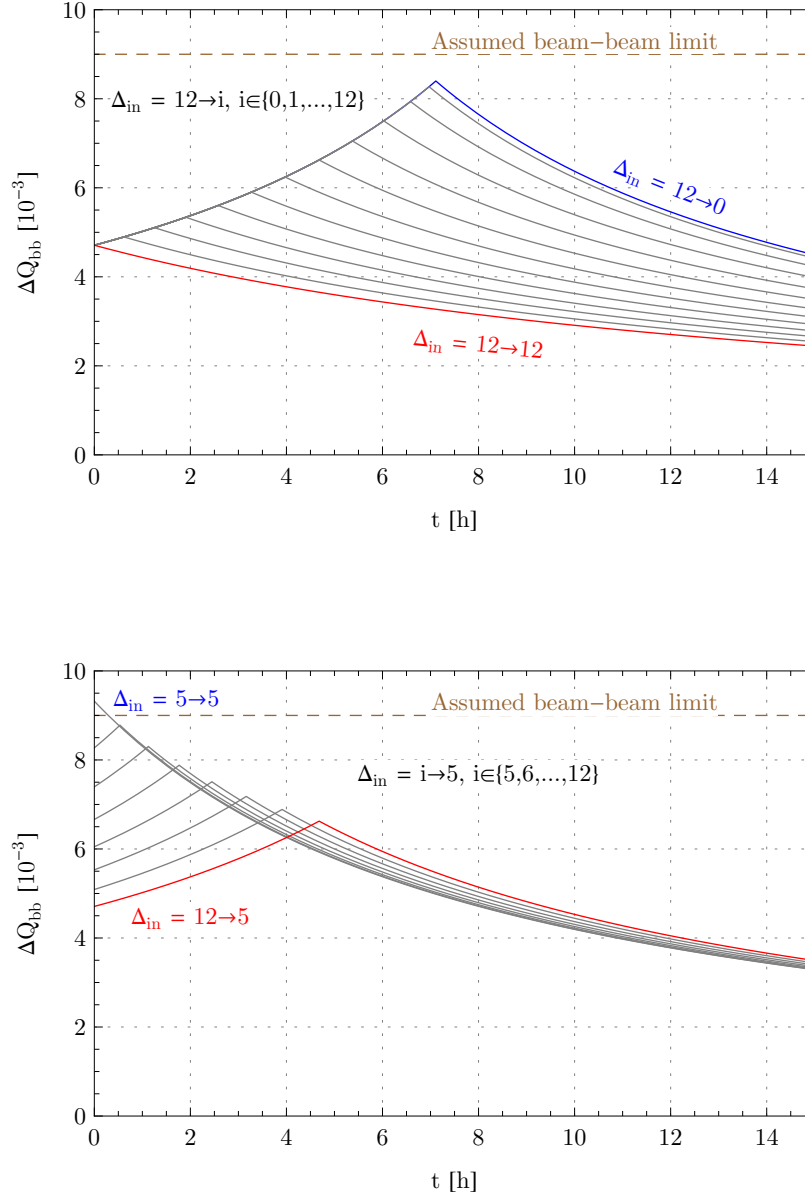


Figure 2.6: A parametric studies of ΔQ_{bb} varying the minimum Δ_{in} (Δ_{in} at the start equal to 12), *top*, and varying Δ_{in} at the start (Δ_{in} at the end equal to 5), *bottom*. It is evident that the leveling, for a given N_{b0} , reduced ΔQ_{bb} . The values assumed are $\beta^* = 0.15$ m, $N_b = 2.3 \cdot 10^{11}$, $n_b = 2808$.

Impact of the turn-around time

In order to compute and optimize the integrated luminosity an other important quantity is introduced: the average turn-around time, TAT, that is the average time between the beam dump and the next beam collision (see Fig. 2.7).

It is possible to define the overall integrated luminosity over several physics runs of the machine as

$$\int_{T_{runs}} L(\bar{t}) d\bar{t} = \frac{T_{runs}}{T_{run} + \text{TAT}} \int_0^{+T_{run}} L(\bar{t}) d\bar{t}, \quad (2.17)$$

where T_{run} is the average duration for one physics run of the machine and the T_{runs} represents the long

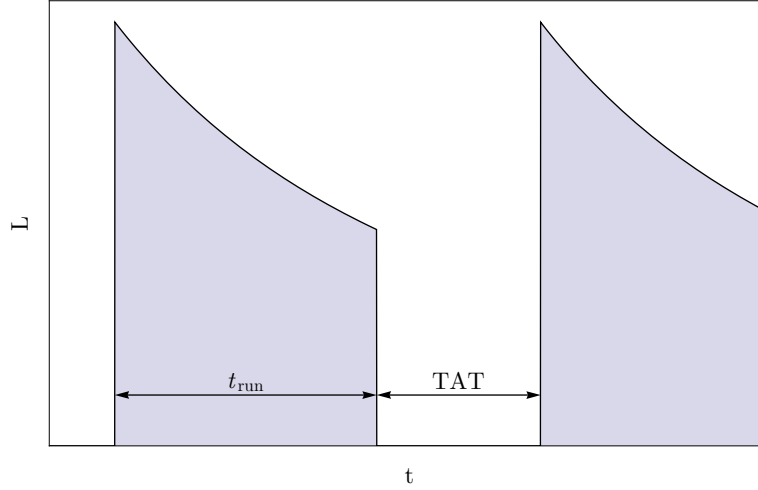


Figure 2.7: The meaning of the average turn-around time (TAT).

period of time during which the machine operates (e.g., 200 days is the expected period of time dedicated to the physics in one year, the rest of the time is devoted to maintenance and technical shut-down). With the present accelerator complex the minimum turn-around time is 70 min [1]. The actual turn-around time is expected to be dominated by the LHC itself and will depend on different interleaved parameters (sensitivity and calibration of the interlock system, quenches recovery time, reliability of the single system, human errors...). The assumed turn-around time for the nominal LHC is 10 h [3] and for the sLHC, due the experience and the possible improvement of the injector chain [33], is assumed to be 5 h [34]. From Eqs. 2.17 and 2.15 it yields that the optimal T_{run} , T_{run}^{opt} , to maximize the integrated luminosity is

$$T_{run}^{opt} = \frac{\sqrt{(\tau - T_l)^2 (T_l^2 + \tau \text{TAT})} + T_l^2}{\tau},$$

therefore

$$\int_0^{T_{run}^{opt}} L(\bar{t}) d\bar{t} = L_0 \frac{\tau^2 T_{runs}}{2\sqrt{(T_l - \tau)^2 (T_l^2 + \tau \text{TAT})} - 2\tau T_l + 2T_l^2 + \tau(\text{TAT} + \tau)}. \quad (2.18)$$

With the Eqs. 2.18 and 2.15 we can compare the efficiency of the leveling with respect to other solutions (see Section 2.5).

Moreover it is possible to clearly show the relationship between the peak luminosity and the integrated luminosity. In Fig. 2.8 the luminosity plane is shown: in this plane we represent the peak luminosity and integrated luminosity, respectively, on the x and y axis. As mentioned in Section 1.1 the ideal working region of a collider should be positioned at low value of peak luminosity and at high value of integrated luminosity. The relation between peak and integrated luminosity is not always linear and depend on the specific parameter that is modified. To simplify the problem we assume no luminosity leveling and to vary one parameter each time keeping the others unchanged.

The load line derived varying the turn-around time is parallel to the y -axis since it allows to gain in integrated luminosity without increasing the peak luminosity: the turn around time in the LHC is dominated by the LHC ring itself and cannot be reduced beyond the minimum turnaround time of ≈ 70 min [3]. With the experience gained during the collider's operation one can consider to reduce by a factor 2 the turn-around time passing from 10 h in the nominal LHC to 5 h in the sLHC.

By increasing the number of bunches (n_b , Fig. 2.8) a perfectly linear and extremely efficient load line is obtained. Nevertheless with the present knowledge of the machine this option has to be excluded: doubling the number of bunches (and keeping the same N_b) will induce a heat load on the beam screen beyond the

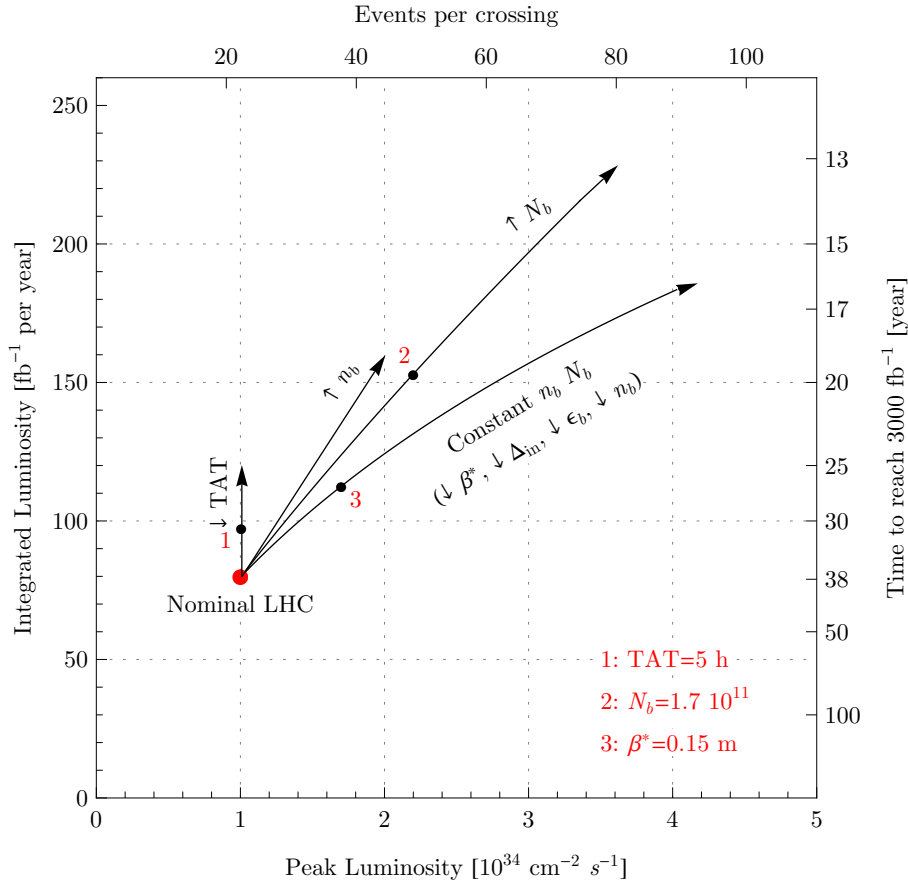


Figure 2.8: The different load lines in the luminosity plane.

limit on the cryogenics system. Increasing the protons per bunch (N_b) is less effective because it contributes quadratically to the peak luminosity but only linearly to the beam current, therefore the time constant of the luminosity decay is decreased (Section 2.3.1). On the other hand, in the working region of the nominal LHC, there is no evident saturation of this load line (linear relationship between the peak and the integrated luminosity). The less convenient load line from the luminosity performance is obtained keeping constant the total beam current ($n_b N_b$) and reducing the β^* (or reducing the beam emittance or the normalized inner separation between the beams or the number of bunches). On this curve the saturation effect is well visible.

We can conclude that:

- in order to increase the integrated luminosity of a collider, without leveling and without considering a reduction of the turn-around time, we have to increase its peak luminosity,
- without increasing the beam current or reducing the turn-around time, there is a rapid saturation of the luminosity load line: a large increase of peak luminosity corresponds to a limited increase of the integrated luminosity. In the nominal LHC, for the first time in hadron colliders due to its unprecedented peak luminosity, we can observe this saturation mechanism. This is the reason why we believe that, to meet the Phase II LHC Luminosity Upgrade target, a significant increase of the beam current is needed, namely to double N_b with respect to its nominal value.

2.4 A numerical model for the luminosity leveling

In this section we present the results of the numerical solution of the differential model for the luminosity decay presented in Section 2.2.

We used the SimulinkTM code [35] to describe this dynamic system: in Fig. 2.9 the overall schematic is shown. There are four feedback paths: three are needed for implementing the three differential equations of Section 2.2, the last one is used for the control of the crossing angle during the luminosity leveling. We

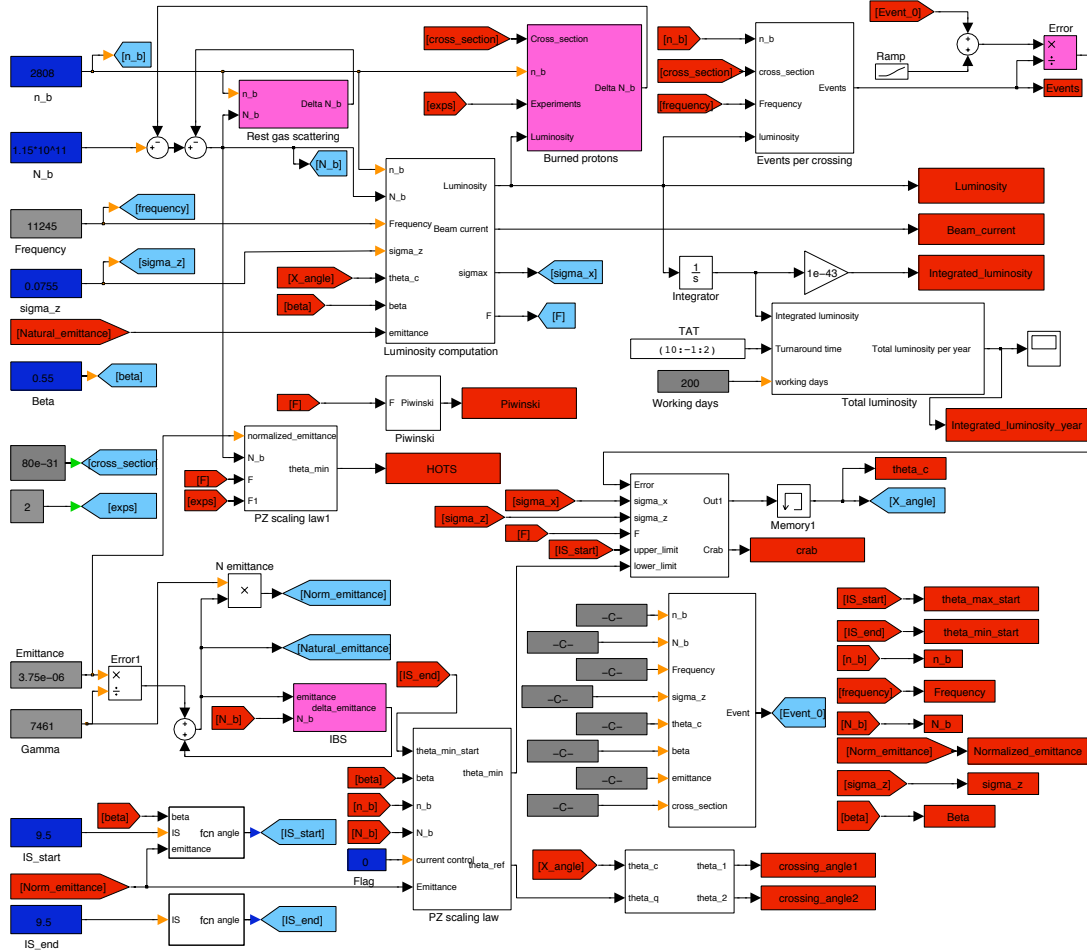


Figure 2.9: A schematic of the SimulinkTM model developed for solving the system of differential equation and to implement the feedback control used for the luminosity leveling.

compared the analytical model with the numerical one in a large portion of the parameters' space. We summarize in the following the results.

In Fig. 2.10, *top*, the luminosity behavior using both the analytical and the numerical model is shown: the peak luminosity (and the maximum multiplicity) is identical in the two cases, as expected since it does not depend on the model of the luminosity decay. The luminosity decay is faster in the numerical model: this is due to the emittance's growth related to the intra beam scattering and due to the additional beam losses related to the rest gas scattering. The impact of the leveling is evident: the duration of the luminosity plateau, T_l , is reduced by 30%. In Fig. 2.10, *bottom*, we compare the integrated luminosity behavior using both the analytical and the numerical model: the shorter luminosity lifetime translates directly into a loss of integrated luminosity by $\approx 10\%$: from this plot we can conclude that, in our assumptions, the sLHC could deliver 3000 fb^{-1} on a period of 6.5-7 years.

The comparison of the beam-beam tune shift between the analytical and numerical model is presented in Fig. 2.11: the difference between the maximum beam-beam tune shift is smaller than 5% for the leveling scenario while there is not difference in the two cases where we have constant separation ($\Delta_{in} = 5$ and 12).

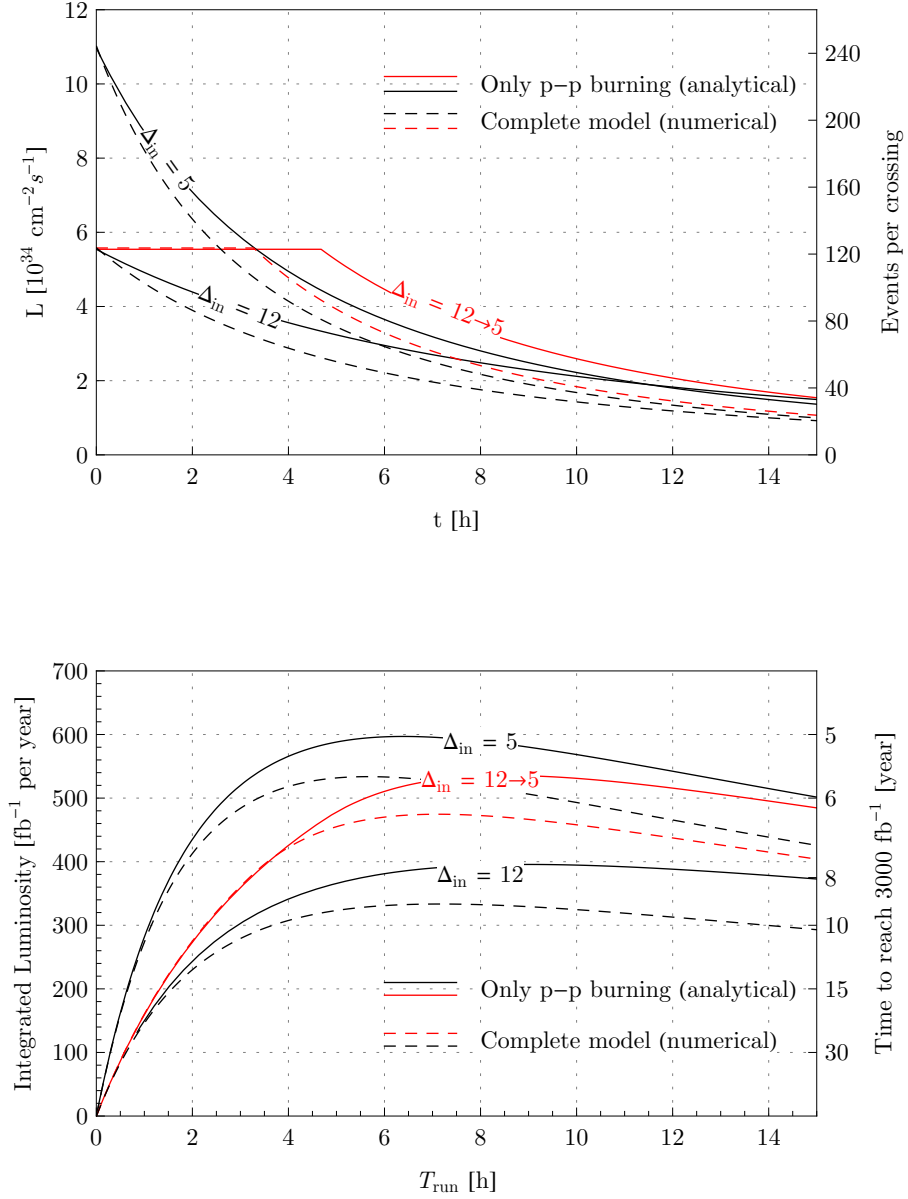


Figure 2.10: Comparison between the analytical and numerical model on the instantaneous and integrated luminosity. The decay of the instantaneous luminosity, *top*, is faster in the numerical model and this shortens the luminosity plateau of the leveling by ≈ 1.5 h. In the numerical model the integrated luminosity, *bottom*, is reduced by 10%: the machine can deliver 3000 fb^{-1} on a period of 6-7 years. The values assumed are $\beta^* = 0.15 \text{ m}$, $N_b = 2.3 \cdot 10^{11}$, $n_b = 2808$ and TAT = 5 h.

We can conclude that the analytical model can predict within good accuracy the peak luminosity and the maximum beam-beam tune shift. On the other hand the integrated luminosity is overestimated by $\approx 10\%$ in the portion of the parameters' space we work are considering.

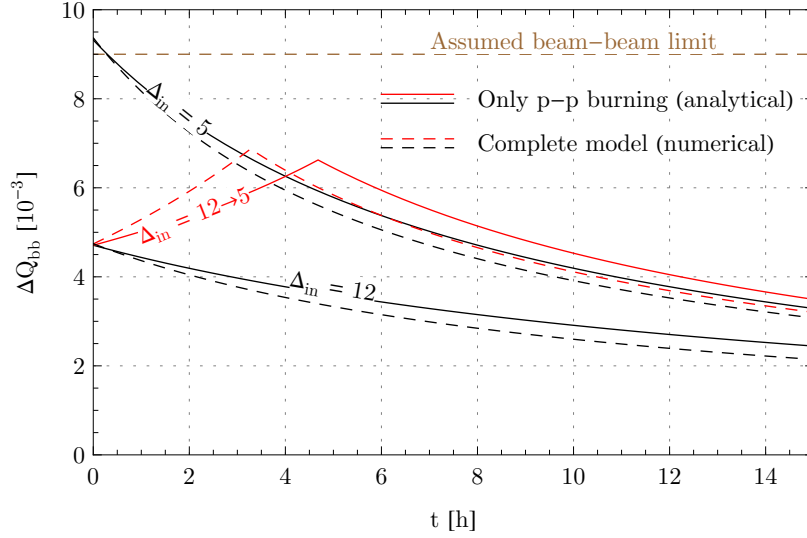


Figure 2.11: Comparison between the analytical and numerical model on the beam-beam tune shift. The maximum tune shift is well predicted even by the analytical model. The values assumed are $\beta^* = 0.15$ m, $N_b = 2.3 \cdot 10^{11}$ and $n_b = 2808$.

2.5 Luminosity performance of the Early Separation Scheme

2.5.1 Scenarios and performance

In this section we discuss in details the potential of the Early Separation Scheme in terms of luminosity gain. At the moment, we do not yet have the important feedback of the LHC operations since the machine is not running and it is not planned to reach the nominal performance before a period of 3-4 years from its start. At that stage we will have a clearer picture of the limits of the injectors and the LHC itself, and we will reduce significantly the uncertainty range of many parameters that are crucial for planning the upgrade. Nevertheless, we need to investigate and develop from now the schemes and the hardware components needed for the sLHC. In an extremely fluid parameter space, it is important to prove the flexibility of the proposed solutions that is their effectiveness in the various scenarios we could face.

We observed in Section 2.3.3 that, in order to increase the integrated luminosity, an increase of the beam current plays a crucial role. We cannot increase the beam current by increasing the number of bunches due to the predicted electron cloud effect limit [3]. For this reason we concentrate here on the 25 ns spaced bunches solution. With a general approach it is possible to define two major limits for the LHC beam current in the LHC accelerator complex:

1. *storage ring limit*: it is the maximum current that can be stored in the LHC rings at the desired collisions energy without putting the beams into collision. It is the smaller of the *injectors limit* and the *synchrotron limit* current.

The *injectors limit* is related to the capability of the injectors to deliver the desired beam filling pattern and intensity to the LHC. The present injectors system can deliver the nominal LHC beam (2808 bunches with $N_b = 1.15 \cdot 10^{11}$, $\epsilon_n = 3.75 \cdot 10^{-6}$ m·rad) [1] but already beyond $N_b \approx 1.2 \cdot 10^{11}$ [11] the Super Proton Synchrotron (SPS) presents some issues related to the electron cloud effect. For higher intensities additional limitation are envisaged (space charge, electron cloud effect, transverse mode coupling instability, beam loading of the RF cavities...): large efforts are concentrated to overcome all these limits in order to reach and go beyond the ultimate current bunch population in SPS ($N_b = 1.7 \cdot 10^{11}$) [11] [12]. To exploit at the maximum the LHC potential a new LINAC is presently going to be built (LINAC4, [10]) and the conceptual design for a new PS (PS2) is under work [36].

The *synchrotron limit*, on the other hand, represents all specific limitations of the main ring(s) (LHC in

our case) encountered when the beams are *not* in collision: mainly during the injection phase, the RF capture, the acceleration... or due to the collimation efficiency, the electron cloud effect, the cryogenics limit of the arcs, the impedance budget of the machine, the magnets field quality...

2. *collider limit*: once the beams are put into collision the beam dynamics is expected to be dominated by the collision itself (head-on beam-beam effect) and by the parasitic interactions of the two beams (long-range beam-beam effect). This effect can increase to unacceptable level the background noise in the experiment and can reduce significantly the beam lifetime (with, consequently, a poor luminosity lifetime and a higher risk of quench, that is a lower integrated luminosity). The collider limit, using the experience derived from other machines, can be for convenience expressed by its linear effect: the total tune shift, ΔQ_{bb} . With this approach, in the case of alternating crossing angle, the long-range beam-beam contribution to the ΔQ_{bb} vanishes since its linear tune shift is compensated: this is an evident limit of the approximation. The assumed collider limit of the LHC is $\Delta Q_{bb} = 9 \cdot 10^{-3}$ [3]: it corresponds to the ultimate bunch current $N_b = 1.7 \cdot 10^{11}$ (25 ns bunch spacing), having two experiments with $\Delta_{in} = 9.5$ and $\beta^* = 0.50$ m.

The optimal exploitation of the machine corresponds to the overlap (if possible) of the storage ring limit and of the collider limit. It is worth noting that, apart all the efforts on going to increase the injectors limit, the synchrotron limit cannot be easily modified without major changes in the LHC arcs (not foreseen for sLHC) and is expected to be between $1.7 \cdot 10^{11} \leq N_b \leq 2.3 \cdot 10^{11}$ (25 ns spacing). On the contrary, the collider limit can be increased by a convenient design of the interaction region. In addition, while the storage ring limit is always reachable in a machine, the collider limit may not. In general two scenarios can be envisaged in a collider:

- the collider limit is more stringent than the storage ring limit: in this case we can use the Early Separation Scheme to increase the crossing angle and to reach, at constant ΔQ_{bb} , the beam current of the storage ring limit,
- the collider limit is less stringent than the storage ring limit: in this case we can use the Early Separation Scheme to reduce the crossing angle and to reach, at constant current the ΔQ_{bb} , of the collider limit.

All these considerations are analyzed in a quantitative way in Figs. 2.12 and 2.13. It is assumed that

- the duration of the physics run $T_{run} = \text{Max}(T_{run}^{opt}, 8 \text{ h})$: this is due to the fact that, apart of the mathematical optimization, we have to take into account the risks connected with the filling for the ring, the beam acceleration, squeeze and collision phases of a large and complex system. From the past colliders experience, we assume that having runs shorter than 8 h does not translate in a real integrated luminosity increase,
- the turn-around-time, TAT is 10 h for the nominal LHC and 5 h for the sLHC,
- the days of operations, T_{runs} , are 200 in a years,
- two alternating crossings are considered with a $\beta^* = 0.15$ m [37].

In Fig. 2.12, the integrated luminosity versus the total beam-beam tune shift is shown using the proposed analytical model. The curves end when the $N_{b0} = 2.3 \cdot 10^{11}$ ppb is reached. The assumed limit of $\Delta Q_{bb} = 9 \cdot 10^{-3}$ is shown (dashed line). If this value can be reached, the most promising scenario in terms of integrated luminosity is $\Delta_{in} = 5$: with this value of bunch population (N_{b0}), to further reduce the Δ_{in} is not allowed by the beam-beam tune shift. The potential of Crab Crossing Scheme, $\Delta_{in} = 0$, would be a priori not exploitable without luminosity leveling: this means we cannot use a $\Delta_{in} = 0$ from the start of the physics run (not shown in the figure), but we can consider a luminosity leveling with Δ_{in} from 12 to 5. With the luminosity leveling (Δ_{in} from 12 to 5) it is possible to reach almost the same integrated luminosity of the $\Delta_{in} = 5$ configuration but with 25% lower beam-beam tune shift.

Similarly, in Fig. 2.13, the integrated luminosity versus the initial bunch population, N_{b0} , is shown using the proposed analytical model. The curves end when the $\Delta Q_{bb} = 9 \cdot 10^{-3}$ is reached and the limit $N_b = 2.3 \cdot 10^{11}$ is shown (dashed line). We can observe again that the scenario with leveling is limited by the beam current and not by the ΔQ_{bb} . The luminosity leveling gives almost the same integrated luminosity of the scenario with $\Delta_{in} = 5$ with a slightly larger beam current.

From Figs. 2.12 and 2.13 we can conclude, with all the assumptions discussed above, that differently from the nominal LHC where the performance is limited by the total beam-beam tune shift ΔQ_{bb} , the sLHC it expected to be limited by the N_{b0} (storage ring limit): this is due to the lower β^* of the sLHC (0.15 m with respect to the nominal 0.55 m) that reduces significantly, at constant $\Delta_{in} \neq 0$, the ΔQ_{bb} . Nevertheless the scenario can change if the beam brightness is increased (the new injectors can deliver a smaller ϵ_n to sLHC, thus increasing the ΔQ_{bb} at constant Δ_{in}) or if more than two experiments are considered (increased total beam-beam): the flexibility offered by the Early Separation Scheme can be very useful to optimize the machine for a large spectrum of scenarios.

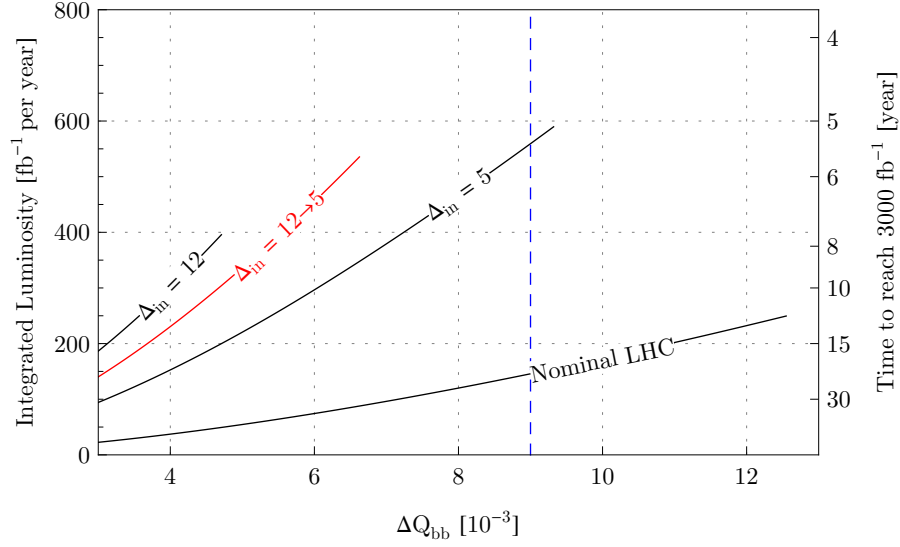


Figure 2.12: The integrated luminosity versus the total beam-beam tune shift (analytical model). The curves end when the $N_{b0} = 2.3 \cdot 10^{11}$ ppb is reached. The assumed limit of $\Delta Q_{bb} = 9 \cdot 10^{-3}$ is shown. If this value can be reached, the most promising scenario in terms of integrated luminosity, is $\Delta_{in} = 5$: with this value of bunch population (N_{b0}), to further reduce the Δ_{in} is not allowed by the beam-beam tune shift (the crab cavities' potential, $\Delta_{in} = 0$, would be a priori not exploitable). With the luminosity leveling (Δ_{in} from 12 to 5) it is possible to reach almost the same integrated luminosity of the $\Delta_{in} = 5$ configuration but with 25% lower beam-beam tune shift.

In Fig. 2.14 the potential of the Early Separation Scheme is presented in the luminosity plane using the numerical solution of the model proposed. Assuming a $N_b = 1.7 \cdot 10^{11}$ the gain in terms of integrated luminosity passing, with the Early Separation Scheme, from $\Delta_{in}=9.5$ to 5 is $\approx 30\%$. The collider limit is reached at $\Delta_{in} \approx 3$: this normalized inner separation between the beams is beyond the Early Separation Scheme possibilities (see Chapter 5). Assuming a $N_b = 2.3 \cdot 10^{11}$ the Early Separation Scheme potential is similar (40% gain). With this beam intensities the leveling appears to be a winning strategy: the gain in term of integrated luminosity is slightly reduced but the peak luminosity remains below 5.5 or $7.7 \cdot 10^{34} \text{ cm}^{-2}\text{s}^{-1}$ respectively with $\Delta_{in} = 12$ or 9 at the start of the physics run. The Crab Crossing Scheme can further boost the machine performance with a total gain of 50% in terms of integrated luminosity: once the technology will be proved in hadron colliders, having better performance than the Early Separation Scheme and the advantage of not needing hardware in the detectors, it is to be preferred to the Early Separation Scheme (see Conclusions).

2.5.2 General remarks on luminosity leveling

In the above sections the potential of the Early Separation Scheme and of the leveling has been discussed. Here we discuss the possible side effects that we envisage: in the following chapters some of these limitation are analyzed in details.

Due to the integration difficulties of the Early Separation Scheme hardware in the detectors, the positions of the D0 dipole (see Fig. 1.18) has important constraints in terms of distance from the Interaction Point (see Chapter 5). This means that there will be some beam-beam encounters at reduced separation in the Interaction Region and more precisely about 6 beam-beam encounters at reduced separation ($\approx 5 \sigma$) for each Interaction Point (that is 12 long-range at $\approx 5 \sigma$ separation in the whole machine). This can have a negative impact on the beam stability reducing the so-called dynamic aperture of the machine. This topic will be discussed in details in the Chapters 3 and 4: we expect that, with a convenient choice of the machine tune, 12 parasitic encounters may be tolerated up to a $N_b = 1.7 \cdot 10^{11}$ and with $\epsilon_n = 3.75 \cdot 10^{-6} \text{ m-rad}$. Referring to

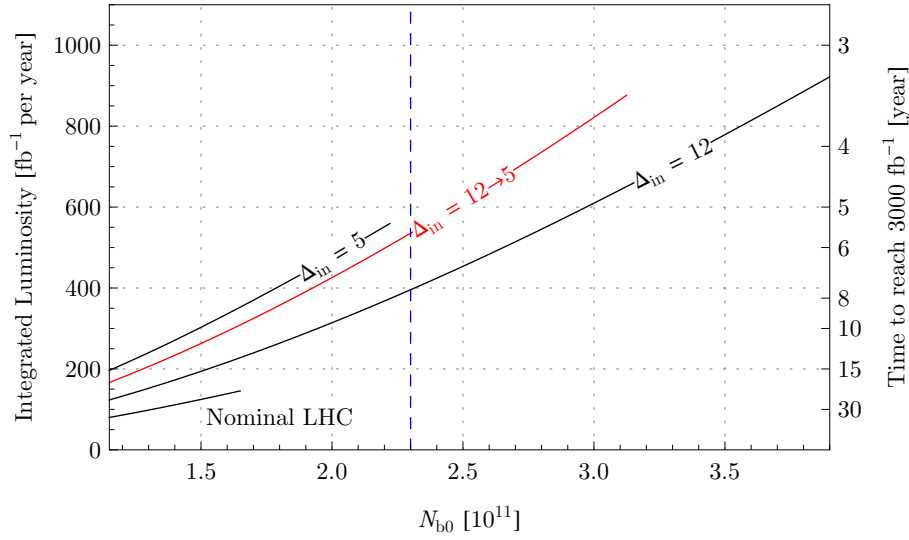


Figure 2.13: The integrated luminosity versus the N_{b0} (analytical model). The curves end when the $\Delta Q_{bb} = 9 \cdot 10^{-3}$ is reached. The limit $N_b = 2.3 \cdot 10^{11}$ is shown. We can observe that the scenario with leveling is limited by the beam current and gives almost the same integrated luminosity of the scenario with $\Delta_{in} = 5$ with a slightly larger beam current.

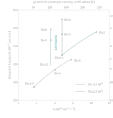


Figure 2.14: The integrated luminosity gain provided by the Early Separation Scheme. The gain between the Early Separation Scheme ($\Delta_{in} = 5$) and the nominal crossing angle ($\Delta_{in} = 9.5$) is about 35 – 40% in term of integrated luminosity depending on actual value of the N_b . The leveling can gives a similar increase of the integrated luminosity without increasing the peak luminosity. The $\Delta_{in} \leq 5$ is possible only using a Crab Crossing Scheme. The blue square markers represent a $\Delta_{in} = 5$ that is the minimum separation the Early Separation Scheme can provide (Chapter 5).

Fig. 2.14, this means that it will be difficult, in practice, to follow the curve with $N_b = 2.3 \cdot 10^{11}$ (no leveling) until $\Delta_{in} = 5$. On the contrary, the leveling seems to be compatible with this constraint: at the start of the run, when the beams are put into collision we have the maximum bunch current ($N_b = 2.3 \cdot 10^{11}$) and the maximum separation ($\Delta_{in} = 9$ or 12 depending on the leveling scenarios, Fig. 2.14). Only when the beam current is decreased we reduce the crossing angle, therefore the $\Delta_{in} = 5$ corresponds to a significantly smaller value of the beam current ($N_b \approx 1.7 \cdot 10^{11}$, see Fig. 2.15).

It is important to point out that, in order to compensate the linear part of the beam-beam long-range tune shift and, therefore, to have the assumed dependence of the ΔQ_{bb} on the geometrical factor F (Section 3.1.3), we need to have alternating crossing in the two Interaction Points (one horizontal and other vertical) and we need to have exactly the same leveling strategy (e.g., equal Δ_{in} at the start and at the end, less critically, equal D0 dipole position). For this reason we will proposed an identical implementation of the scheme in the two high luminosity Interaction Points (see Chapter 5).

Another possible drawback of the luminosity leveling is the modification of longitudinal size σ_{lum} of the

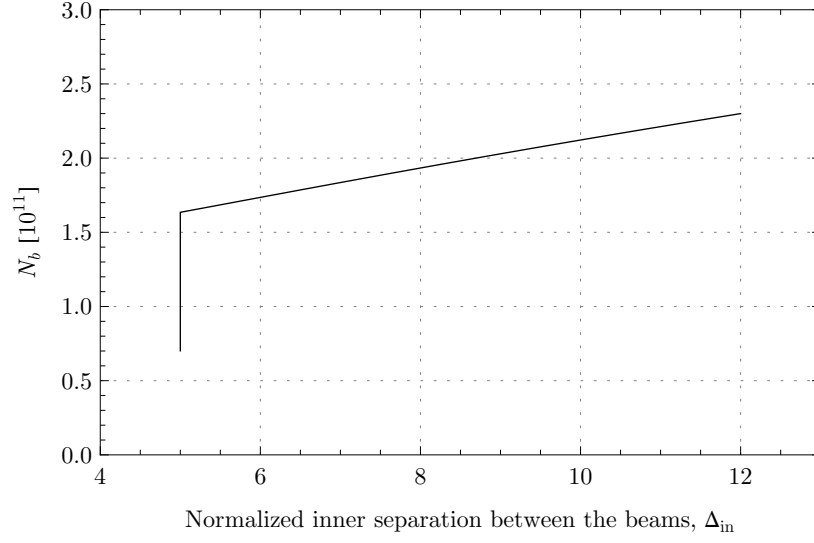


Figure 2.15: The bunch population, N_b , as function of the inner separation during the leveling (Δ_{in} from 12 to 5σ).

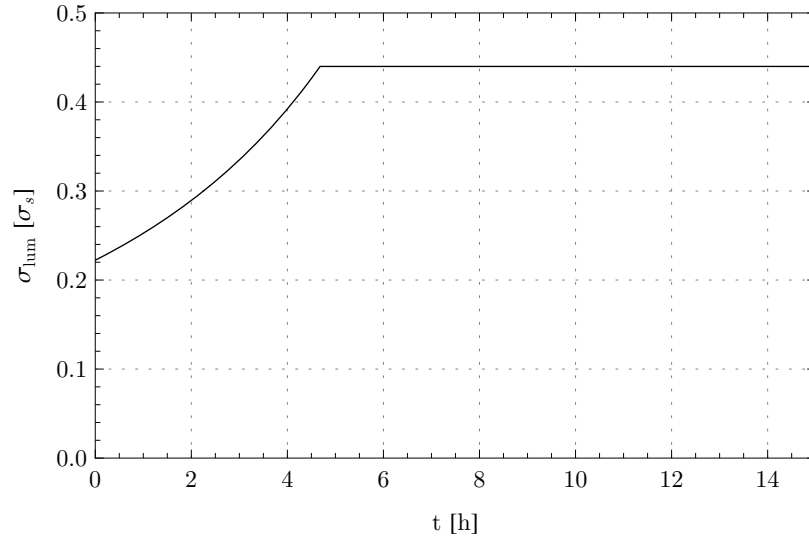


Figure 2.16: The luminous region size (RMS) during the run time.

luminous region [38]

$$\frac{1}{\sigma_{lum}} \approx \sqrt{\frac{2}{\sigma_s^2} + \frac{\theta_c^2}{2\sigma^{*2}}},$$

that is to say

$$\sigma_{lum} \approx \frac{\sigma_s}{\sqrt{2}} F$$

where the σ_s represents the RMS longitudinal size of the bunch ($\sigma_s = 7.55 \cdot 10^{-2}$ m in the nominal LHC at collision energy). As shown in Fig. 2.16 the leveling has a significant impact on the luminous region size (it varies almost by a factor 2): from a first iteration with the detectors experts this seems not to reduce in a significant way the interest and the potential of the luminosity leveling.

The luminosity leveling using the Crab Crossing Scheme has similar drawback but has the potential to reach a vanishing crossing angle ($\Delta_{in} = 0$). On the contrary, the luminosity leveling done controlling the beam crossing angle by using the nominal orbit correctors (see Fig. 1.13) instead of the Early Separation dipoles, apart from the additional steering difficulties (the bump extends to a larger region and goes through the final focusing quadrupoles), cannot reach, with our present knowledge of the problem, the 5σ beam separation since it would imply too many beam-beam long-range encounters at reduced separation.

Instead of controlling the beam crossing angle, a different method to level the luminosity is, as already mentioned, by varying the β -function at the Interaction Point, β^* : it is equivalent to changing the beam size at the collision point and it can be done at constant normalized separation, Δ_{in} constant, or at constant physical angle, θ_c constant. In both cases, the chromaticity of the machine has to be controlled during the β -function modification and in the first case also the closed orbit has to be modified: these additional controls increase the overall complexity of the operations. In addition to that, during this kind of luminosity leveling, the Piwinski angle (see Eq. 1.9) increases as $1/\beta^*$ (at Δ_{in} constant) or $1/\sqrt{\beta^*}$ (at θ_c constant). On the contrary, during the luminosity leveling with the crossing angle, the Piwinski angle is reduced. This last condition is more favorable for the optimization of the luminosity performance since it minimizes the total tune shift at the start of the run when the N_b is larger, allowing to store more beam current. On the contrary, the leveling with β^* , in presence of a non vanishing beam crossing angle and due the induced increase of the total tune shift of the collider, would possibly prevent to store the same amount of beam current with a significant impact on the machine integrated luminosity.

Chapter 3

The beam dynamics effects

Contents

3.1 Linear beam dynamics effects	43
3.1.1 The dispersion induced by the scheme	43
3.1.2 The on-momentum β -beating induced by the scheme	44
3.1.3 The impact of the scheme on the beam-beam tune shift	47
3.2 Non-linear beam dynamics effects	48
3.2.1 Diffusion due to the machine non-linearities	49
3.2.2 Analytic expression of the beam-beam interaction	52
3.2.3 Scaling laws for the beam-beam interaction	57

In the present chapter the effects of the Early Separation Scheme on the beam dynamics are analyzed. The chapter is divided in two main sections to address separately the linear and non-linear effects induced by the Early Separation Scheme. In Section 3.1 the induced dispersion, β -beating and some important considerations on the beam-beam tune shift are presented (linear effects). In Section 3.2, we consider the non-linear perturbations of the beam dynamics related to the parasitic interactions between the beams. The last part of this second section is dedicated to the analysis of the scaling laws that allow to compare two distinct non-linear machines: they are the theoretical foundation to perform beam-beam experiments in the Super Proton Synchrotron (SPS) in order to reproduce the LHC beam dynamics, as reported in the following chapter.

3.1 Linear beam dynamics effects

The aim of the Early Separation Scheme is to modify the machine closed orbit in the Interaction Region. Nevertheless it could parasitically affect the linear dynamics of the machine, namely the dispersion and, due to the dipole's weak focusing effect, the β -function.

3.1.1 The dispersion induced by the scheme

The dispersion is related to the modification of the closed orbit for the off-momentum particle. It has, in general, a negative effect on the machine performance since it increases the transversal dimensions of the beam and induces coupling between the longitudinal and transversal degrees of freedom. In the following sections we show that this effect is negligible.

In an accelerator the dispersion, $D(s)$, can be computed using the following equation [22]

$$D(s) = \frac{\sqrt{\beta(s)}}{2 \sin(\pi Q)} \int_0^L \frac{\sqrt{\beta(t)} \cos(\pi Q - |\mu(t) - \mu(s)|)}{\rho(t)} dt \quad (3.1)$$

where L is the machine length, β and μ represent, respectively, the β -function and the phase advance function, Q is the tune of the machine and ρ is the radius of curvature of the beam trajectory [22]. Due to the linearity of the problem, the total dispersion can be expressed (Eq. 3.2) as the sum of the dispersion

induced by the Early Separation Scheme (D_{ES}) and the one induced by all the other components of the machine (D_{OTHER})

$$D(s) = D_{ES}(s) + D_{OTHER}(s). \quad (3.2)$$

We focus on the $D_{ES}(s)$. On the other hand, in general, the closed orbit (CO) can be expressed as [22]

$$CO(s) = \frac{\sqrt{\beta(s)}}{2 \sin(\pi Q)} \int_0^L \frac{B(t)}{B\rho} \sqrt{\beta(t)} \cos(\pi Q - |\mu(t) - \mu(s)|) dt. \quad (3.3)$$

where the B represents the magnetic field of the orbit correctors (or machine errors and imperfections) and the $B\rho$ the beam magnetic rigidity.

In Eq. 3.3 the $B(t)$ refers only to the magnetic elements that define the closed orbits (orbit correction and machine imperfection) and not to the elements that determine the alignment orbit (arc dipoles, separation-recombination dipoles). The $\rho(t)$ in Eq. 3.1 is instead related to the dipolar component of each single magnetic source.

The contributions to the dispersion of the orbit correctors and arc dipoles can be separated since they are not coupled: the magnetic field felt by the particle does not depend on the particle position in a dipole. This is not anymore true for the quadrupoles (and for all higher order magnetic elements). From the previous sentence and from Eqs. 3.1 and 3.3, it yields that the dispersion induced by the orbit correctors is proportional to the closed orbit only if the orbit correctors' bump ($\rho(t) \neq 0$ in Eq. 3.1) occurs in a drift space region (dipoles can be present, quadrupole and higher multipoles not). This is the case of the Early Separation Scheme and in particular, in our reference system, the following holds

$$\frac{B(t)}{B\rho} = -\frac{1}{\rho(t)} \quad \text{that is} \quad D_{ES}(s) = -CO_{ES}(s) \quad (3.4)$$

where $CO_{ES}(s)$ represents the closed orbit contribution of the Early Separation Scheme. This means that its induced dispersion at the Interaction Point (IP) is null since $CO_{ES}(IP) = 0$, its derivative of the IP is not vanishing and is proportional to the slope of the Early Separation bump at the IP, the maximum of the dispersion will correspond to the maximum of the bump amplitude (few millimeters) and the induced dispersion in the triplets is vanishing. On the contrary, the nominal bump scheme (not occurring in a drift space) induces, in general, a spurious dispersion all around the ring (dispersion leakage). In the Fig. 3.1 the Early Separation closed orbit and induced dispersion are shown: it represents correctly the Eq. 3.4. The computation has been performed using the nominal optics (V6.503 [39], thick lens) and MAD-x (version 4.00.XX [40]). In our assumption we consider that the D0 dipole, 2 m long, is centered at 14 m from the IP and the OC dipole, 1.5 m long, at 21 m from the IP (Fig. 1.18). The normalized outer separation between the beams, Δ_{out} , is given by the nominal crossing angle ($\Delta_{out} = 9.5$) and the normalized inner separation between the beams, Δ_{in} , is 5.

Comparing the Figs. 3.1 and 3.2, it is possible to conclude that the dispersion induced by the Early Separation Scheme is negligible since it is orders of magnitude lower than the one induced by the crossing scheme (that is comparable with the expected spurious one). This is in particular important for the luminosity leveling with the Early Separation Scheme because we show that, during the leveling, the dispersion of the collider is constant along the ring and therefore no correction is needed.

3.1.2 The on-momentum β -beating induced by the scheme

Another linear effect related to the Early Separation Scheme is the induced on-momentum β -beating. This is caused by the dipoles' weak focusing effect. The on-momentum β -beating is a modification of the β -function all along the machine that has, in general, a negative impact on the machine since its linear optics is modified (tunes, phase advances, beam size...).

The Early Separation Scheme requires single-aperture magnets: this, together with its very modest integrated field (compared to an arc-dipole), implies that, for its analytical description, rectangular dipoles model instead of sector dipole ones should be adopted [22]. From [22] and for a vertical Early Separation Scheme (that is vertical crossing), we have the following transformation matrices

$$M_x = \begin{pmatrix} 1 & \rho \sin(\phi) \\ 0 & 1 \end{pmatrix} \quad \text{and} \quad M_y = \begin{pmatrix} \cos(\phi) & \rho \sin(\phi) \\ -\frac{1}{\rho} \sin(\phi) & \cos(\phi) \end{pmatrix} \quad (3.5)$$

where ϕ is the angle provided by the magnet and ρ is its radius of curvature. Assuming a magnet of length l , we have that $\phi = l/\rho$.

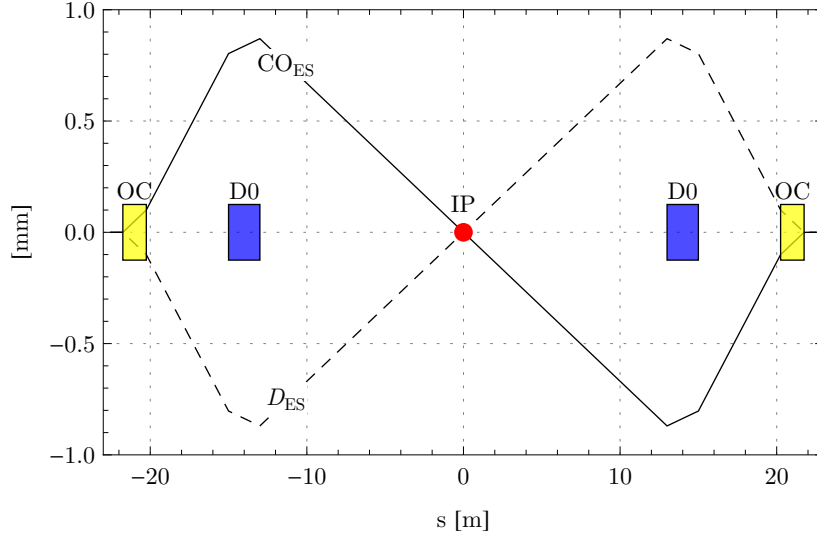


Figure 3.1: The Early Separation Scheme closed orbit and induced dispersion (MAD-X results). It is in perfect agreement with our analytical analysis.

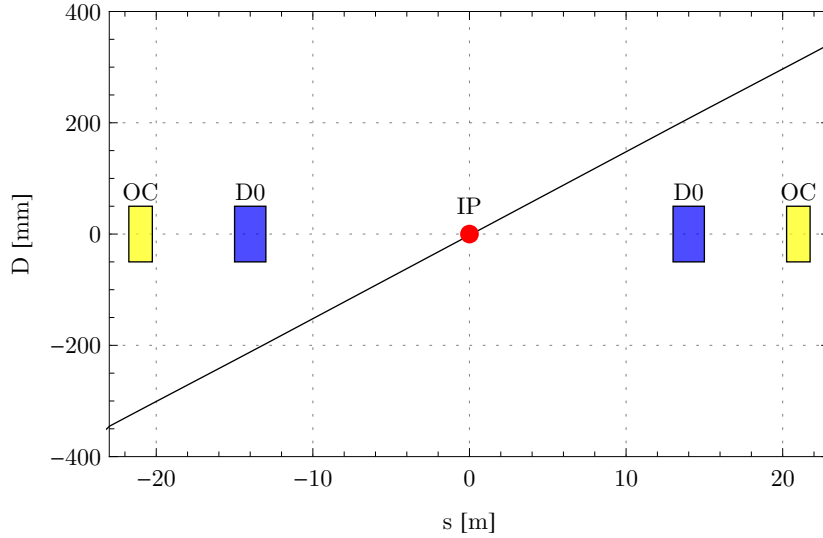


Figure 3.2: The total dispersion of the machine (nominal LHC + Early Separation Scheme effect).

Typical values for the Early Separation Scheme integrated field of the magnets are $\approx 10 \text{ T}\cdot\text{m}$ (Fig. 1.22). Given the LHC magnetic rigidity ($B\rho \approx 23349.2 \text{ T}\cdot\text{m}$), it yields typical values of $\phi = \frac{\int_{D0,OC} B dl}{B\rho} = 4 \cdot 10^{-4} \text{ rad}$ and $\rho = 5 \cdot 10^3 \text{ m}$. From Eq. 3.5, it gives that the transformation matrix in the x -plane (M_x) behaves, on one hand, like a drift of length $l + 5 \cdot 10^{-8} \approx l$ (paraxial approximation). On the other hand, M_y represents two thin quadrupoles having the same polarity with a focal lengths equal to $2|\rho^2/l| \approx 25 \cdot 10^6 \text{ m}$ (extremely weak focusing, see following) and positioned at a distance equal to l (edge focusing in the dipoles [22]).

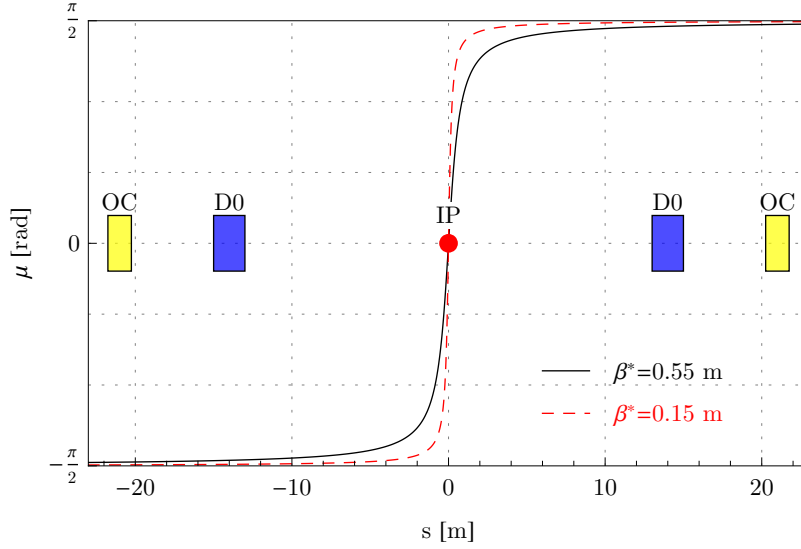


Figure 3.3: The phase advance in the drift space of the Interaction Region.

For comparison, in thin approximation, the focal length $f = 1/(KL)$, where K and L are the quadrupole normalized gradient and length, of the collider's quadrupole closer to the Interaction Point (Q1, Fig. 1.9), is ≈ 18 m. It is worth noting that while the thin lens approximation is inadequate for the Q1 (its focal length, 18 m, is comparable to its length, 6.37 m), it is extremely good ($25 \cdot 10^6$ m \gg 2 m) for computing the weak focusing contribution of the Early Separation Scheme.

The β -beating (linear contribution for small perturbations) is given by [22]

$$\frac{\Delta\beta(s)}{\beta(s)} = \frac{1}{2\sin(2\pi Q)} \int_0^L \beta(t) \Delta K(t) \cos(2|\mu(t) - \mu(s)| - 2\pi Q) dt$$

that in thin lens approximation becomes

$$\frac{\Delta\beta(s)}{\beta(s)} = \frac{1}{2\sin(2\pi Q)} \sum_{i \in \mathcal{S}} \beta(s_i) \frac{l_i}{2\rho_i^2} \cos(2|\mu(s_i) - \mu(s)| - 2\pi Q) \quad (3.6)$$

where $\mathcal{S} = \{D0_{L_{end}}, D0_{L_{start}}, D0_{R_{end}}, D0_{R_{start}}, OC_{L_{end}}, OC_{L_{start}}, OC_{R_{end}}, OC_{R_{start}}\}$, s_i represents the specific position of the lens (end or start of the corresponding magnet), ρ and l are, respectively, the bending radius and the length of the magnets to whom the edge quadrupole belongs.

It is known [22] that the phase advance in the drift space of the Interaction Region (IR) is (Fig. 3.3)

$$\mu(s) = \arctan\left(\frac{s}{\beta^*}\right). \quad (3.7)$$

The phase advance between the two edge quadrupoles of the same magnet is very small (so their effects add almost perfectly in phase). On the other side, a strong compensation (Fig. 3.3) between the left and right magnets ($D0_L$ - $D0_R$ and OC_L - OC_R) occurs due to the specific phase advance condition $\Delta\mu \approx \pi$. Finally, a partial compensation occurs between $D0$ and OC (in the IR drift space).

In Figs. 3.4 the β -beating is shown for a $Q=0.31$ (from Eq. 3.6). The three curves on the plot represent the effects of a single dipole ($D0_R$), the partial compensation right-left ($D0_R + D0_L$) and the overall compensation (the complete Early Separation Scheme). In the Figs. 3.4 the values of Table 1.1 have been used: the Early Separation Scheme induced β -beating in the drift space is below the 10^{-4} level and is even lower in the rest of the machine. It is possible, therefore, to conclude that the Early Separation Scheme induced β -beating is negligible. Due to the symmetry left-right the tune shift induced by the β -beating vanishes. For the leveling with the Early Separation Scheme this is extremely convenient since it implies that during the leveling the

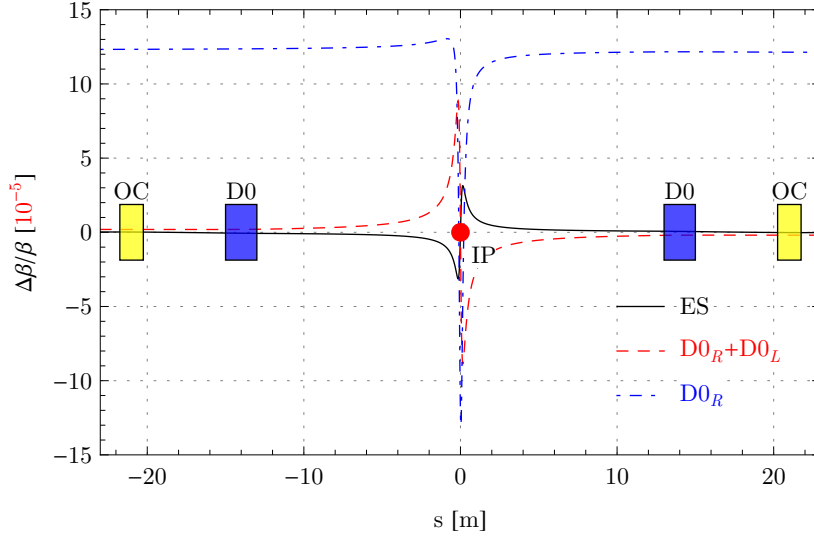


Figure 3.4: The induced on-momentum β -beating for $Q=0.31$. The y -axis is in units of 10^{-5} .

linear tunes of the machine cannot change. This is true, as explained in the following section, only if we neglect the beam-beam effect.

3.1.3 The impact of the scheme on the beam-beam tune shift

The interaction between the beams, *beam-beam effect*, is intrinsically a non-linear problem (see Section 3.2). Nevertheless its first order approximation, the so-called beam-beam tune shift, has been, in the past colliders, a successful criterion to judge and steer the machine performance. As we show in the following, this effect depends on the crossing angle between the beams at the interaction point (θ_c): for this reason the Early Separation Scheme can have a significant impact on it.

A tune shift, $\Delta Q_{x,y}$, is due to a quadrupolar gradient error $\Delta K_{x,y} = \frac{1}{B\rho} \frac{d\Delta B_{y,x}}{dx,y}$ [22]

$$\Delta Q_{x,y} = \pm \frac{1}{4\pi} \int \Delta K_{x,y}(t) \beta_{x,y}(t) dt. \quad (3.8)$$

It is known [3] that, for Gaussian bunches and equal beams ($\epsilon_x = \epsilon_y = \epsilon$, $\beta_x^* = \beta_y^* = \beta^*$), the tune shift induced by one pp collision with a crossing angle θ_c can be expressed (horizontal crossing) as

$$\begin{aligned} \Delta Q_x &= \xi \int_{-\infty}^{+\infty} \frac{2\sqrt{2} \epsilon \exp(-2s^2/\sigma_s^2)}{\sqrt{\pi} \sigma_s} \left(\frac{s^2}{\beta^*} + \beta^* \right) \times \\ &\quad \left(\left(\frac{1}{s^2\theta_c^2} + \frac{1}{\epsilon(s^2/\beta^* + \beta^*)} \right) \exp\left(-\frac{s^2\theta_c^2}{2\epsilon(s^2/\beta^* + \beta^*)}\right) - \frac{1}{s^2\theta_c^2} \right) ds \\ \Delta Q_y &= \xi \int_{-\infty}^{+\infty} \frac{2\sqrt{2} \epsilon \exp(-2s^2/\sigma_s^2)}{\sqrt{\pi} s^2 \theta_c^2 \sigma_s} \left(\frac{s^2}{\beta^*} + \beta^* \right) \times \\ &\quad \left(1 - \exp\left(-\frac{s^2\theta_c^2}{2\epsilon(s^2/\beta^* + \beta^*)}\right) \right) ds \end{aligned} \quad (3.9)$$

where

$$\xi = -\frac{N_b r_p}{4\pi \epsilon_n} \quad (3.10)$$

and r_p and ϵ_n are, respectively, the classical radius of the proton and the beam normalized emittance.

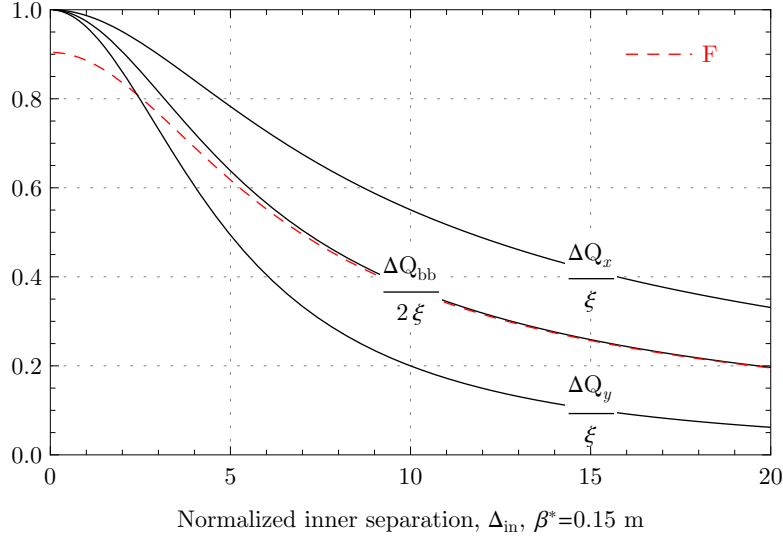


Figure 3.5: The dependence of the total tune shifts on the normalized inner separation between the beams. It is possible to observe that $\Delta Q_{bb}/(2\xi) \simeq F$ for $\Delta_{in} \gtrsim 4$.

Assuming two beam collision points in the machine in the two different planes (one horizontal, one vertical) the linear component of the tune shift due to the long-range beam-beam collision is compensated and the total tune shift ΔQ_{bb} , equal in the vertical and horizontal planes, is given by

$$\Delta Q_{bb} = \Delta Q_{tot,x} = \Delta Q_{tot,y} = \Delta Q_x + \Delta Q_y. \quad (3.11)$$

From Eqs. 3.10 and 3.11 we have

$$\Delta Q_{bb} = 2\xi \int_{-\infty}^{+\infty} \frac{2\sqrt{2} \exp\left(-\frac{1}{2}s^2 \left(\frac{\beta^* \theta_c^2}{s^2 \epsilon + \beta^{*2} \epsilon} + \frac{4}{\sigma_s^2}\right)\right)}{\sqrt{\pi}\sigma_s} ds.$$

The Fig. 3.5 shows (for a $\beta^* = 0.15$ m) the horizontal and vertical tune shifts divided by ξ ($\Delta Q_x/\xi$, $\Delta Q_y/\xi$) and the total tune shift, $\Delta Q_{bb}/(2\xi)$ as function of the normalized inner separation between the beams, Δ_{in} , if two Interaction Points with alternating crossing are assumed. From the plot we can observe that for a $\Delta_{in} \gtrsim 4$ the reduction factor on the total beam-beam tune shift is equivalent to the geometrical reduction factor of the luminosity. For reduced normalized inner separation ($\Delta_{in} \lesssim 4$), this is not valid anymore since the tune shift is not affected by the hourglass effect while the luminosity is.

This yields the fundamental conclusion (Chapter 2, Eq. 2.16) that for *two alternating* Interaction Points

$$\Delta Q_{bb} \simeq 2\xi F \quad \text{for} \quad \Delta_{in} \gtrsim 4,$$

and, as explained before (see Section 2.5), this allows to push further the *collider limit* of the machine.

3.2 Non-linear beam dynamics effects

In an ideal circular machine only perfect dipoles and quadrupoles are present and the beam dynamics is linear [22]. This implies that the action of the particle motion and the beam emittance is conserved in each of the two transverse planes (assuming no coupling between the horizontal and vertical plane). The machine lattice, the sequence of the magnetic elements in the accelerator, is *stable* if the motion of the single particle is bounded for all initial conditions that satisfy the paraxial approximation in the reference orbit frame (their momentum in the transversal plane, \vec{p}_t , is much smaller than the one in the longitudinal, \vec{p}_l , that is $|\vec{p}_t| \ll |\vec{p}_l|$). In this case it is possible to associate a periodic β -function to the machine [22].

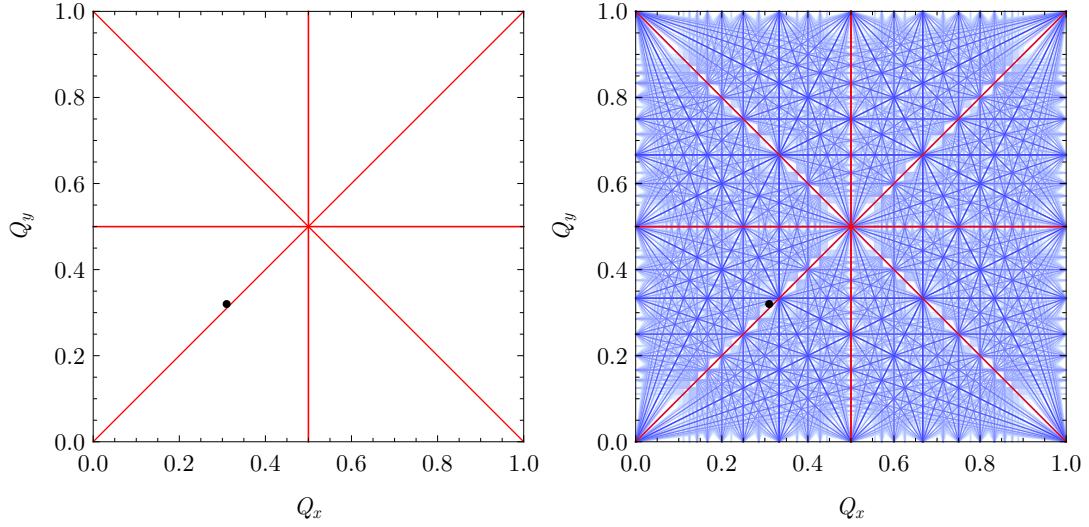


Figure 3.6: *Left*: forbidden lines in a linear machine (that is first and second order). *Right*: forbidden lines in a non-linear machine (all resonances, shown up to the 10th order). In both the plots, the black point represents the LHC collision tunes (0.31, 0.32).

Even if a linear machine is stable, a *linear* perturbation of the lattice can give rise to an instability, and more precisely a resonant mechanism that transfers, always in the same direction and in a periodic way, the energy from the longitudinal plane to the transversal one (the 3-dimensional beam emittance is conserved): the betatron oscillations of the particles increase until the particle reaches the aperture limit of the machine. For this reason even a linear machine (with linear perturbations) cannot operate on specific resonant points of the tune diagram (first and second order resonances, Fig. 3.6, left).

In practice real magnets have non vanishing high multipolar components (multipolar errors like parasitic sextupoles, octupoles, decapoles in the linear magnets) and sextupoles magnet are anyhow needed in the machine to correct its chromatic aberrations as real beams are only approximately monoenergetic. These non-linear elements modify the linear beam dynamics. They have three major effects on the beam:

- the single particle motion is no longer harmonic, that is the *pseudo* β -function depends on the particle starting condition (action) and the frequency spectrum of the single particle is broadened,
- they introduce high order resonant conditions (Fig. 3.6, right),
- they couple in a *non resonant* way the longitudinal and transverse degrees of freedom increasing the transverse emittance of the beam (diffusion process).

All these effects impact on the luminosity performance of the machine since they cause beam losses. They can be fast (few turns in the machine, resonant process) or slow (millions of turns, diffusive process). The first may provoke quenches in the superconductive magnets or trigger the collider dumping system, the latter may increase the background in the experiments and reduce the beam lifetime.

3.2.1 Diffusion due to the machine non-linearities

In the present section we concentrate on the study of the diffusive processes caused by one non-linear lens: a non-linear lens is an element in the machine lattice that modifies the particle trajectory by means of non-linear function of the particle coordinates. Sextupoles, multipoles and beam-beam long-range interactions are an example of non-linear lenses.

We demonstrate, under specific assumptions, that a non-linear lens increases the beam transverse emittance (diffusion process). The beam emittance, ϵ_b , is a statistical quantity (a positive scalar) that can be associated with the beam and more in general with every ensemble of \mathbb{R}^2 [18, 22]. For a beam we have one emittance for each of the three space directions (corresponding to the three conjugate variables ensembles $\{x, x'\}$, $\{y, y'\}$, $\{t, \Delta E\}$). We focus here on the transverse plane and consider the horizontal direction, that is the plane $\{x, x'\}$ (similar conclusions can be drawn for the vertical direction). The beam emittance, ϵ_b , is defined by

$$\epsilon_b = \sqrt{\overline{x^2 x'^2} - \overline{xx'}^2}. \quad (3.12)$$

If the beam is matched to the machine optics, there is an equivalence between the machine optical function (β, α, γ) and the statistical quantities related to the beam:

$$\beta = \frac{\overline{x^2}}{\epsilon_b}, \quad \gamma = \frac{\overline{x'^2}}{\epsilon_b}, \quad \alpha = \frac{\overline{xx'}}{\epsilon_b}.$$

Description of the working hypotheses

In the following four hypotheses are assumed:

1. the x and x' are centered distributions ($\overline{x} = 0$, $\overline{x'} = 0$). Therefore the emittance becomes the combination between the variances and the covariance of the x , x' . If they are uncorrelated variables then $\overline{xx'} = 0$.
2. the $\{x, x'\}$ is a joint normal distribution. This implies that the variables can be made independent with a convenient linear transformation of the plane $\{x, x'\}$. From the physical point of view it means that the beam has a two-dimensional Gaussian footprint in the $\{x, x'\}$ plane and can be conveniently focused in order to have its axes parallel to the x and x' axes. In addition, the assumption that $\{x, x'\}$ is a joint normal distribution implies that, if the x and x' variables are uncorrelated [41], they are independent (in general this holds only in the other direction, if two variables are independent they are uncorrelated).
3. the force of the lens depends only on the x and/or y coordinates (paraxial approximation) and affects only the x' coordinate (thin lens approximation). It acts, therefore, like a transformation of the type

$$(x, x') \rightarrow (x, x' + \Delta(x, y)). \quad (3.13)$$

The $\Delta(x, y)$ is referred to as the *kick* given by the lens. The paraxial approximation holds only if the momentum in the longitudinal direction is much greater than the transverse one: in LHC, at the designed collision momentum (7 TeV/c), the longitudinal momentum is ≈ 7 TeV/c while the transverse one is ≈ 200 MeV/c (assuming $\beta = 0.55$ m, $\alpha = 0$) therefore the paraxial approximation is valid. Regarding the thin lens approximation, it does not affect the generality of the result, since using a conveniently large number of thin lenses, it is possible to reproduce a thick lens within the desired level of accuracy.

4. in the beam distribution the $\{x, y\}$ and the $\{x', y\}$ ensembles are independent. This means that if we select two subsets of the beam, A and B , to have respectively $y = y_A$ and $y = y_B$, the horizontal emittance in the subset A is the same of the one in the subset B and is equal to the horizontal beam emittance: in fact the emittance in the $\{x, x'\}$ plane (Eq. 3.12) does not depend upon y because of our hypothesis. From the physical point of view this means that the beam ellipse in the $\{x, y\}$ plane has its axes parallel to the x and y axes and the coupling on the two planes is negligible.

Demonstration

As first step towards the demonstration, we show that a linear transformation in the $\{x, x'\}$ plane preserves the emittance if and only if the corresponding matrix has determinant equal to one or minus one. This is a well known property [18] here used to show the approach we adopt later in the non-linear case. Initially we assume that the x and x' variables are uncorrelated, that yields, from our first assumptions, $\overline{xx'} = 0$ (this hypothesis will be relaxed later). Let us consider the single particle linear transformation

$$\begin{pmatrix} \eta \\ \eta' \end{pmatrix} = \mathcal{M} \begin{pmatrix} x \\ x' \end{pmatrix} = \begin{pmatrix} m_{11} & m_{12} \\ m_{21} & m_{22} \end{pmatrix} \begin{pmatrix} x \\ x' \end{pmatrix}. \quad (3.14)$$

We have, from a statistical point of view

$$\begin{aligned} \overline{\eta^2} &= m_{11}^2 \overline{x^2} + m_{12}^2 \overline{x'^2} + 2m_{11}m_{12} \underbrace{\overline{xx'}}_{=0} \\ \overline{\eta'^2} &= m_{21}^2 \overline{x^2} + m_{22}^2 \overline{x'^2} + 2m_{21}m_{22} \underbrace{\overline{xx'}}_{=0} \\ \overline{\eta\eta'} &= m_{11}m_{21} \overline{x^2} + m_{11}m_{22} \underbrace{\overline{xx'}}_{=0} + m_{12}m_{21} \underbrace{\overline{xx'}}_{=0} + m_{12}m_{22} \overline{x'^2}. \end{aligned} \quad (3.15)$$

We refer to the emittance before and after the transformation \mathcal{M} , respectively, with the symbol $\epsilon_b|_{before}$ and $\epsilon_b|_{after}$. From Eqs. 3.12 and 3.15 it yields

$$\begin{aligned}\epsilon_b^2|_{before} &= \overline{x^2} \overline{x'^2} \\ \epsilon_b^2|_{after} &= \overline{+m_{11}^2 m_{21}^2 \overline{x^2} \overline{x'^2}} + \overline{m_{11}^2 m_{22}^2 \overline{x^2} \overline{x'^2}} + \overline{m_{12}^2 m_{21}^2 \overline{x^2} \overline{x'^2}} + \overline{m_{12}^2 m_{22}^2 \overline{x'^2} \overline{x'^2}} + \\ &\quad \overline{-m_{11}^2 m_{21}^2 \overline{x^2} \overline{x'^2}} - \overline{m_{12}^2 m_{22}^2 \overline{x'^2} \overline{x'^2}} - 2\overline{m_{11} m_{12} m_{21} m_{22} \overline{x^2} \overline{x'^2}},\end{aligned}\quad (3.16)$$

therefore

$$\epsilon_b^2|_{after} = (m_{11}m_{22} - m_{12}m_{21})^2 \overline{x^2} \overline{x'^2},$$

this means that, given the linear transformation \mathcal{M} , $\epsilon_b|_{after} = \epsilon_b|_{before}$ if and only if $|\det(\mathcal{M})| = 1$.

To demonstrate that the previous statement holds even if x and x' are statistically correlated, let us consider the following transformation \mathcal{C}

$$\begin{pmatrix} \xi \\ \xi' \end{pmatrix} = \mathcal{C} \begin{pmatrix} x \\ x' \end{pmatrix} = \begin{pmatrix} 1 & 0 \\ -\frac{xx'}{x^2} & 1 \end{pmatrix} \begin{pmatrix} x \\ x' \end{pmatrix}.$$
 (3.17)

This linear transformation \mathcal{C} preserves the emittance (in this specific case the result can be obtained using Eq. 3.15 even without the hypothesis of x and x' independence) and transforms the correlated variables x, x' in the uncorrelated variables ξ, ξ' . In fact

$$\overline{\xi\xi'} = -\frac{\overline{xx'}}{\overline{x^2}} \overline{x^2} + \overline{xx'} = 0.$$

The transport Eq. 3.14 can be put, using the Eq. 3.17, in the form

$$\begin{pmatrix} \eta \\ \eta' \end{pmatrix} = \mathcal{C} \mathcal{M} \mathcal{C}^{-1} \begin{pmatrix} \xi \\ \xi' \end{pmatrix}.$$
 (3.18)

We observe that $|\det(\mathcal{C} \mathcal{M} \mathcal{C}^{-1})| = 1$ if and only if the $|\det(\mathcal{M})| = 1$. Therefore we demonstrated that, even if x and x' are correlated variables, the Eq. 3.14 preserves the emittance if and only if the $|\det(\mathcal{M})| = 1$.

For demonstrating that a non-linear lens increases the beam emittance, it is convenient to transform the ensemble $\{x, x'\}$ by means of the \mathcal{C} matrix, to work in the uncorrelated space $\{\xi, \xi'\} = \{x, x' + Kx\}$. After this transformation, we evaluate the effect of the lens and finally we apply the \mathcal{C}^{-1} matrix to be back in the correlated (and transformed) space.

The previous steps are shown in Fig. 3.7.

$$\begin{array}{ccc} \{x, x'\} & & \{x, x' + \Delta(x, y)\} \\ \downarrow \mathcal{C} & & \uparrow \mathcal{C}^{-1} \\ \{\xi, \xi'\}_{before} = \{x, x' + Kx\} & \xrightarrow{\text{non-linear lens}} & \{\xi, \xi'\}_{after} = \{x, x' + Kx + \Delta(x, y)\}. \end{array}$$

Figure 3.7: The similarity transformation \mathcal{C} used to demonstrate that a non-linear lens increases the transverse beam emittance.

It is important to observe that the non-linear lens has not to be transformed going from $\{x, x'\}$ to $\{\xi, \xi'\}$ since the \mathcal{C} matrix does not modify the x and y coordinates and the lens effects depends only on them, from our third hypothesis. For linear transformations this hypothesis is not needed.

We demonstrate now that the emittance of the ensemble $\{\xi, \xi'\}_{after}$ is larger or equal than the one of ensemble $\{\xi, \xi'\}_{before}$. We do it for a specific $y = y_A$ knowing that, from our fourth hypothesis, the results

is valid for the whole beam. We have from Eq. 3.12

$$\begin{aligned}
\epsilon_b^2|_{after} &= \overline{\xi^2 (\xi' + \Delta(\xi, y_A))^2} - \overline{\xi (\xi' + \Delta(\xi, y_A))^2}^2 = \\
&= \overline{\xi^2 \xi'^2 + \Delta(\xi, y_A)^2 + 2\xi' \Delta(\xi, y_A)} - \overline{\xi \xi' + \xi \Delta(\xi, y_A)}^2 = \\
&= \overline{\xi^2 (\xi'^2 + \Delta(\xi, y_A)^2 + 2 \underbrace{\xi' \Delta(\xi, y_A)}_{=0})} - (\underbrace{\overline{\xi \xi'}}_{=0} + \overline{\xi \Delta(\xi, y_A)})^2 = \\
&= \epsilon_b^2|_{before} + \overline{\xi^2 \Delta(\xi, y_A)^2} - \overline{\xi \Delta(\xi, y_A)}^2
\end{aligned}$$

where $\overline{\xi' \Delta(\xi, y_A)}$ vanishes as shown below: the ξ and ξ' variables are uncorrelated then from our second hypothesis this implies that they are independent and therefore [41]

$$\overline{\xi' \Delta(\xi, y_A)} = \overline{\xi'} \overline{\Delta(\xi, y_A)}.$$

Since $\overline{\xi'} = 0$ (derived from the first hypothesis), it yields $\overline{\xi' \Delta(\xi, y_A)} = 0$. We have that $\overline{\xi^2 \Delta(\xi, y_A)^2} - \overline{\xi \Delta(\xi, y_A)}^2 \geq 0$ (e.g., it can be associated to the square of an equivalent emittance of the $\{\xi, \Delta(\xi, y_A)\}$ plane) then we conclude that the

$$\epsilon_b|_{after} \geq \epsilon_b|_{before}.$$

The sign equal holds when $\Delta(\xi, y_A)$ is a linear function of ξ (quadrupolar lens). Multipoles higher than the quadrupolar one increase the emittance being responsible of the diffusion mechanism.

From the physical point of view this is due to the magnetic field that bends the single particle trajectory exchanging the energies between the longitudinal and transverse directions. This process is always reversible in the case of the linear magnets (dipoles and quadrupoles): it is possible to recover the statistical properties of the beam after it passed through a finite sequence of dipoles (i.e., drift space from the beam dynamics point of view) and quadrupoles by using a finite sequence of quadrupoles and drift spaces. This is not true anymore if we consider non-linear magnets, for example it is not possible, in general, to recover the statistical properties of the beam after being passed through a finite sequence of dipoles, quadrupoles and sextupoles by using a finite sequence of sextupoles, quadrupoles and drift spaces. This concept of irreversibility of the physics process has its mathematical counterpart in the emittance growth of the diffusion process. It is possible to consider the diffusion process as a heat exchange between the longitudinal and transverse directions: due the higher temperature of the longitudinal direction (the paraxial hypothesis holds only if the longitudinal momentum is much greater than the transverse one) the transverse direction will get warmer (emittance increase and, therefore, diffusion).

3.2.2 Analytic expression of the beam-beam interaction

After having introduced the non-linear beam dynamics effects in a circular machine in a general way, we focus our attention on the beam-beam effect [42]. The beam-beam effect is present in colliders only. It is caused by the electromagnetic interaction between the two beams of the collider itself.

The beam-beam interaction at the collision point is called head-on beam-beam interaction (HO beam-beam): it is unavoidable in a collider since the goal of the machine itself is to make the beams interact. On the other hand, all the parasitic interactions that occur when the beams share the same vacuum pipe and are not well separated (see Fig. 1.7) could in principle be avoided. They are called long-range beam-beam interactions (LR beam-beam).

In contrast with the machine multipolar errors, the beam-beam effect has its source in the beam itself and its distribution: since the beam varies during the run, the beam-beam effect is a function of the time. There are two different approaches to describe the beam dynamics:

- the weak-strong description [43] where only one beam, the *weak beam*, is modified during the interaction. The other beam, the *strong beam*, is considered unperturbed, i.e., it has a constant beam current and constant transverse distribution. This description is a simplification of the reality valid when the electromagnetic field of the beams can be considered constant, that is the beam-beam interaction modifies the tails of the beam profile but the beam core is not perturbed,
- the strong-strong description [44] where both beams are modified during their interactions.

In this study, we assumed to be in the weak-strong regime. With this approach it is possible to consider that the non-linearities due to the *strong beam* are constant in time like in the case of the imperfections of the machine magnets. Nevertheless, differently from the magnets non-linearities, the beam-beam effect, assuming Gaussian beam profiles, cannot be expressed by means of multipolar expansion.

We study the single particle dynamics only for the regular bunch, neglecting the case of the so-called PACMAN bunches [45]: those bunches that, due to the specific filling pattern of the beam, experiences only a part of the long-range beam-beam encounters.

The beam-beam force

In this section we derive with specific assumptions the force felt by the beam particles due to the beam-beam effect.

The Lorentz force, $\vec{F}(\vec{r})$, on a test particle of charge q , positioned at \vec{r} and with a speed v_1 is [46]

$$\vec{F}(\vec{r}) = q \left(\vec{E}(\vec{r}) + \vec{v}_1 \times \vec{B}(\vec{r}) \right) \quad (3.19)$$

where \vec{E} is the electric field and \vec{B} is the magnetic induction's field. The Eq. 3.19 is valid in all frames of reference provided that all quantities are expressed in the same frame. A moving bunch of charged particles has a magnetic field (due to the moving charges) and an electric one (due to the free charge).

The force in Eq. 3.19 may be computed in the bunch rest frame observing that, there, the bunch length is γ_{r2} time longer than in the laboratory frame and there is only electrostatic field. Since the bunch's length becomes much greater than the transverse size, we can use a cylindrical approximation and, therefore, the electric field has only a radial component.

If we compute the electric field in the bunch's frame of reference we transform it back in the laboratory frame using the Lorentz transformations [46], that in our specific case are

$$\begin{aligned} E_s &= 0 \\ E_r &= \gamma_{r2} E'_r \\ E_\theta &= 0 \\ B_s &= 0 \\ B_r &= 0 \\ B_\theta &= -\frac{\gamma_{r2}}{c^2} v_2 E'_r \end{aligned} \quad (3.20)$$

where s is the frame moving direction and the primed quantities refer to the bunch rest frame $\{x', y', s'\}$. In the laboratory's frame $\{x, y, s\}$ we assume that the bunch is moving towards the negative s . In the Eq. 3.20, v_2 is the velocity of the bunch and γ_{r2} is its corresponding relativistic factor. Combining Eq. 3.19 and Eqs. 3.20 and assuming \vec{v}_1 opposite to \vec{v}_2 (colliding beams), it yields

$$F = q\gamma_{r2} (1 + \beta_1\beta_2) E'_r. \quad (3.21)$$

Therefore, in order to obtain the Lorentz force, it is sufficient to find the solution for the electrostatic field in the rest frame E'_r and to multiply the result by $q\gamma_{r2} (1 + \beta_1\beta_2)$. When the beam and the test particle travels in the same direction, our factor becomes $q\gamma_{r2} (1 - \beta_1\beta_2)$ and gives rise to the cancellation of space charge effects as $1/\gamma_r^2$, assuming $\beta_1 = \beta_2$.

The beam-beam force for a Gaussian beam

We consider a Gaussian bunch with N_b particles. Its charge density distribution in the laboratory's frame can be expressed as

$$\rho(x, y, s) = \frac{q N_b}{(2\pi)^{3/2} \sigma_x \sigma_y \sigma_s} \cdot \exp \left(-\frac{x^2}{2\sigma_x^2} - \frac{y^2}{2\sigma_y^2} - \frac{s^2}{2\sigma_s^2} \right) \quad (3.22)$$

where q represents the particle's charge (we assume that the charge of the particles in the two colliding bunches is the same, see Eq. 3.19), $\sigma_x, \sigma_y, \sigma_s$ the standard deviations of the distribution in the particular direction, x, y, s , in the laboratory's frame. In the beam rest frame the Eq. 3.22 becomes

$$\rho'(x', y', z') = \frac{q N_b}{(2\pi)^{3/2} \sigma_x \sigma_y (\gamma_2 \sigma_s)} \cdot \exp \left(-\frac{x'^2}{2\sigma_x^2} - \frac{y'^2}{2\sigma_y^2} - \frac{s'^2}{2(\gamma_{r2} \sigma_s)^2} \right). \quad (3.23)$$

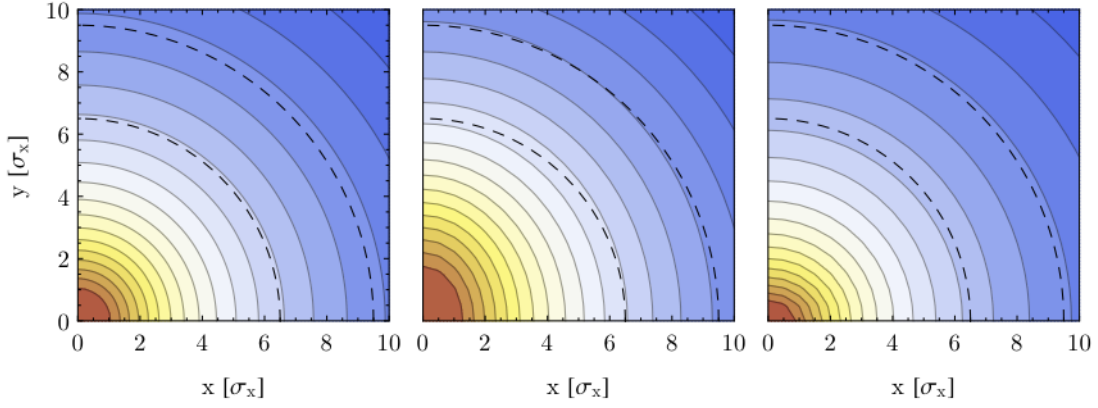


Figure 3.8: The electric potential for a Gaussian charge distribution with $\sigma_y = \sigma_x$ (left), $\sigma_y = 2 \sigma_x$ (center) and $\sigma_y = 0.5 \sigma_x$ (right). On the latter to plots (center and right) the circles at 6.5 and 9.5 σ_x are shown to compare them with the symmetrical bunch ($\sigma_x = \sigma_y$, left).

Assuming that that $\gamma_{r2}\sigma_s \gg \sqrt{\sigma_x^2 + \sigma_y^2}$ (cylindrical approximation) the Eq. 3.23 becomes

$$\rho'(x', y') = \frac{q N_b}{2\pi\sigma_x\sigma_y(\gamma_{r2} l_b)} \cdot \exp\left(-\frac{x'^2}{2\sigma_x^2} - \frac{y'^2}{2\sigma_y^2}\right)$$

where the l_b represents the equivalent length of the bunch at the collision energy in the laboratory's frame.

There is not a closed form to express the electric field of a not round Gaussian charge distribution ($\sigma_x \neq \sigma_y$). In Fig. 3.8 we used a Finite Element code [47] to compare the electric potential for $\sigma_y = \sigma_x$, $\sigma_y = 2 \sigma_x$ and $\sigma_y = 0.5 \sigma_x$. It can be observed that already at a distance of 9.5 σ it is possible to approximate the equipotential curves with circles in all three cases. This implies that for well separated beams (separation $> 9.5 \sigma$) a factor two between σ_x and σ_y in the beam can be still well approximated by a round Gaussian beam.

In most beam-beam parasitic encounters we have $\beta_x \neq \beta_y$ (therefore, for $\epsilon_x = \epsilon_y$, $\sigma_x \neq \sigma_y$). As shown in Fig. 3.9, in nominal LHC, the transverse aspect ratio of the beam (σ_x/σ_y), near the Interaction Point, ranges between 0.5 and 2.

Assuming that $\sigma_x = \sigma_y = \sigma$ (round Gaussian beam), we have

$$\rho'(r') = \frac{q N_b}{2\pi(\gamma_2 l_b) \sigma^2} \cdot \exp\left(-\frac{r'^2}{2\sigma^2}\right) \quad (3.24)$$

where $r' = \sqrt{x'^2 + y'^2} = r$. The radial electric field E'_r can be obtained from Gauss' flux theorem considering $|\vec{E}'| = E'_r$

$$2\pi r E'_r = \int_0^{2\pi} \int_0^r \rho'(t) t dt d\phi \quad (3.25)$$

that yields

$$E'_r = \begin{cases} \frac{q N_b}{2\pi\gamma_2 l_b r \epsilon_0} \left(1 - \exp\left(-\frac{r^2}{2\sigma^2}\right)\right) & \text{if } r \neq 0 \\ 0 & \text{if } r = 0 \end{cases} \quad (3.26)$$

The vanishing value of E'_r for $r = 0$ will be omitted in the following.

Combining the Eqs. 3.21 and 3.26 we obtain

$$F_r = (1 + \beta_1 \beta_2) \frac{q^2 N_b}{2\pi l_b r \epsilon_0} \left(1 - e^{-\frac{r^2}{2\sigma^2}}\right)$$

and finally assuming $\beta_1 = \beta_2 \simeq 1$ (therefore $\gamma_1 = \gamma_2 = \gamma$) we obtain

$$F_r = \frac{q^2 N_b}{\pi l_b r \epsilon_0} \left(1 - e^{-\frac{r^2}{2\sigma^2}}\right). \quad (3.27)$$

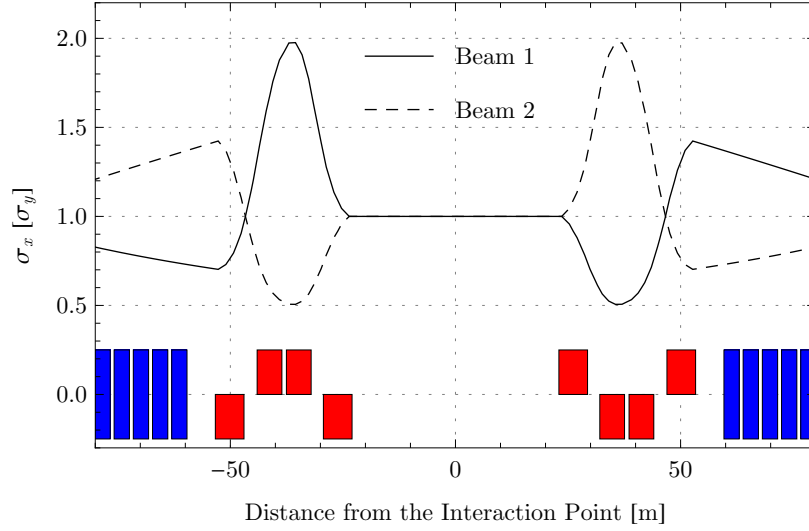


Figure 3.9: The ratio between σ_x and σ_y for the Beam 1 and the Beam 2 at IP1 and IP5.

If, as in LHC, the $\sigma_x \neq \sigma_y$, the σ considered in the previous equation refers to σ of the strong beam in the plane of the beam crossing.

The effect of the beam-beam force on the particles' trajectories

In this section, starting from the Eq. 3.27, we derive the effect of the beam-beam force on the single particle dynamics.

Let us consider the one-dimensional problem for the particles' trajectory starting from the equation

$$\ddot{x} = \frac{F}{m}$$

and transform the differential equation in time in a differential equation in the longitudinal direction s . Remembering that, at constant velocity and in paraxial approximation, $\frac{d}{ds} = \frac{d}{v dt}$, we have

$$x'' = \frac{F}{v^2 m} = \frac{F}{v} \frac{1}{p}$$

where v is the modulus of the particle's velocity and the apex notation (\cdot') stands for the longitudinal direction derivative. The integral effect of the force upon the trajectory is the key ingredient to describe the particle dynamic. In fact, the variation of the particle angle due to a force is in general denoted as *kick* ($\Delta x'$) and is given in

$$\Delta x' = \int_{s_1}^{s_2} \frac{F}{v} \frac{1}{p} dz. \quad (3.28)$$

From Eq. 3.28 in thin lens approximation, it yields

$$\Delta x' = \frac{F}{v} \frac{1}{p} \frac{l_b}{2}$$

where $l_b/2$ is the effective length of the beam-beam interaction (half the bunch's length). Two counter-rotating beams experience an interaction during a $\Delta t = l_b/2v$: in our transformation we assume that $s = vt$ so the effective length of interaction becomes $l_b/2$.

We can generalize the results in the two-dimensional transverse space $\{x, y\}$

$$\begin{aligned}\Delta x' &= \frac{F_x}{v} \frac{1}{p} \frac{l_b}{2} \\ \Delta y' &= \frac{F_y}{v} \frac{1}{p} \frac{l_b}{2}\end{aligned}\quad (3.29)$$

where p, v, l_b are not projected on the longitudinal axis because of the paraxial hypothesis. In ultra-relativistic approximation, projecting and replacing the Eqs. 3.26 in the 3.29 and expressing the kicks in the reference frame relative to the center of the weak beam, we obtain ($pv \approx mc^2$)

$$\begin{aligned}\Delta x' &= -\frac{N_b}{2\pi} \frac{q^2}{r^2} \frac{\bar{x}}{\epsilon_0 mc^2} \left(1 - e^{-\frac{r^2}{2\sigma^2}}\right) = -\frac{2}{\gamma_r} \frac{N_b}{r^2} \frac{r_p}{r^2} \bar{x} \left(1 - e^{-\frac{r^2}{2\sigma^2}}\right) \\ \Delta y' &= -\frac{N_b}{2\pi} \frac{q^2}{r^2} \frac{\bar{y}}{\epsilon_0 mc^2} \left(1 - e^{-\frac{r^2}{2\sigma^2}}\right) = -\frac{2}{\gamma_r} \frac{N_b}{r^2} \frac{r_p}{r^2} \bar{y} \left(1 - e^{-\frac{r^2}{2\sigma^2}}\right)\end{aligned}\quad (3.30)$$

where

$$r = \sqrt{\bar{x}^2 + \bar{y}^2}, \quad \bar{x} = X - x, \quad \bar{y} = Y - y \quad \text{and} \quad r_p = \frac{q^2}{4\pi\epsilon_0 m_0 c^2} \approx 1.53 \cdot 10^{-18} \text{ m} \quad (3.31)$$

with (X, Y) the strong beam center and (x, y) the particle position with respect to the center of the weak beam. The negative sign comes from the definition of x and y .

The equivalence beam-wire

If we are sufficiently far away from the center of the beam, its electromagnetic field decays with a $1/r$ law like the magnetic field produced by a wire carrying a current I_w (see Fig. 3.10) with respect to the frame centered on the wire. In the following we analyze in a quantitative way the equivalence beam-wire.

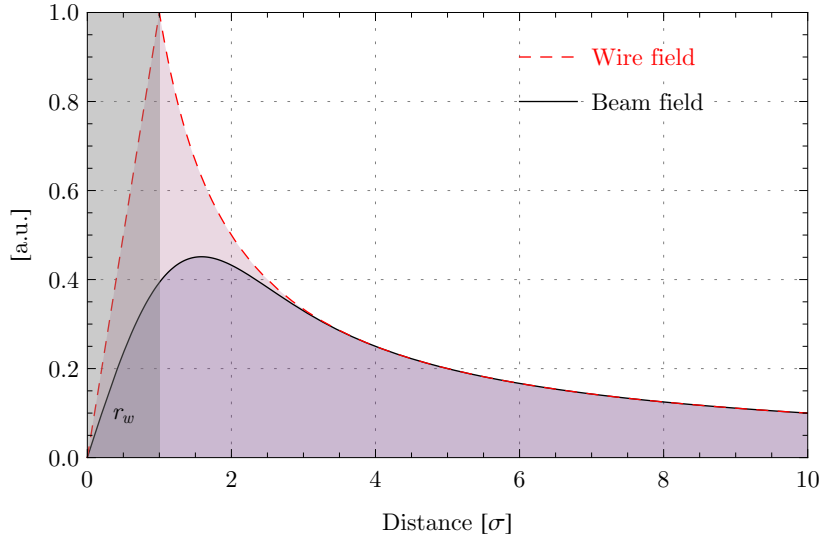


Figure 3.10: The beam-wire approximation. We assumed $r_w = 1 \sigma$.

For $r \gg \sigma$ and from Eq. 3.30 it yields

$$\Delta x' \approx -\frac{2}{\gamma_r} \frac{N_b}{r^2} \frac{r_p}{r^2} x. \quad (3.32)$$

On the other hand, the kick $\Delta x'$ given by a wire carrying a current I_w , with a length l_w and a radius r_w can be expressed in the laboratory's frame and in the ultra-relativistic approximation ($r \geq r_w$)

$$\Delta x' = -\frac{q c B_w l_w}{m c^2} = \frac{q c \mu_0 I_w l_w x}{2\pi r^2 m c^2} \quad (3.33)$$

where B_w represents the magnetic induction of the wire's field, μ_0 represents the magnetic permeability of the vacuum while x , and r are used in the meaning of Eq. 3.30. From the Eqs. 3.32 and 3.33, remembering the relation $\mu_0 \epsilon_0 = 1/c^2$, it yields that the asymptotic behavior of the beam ($r \gg \sigma$) on the beam is equivalent to that of a wire placed in the center of the beam, at rest in the laboratory's frame, and having

$$I_w l_w = q c N_b. \quad (3.34)$$

This relation allows to mimic in ultra-relativistic regime and for $r \gg \sigma$ the effect of beam-beam parasitic encounters (long-range) by means of a wire. To mimic the one nominal LHC beam (for a beam with the normalized emittance of the nominal LHC) we need therefore $I_w l_w = 5.6 \text{ A}\cdot\text{m}$.

3.2.3 Scaling laws for the beam-beam interaction

In the following we develop and discuss the basic scaling laws that describe how and under which approximations we can scale a non-linear lens, and in particular the beam-beam long-range effect, of a particular machine to another one. The aim is to reproduce the LHC long-range interaction in other accelerators (RHIC, SPS...). These laws are already partially presented in literature [48], [49] and [43] and used in experiments on beam-beam effect: due to their importance we report in a systematic way and with and original approach all these considerations.

Going from LHC to another machine many parameters may change: the energy, the geometry (ring circumference), the optics (β -function), the particles mass (but also the charge-mass ratio), the energy, the normalized emittance... The results obtained in an analytical way are, in large part, checked using tracking simulation.

It is worth underlining that these scaling laws are not intended to evaluate the effect of a parasitic beam-beam encounter occurring at a beam separation of $\mathbf{n} \sigma$ provided the effect of one other encounter at $\mathbf{m} \sigma$ is known: in this case scaling laws cannot be applied.

Concept of equivalent beam dynamics for two different machines

The aim of these scaling laws is to assess under which conditions two machines have an equivalent beam dynamics: this means that all particles, with the same initial conditions in the normalized phase space, follow the same normalized trajectory in the two machines. For example, all linear machines with the same tunes and without linear coupling between their planes are equivalent.

The normalization we referred to in the previous paragraph is a convenient linear transformation \mathcal{M} of the phase planes $\{x, x'\}$ and $\{y, y'\}$ that, in a linear machine, transforms the particle ellipses of the Poincaré section [22], at the longitudinal position s_0 , into circles. In the following, for simplicity, we will concentrate on the $\{x, x'\}$ plane. The linear transformation \mathcal{M} is a function of the machine optics (it depends on the β and α functions) and of the beam emittance (ϵ). It can be written as

$$\mathcal{M} = \begin{pmatrix} \frac{1}{\sqrt{\beta} \epsilon} & 0 \\ \frac{\alpha}{\sqrt{\beta} \epsilon} & \sqrt{\frac{\beta}{\epsilon}} \end{pmatrix}. \quad (3.35)$$

The transformation \mathcal{M} for a linear machine is illustrated in Fig. 3.11. The $\{x, x'\}$ plane is the natural plane and $\{\xi, \xi'\}$ is the normalized one. The same normalization can be applied to a non-linear machine but in this case the particle motion is not anymore circular in the $\{\xi, \xi'\}$ plane (see Fig. 3.12).

Condition of equivalent beam dynamics for two different machines

We can say that two machines are equivalent if the particle trajectories in the $\{\xi, \xi'\}$ plane are identical for all possible initial conditions.

Let us consider a machine (Ring A, Fig. 3.13, *left*) that has a linear lattice except for a non-linear thin lens (lens A) positioned in a . We want to study in the following the condition that a second non-linear lens (lens B), positioned at b in the Ring B (Fig. 3.13, *right*), has to satisfy in order to make the Rings A and B

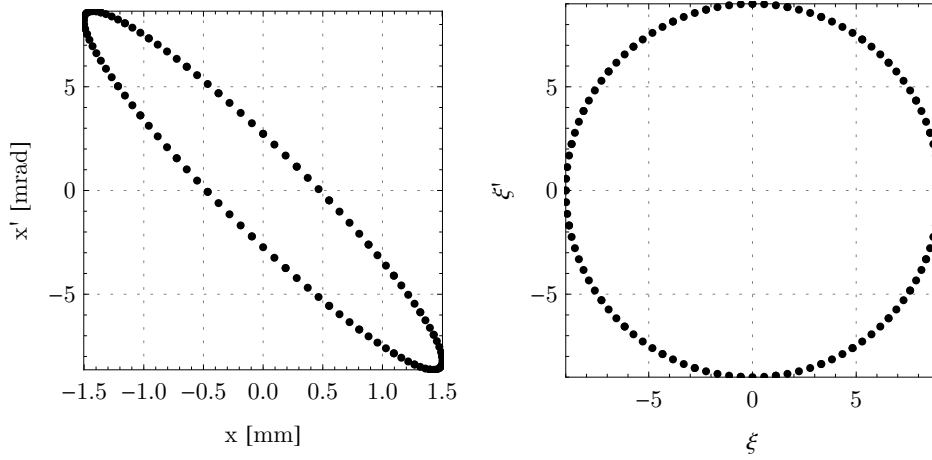


Figure 3.11: A transformation of the natural phase space (*left*) to the normalized one (*right*) in a linear machine.

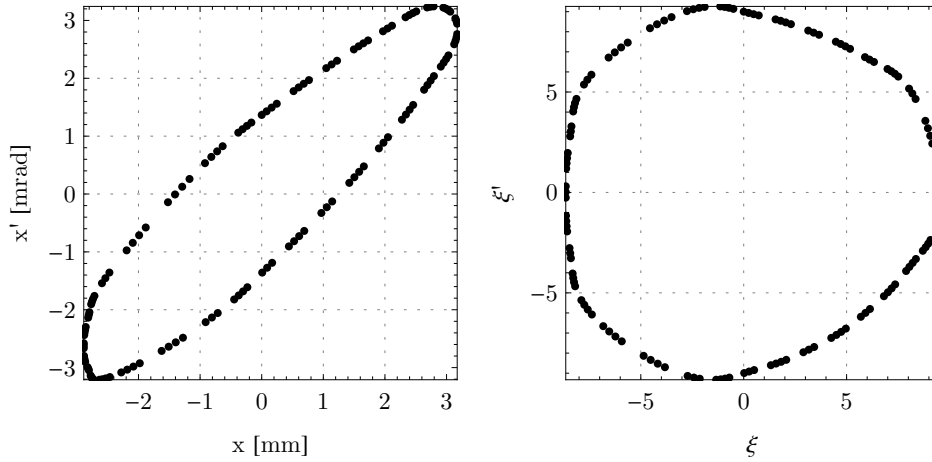


Figure 3.12: A transformation of the natural phase space (*left*) to the normalized one (*right*) in a non-linear machine.

equivalent. The linear tunes of the two machines have to be the same otherwise, even in the linear case, the beam dynamics cannot be equivalent.

A thin lens has an effect on the x' coordinate only. Recalling the Eq. 3.13, it is a transformation of the type

$$(x, x') \rightarrow (x, x' + \Delta(x, y)).$$

Due to the choice of the \mathcal{M} matrix this is true even for the $\{\xi, \xi'\}$ plane: the ξ depends only on x , that, on its turn, is not modified by the thin lens. Therefore we concentrate only on the ξ' and its variation: the variation of the ξ' due to the effect of the lens is, by definition, the kick ($\Delta\xi'$) given by the lens itself. The two rings are equivalent if for every point in the $\{\xi, \xi'\}$ plane the $\Delta\xi'$ is equal for the Ring A ($\Delta_A\xi'$) and for the Ring B ($\Delta_B\xi'$):

$$\Delta_A\xi' = \Delta_B\xi'. \quad (3.36)$$

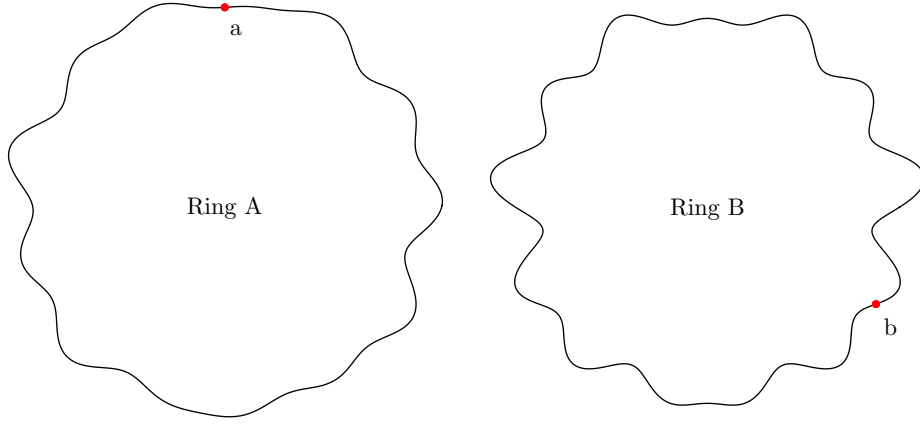


Figure 3.13: The equivalence in the beam dynamics behavior between the Ring A and the Ring B with the present of a non-linear thin lens at the position A and B.

From the Eq. 3.35, for both rings, we have:

$$\begin{aligned}\xi' &= \frac{\alpha}{\sqrt{\beta\epsilon}}x + \sqrt{\frac{\beta}{\epsilon}}x' \quad \text{before the kick,} \\ \xi' + \Delta\xi' &= \frac{\alpha}{\sqrt{\beta\epsilon}}x + \sqrt{\frac{\beta}{\epsilon}}(x' + \Delta x') \quad \text{after the kick}\end{aligned}$$

and therefore, subtracting the first equation from the second equation,

$$\Delta\xi' = \sqrt{\frac{\beta}{\epsilon}}\Delta x'.$$

This allows us to express the condition of the scaling law from the normalized space $\{\xi, \xi'\}$, Eq. 3.36, to the two natural phase spaces $\{x_A, x'_A\}$ and $\{x_B, x'_B\}$:

$$\sqrt{\frac{\beta_A}{\epsilon_A}}\Delta_A x'(x_A, y_A) = \sqrt{\frac{\beta_B}{\epsilon_B}}\Delta_B x'(x_B, y_B) \quad (3.37)$$

where we indicated explicitly the dependence of the kick of the lens, $\Delta x'$, on the position of the particle, (x, y) , in the physical plane $\{x, y\}$ assuming that the kick depends only on the particle's position and not on the particle's divergence (x', y') : this is in general true in an accelerator (paraxial hypothesis). It is important to note that we start to re-consider the y -direction because with non-linear lenses the particle motion in the x and y directions are coupled, i.e., the $\Delta x'$ depends on y and $\Delta y'$ depends on x . We refer to the Eq. 3.37 as *strength condition* equation: it is a condition on the strength of the two kicks, in Ring A and Ring B. It has to be satisfied by every pair of points, (x_A, y_A) and (x_B, y_B) that corresponds to the same position in the normalized plane or, equivalently from Eq. 3.35, that satisfies the following equations:

$$\begin{aligned}\frac{1}{\sqrt{\beta_A\epsilon_A}}x_A &= \frac{1}{\sqrt{\beta_B\epsilon_B}}x_B \\ \frac{1}{\sqrt{\beta_A\epsilon_A}}y_A &= \frac{1}{\sqrt{\beta_B\epsilon_B}}y_B\end{aligned} \quad (3.38)$$

where for simplicity we assumed the same β -functions and emittances in the x and y directions. We refer to the previous equations as *geometric condition* equations. As conclusions of all these consideration we can say that it is possible to scale a non-linear lens from the Ring A and the Ring B provided that:

- the tunes (Q_x, Q_y) are the same in the two machines and both machines have no linear coupling,
- given the beam properties and the machine optics, the two non-linear lenses satisfy a system of equations composed by the *strength condition* and the *geometry conditions*. It is important to note that this system may not have solution: the (parametric) solution of the system, if it exists, represents the scaling law or laws between the Ring A and the Ring B.

Scaling laws if the non-linear lens is a wire

After having presented the general approach used for the scaling laws, in the following we apply it to study the non-linearities induced by a wire carrying DC current and positioned parallel to the beam direction. Our goal is to define the relation between the wire in the Ring A and Ring B to obtain an equivalent dynamics in the two machines.

From Eqs. 3.37 and 3.33 assuming that the beam are ultra-relativistic and referring the quantity to the reference frame positioned in the beam center, the *strength condition* becomes

$$\underbrace{\sqrt{\frac{\beta_A}{\epsilon_A}} \frac{q_A}{m_{0A}} \frac{Il_A}{\gamma_{rA}}}_{K_A} \times \underbrace{\frac{(X_A - x_A)}{r_A^2}}_{x_A \text{ and } y_A \text{ dependence}} = \underbrace{\sqrt{\frac{\beta_B}{\epsilon_B}} \frac{q_B}{m_{0B}} \frac{Il_B}{\gamma_{rB}}}_{K_B} \times \underbrace{\frac{(X_B - x_B)}{r_B^2}}_{x_A \text{ and } y_A \text{ dependence}} \quad (3.39)$$

where the subscripts refer to the ring we are considering, Il represents the wire integrated current (wire current \times wire length),

$$r = \sqrt{(X - x)^2 + (Y - y)^2},$$

(X, Y) represents the position of the wire center and (x, y) the position of the particle in the frame positioned in the beam center. For simplicity we assume $Y=0$.

We explicitly indicate in Eq. 3.39 the parts of the *strength condition* depending on the geometry of the problem (i.e., x and y) and the parts that do not depend on it (K_A, K_B). We try to resolve our system of equations, replacing the *geometric condition* (Eq. 3.38) in the *strength condition* (Eq. 3.37)

$$K_A \frac{(X_A - x_A)}{(X_A - x_A)^2 + y_A^2} = K_B \frac{(X_B - \frac{\sqrt{\beta_B \epsilon_B}}{\sqrt{\beta_A \epsilon_A}} x_A)}{(X_B - \frac{\sqrt{\beta_B \epsilon_B}}{\sqrt{\beta_A \epsilon_A}} x_A)^2 + \frac{\beta_B \epsilon_B}{\beta_A \epsilon_A} y_A^2}. \quad (3.40)$$

The unknown of the previous equation is K_A (or equivalently K_B): since it cannot depend on x_A or y_A (see Eq. 3.39), the system in general has no solution. Nevertheless if we impose that

$$X_B = \frac{\sqrt{\beta_B \epsilon_B}}{\sqrt{\beta_A \epsilon_A}} X_A = \frac{\sigma_B}{\sigma_A} X_A, \quad (3.41)$$

i.e., the beam-wire distance in normalized units is the identical in Ring A and Ring B, then the system has the solution:

$$K_A = K_B \frac{\sqrt{\beta_A \epsilon_A}}{\sqrt{\beta_B \epsilon_B}} \quad \text{that is} \quad \frac{q_A}{m_{0A}} \frac{Il_A}{\epsilon_{nA}} = \frac{q_B}{m_{0B}} \frac{Il_B}{\epsilon_{nB}} \quad (3.42)$$

where we approximate, for ultra-relativistic beams, the $\gamma_r \cdot \epsilon$ equal to the normalized beam emittance (ϵ_n). The Eq. 3.42 represents the scaling law that makes equivalent the machine A e B in presence of thin non-linear lens equivalent to a wire. It is valid under the following conditions:

- the tunes (Q_x, Q_y) are the same in the two rings and both rings have no linear coupling,
- the beam-wire normalized distance in the same in Ring A and Ring B (Eq. 3.41),
- the β -functions and emittances are identical in the x and y directions in the two rings ($\sigma_x = \sigma_y$).

The last condition can be relaxed: it is possible to demonstrate that the Eq. 3.42 is still valid even for $\sigma_x \neq \sigma_y$ provided that the aspect ratio of the two beams is the same in the two rings (i.e., $\sigma_{xA}/\sigma_{yA} = \sigma_{xB}/\sigma_{yB}$). In this case the normalization of the beam-wire separation can be done, indifferently, with respect to σ_x or σ_y (the choice has to be the same in the two rings).

Observing the Eq. 3.42 we can conclude that the scaling law for the wire does not depend, directly, on the optical functions (β and α -function) and the beam rigidities of Ring A and Ring B. On the contrary, the normalized beam emittance has to be taken into account. For example if we need to mimic the beam dynamics induced by a 1 m long wire carrying 100 A installed in LHC (e.g., protons at 7 TeV/c and $\epsilon_n = 3.75 \mu\text{m}\cdot\text{rad}$) with a 2.5 m long wire in the Super Proton Synchrotron (SPS, e.g., protons at 120 GeV/c and $\epsilon_n = 3.75 \times 2 \mu\text{m}\cdot\text{rad}$), this is possible only if

- the wire can be approximated by a thin lens in the two rings (i.e., the optical functions of the machine do not vary significantly along its length),
- the tunes are the same in LHC and SPS,
- there is no linear coupling in the machines (in practice, if it is negligible),
- the aspect ratio of the beams is the same in LHC and SPS at the position of the wires,

- the normalized distance beam-wire is the same in the two machines.

Neglecting all other sources of the non-linearities and given the previous conditions, the two machines are equivalent if we power the SPS wire with 80 A (Eq. 3.42).

Scaling laws for the beam-beam interaction

If the non-linear lens does not represent a wire but a beam-beam interaction the approach and the conclusion are similar. The Eq. 3.42 still holds. Nevertheless, it is possible to demonstrate, in the case of a circular strong beam (only in this case we have a closed form to express the kick, see Section 3.2.2 and Eq. 3.30), that we need an additional constraint on the σ of the strong beam, σ_S , that is $\sigma_{xA}/\sigma_{SA} = \sigma_{xB}/\sigma_{SB}$: this means that the aspect ratio between the weak and strong beams has to be the same in the Collider A and in the Collider B.

Using scaling laws for compensating non-linear effects

Until now we introduced the scaling laws to compare two different machines: indeed the scaling law can be used in the same machine. It can be used to move a non-linear lens from one position of the lattice to another one keeping the same beam dynamics or to compensate a non-linear lens by using in a convenient position a second non-linear lens. The compensation can be performed considering:

- a phase advance of $2\pi \cdot n$ with $n \in \{0, 1, 2, \dots\}$ between the exciting and compensating non-linear lens,
- the geometrical condition

$$\begin{aligned} \frac{1}{\sqrt{\beta_A}} x_A &= \frac{1}{\sqrt{\beta_B}} x_B \\ \frac{1}{\sqrt{\beta_A}} y_A &= \frac{1}{\sqrt{\beta_B}} y_B, \end{aligned}$$

- the strength condition for compensation (note the “−” sign)

$$\sqrt{\beta_A} \Delta_A x'(x_A, y_A) = -\sqrt{\beta_B} \Delta_B x'(x_B, y_B)$$

where the subscripts refer to the excitation and compensation lens in the same machine and we consider $\epsilon_A = \epsilon_B$ (the beam emittance is constant all along the ring). For the compensation strength condition the ideal beam-beam compensation can be done only using a beam with a charge opposite to that of the strong beam: in the case on LHC we need an electron beam (electron lens, [50]). Nevertheless, as explained in Section 3.2.2, due to the similarity between the beam field and the wire field (see Fig. 3.10), it is possible to compensate, within some limits, the long-range beam-beam interactions using a wire [51]. For the specific case of LHC and sLHC the beam-wire separation cannot be reduced below about 8σ in order not to expose the wire to the beam halo that would destroy it. In general we have to provide a sufficient beam-wire separation (above 5σ , see Chapter 4) in order to reduce the number of beam particles that sample the diverging field of the wire. The transverse size of the wire should not exceed $1 - 2\sigma$ in order not to scrape the beam with the wire, in particular for beam-wire reduced separation.

Further considerations and limits on the scaling laws

It is still possible to use the Eq. 3.42 even if, in the rings of Fig. 3.13, there are several non-linear lenses but, in addition to the geometrical conditions, the relative phase advances between all the lenses have to be identical in both rings.

Assuming that the dominant non-linear effect of the machine is due to the beam-beam effect, it is possible to model the ring as a linear lattice with localized beam-beam non-linearities. Using the scaling laws, we can take advantage of the particular phase advance in the Interaction Region (see Fig. 3.3) and of the aspect ratio of the beam in the triplets (see Fig. 3.9) to approximate with one single thin lens multiple beam-beam encounters.

It is important to observe that, even if in the ideal case of equivalent machines with the same beam dynamics, the relative beam losses ($dN_b/dt/N_b$) and therefore the beam-lifetime, in general, are not the same. This is true even if the machine normalized aperture limit is identical in the Rings A and B. In fact we have to consider that the beam revolutions frequency may vary between the machines and, assuming ultra-relativistic beams, it depends on the length of the machine circumference. This means that a beam

lifetime of 5 h in SPS (≈ 6.9 km long) corresponds to a beam lifetime of about 20 h in LHC (≈ 27 km long) assuming that the two machines have an equivalent non-linear beam dynamics.

In addition to that, even if two equivalent machine have the same frequency and the same normalized aperture, the beam lifetimes may be different because their beams have different particle distributions: the tails of the beam profiles in the transverse plane or the energy distribution of the particle in the bunch (together with chromaticity and dispersion functions) can have a significant impact on the beam lifetime. This is an important limit to take into account when comparing the beam lifetime between different machines with the same single particle beam dynamics.

All the previous considerations on the scaling laws will be applied in Chapter 4.

Chapter 4

Simulations and experiments

Contents

4.1	The simulations for the Early Separation Scheme	63
4.1.1	The choice for the indicator of the dynamic aperture	63
4.1.2	The simulation code written in CUDA TM	66
4.1.3	The simulations results	72
4.2	The wire experiment in the SPS	78
4.2.1	The experimental setup	78
4.2.2	Experiments at 37 GeV/c	86
4.2.3	Experiments at 55 GeV/c	92
4.2.4	Experiments at 120 GeV/c	96
4.3	Summary and interpretation of the experiments	99

In the first part of this chapter we describe the general approach we adopted and the simulation code developed in order to evaluate the impact of the Early Separation Scheme on the LHC beam stability. The second part is devoted to the description of the experimental results obtained in the Super Proton Synchrotron (SPS) with a comparison between them and the simulations outcome.

4.1 The simulations for the Early Separation Scheme

In the case of a linear machine the problem of the stability of the single particle motion has a natural unambiguous definition since it does not depend on the particle initial amplitude but only on the properties of the machine lattice. To verify the stability of a linear lattice is a trivial task and can be done analyzing the machine one turn matrix [22]. In this case the particle, at a given position of the ring and for the different turns (represented in the so-called Poincaré section, [22]), behaves like a harmonic oscillator. In Fig. 4.1 an example of a linear machine is given. In the left plots we represent, in normalized units (see Section 3.2.3), the two Poincaré sections of the transverse coordinates x and y . On the right plots the frequency analysis is shown: it is the Fourier transformation of the position coordinate (x or y) and its peak shows the tune of the machine, in our example we can recognize the nominal LHC tune at collision ($Q_x = 0.31$ and $Q_y = 0.32$).

In a linear machine with non-linear perturbations (Fig. 4.2, in the following referred to as non-linear machine), the definition of stability is less straightforward: this is due to the fact that the stability becomes a property of the particle initial condition too and not solely of the machine optics. The motion of the particle is not harmonic anymore and the particle action (related to the particle Courant-Snyder constant that we refer to as *particle emittance* [22]) is not conserved (Fig. 4.2, *left*). The non-linear behavior of the particle is evident in the frequency domain too (Fig. 4.2, *right*): in fact the spectral content of the motion is not anymore monochromatic and presents a broadening of the resonant peak and several spurious resonant frequencies.

4.1.1 The choice for the indicator of the dynamic aperture

A fundamental tool to evaluate the beam dynamics of a non-linear machine is the simulation by means of numerical tracking: it consists in the evaluation of the particles trajectory for a large number of turns all

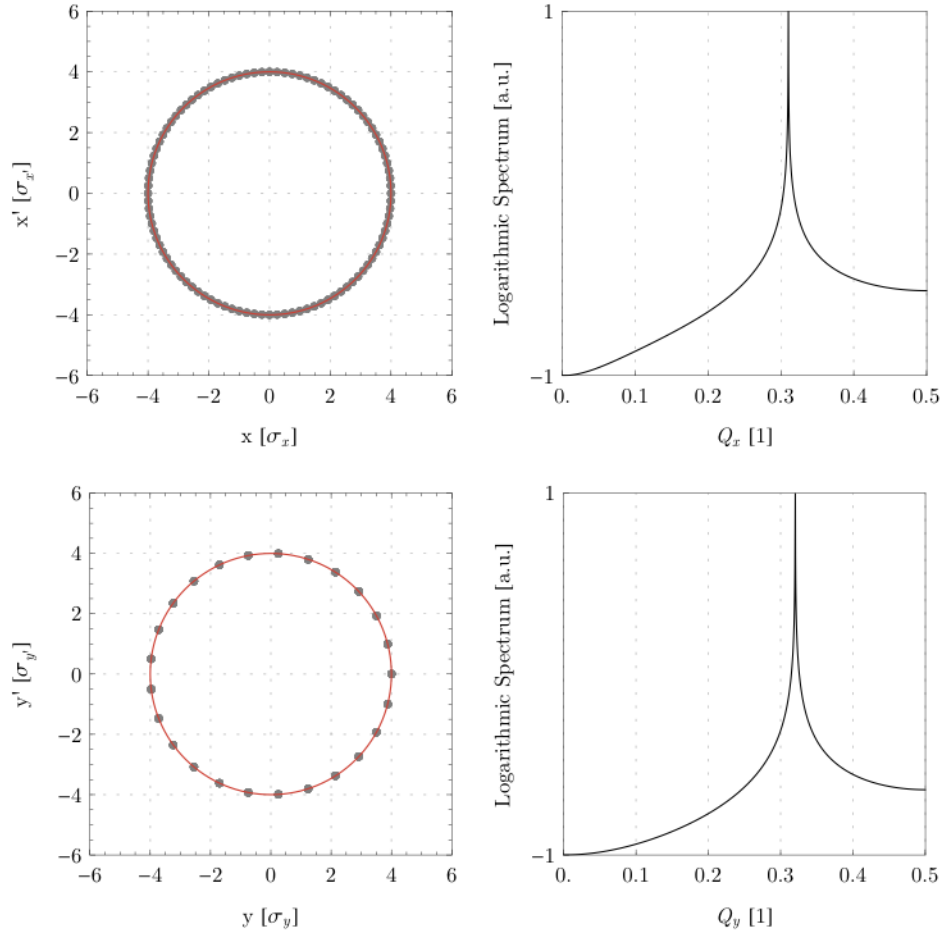


Figure 4.1: A linear machine in the normalized phase space, *left*, and in the frequency domain, *right*. The LHC nominal collision tunes are assumed. The particle describes a circle in the normalized phase space and in the frequency domain it has a perfect resonant behavior.

along the machine. An example of tracking in a non-linear machine and in the normalized phase space, is given in Figs. 4.3 and 4.4: they are an example of two opposite particle behaviors, that is, respectively, a stable and an unstable motion.

In Fig. 4.3, a particle with an initial horizontal amplitude of $\sqrt{\epsilon_x \beta_x} = 4 \sigma_x$ and a vertical one of $\sqrt{\epsilon_y \beta_y} = 4 \sigma_y$ (vanishing initial phases) is tracked over more than $3 \cdot 10^5$ turns. The particle amplitudes are non conserved: the radius of red solid circle represents the initial amplitude (in x , *top* plots, and in y , *bottom* plots) while the dashed black circle represents the amplitude averaged on the first 1024, *left* plots, and on the last 1024 turns, *right* plots. Even if we can observe a non regular motion of the particle, there is an exchange of emittance between the horizontal (ϵ_x decreases) and vertical plane (ϵ_y increases) and the increase of emittances between the first and the last turns is limited.

In Fig. 4.4, on the contrary, considering the same machine but an initial horizontal amplitude of $7 \sigma_x$ and a vertical one of $7 \sigma_y$ (vanishing initial phases), the situation drastically changes: even if there is a similar coupling of emittances in the first 1024 turns, the increase of the amplitudes at the end of the tracking is much larger. The horizontal and vertical amplitudes are respectively $\approx 20 \sigma_x$ and $\approx 14 \sigma_y$. In that case the particle can be considered unstable.

To evaluate and distinguish these different behaviors, the concept of *dynamic aperture*, DA, has been introduced. It represents the maximum particle amplitude (in x and y) for which the motion is considered to be stable. The aim of the tracking is to evaluate the dynamic aperture of the machine. In the specific case of the beam-beam effect, the dynamic aperture appears as *diffusive aperture*.

Several “indicators” can be considered for evaluating the dynamic aperture:

- the so-called *tune footprint* (Fig. 4.5): the tune of the particle depends on its amplitude, so even without

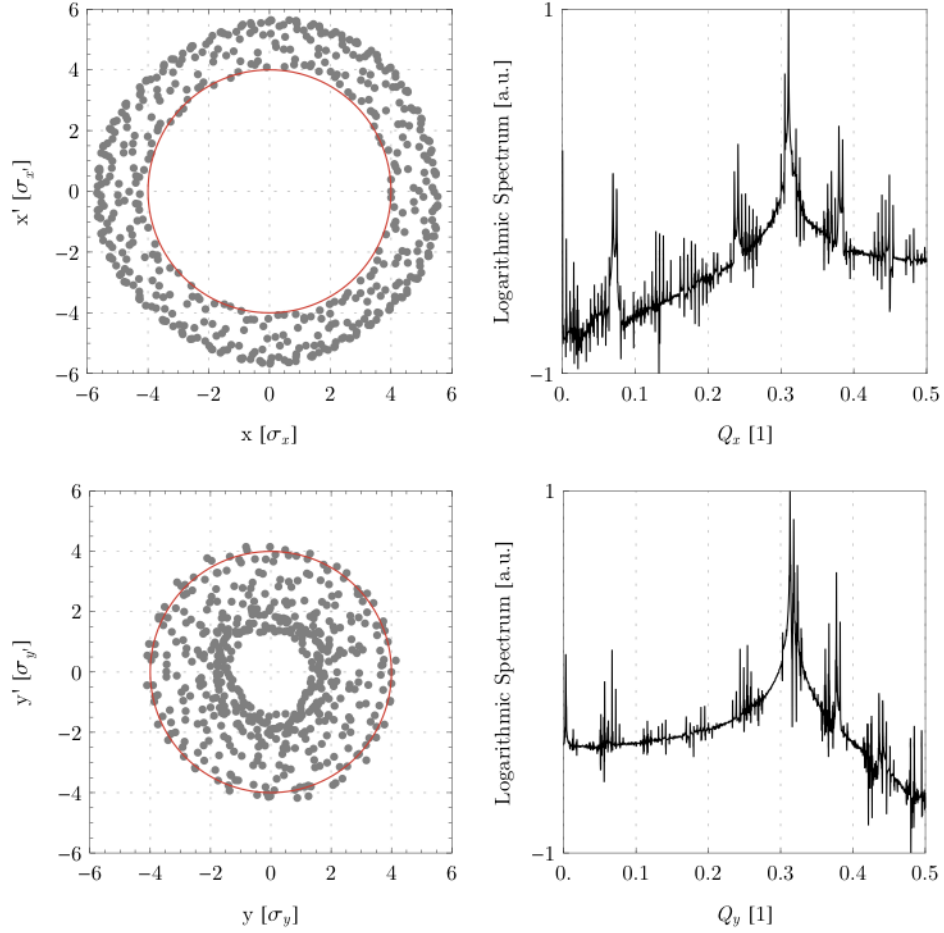


Figure 4.2: An example of machine with non-linearities. The effects on the normalized phase space, *left*, and on the frequency domain, *right*, are well visible. The radius of red solid circle represents the initial amplitude.

considering the chromatic aberration of the machine, the working point of the machine becomes an area (footprint) on the tune diagram. The dynamic aperture is the lowest amplitude whose tune reach a “forbidden” resonant line. In hadron colliders a 13th order resonance is considered already dangerous,

- an *index of chaos*, like the Lyapunov exponent, that measures *chaoticity* of the motion that is the velocity of separation of particles trajectories with very similar (close) initial conditions,
- the *evolution of the particle amplitude*: in a linear machine the particle amplitude is conserved therefore, by observing its evolution for a non linear machine, we can discriminate a stable initial amplitude from an unstable one.

In our study we have privileged the use of the last indicator (evolution of the particle amplitude) for the following two reasons:

- the tune footprint is a useful way to compare similar machine, showing the tune shift as function of the particle amplitude (tune spread). It is not possible to infer from it the stability of the particle motion in a quantitative way. Nevertheless we used this indicator as confirmation of specific features that we observed analyzing the evolution of the particle amplitude,
- the index of chaos requires the definition of distance in phase space making less direct the physical meaning of the results: some particle can have a chaotic but bounded motion being, in principle, stable. On the contrary, the evolution of the particle amplitude gives a more physical and easy to interpret information of the particle behavior, i.e., with respect to the beam size and the collimation system.

The drawback of the approach based on the particle amplitude evolution is that the tracking becomes extremely time consuming. We need, in fact, to track a large number of particles to cover with a reasonably good resolution all possible amplitudes ranging from 0 to $10 \sigma_{x,y}$. This corresponds to $\approx 10^4$ particles. The

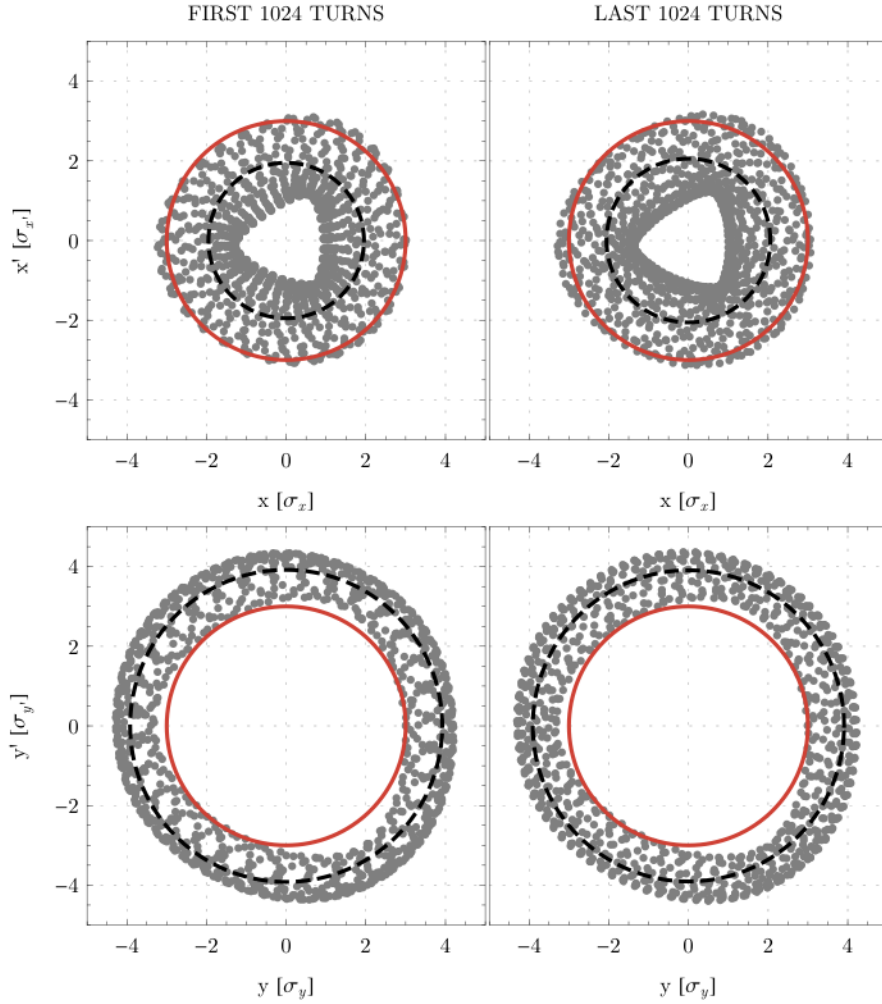


Figure 4.3: A “stable” particle in a non-linear machine. The radii of the red solid and black dashed circles represent, respectively, the initial and average amplitude. The increase of the emittance (dashed circle) between the first and last 1024 turns is almost negligible.

number of turns we considered in the tracking is $3 \cdot 10^5$. This is equivalent to ≈ 30 s in LHC and ≈ 7 s in SPS: it is a compromise between the speed of the computation and the time constants of the phenomena we want to investigate.

4.1.2 The simulation code written in CUDATM

Due to these very heavy simulations, we decided to implement a specific tracking code in the CUDATM language (Compute Unified Device Architecture, [52]): it is a pseudo-C code running on high performance nVIDIA Graphics Processing Unit (GPU) [53]. The use of GPUs to make tracking simulation has already been proposed [54] but it is not yet largely adopted.

The hardware used in our simulation is a GeForce GTX 280: it has 240 single precision CPUs running with a clock of 1.3 GHz for a total of 933 GFLOPs in single precision (to compare with the fastest 2008 processor, Intel Core i7 965 XE: a quad-core who performs over 70 GFLOPS in double precision). Out of the 240 CPUs, thirty are provided with double precision Arithmetic Logic Units. In spite of that, we compile the code to run in single precision to maximize the number of available CPUs: we found a gain in performance of two orders of magnitude with respect to an equivalent C-code running, in double precision, on an Intel CPU running at 3 GHz.

The tracking of weak-strong beam-beam simulation can be done using a task-parallelism approach, the simpler form of parallel computation: each particle is tracked independently from the other particles on a

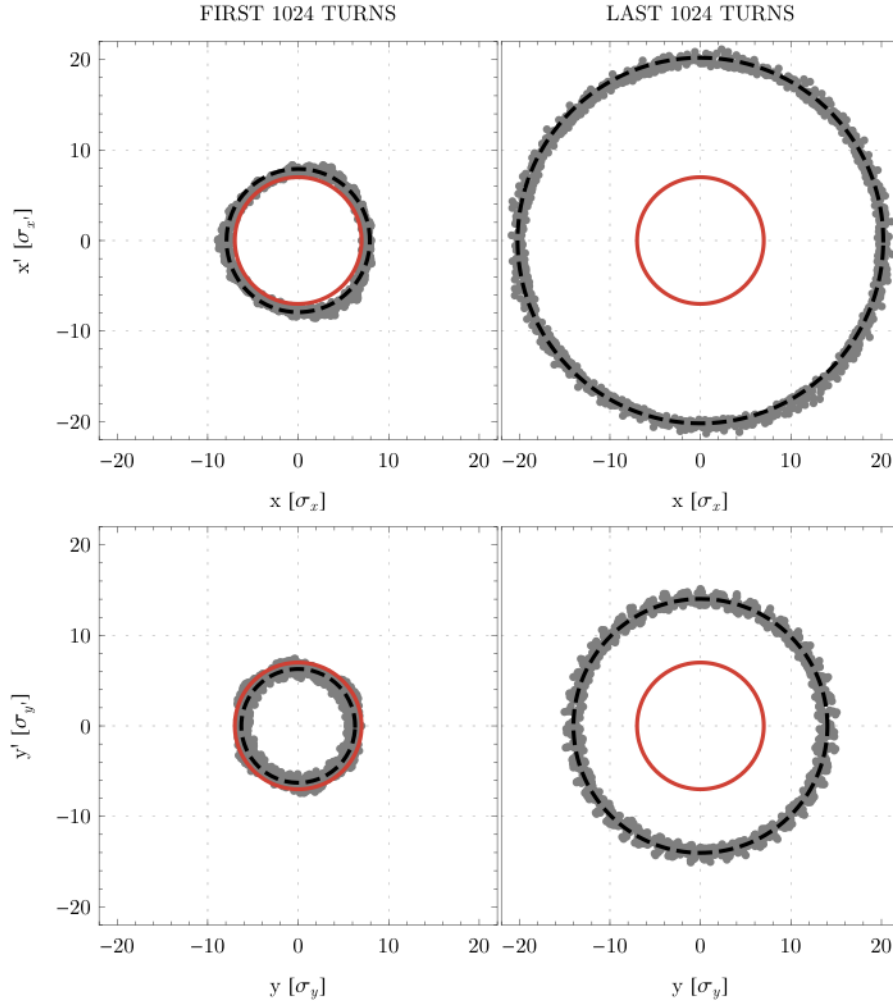


Figure 4.4: An “unstable” particle in a non-linear machine. The radii of the red solid and black dashed circles represent, respectively, the initial and average amplitude. The particle is considered unstable due to the large increase of the particle amplitude (see dashed circles).

given processing unit. The code we wrote uses the 6×6 linear matrices of the MAD-X *sectormap* output [40]. They are symplectic if a thin lens optics is considered [40].

The code requires a CUDATM enabled nVIDIA graphics card: being hardware dependent, this put a strong limit on its portability. An other limit derives from the small cache memory available on the CPUs (16 KB on each multiprocessor of 8 CPUs compared to 3 MB of second level cache memory of a standard CPU). This can significantly slow down the performance since to access the RAM memory of the graphics card can require 300 – 400 clock cycles (only four for the cache memory access).

The solution we adopted is to write automatically the kernel function, the routine that runs on the GPU, with all the values of the optics matrices already embedded in it: we replace the matrix multiplications needed to describe one turn of the particle in the accelerator by a set of linear equations. In this way we save, on one hand, a lot of memory and computations time: since the matrices are usually populated of a very large number of 0’s and 1’s, the trivial multiplications and sums are suppressed or directly solved. On the other hand, the drawback of this approach is, at the moment, the limited number of 6×6 matrices that can be loaded on the cache memory (of the order of one hundred).

For the same reason the code, as it is conceived, cannot implement second-order matrices. They are symplectic only if, for each sextupoles of the ring, a transport matrix is considered. In fact, combining two second-order matrices in a second-order one implies a truncation that compromises its symplecticity. Considering the number of LHC sextupoles and the limited CPUs cache memory, it turns out that a second-order symplectic tracking cannot easily be implemented. Nevertheless, even without the second-order tracking,

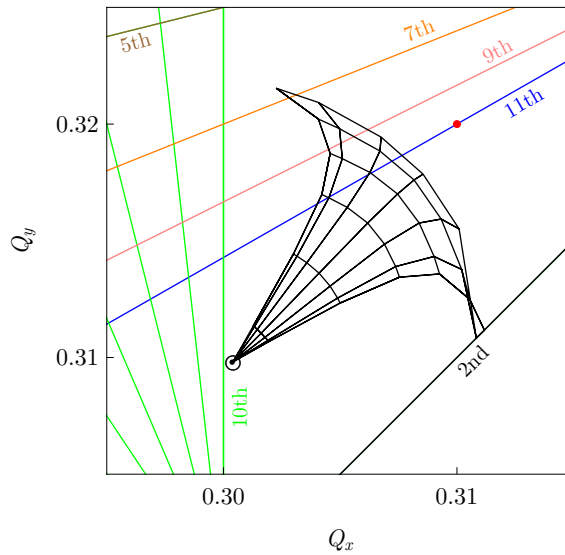


Figure 4.5: The nominal LHC tune footprint. The red dot represents the unperturbed tunes. The resonant lines up to the order 11th are shown.

the machine linear chromaticity can be taken into account by a convenient function that adds a phase advance proportional the particle off-momentum. This phase advance can be lumped at the end of the lattice observing that, in general and in particular in LHC, the synchrotron motion is much slower than the betatron one [1][22].

The single precision tracking we propose may, in principle, produce non physical results because of the higher numerical noise of the computation in comparison to double precision tracking. We verified that single precision tracking is sufficiently reliable by verifying with our CUDATM code the conservation of the emittance on a linear machine. Before quantifying the results of this simulation we describe in the following paragraph the formalism of the amplitude plane, that is the plane where we show the amplitude evolution of the tracked particles.

The simulations in the amplitude plane

In the following we always assume a Gaussian bunch in the physical xy -plane: the beam in the normalized physical plane is shown in Fig. 4.6, *left*. Due to the betatron motion, even in a linear machine, the position of the particle changes turn by turn in that plane: this means that, even if the overall beam representation does not change in time, the position of a single particle oscillates. On the contrary, the particle coordinates stay constant in what we call the amplitude plane (Fig. 4.6, *right*): in this plane, at the place of the particle horizontal and vertical positions, the particle amplitudes, x -amplitude ($\sqrt{\epsilon_x \beta_x}$, also referred to as horizontal amplitude) and y -amplitude ($\sqrt{\epsilon_y \beta_y}$, also referred to as vertical amplitude), are represented. The advantage to use this plane is that, for linear machines, all the particles keep their coordinates turns after turns.

It is worth noting how the transversal bunch distribution varies passing from the physical plane to the amplitude plane (Fig. 4.6): this is due to the fact that the amplitude is the square root of the quadratic combination of two (centered) normal distributed variables ($\{x, x'\}$ and $\{y, y'\}$, respectively, for the horizontal and vertical amplitude). Therefore it follows, in each of the two transverse planes, the Rayleigh distribution, p_R [55]:

$$p_R(x, \sigma_x) = \frac{x}{\sigma_x} e^{-\frac{x^2}{2\sigma_x^2}} \quad \text{for } x \geq 0.$$

The core of the beam is therefore between 1 and 3 σ in the amplitude plane (Fig. 4.6, *right*) with 6 % of the beam beyond the 3 σ amplitude, to compare with the only 0.3 % in the physical plane.

As already observed, in a non linear machine the amplitude of the particles is not invariant anymore and can vary from turn to turn (Fig. 4.4). This can be clearly represented in the amplitude diagram (Fig. 4.7, *left*). Instead of representing two points (corresponding to the initial and the final amplitudes), it is more

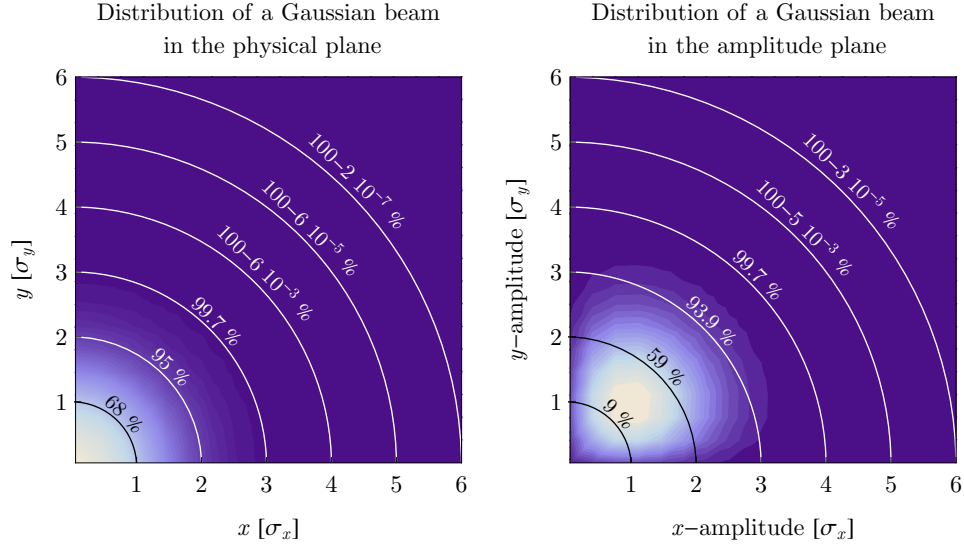


Figure 4.6: A Gaussian beam in the physical plane (*left*) and in the amplitude plane (*right*). On the different arcs we give the percentage of the beam charge enclosed in the different sector regions.

convenient, for our purpose, to plot a single point whose position represents the initial amplitudes and whose color shows, by means of a specific color coding, the final amplitude. Since a color can represent only a single scalar, to describe the initial a final position in the x and y direction we need two different plots as shown in Fig. 4.7, *center* and *right*. The color coding proposed is shown in Fig. 4.8 and it is used throughout the whole chapter.

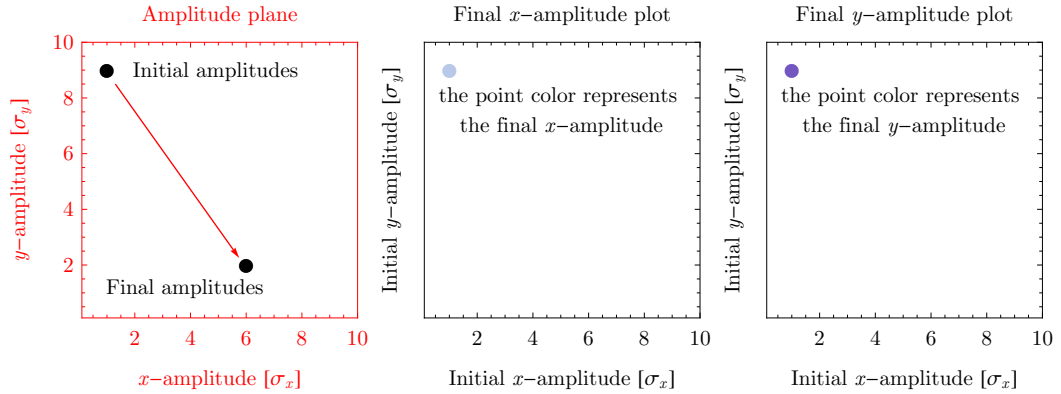


Figure 4.7: Two different ways to show the evolution of the particle amplitude are presented. On the *left*, two points are used to represent the initial and the final amplitudes (amplitude plot). On the *center* and on the *right*, the coordinates of the point give the initial amplitudes of the particle while the colors of the point give the particle final x -amplitude and the final y -amplitude (see the color scale in Fig. 4.8): since the color represents a single scalar and we need to represent a point in a plane we use two plots, labelled as “Final x -amplitude plot” and “Final y -amplitude plot”.

The initial conditions of our tracking consist in 10^4 particles uniformly distributed in the region between 0.1 and 10σ (in steps of 0.1σ) in x and in y direction (Fig. 4.9). The particle phases are randomly chosen between 0 and 2π . We checked that, for our specific purpose, the initial phase has no significant impact.

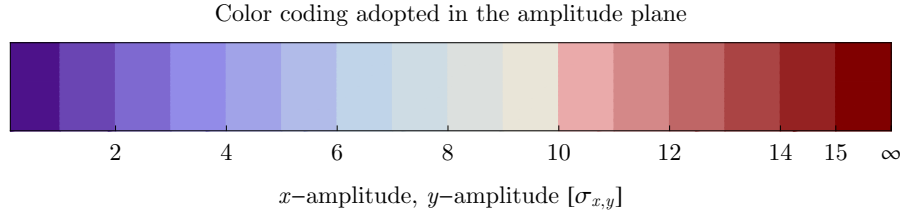


Figure 4.8: The color codes used in all the following amplitudes plots. The red color represents all the particle whose amplitude is larger than 10σ .

This is due to the fact that, in the range of our tunes, after only $3 - 5$ turns the particles samples the complete phase range. The beam-beam interaction will have a time constant longer than the one required by the particle to explore the 2π phase range, therefore the amplitude evolution of the particle does not appear to depend on its initial phase: it has been confirmed by the specific simulations we performed. The independence of the particle stability from its initial phase reduces greatly the complexity of the problem and makes possible to have the whole information on the beam dynamics in the amplitude plane even if the initial phases are not shown.

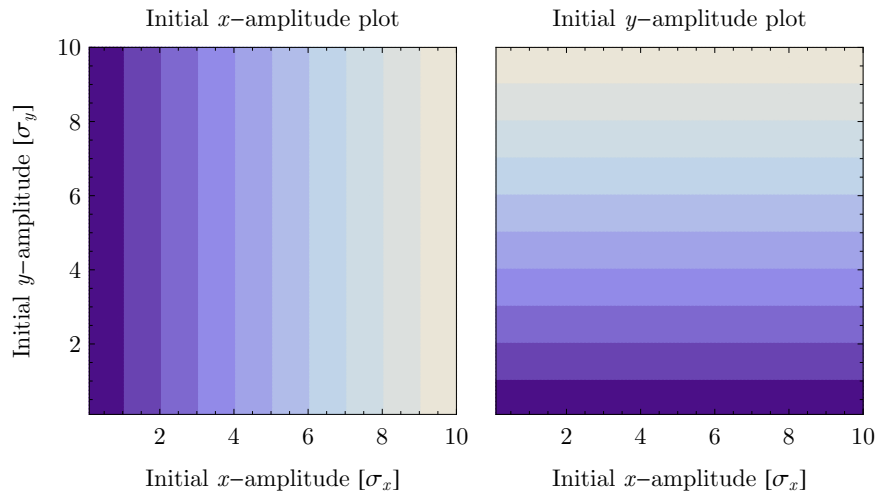


Figure 4.9: Particle initial conditions used in the tracking studies: horizontal amplitude (*left*) and vertical ones (*right*) plotted in the initial amplitude plane. In a linear machine, after the tracking and neglecting the tracking numerical errors, the final and initial amplitudes of the particle are identical and the plots show are valid also for the final x and y amplitudes.

Since, in a linear machine, the amplitudes of the particles are preserved there are no changes between the initial condition plot and an equivalent plot representing the same beam at a specific turn. We checked it in order to evaluate the impact of the single precision of the CUDATM code. The results are reported in Fig. 4.10. We can see that the "linear bands" are well preserved by the tracking but there is a numerical "compression" of the bands (Fig. 4.10, light red region: corresponds to 11σ amplitude particles, see color coding in Fig. 4.8): it expresses an emittance blow up, due, to numerical truncations introduced with the single precision tracking (this blow up disappears in double precision tracking).

Our conclusion is that the single precision can describe the linear machine dynamics with an error of $\approx 5\%$ for large initial amplitudes ($\approx 10 \sigma$). This is small with respect to the expected magnitude of the beam-beam effect as we shall study the threshold for onset of fast diffusion but may give slightly pessimistic estimate of the thresholds.

Examples of the beam-beam interaction in the LHC with the nominal and ultimate beam current

In order to cross check our code with the previous tracking results, the nominal LHC case has been studied: starting from the nominal separation pattern (see Fig. 1.7) and considering two interaction points with alternating crossing angle, it yields a total of two head-on collisions and 60 long-range beam-beam interactions at 9.5σ with the nominal bunch population ($N_b = 1.15 \cdot 10^{11}$ ppb). For these simulations we apply the scaling laws presented in Section 3.2.3 lumping the different beam-beam interactions using their invariance with respect to the optical functions (at constant normalized separation) and taking advantage of the particular phase advance in the proximity of the Interaction Point (see Fig. 3.3).

The amplitude planes after $3 \cdot 10^5$ turns are shown in Fig. 4.11: in the vertical amplitude plane (*right*) there is a significant amplitude growth between 6.5 and 7.5σ , that is in well agreement with the results of similar tracking studies [43].

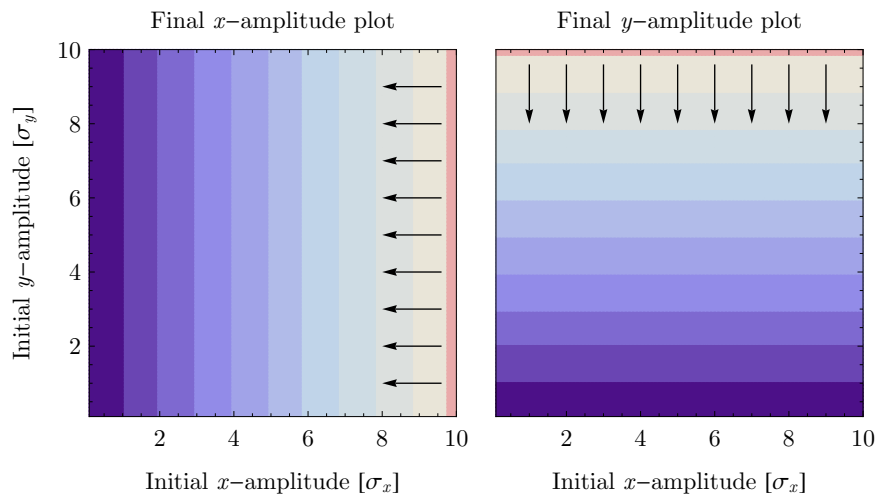


Figure 4.10: Final conditions after $3 \cdot 10^5$ turns in the tracking studies (single precision tracking). The red band should not appear in a linear machine. It is due to the numerical truncation introduced with the single precision tracking: it induces a band “compression” (see arrows). This effect is small with respect to the expected magnitude of the beam-beam effect as we shall study the threshold for onset of fast diffusion but may give slightly pessimistic estimate of the thresholds.

In Fig. 4.12 a similar simulation considering a higher beam current ($N_b = 1.7 \cdot 10^{11}$) is presented: there is a reduction of 1 to 1.5σ in terms of dynamic aperture and there is a some perturbation of the beam core that can be seen in the increased noise level between the bands corresponding to 1 to 3σ .

It is worth noting that in the two previous cases (Fig. 4.11 and 4.12) the y -amplitude evolution is the one that limits the dynamic aperture of the machine.

Example of beam-wire compensation

As already reported in Section 3.2.2 and 3.2.3, it is possible to compensate, within some limits, the effect of the beam-beam interactions by means of a wire carrying DC current.

In Figs. 4.13-4.14 an example of beam-beam excitation and wire compensation is given. We assume an extremely large number of beam-beam parasitic encounters (300 long-range beam-beam interactions at 9.5σ , all in the vertical plane, with nominal LHC tune and $N_b = 1.7 \cdot 10^{11}$) in order to see large effects. The condition for the compensation is ideal, that is no phase advance between excitation and compensation, round strong beam at the excitation point ($\beta_x = \beta_y$) and same aspect ratio (β_x/β_y) for the weak beam at the excitation and compensation points (see Section 3.2.3). The effect of the compensation is evident in the beam core while, as expected, the compensation fails when the particle’s amplitude is too close to the wire

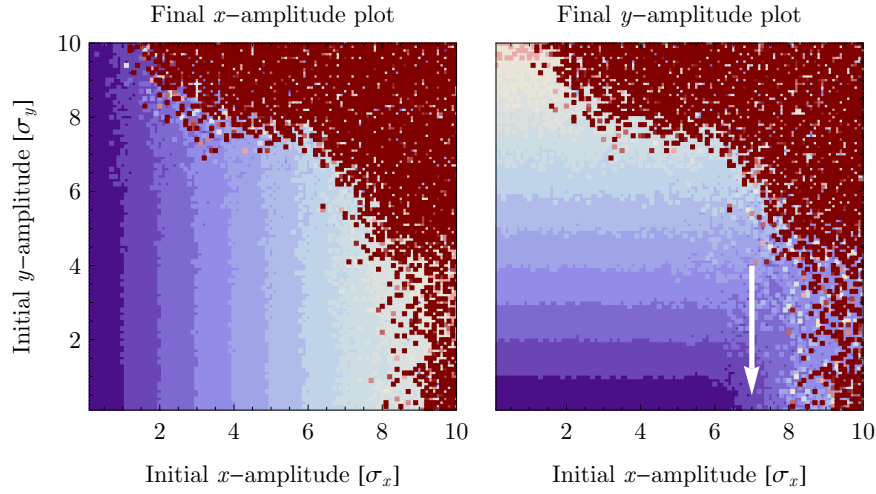


Figure 4.11: Nominal LHC tracking results (after $3 \cdot 10^5$ turns, $N_b = 1.15 \cdot 10^{11}$). It is possible to observe a different behavior in the horizontal and vertical amplitude. The vertical one shows a much stronger compression around $6.5 - 7.5 \sigma$ (see plotted arrow) and indeed limits the dynamic aperture of the machine.

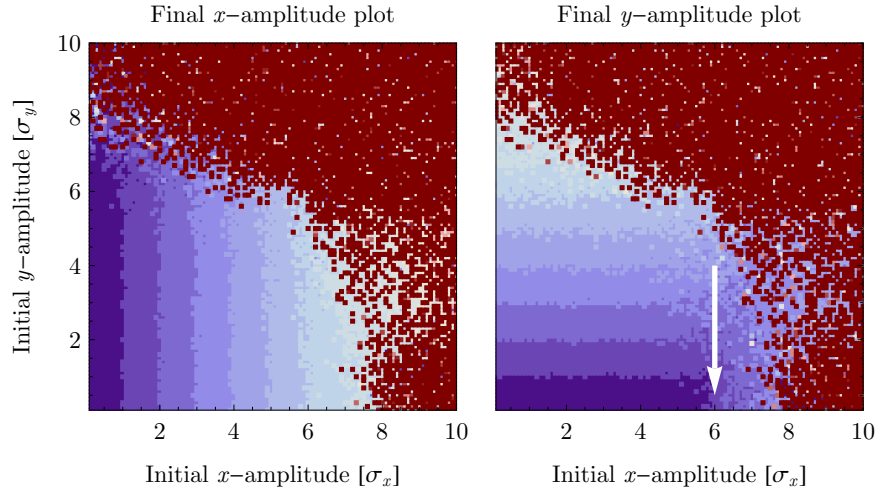


Figure 4.12: Nominal LHC with ultimate current ($N_b = 1.7 \cdot 10^{11}$ ppb) tracking results (after $3 \cdot 10^5$ turns). Like in Fig. 4.11, the vertical amplitudes limits the dynamic aperture of the machine (see plotted arrow).

center: for particles closer than $\approx 2 \sigma$ to the wire center, since the wire cannot mimic the beam field in an efficient way, the compensation is not possible.

4.1.3 The simulations results

In this section, after having introduced the assumptions we used for the tracking, we present the results of the beam dynamics simulations for the Early Separation Scheme.

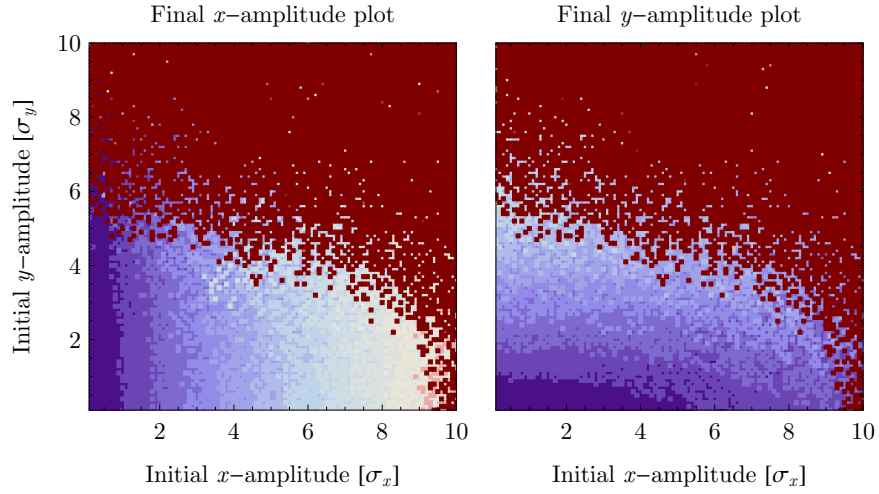


Figure 4.13: An example of beam-beam excitation (300 long-range beam-beam interactions at 9.5σ , all in the vertical plane, with nominal LHC tune and $N_b = 1.7 \cdot 10^{11}$) tracking results after $3 \cdot 10^5$ turns. The beam-beam excitation has a violent effect on the beam.

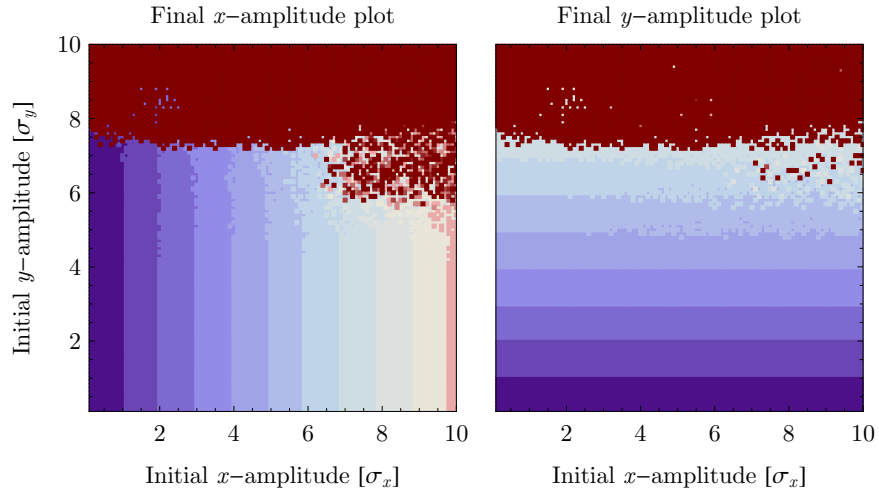


Figure 4.14: The result of wire compensation (ideal case). The non compensated amplitude planes are shown in Fig. 4.13 and the effect of the compensation is evident. LHC nominal tunes assumed. It is worth observing that the wire can mimic the field of beam until $\approx 2 \sigma$ from its center.

The beam separation pattern for different positions of the D0 dipole

As pointed out in Section 1.3, one of the main advantage offered by the Early Separation Scheme is the possibility to reduce the beam crossing angle. Nevertheless, since the dipoles of the scheme have to be positioned out of the inner detector region (see Chapter 5), there will be some parasitic encounters at reduced separation that can potentially harm the beam stability. We refer, hereby, to a *reduced separation encounter* if the beam separation is lower than the nominal one, that is 9.5σ : the range of separation that we consider is between 5 and 7σ . A 5σ separation corresponds almost to halving the nominal crossing angle. A lower separation, apart from beam dynamics considerations, appears difficult to reach with the present magnet technology given all the detectors constraints (see Chapter 5).

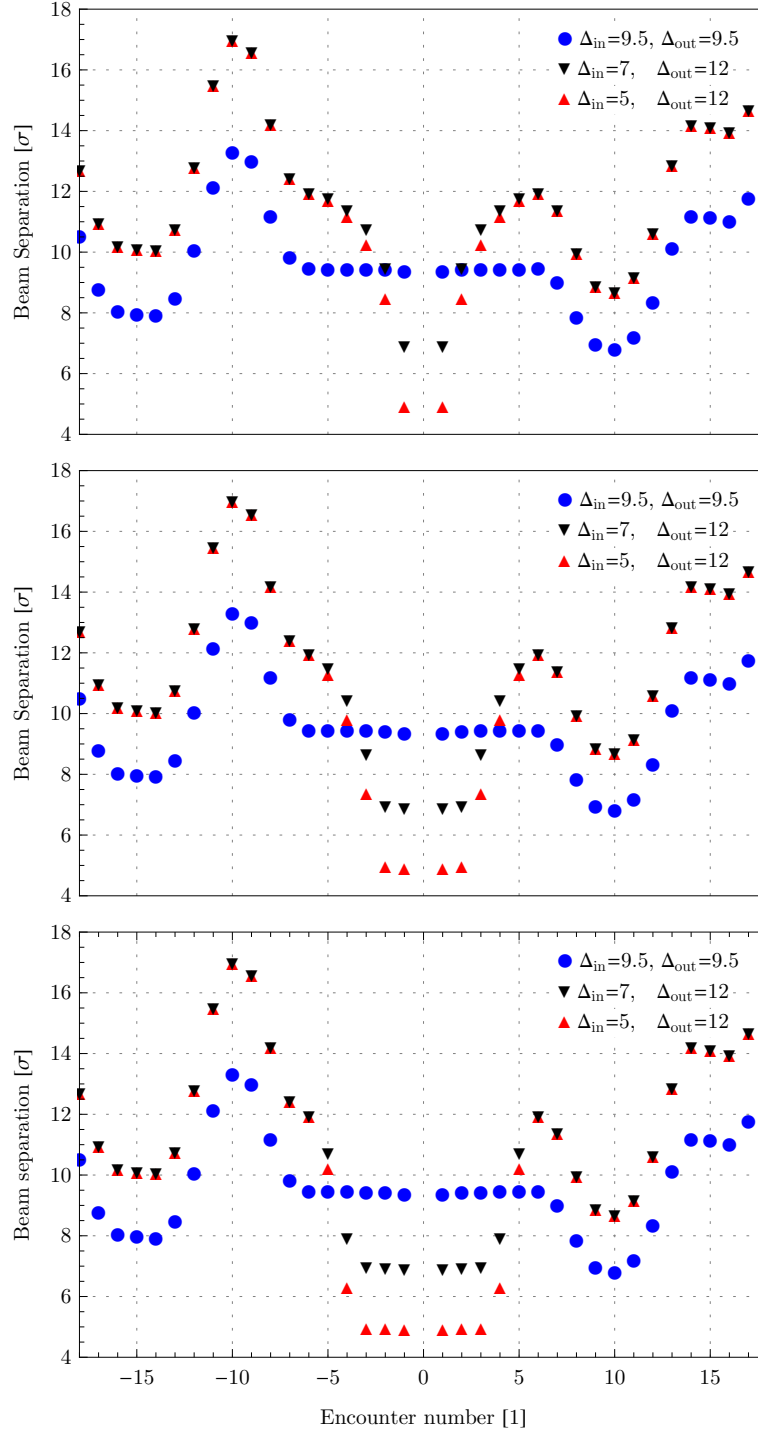


Figure 4.15: The beam separation pattern with the D0 dipole at different distances from the Interaction Point, with one (*top*), two (*center*) or three (*bottom*) parasitic encounters at reduced beam separation (5 or 7 σ) per side and per Interaction Point. The nominal separation (9.5 σ) is shown as reference.

In Fig. 4.15 the beam separation patterns for three different positions of the D0 (the dipole of the Early Separation Scheme that is closer to the Interaction Point, Fig. 1.18) are plotted. The beam separation pattern shows, in the proximity of the Interaction Point, the normalized beam separation (see Fig. 1.7). These three positions correspond to the possible integration slots proposed by the ATLAS collaboration [56, 57]. They are located at about 3.5 – 4.5 m (Slot 1), 7 – 13 m (Slot 2 + Slot 3), and 13 – 18 m (Slot 4) from the Interaction Point (see Chapter 5). Assuming the nominal 25 ns bunch spacing, these positions correspond, respectively, to have 1, 2 and 3 parasitic encounters at reduced normalized separation, Δ_{in} , per each side of the Interaction Point. Moreover we assume to have an outer separation (Δ_{out} , see Section 1.3) of 12. This may be possible thanks to a significant increase of the triplet aperture [37] even if this strongly depends on the triplet field quality and on the collimation system efficiency.

The assumptions considered for the simulations

From the scaling laws discussed in Section 3.2.3, we know that the beam-beam long-range effect does not depend on the optics functions provided that the separation is expressed in term of beam σ : this simplifies significantly the problem since it implies that, for specific inner and outer separation (Δ_{in} and Δ_{out}), the β -function (and hence its value at the Interaction Region, β^*) does not play a role for the long-range interaction. On the contrary, the length of the triplet and the position of the separation dipole (D1, see Fig. 1.9) are critical because they set the total number of long-range encounters. Moreover, the triplet is responsible of the details of the beam separation pattern due to the modulation of the beam separation provided by the interplay between the optical functions and the closed orbit (see Fig. 4.15).

It is worth noting that, differently from the long-range beam-beam effect, the head-on beam-beam effect does depend on the β^* in presence of non vanishing beam crossing angle (see Eq. 1.8). Anyhow, in the following simulations, we assume to have perfect head-on collisions, i.e., we neglect the effect of the crossing angle in the head-on collisions. This hypothesis is conservative because the effect of the head-on is maximum for vanishing crossing angle and, in addition, other studies show [43] that the impact of the head-on interaction is small compared to the one due to the long-range beam-beam encounters.

From the scaling laws it is possible to conclude that, due to the particular phase advance in the Interaction Region, all the kicks of the parasitic encounters add in phase. This allows us to “sort” the separation pattern in order to better compare the proposed ones (5 and 7 σ inner separation and 12 σ outer separation) to the nominal (Fig. 4.16). It is possible to observe that the solutions with the $\Delta_{in} = 7$ is similar to the nominal separation pattern (whose simulation results, for the nominal and ultimate bunch charge, are reported, respectively, in Figs. 4.11 and 4.12): excluding the three encounters at 7 σ instead of 8 σ , the beams would be, in fact, better separated in the proposed scheme than in the nominal one. The situation for $\Delta_{in} = 5$ σ appears qualitatively different. For this reason the simulation results reported refers to this more critical case.

In the simulations we assume

- to have collisions only in ATLAS and CMS detectors,
- to have alternating crossing angles: this choice is related to the compensation of the linear tune shift of the beam-beam long-range encounters,
- to have 30 parasitic encounters per Interaction Point with $1.7 \cdot 10^{11}$ protons per bunch. For the luminosity leveling, this does not correspond to the initial N_b but the actual one when the minimum beam separation is reached (see Fig. 2.15)
- four-dimensional tracking: the chromatic behavior of the machine is not taken into account. Other studies [58] show that increasing the chromaticity of the machine in presence of beam-beam effect reduces the beam lifetime. This effect is associated to the larger tune footprint of the beam.

Presentation and discussion of the simulation results

Some results of the performed tracking are shown in Fig. 4.17. In all the plots we assumed $\Delta_{in} = 5$ and $\Delta_{out} = 12$. We considered 2, 4 or 6 beam-beam encounters per Interaction Point at reduced separation, depending on the D0 dipole’s position (respectively *top*, *middle* and *bottom* plot). The result of the simulation with 2 encounters at reduced separation shows a larger dynamic aperture (≈ 9 σ , see arrow in Fig. 4.17, *top*) than the one of the nominal LHC (Fig. 4.11). By adding other 2 encounters at 5 σ beam separation, the dynamic aperture shrinks (7 to 8 σ) but it is still larger than in the nominal case. Some perturbations of the motion are visible for the particles with an initial horizontal amplitude between 5 and 7 σ . The simulation with the 6 beam-beam encounters per Interaction Point at reduced separation shows a dynamic aperture of 4 σ , that is significantly lower than the nominal.

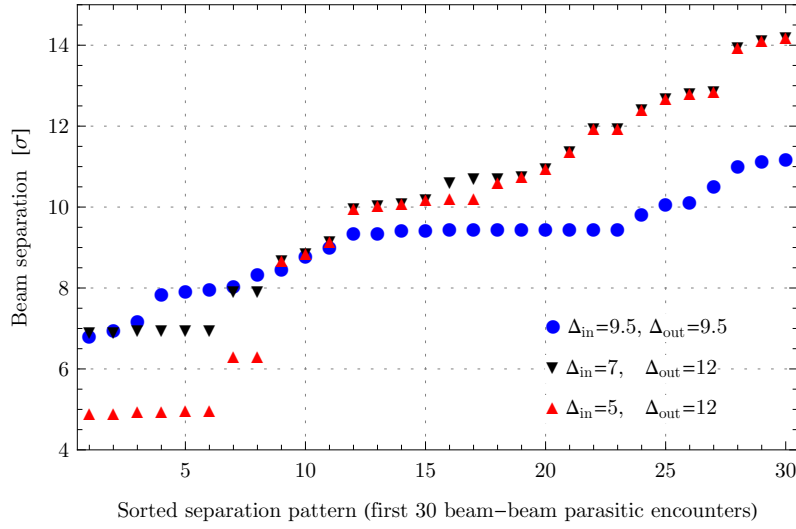


Figure 4.16: Comparison of the separation pattern of the nominal LHC and for the Early Separation Scheme assuming the D0 dipole at 14 m from the Interaction Point, that is 3 parasitic encounters at reduced distance. The average normalized beam separation in the triplets (Δ_{out}) is assumed to be 12 taking advantage of the 150 mm aperture quadrupole [37]. It is possible to observe that the solution with the of $\Delta_{in} = 7$ is similar to the nominal separations pattern (its simulation’s result, for the ultimate bunch charge, are reported in Fig. 4.12). The $\Delta_{in} = 5$ separation pattern appears qualitatively different.

As for the nominal LHC, the vertical amplitude seems to be more excited by the beam-beam interactions than the horizontal one even if the conditions in the two planes are symmetric except from the tunes. For this reason this effect can be interpreted as a feature depending on the vertical tune. We study in more details the problem making simulation for several vertical tunes: in our simulations the tunes (0.31, 0.28) is better than the nominal tunes (0.31, 0.32). The amplitude plot for the three encounters per side per Interaction Point is presented in Fig. 4.18 ($\Delta_{in} = 5$ and $\Delta_{out} = 12$). The “instability region” (particles with final amplitudes greater than 15 σ , brown region) has been pulled back and the regularity of the motion for the particle with small initial vertical amplitude has been significantly increased: we observe a weak amplitude blow up starting at 5 σ (small arrow) and a stronger one at 6 σ (large arrow). Notably, the larger amplitudes recover stability.

The better behavior of this working point can be interpreted looking at the beam footprints in the tunes plane. In Fig. 4.19 we show the footprint plots for the nominal working tune (0.31, 0.32), on the *left*, and for the proposed working tune (0.31, 0.28), on the *right*. We assume $1.7 \cdot 10^{11}$ particles per bunch and 6 encounters at the reduced separation of 5 σ (footprints in black solid lines). It is possible to see that at the nominal tune, part of the beams appear locked on the diagonal resonance: some particles, with amplitude ranging between 4 and 6 σ , are pushed exactly on the diagonal line of the tune diagram by a resonant mechanism. This can be associated to the strong reduction of the dynamic aperture shown in Fig. 4.17, *bottom*. At the working point (0.31, 0.28) the footprint can open without being intercepted by any dangerous resonance that locks the particles on the resonant lines: this can be associated to the better dynamic aperture shown in Fig. 4.18.

We add hereby some consideration on luminosity leveling with respect to the beam footprint behavior. In general the footprint increases with the number of particles per bunch (N_b) for a given inner separation between the beams, this means that during the run of nominal LHC the footprint shrinks as N_b reduces. On the contrary, with the luminosity leveling, the footprint is smaller at the start of the run (blue dashed footprint) than at the end (black solid footprint). This is due to the larger separation between the beams at the starting of the leveling that, in spite of the larger beam current, reduces the beam-beam interaction and therefore the footprint itself. This completes and extends the considerations done in Chapters 2 and

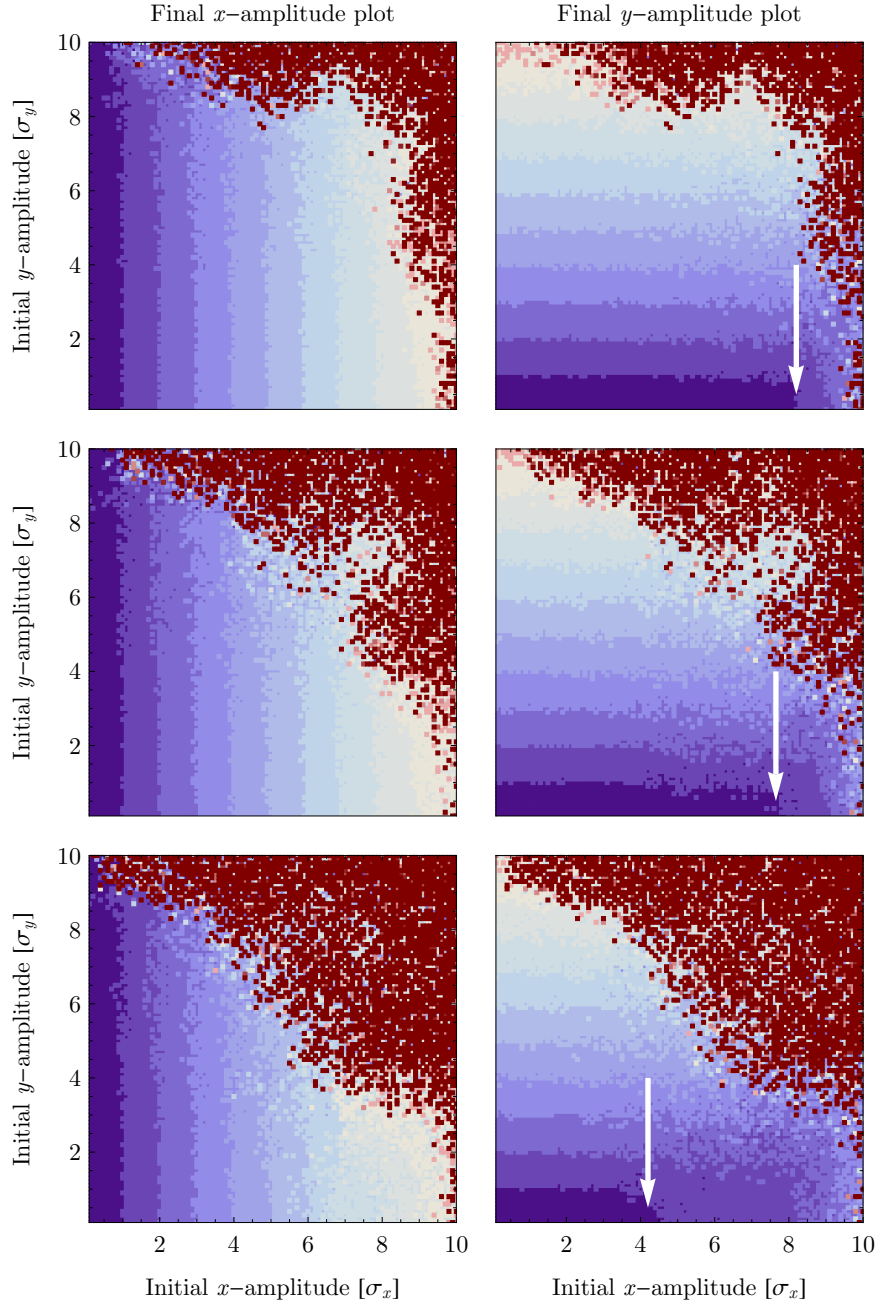


Figure 4.17: The beam dynamic aperture induced by the Early Separation Scheme having, per each of the 2 Interaction Points, 2 long-range beam-beam encounters at 5σ and 28 at 12σ (*top*), 4 encounters at 5σ and 26 at 12σ (*middle*), 6 encounters at 5σ and 24 at 12σ (*bottom*). The LHC nominal tunes are assumed.

3 on the potential of the luminosity leveling to push further the collider limit of the machine by reducing the head-on tune shift. The tune footprint in fact, differently from the linear head-on tune shift, takes into account all the non-linear effect of the beam-beam interaction.

From the simulations results, we can conclude that an Early Separation Scheme, with 2 or 4 beam-beam encounters (per Interaction Point) and ultimate bunch current, has, respectively, a better or similar dynamic aperture than the one of the nominal LHC. By having 6 encounters at reduced separation, we observed a significant reduction of the beam dynamics. Nevertheless we showed that, passing from the nominal tunes $(0.31, 0.32)$ to $(0.31, 0.28)$, it is possible to partially recover the regularity of the particle

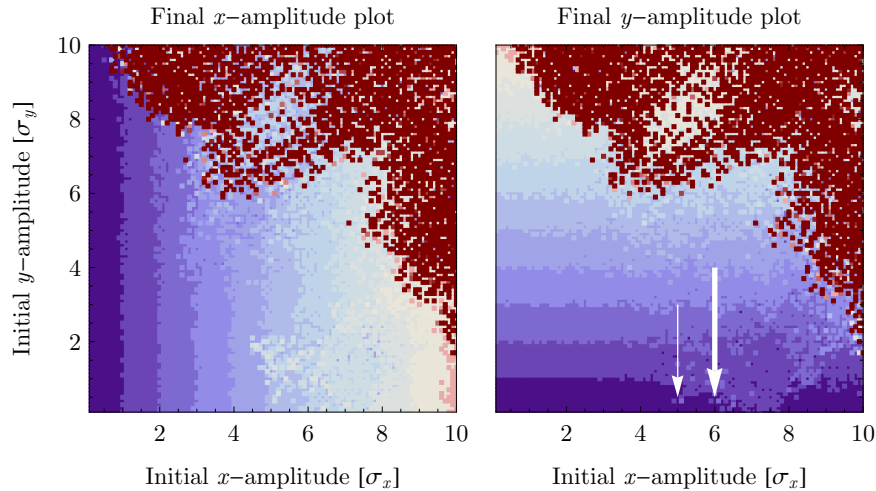


Figure 4.18: The dynamic aperture having, per each of the 2 Interaction Points, 6 long-range beam-beam encounter at 5σ beam separation and 24 at 12σ . The tune is $(0.31, 0.28)$: it is possible to observe an increase in the diffusive aperture with respect the corresponding case in Fig. 4.17, *bottom*. A weak emittance blow up starts at 5σ (small arrow) and a stronger one at 6σ (large arrow).

motion. In the next section we will present the results of the experiments performed in the Super Proton Synchrotron (SPS) in order to mimic and observe the impact of the Early Separation Scheme on the LHC beam.

4.2 The wire experiment in the SPS

Since 2002, experiments on the beam-beam effect [48, 59] have been carried out at the Super Proton Synchrotron (SPS), the LHC main injector. Their goal is to mimic with a wire (see Section 3.2.2) the effect of a second beam in the SPS and to evaluate its impact on the beam lifetime varying the beam-wire distance and the wire current (wire excitation experiments). These experiments are performed in order to elucidate the role of the beam-beam effect at the nominal LHC and for its upgrade. In addition to the excitation experiments, compensation experiments are also carried out: a second wire is used with the aim to compensate the effect of the first one and to check at different tunes, emittances and energy the efficiency of the compensation. The compensation experiments would serve as proof of principle for a possible wire compensation at the LHC [58].

Differently from the case of the Relativistic Heavy Ions Collider (RHIC) at Brookhaven National Laboratory where a similar setup is used [49], in SPS there are not head-on encounters: as a consequence, all the SPS studies cannot explore the coupling between the head-on and the long-range interactions. Anyhow, it has been shown [43] that, for beam-beam interaction similar to those of LHC, the figures are dominated by the long-range effect.

In the following section the experimental setup and the experimental results obtained in the past two years are described. We took part in the preparation, the execution and the analysis of about 100 hours of experiments.

4.2.1 The experimental setup

The Super Proton Synchrotron (SPS) is a synchrotron of 6.9 km of circumference operated by CERN. It is the main injector of the LHC, being able to accelerate protons to the energy of 450 GeV with normal conducting magnets (warm magnets). It has been used in the past for several beam dynamics studies in order to steer the design of the LHC. It is still being used for a similar purpose in the perspective of the LHC upgrade. The wire experiments stand among these beam dynamics studies.

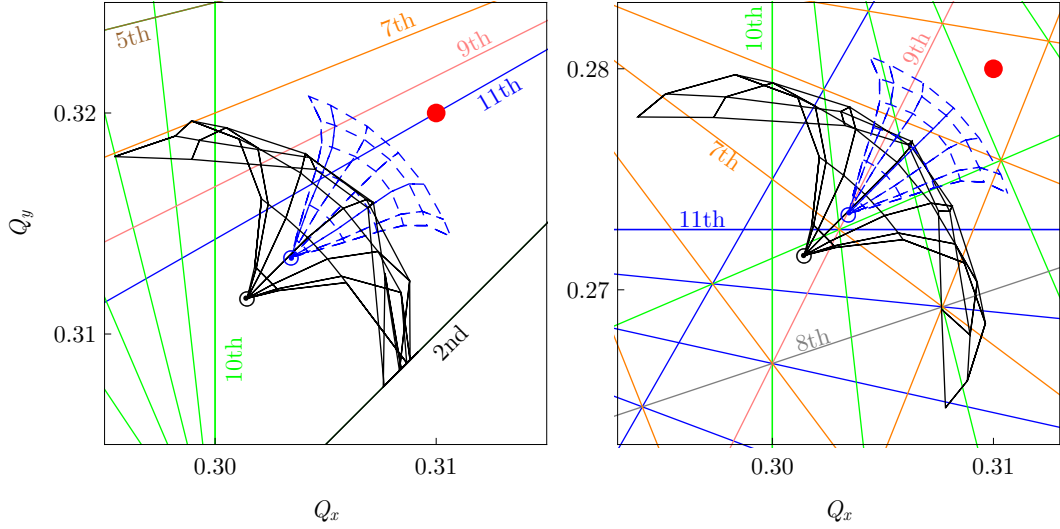


Figure 4.19: The tune footprint with the Early Separation Scheme at the start (dashed blue) and at the end of the leveling (solid black). The unperturbed tune represented with the red point. We assumed a D1 dipole position (see Fig. 1.9) equals to the nominal (30 parasitic encounters per IPs), a $\Delta_{out} = 12$ and a $\Delta_{in} = 12$ or 5, respectively, at the start and at the end of the leveling (dashed and solid footprint). The N_b at the start of the run is $2.3 \cdot 10^{11}$ ppb and is reduced to $1.7 \cdot 10^{11}$ ppb at the end of the leveling. On the *left*, working at (0.31, 0.32), some particles (with amplitude from 4 to 6 σ , solid black) get locked to the diagonal resonance, i.e., are pushed exactly on the diagonal line of the tune diagram by a resonant mechanism. On the *right*, working at (0.31, 0.28), no evident locking mechanism takes place.

In the SPS there are 4 wire elements (boxes) installed in the Long Straight Section 5 and parallel to the longitudinal beam direction. They are shown in Fig. 4.20. The wire boxes are grouped in two families designated as BBLR1 (first two wires with respect the beam direction) and BBLR2 (last two wires). The BBLR1 (elements “BBLR.51760” and “BBLR.51771” of the MAD-x lattice sequence) consists of a 600 mm long copper wire in each of the two boxes (installed in the tunnel in 2002, see Fig. 4.21, *left*). The BBLR2 (elements “BBLR.51772” and “BBLR.51774” of the MAD-x lattice sequence) consists of a set of 3 copper wires (again 600 mm for each of the two boxes) on the vertical, horizontal and diagonal plane (installed in the tunnel in 2004, see Fig. 4.21, *right*). Each family of wires is powered by a dedicated power supply (the power supply “BBLR5176M” for BBLR1, whose DC current is designated as I1, and the power supply “BBLR5177M” for BBLR2, whose DC current is designated as I2). During all our experiments we limit the current to the conservative value of 250 A.

In 2008 the BBLRs were rotated to be on the vertical plane below the beam and, out of the three wires of the BBLR2, only the vertical one was connected to the power supply. This configuration, with the two BBLRs on the same plane, makes possible both the excitation and compensation experiment. The BBLR1 and BBLR2 have opposite polarities: when I1 and I2 have the same sign, due to the specific cabling of the hardware, the current direction of the two element is opposite, so they are in compensation mode.

Each copper wire consists in a hollow cylinder with an outer diameter of 2.54 mm (0.1 in). Through the inner hole the wire is cooled by a constant flux of demineralized water. During the 2009, the wires were realigned: the BBLR1 and BBLR2 have, respectively, their top edges at 19 and 22 mm below the vacuum center (this means that the wires center is, respectively, at -20.27 and -23.27 mm from the beam-pipe center).

While the BBLR1 is fixed, each of the two wires of BBLR2 can move vertically acting on two independent step motors (one for each of its two boxes). The range of position that can be covered is between -22 (garage position) and -17 mm from the wire upper edge and the center of the vacuum pipe [60]. The separation between the beam and the wires is mainly controlled moving the beam with closed orbit bumps. The stepping motors on BBLR2 are used for the fine tuning of the position of the BBLR2 in order to optimize the compensation.

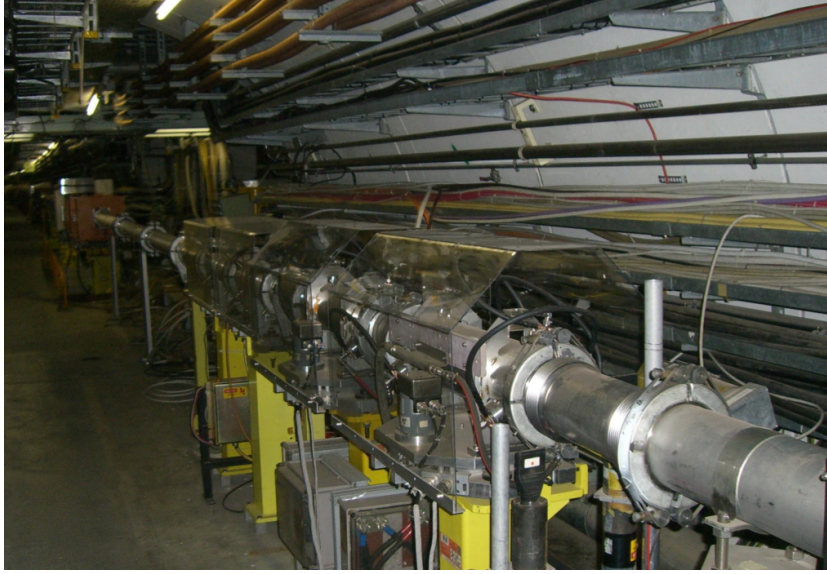


Figure 4.20: The SPS wires in the Straight Section 5 of the SPS tunnel (courtesy of U. Dorda). The boxes 1 and 2 belong to the BBLR1 equipment while the 3 and 4 to the BBLR2 one.

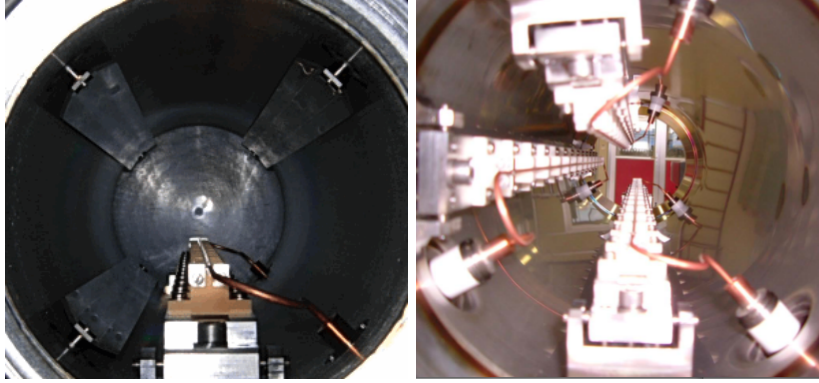


Figure 4.21: The wires of the BBLR1 (*left*) and the of the BBLR2 equipments (*right*). Only one box out of the two belonging to each BBLR is shown (courtesy of G. Burtin).

The SPS optics at the wires position

The positions of the wires in the SPS ring were chosen in order to meet as much as possible the two following constraints:

- same β -function in the two transverse directions: this is the better approximation to reproduce the LHC beam dynamics since a large part of the LHC long-range encounters occurs when the beam has $\beta_x \simeq \beta_y$ (see Fig. 3.9),
- a phase advance between the BBLR1 and the BBLR2 equipment of 3° : it is the phase shift between the LHC long-range encounters and the slot that has been already assigned for the installation of the wire compensator in the LHC tunnel.

In Fig. 4.22 and 4.23 we show the actual optics function (the β -functions and phase advances) at the wire positions.

The horizontal dispersion at the wire position is ≈ -0.6 m while there is no vertical dispersion. For the normalization of the beam-wire separation we use the vertical beam σ therefore the dispersion does not play any role in the setting of the experiment. Regarding the experiment results, the horizontal dispersion together with the r.m.s. off-momentum of the beam are small to change in a significant way the transverse aspect ratio of the beam itself.

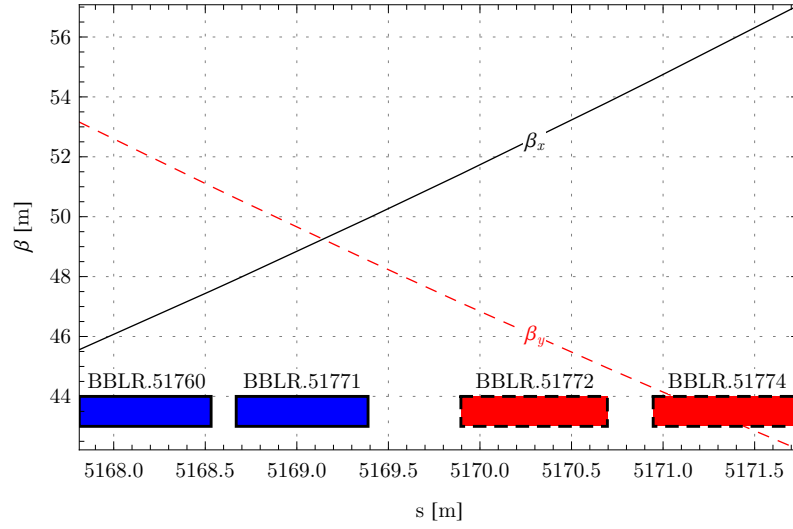


Figure 4.22: The β -functions at the SPS wire positions. The colored rectangles represent the position of the boxes containing the wires.

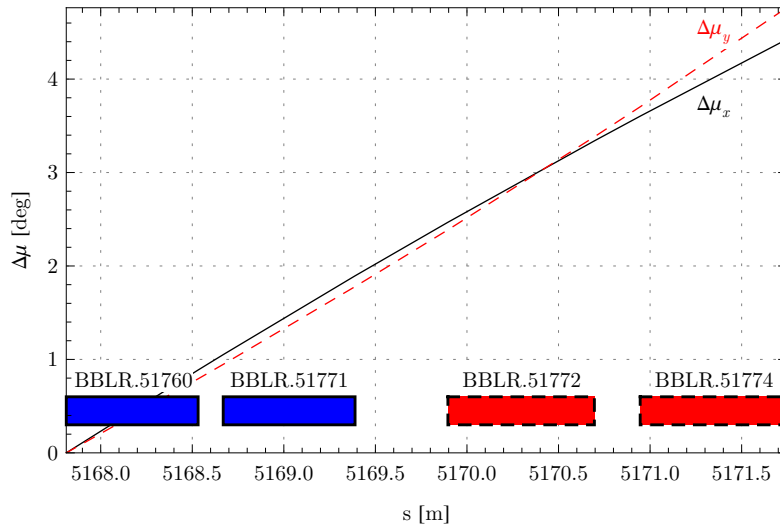


Figure 4.23: The phase advances at the SPS wire positions. The colored rectangles represent the position of the boxes containing the wires.

The orbit correction and the emittance blow-up

During the wire experiments of the last two years, three different beam momenta have been used during the experiments: 37, 55 and 120 GeV/c. This was important to test the scaling laws (see Section 3.2.3) and, therefore, to rescale the SPS behavior to the LHC machine. These three energies correspond to the three different cycles shown in Fig. 4.24: it is important to note that the measurements were done, within a

specific cycle, at constant energy, generally the higher constant energy of the cycle (referred also as *flat-top*). The length of the period of observation ranges for each cycle between ≈ 1.5 and ≈ 6 s. Differently from the others, with the cycle at 120 GeV/c it is possible to store the beam in the machine for hours: the beam, instead of being dumped at the end of the cycle, can be kept in the machine at constant energy (*coast*). This allows us, for the first time in the SPS, to study the beam-wire interaction in a longer time-window (≈ 30 min).

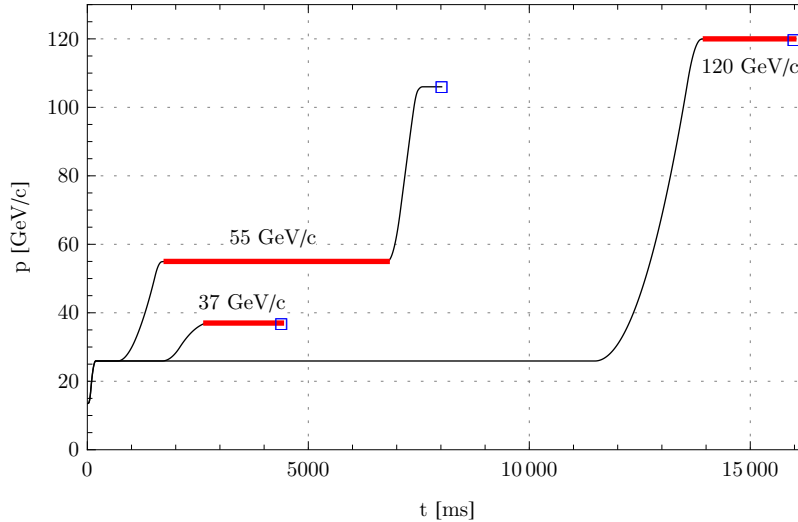


Figure 4.24: The three SPS cycles used during the 2008 and 2009 wire experiments at the SPS. The measurements are done on the flat-top (red thick lines).

Increasing the beam energy has a beneficial effect on the beam lifetime. This is due to the fact that the machine is more stable, i.e., the ripple of the power supplies of the main magnets get reduced and the machine, due to the “adiabatic shrinking” of the beam emittance [22], has an increased admittance. In addition to that, the oscillation of the orbit due to the injection phase are completely stabilized after the acceleration and, in general, the effect of the non linearities of the lattice magnet is minimized.

A long beam lifetime is the ideal condition to study the impact of the wires on the beam because the wire effect appears completely isolated by all the other uncontrollable non-linearities of the machine. Nevertheless, as we reported in the previous section, the separation between the beam and the wire is mainly set by modifying the beam closed orbit. Therefore, by increasing the magnetic rigidity of the beam, the steering of the orbit requires a corresponding increase in the strength of the orbit correctors. The SPS orbit correctors are dimensioned for the injection energy ($p = 26$ GeV/c) and are already too weak at 120 GeV/c. In addition to that, at higher energy, the beam size gets smaller and since the normalized separation between the beam and the wire has to stay constant we need a larger correction of the closed orbit (larger bump).

In practice, using the orbit correctors at their maximum current (3.5 A [61]), they provide a kick of $\approx 100 \mu\text{rad}$ for a proton beam at 55 GeV/c. At this energy, the maximum offset of the closed orbit that can be reached by using three orbit correctors (called π -bump for the specific phase advance between the first and the third correctors) is ≈ 6 mm at the wire position (see Fig. 4.25). Using five correctors ($\pi + 3\pi$ bump) the beam can be moved twice further (≈ 13 mm, see Fig. 4.25). This is the limit of the correction used during the experiments: even using more of five orbit correctors or, if possible, increasing their current beyond 3.5 A, the slope of the bump, that is its variation along the longitudinal coordinate, s , would increase and the beam-wire separation would vary significantly along the wire itself. Adding to this effect the behavior of the β -function, the normalized beam-wire separation would vary significantly along the wire ($> 1 \sigma$ at the LHC normalized emittance) with a consequent reduction of the clearness in the experimental results. To solve this problem the installation of additional strong orbit correctors in the proximity of the wires was considered but, due to room constraints, we did not find a viable solution.

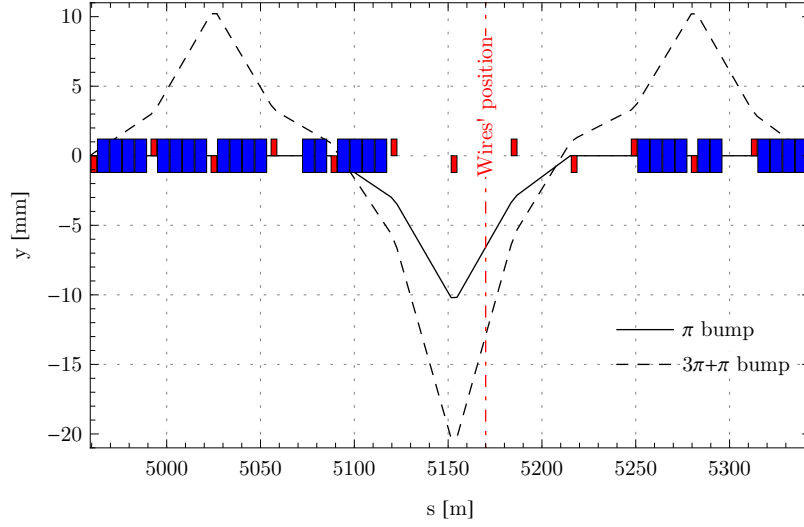


Figure 4.25: The orbit correction at 55 GeV/c. We show the bump using 3 orbit correctors (π bump) and the one using 5 orbit correctors ($3\pi + \pi$ bump). The two bumps are computed considering that the maximum current of the correctors is 3.5 A. The offset of the closed orbit is, respectively, ≈ 6 and ≈ 13 mm at the position of the wires (red dotted line).

A completely different approach to reduce the normalized separation between the beam and the wire is to increase the beam emittance by a controlled transverse emittance blow-up [62]: this is a procedure that allows to transfer energy to the beam transverse plane using a device that interacts with the beam at its betatron frequency or with a white noise excitation. In the case of the SPS, the transverse feedback system has been adapted to this purpose. Differently for the orbit correction, the emittance blow-up can keep the normalized separation beam-wire constant for all the length of the wire. Its main drawbacks are:

- the increased complexity of the experiment since its setting procedures are more complicated than the steering of the beam orbit,
- at larger beam emittance, more wire current is required in order to reproduce a fixed number of long-range beam-beam interactions (see scaling laws in Section 3.2.3),
- the beam lifetime may be reduced partly offsetting the advantage of the higher beam energy. This is primarily due to the reduction of effective aperture of the machine due to the increase of the beam emittance.

To preserve the round aspect ratio of the beam we have to increase both the horizontal and the vertical emittance. Due to the present hardware constraint of the transverse feedback system it is not possible to increase the emittances of the two planes at the same time. In practice we increase the emittance in the vertical plane and, crossing the diagonal resonance by moving the machine tune, we redistribute equally the emittances in the two planes.

In order to have a greater flexibility during the experiments we combined the two methods (orbit steering and emittance blow-up). In Fig. 4.26 we show as function of the normalized emittance of the beam, the minimum normalized beam-wire separation for a maximum amplitude $3\pi + \pi$ bump and for the BBLR1 wires. Without emittance blow-up the normalized emittance of the SPS beam, for low intensity bunches, range between 1 and 2 $\mu\text{m}\cdot\text{rad}$. This means that it is easy to reach the 5σ separation with the beam at 55 GeV/c but going below 7σ separation at 120 GeV/c appears difficult. It would require an increase of emittance by a factor larger than 5, that appears already an ambitious target.

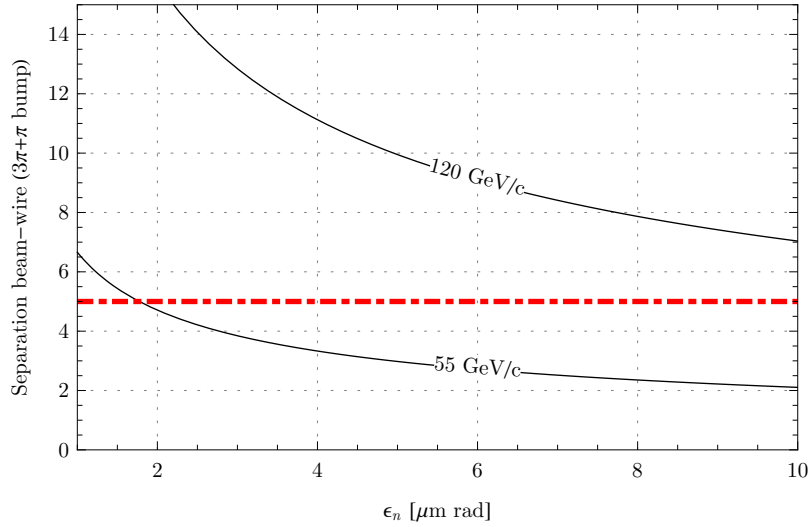


Figure 4.26: The minimum normalized beam-wire separation for different values of normalized emittance and beam rigidity assuming a $3\pi + \pi$ bump of Fig. 4.25 and for the BBLR1 equipment. We are interested to reach the minimum separation of 5σ in order to investigate the Early Separation Scheme condition but, for the 120 GeV/c cycle, the reasonable limit appears to be $8 - 7\sigma$. This implies a normalized emittance of $8 - 10 \mu\text{m}\cdot\text{rad}$: it corresponds to an emittance blow-up by a factor four assuming an initial normalized emittance of $2 \mu\text{m}\cdot\text{rad}$.

The settings of the experiment

The beam used during the experiment consists of 4 bunches with an intensities of $5 - 6 \cdot 10^{10}$ protons per bunch. In Fig. 4.27 we show a typical signal recorded from the Fast Beam Current Transformer (FBCT) monitor showing the bunch pattern of the beam. This value comes from the compromise between the need of a sufficiently strong signal to reduce the noise of the measurements and the minimization of the risk and the irradiation of the SPS equipment related to the beam losses induced by the wire.

The main observable we use in the experiment is the beam current measured with the high SPS Beam Current Transformer (BCT). More specifically, we observe the decay rate of the beam current as function of the wire position and its current. Without the wire excitation we have, in general, a very long beam lifetime (≈ 1 h, see Fig. 4.28). The beam lifetime, τ_b , is the time the beam current, I_b , takes to reduce by a factor $1/e$. If $\Delta t \ll \tau_b$, we can linearize the problem considering

$$\tau_b = \frac{I_b \Delta t}{\Delta I_b} \quad (4.1)$$

where the initial beam current is reduced by an amount $\Delta I_b > 0$ in the time interval Δt .

Before each experiment, after having chosen the operating tunes, we measured the beam emittances and depending on our specific needs we set-up the emittance blow-up. We then start the calibration of the wire position. This is needed since the signal accuracy of the Beam Position Monitors (BPM's) is insufficient for our needs: they can be used for relative measurements (i.e., the orbit bumps) but not to measure the absolute closed orbit and therefore the distance between the wires and the beam. In order to measure it, two methods are possible:

- measuring the effect of the wire on the beam closed orbit,
- measuring the effect of the wire on the beam tunes.

We used the second method because much more sensitive with the present instrumentation.

The formula that relates the distance of the beam-wire, d , to tune shift, $\Delta Q_{x,y}$, can be derived recalling

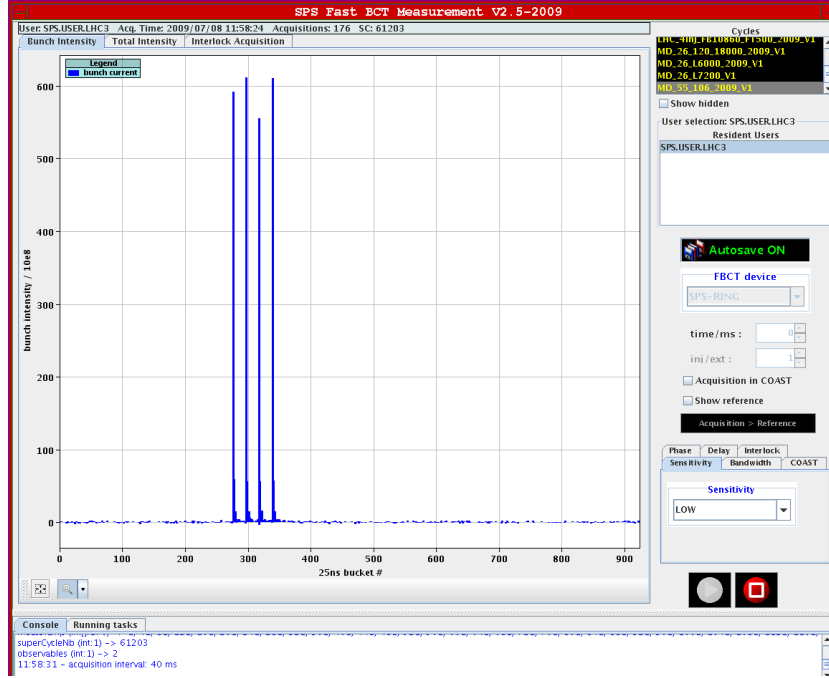


Figure 4.27: The beam structure used in the SPS experiment observed from the monitor of Fast Beam Current Transformer: four bunches with $5 - 6 \cdot 10^{10}$ protons per bunch.



Figure 4.28: An example of beam current behavior during the SPS experiments observed from the monitor of the Beam Current Transformer: the losses corresponds to the injection an acceleration phase, on the flat-top there is not significant loss on this scale and the beam lifetime is good. The two curves represent two consecutive turns: we can infer that the reproducibility of the machine, in that condition, was good.

the Eq. 3.8

$$\Delta Q_{x,y} = \pm \frac{1}{4\pi} \int \Delta K_{x,y}(t) \beta_{x,y}(t) dt \quad \text{where} \quad \Delta K_{x,y} = \frac{1}{B\rho} \frac{dB_{y,x}}{dx, y} \quad (4.2)$$

where the value of the derivative of the field have to be computed on the beam closed orbit, $B\rho$ is the beam magnetic rigidity and $B_{y,x}$ is the magnetic y or x -component of the field of the wire in the reference frame centered on the beam closed orbit: we refer to this reference frame. In the following we consider a vertical wire, i.e., positioned in $(0, d)$. For a wire carrying the DC current I_w , we have

$$B_x(0, y) = \frac{\mu_0 I_w}{2\pi(d-y)}, \quad \text{then} \quad \left. \frac{dB_x}{dy} \right|_{(0,0)} = \frac{\mu_0 I_w}{2\pi d^2} \left(= \left. \frac{dB_y}{dx} \right|_{(0,0)} \right). \quad (4.3)$$

Replacing the Eq. 4.3 in the Eq. 4.2, assuming that the β -functions are constant along the wire's length, l_w , and neglecting the fringe field effect of the wire, we have

$$\Delta Q_{x,y} = \pm \frac{\mu_0 I_w l_w \beta_{x,y}}{8 \pi^2 B\rho d^2}. \quad (4.4)$$

The module of the tune shift in the two planes is the same if $\beta_x = \beta_y$. As an example we plot in Fig. 4.29 the dependence of $|\Delta Q_{x,y}|$ with respect to d at $p = 55$ GeV/c for the second wire of the BBLR1. The noise of the tune meter measurements is at the $5 \cdot 10^{-4}$ level (recording 4096 turns). Since the tune shift we are interested in are at the 10^{-3} level (see Fig. 4.29) we have to maximize the wire effect using a large wire current or moving the beam toward the wire. Increasing the number of turns recorded by the tune meters would not increase by a significant amount the precision of the measurement due to the damping of the betatron oscillations (decoherence) of the beam induced by the machine chromaticity.

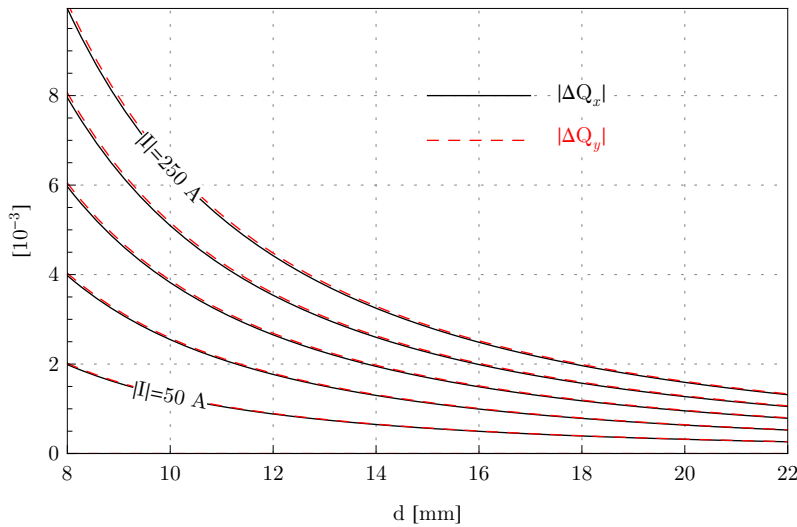


Figure 4.29: The dependence of $\Delta Q_{x,y}$ with respect to d at $p = 55$ GeV/c for the second wire of the BBLR1.

4.2.2 Experiments at 37 GeV/c

In the three following sections we analyze the results of the beam-wire experiments done in the SPS during the last two years. The results obtained in 2008 refers to a beam rigidity of 37 GeV/c while in 2009 we did measurements at 55 and 120 GeV/c.

The experiment consist in observing the beam current decay under the wire influence. During the measurement we vary, mainly, three parameters: the tunes, the position of the wire and the current of the wire. In general we vary a single parameter between a consecutive set of measurements obtaining, respectively,

- a tune scan,
- a current scan,

- a distance scan.

In general, after having changed the desired parameter, all the others are affected by the beam-wire interaction (e.g., if we change the wire current, the beam tunes and the beam-wire separation change). For this reason, we perform at each step of the scan a correction on the two parameters that have to stay constant.

We mainly report the results of the excitation experiments, that is the experiment in which we use only one (BBLR1) out of the two wire equipments installed in the SPS. In addition to the wire excitation experiments, we participated to long-range beam-beam compensation experiments where both the wire sets (BBLR1 and BBLR2) are powered and the positions and the current of the BBLR2 are optimized to compensate the effect of the BBLR1. Most part of the compensation experiments are described in [58].

Current scan experiments

In Fig. 4.30 we show four different scans of wire current done during an excitation experiment at 37 GeV/c. The four curves correspond to four different normalized separations between the beam and the wire: 9.5 (nominal beam separation in LHC), 7, 6, and 5 σ . As represented in Fig. 4.24 the flat-top at 37 GeV/c is extremely short (less than 2 s). Since part of the time is used for the ramping of the wire current, in reality, the observation time reduces to ≈ 1.1 s. The y -axis in Fig. 4.30 refers to the beam loss between the start and the end of this short interval. The tunes of the measurement corresponds to the nominal LHC tune (0.31, 0.32). We move the SPS tunes to the LHC ones during the ramp from 26 to 37 GeV/c (see Fig. 4.24) and, crossing some low order resonances, we blow up the beam normalized emittance up to 6 $\mu\text{m}\cdot\text{rad}$: in this situation we can easily reduce the beam wire separation to 5 σ using only three orbit correctors (π -bump, see Fig. 4.26).

The dependence of the losses with the wire current appears to be parabolic while their dependence with respect to the beam-wire separation is almost exponential. We propose the following numerical fit for the losses (dashed lines in Fig. 4.30)

$$\text{SPS beam losses } [\%/s] = 0.07 e^{-d_n} I_w^2 \quad (4.5)$$

where d_n is the beam-wire normalized distance (respect to σ_y) and the I_w is the wire current in SI units.

From Fig. 4.30, within the accuracy of the measurement, $2 \times 5 \sigma$ beam-beam long-range encounters can be tolerated.

A Early Separation Scheme requiring 12 encounters (at the ultimate bunch intensity, $N_b = 1.7 \cdot 10^{11}$ ppb) are mimicked by the wires for a current of 125 A. This configuration produces a beam losses between $\approx 10 \%$ in 1.1 s: a similar loss rate would be incompatible with LHC operation whose present collimation system is designed to handle a maximum loss of 1% of the beam in 10 s [63]. Nevertheless, the SPS losses cannot be *directly* extended to the LHC for the following reasons:

- the LHC encounters do not add all in phase, since there is a specific phase advance between the ATLAS and the CMS experiment. In the same interaction region, the beam-beam kicks add almost in phase,
- the SPS wire introduces a limitation in the mechanical aperture at 5 σ while the beam interaction does not,
- the revolution frequency of the SPS beam is about four time larger than the LHC one, therefore (see Section 3.2.3) the beam losses in the LHC are about four time slower (for an equivalent beam dynamics),
- the particle distribution of the LHC beam can be significantly different from the one of SPS.

From the previous consideration we can expect lower beam losses in the sLHC. Anyhow we have to consider that the head-on collisions and all the other long-range collisions (see Fig. 4.15) are not taken into account in the SPS experiment and that the non-linearities and chromatic aberration of the LHC lattice at collision energy are expected to be larger than those of the SPS: their contribution may modify the beam losses.

It is worth completing the information given in Fig. 4.30 recalling that, when the SPS ring operated as proton-antiproton collider (Sp $\bar{\text{p}}$ S), it had the separation patterns represented in Fig. 4.31 [42, 64]. At the injection energy (26 GeV) there were twelve encounters with a separation between 2 and 4 σ . At the collision energy (315 GeV), apart the three head-on collisions, the separation scheme was modified to increase the beam lifetime (too low with the separation pattern of the injection). There were 7 encounters at 6 σ , one at 3.5 σ and an other at 9 σ . In this situation the beam lifetime and the background in the experiments were compatible with the operations. It is important to remember that the intensity of the proton was $1.7 \cdot 10^{11}$ proton per bunch, i.e., the ultimate LHC intensity, and the normalized emittance of the beams ranged between 3.75 – 5 $\mu\text{m}\cdot\text{rad}$, that is, in average, larger than the LHC one. A larger normalized emittance,

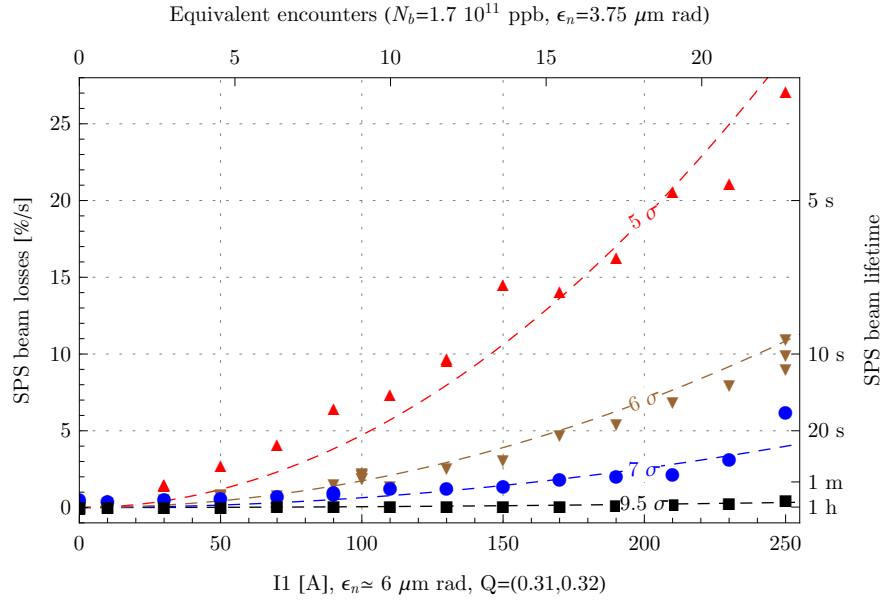


Figure 4.30: The beam losses induced by the wire versus wire current and for four different beam-wire separation. Only the BBLR1 is used ($I_2=0$).

ϵ_n , as explained in Sec. 3.2.3, implies that the effective strength of the beam interaction is lower (e.g., 7 encounters with $\epsilon_n = 4.35 \mu\text{m}\cdot\text{rad}$ correspond to 6 encounters with $\epsilon_n = 3.75 \mu\text{m}\cdot\text{rad}$, at the same normalized separation).

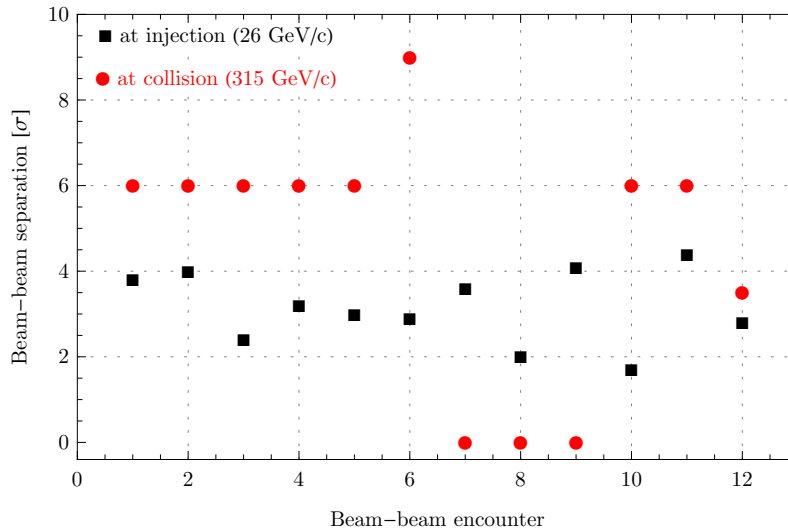


Figure 4.31: The Sp̄pS beam separation pattern.

The Sp̄pS example shows that, rescaling to the LHC emittance, 6 encounters at 6σ have been tolerated in SPS ring while our results show a beam loss rate of $\approx 1 \text{ %/s}$ (Fig. 4.30), in contradiction with the Sp̄pS experience.

The Sp \bar{p} S encounters were not in phase while the excitation of the wire, being concentrated in one point of the ring, mimics several beam-beam interaction adding all in phase. In order to investigate the effect that the phase advance has on the beam-beam effect, it is possible to study the dependence of the beam losses with the machine tune: this is equivalent to changing the phase advance of the wire excitations between two consecutive turns. As shown in the Section 4.1.3 we expected, from the simulations of the Early Separation Scheme, a dependence of the dynamic aperture of the machine with respect to the tune. The results of the experiments are reported in the following section.

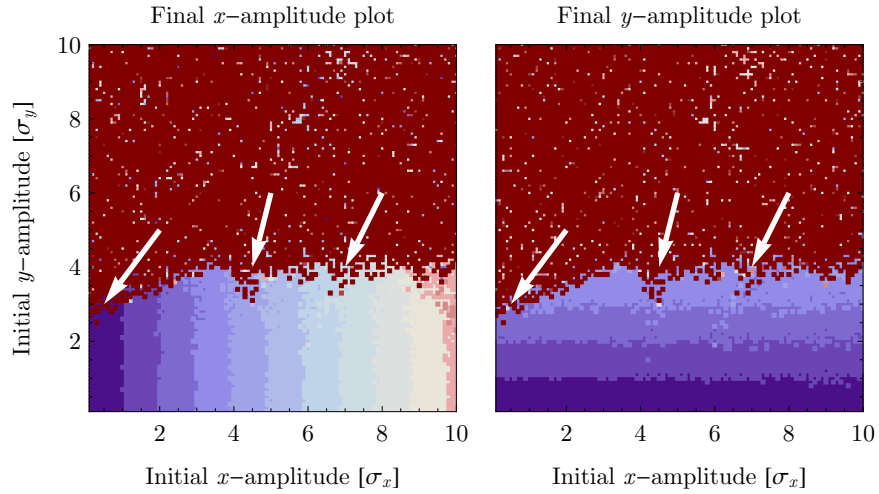


Figure 4.32: The dynamic aperture simulated at (0.31, 0.32) considering a vertical wire at 5σ with an equivalent strength of 12 BBLR's at ultimate bunch current. The arrows indicate three extraction directions: the particle lying on these lines increase their amplitudes.

We reproduce in simulation one point of this SPS experiment: in Fig. 4.32 we show the amplitude plane after $3 \cdot 10^5$ of a simulation with working point (0.31, 0.32) and with the wire powered to mimic 12 encounters at 5σ (it corresponds to $I_1 \approx 125$ A). The impact of the wire is evident. It is important to compare this results with the one shown in Fig. 4.17, *bottom* for the Early Separation Scheme in LHC upgrade: in both we have the same total number of encounters at 12σ and the same tunes. In the sLHC simulation, we consider, in addition, the two head-on and the 48 long-range collisions at 12σ . The nominal phase advance between the Interaction Point 1 and 5 is also taken into account: the dynamic aperture of sLHC simulations appears significantly larger than in the SPS case, most likely related to the difference of the field of an actual beam and its wire simulator. This consideration, together the Sp \bar{p} S data, suggests that the beam losses observed in SPS and rescaled to sLHC (dividing by four the beam loss rate) are too pessimistic.

Tune scan experiments

In Fig. 4.33 we present the results of a tune scan during a wire excitation experiment with 5σ beam-wire separation: the horizontal tune is kept constant at 0.31 while the vertical one varies between 0.275 and 0.32. For comparison, two points for the beam losses with no current in the wire are shown: the wire effect is evident. The second wire set (BBLR2) is switched off while the BBLR1 is powered with 250 A, that corresponds, for a normalized emittance of about $6\mu\text{m}\cdot\text{rad}$, to ≈ 23 long-range encounters at the ultimate bunch population ($N_b = 1.7 \cdot 10^{11}$ ppb). It is worth to note that the beam losses found in this second measurements for the tunes (0.31, 0.32) are consistent with the values in Fig. 4.30 and are a measure of the reproducibility of the machine.

From the results shown in Fig. 4.33, we observe that there is a strong tune dependence of the beam losses: the variation of the beam losses can be larger than a factor 15 (from $\approx 1.5\%$, $Q_y = 0.285$, to $\approx 25\%$, $Q_y = 0.32$). The relative maximum of the beam losses appears in the proximity of the 3rd, $Q_y = 1/3$, and 4th, $Q_y = 1/4$, order resonances while the absolute maximum, in the explored range, corresponds to the LHC nominal tune ($Q_x = 0.31$, $Q_y = 0.32$).

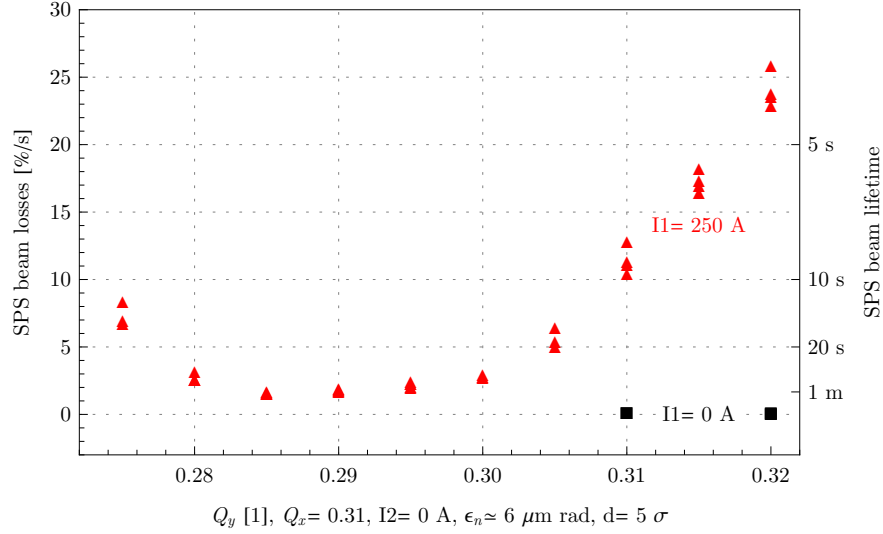


Figure 4.33: The losses due to the wire changing the vertical tune. For $I_1 = 250$ A it corresponds to 23 encounters at ultimate bunch current.

In Fig. 4.34 we show a tune scan done in an excitation (BBLR1 only powered) and compensation (BBLR1 and BBLR2 powered) experiment. The beam-wire separation is 9σ and the normalized emittance is $1.8\mu\text{m}\cdot\text{rad}$. In the plot some points with no wire excitation are present to show the noise level of the measurement and its dependence on the tune. On this scale there are almost no beam losses without excitation. Even in this case of larger separation, we observe a strong dependence of the losses on the vertical tune and this dependence is very similar to the one plotted in Fig. 4.33 although the condition of the experiment are significantly different in term of beam-wire separation and beam emittance. The only exception is for the point with the tune (0.31, 0.31): this is most likely due to different coupling strength between the transverse planes during the two experiments. The best compensation is obtained by powering the second wire with 210 A while the first one has a current of 250 A: its positive effect is evident from Fig. 4.34. The fact that we need less current in the BBLR2 than the one in BBLR1 and the unexpected dependence of the compensation on the tune have to be still understood: some possible causes are related to errors in the separation between the BBLR2 elements and the wire or to the different aspect ratio of the beam at the BBLR1 and at the BBLR2.

Distance scan experiments

We plot in Fig. 4.35 three distance scans done during a wire excitation experiment where we consider three different tunes in a larger range than the one shown in Figs. 4.33 and 4.34. The BBLR1 is powered with 250 A (corresponding to ≈ 23 equivalent LHC encounters for the ultimate intensities, $N_b = 1.7 \cdot 10^{11}$ ppb, and the nominal normalized emittance, $\epsilon_n = 3.75\mu\text{m}\cdot\text{rad}$) while the BBLR2 is switched off. We considered the following three tunes (0.31, 0.29), (0.12, 0.16) and (0.234, 0.226). The tune (0.31, 0.29) behaves similarly to (0.12, 0.16) and much better than (0.234, 0.226).

This dependence of the beam losses on the tune can be qualitatively predicted by our simulations: in Fig. 4.37 we show the dynamic aperture in the amplitude plane for the three mentioned tunes. For convenience, the strength of the excitation considered in the simulations corresponds to 12 long-range encounters with the LHC ultimate bunch population ($N_b = 1.7 \cdot 10^{11}$ ppb). This is equivalent, for a normalized emittance of $6\mu\text{m}\cdot\text{rad}$, to a wire current of 125 A (half of the one used during the experiment of Fig. 4.35). The beam-wire separation assumed in the simulation is 5σ .

Like the experimental result, the dynamic aperture are similar in the *top* and *middle* plots of Fig. 4.37 that correspond, respectively, to the tunes (0.31, 0.29) and (0.12, 0.16). The *bottom* plot refers to the tune

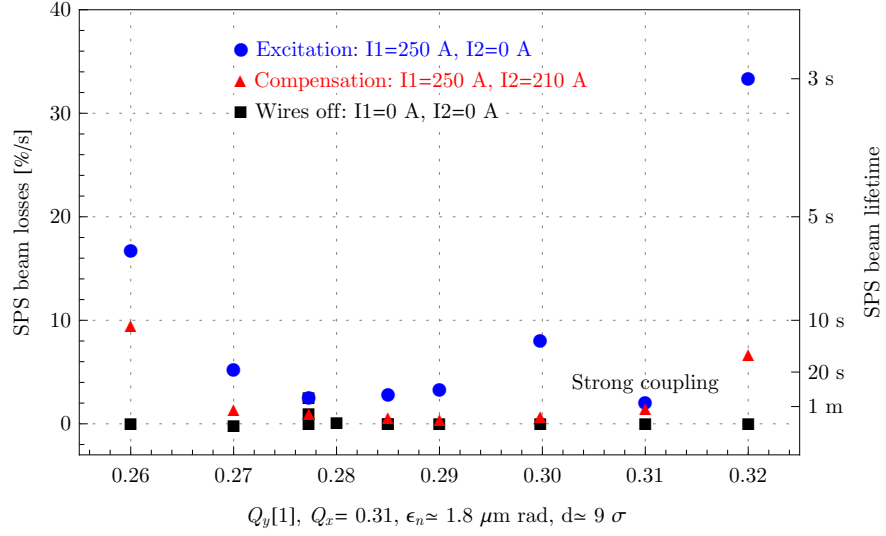


Figure 4.34: This experiment confirms that the best vertical tunes of the SPS for minimizing the losses ranges between 0.28 and 0.29. It is worth noting that this is true even with a significant change of the normalized emittance and the beam-wire separation (see Fig. 4.33). For $I_1 = 250$ A it corresponds to 77 encounters at ultimate bunch current.

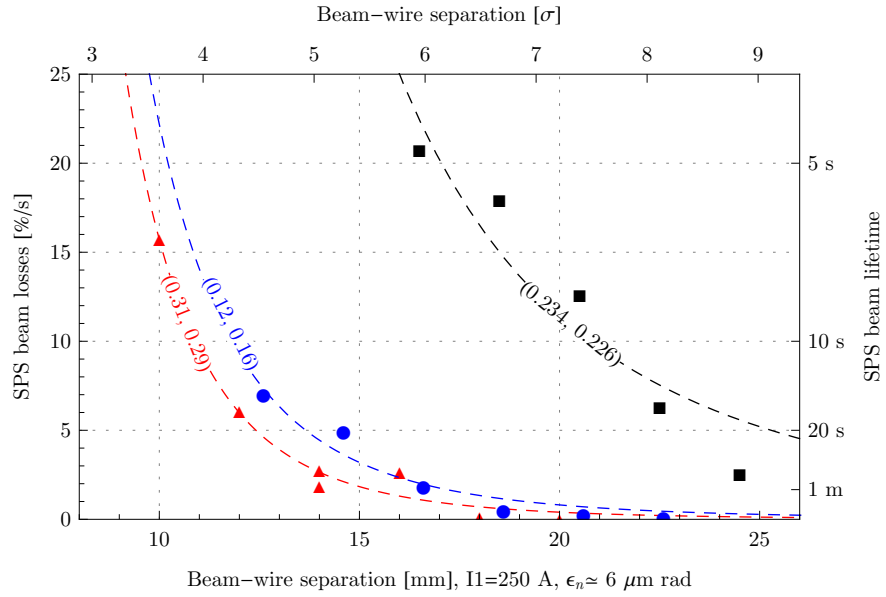


Figure 4.35: Three distance scans are shown considering three different tunes: (0.31, 0.29), (0.12, 0.16) and (0.234, 0.226). This result confirms, on one hand, that the vertical tune between 0.28 and 0.29 reduces the effect of the beam-beam interaction even varying the tunes in range larger than the one explored in Figs. 4.33 and 4.34. On the other hand, the reduction the beam-wire separation increase rapidly the beam losses. For $I_1 = 250$ A, the wire corresponds to 23 encounters at ultimate bunch current.

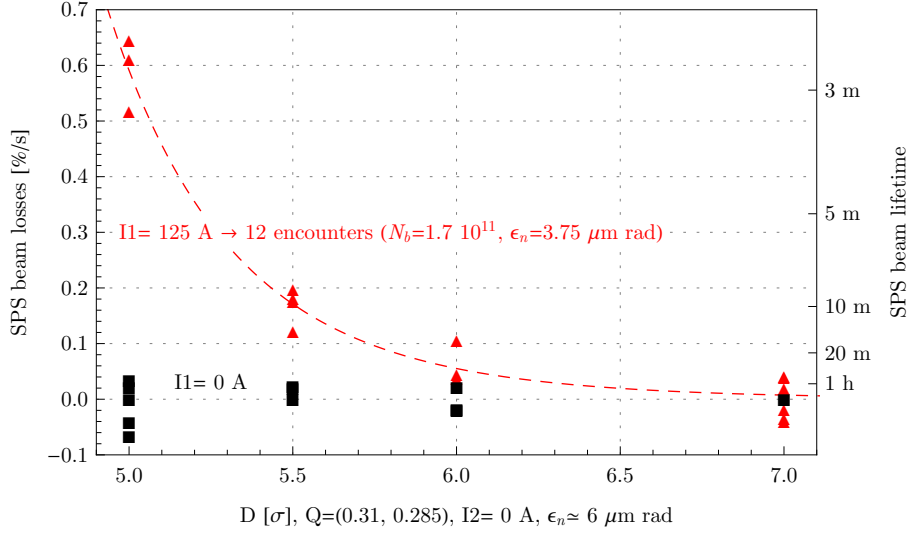


Figure 4.36: The losses induced by the wire varying the separation beam-wire with the optimized vertical tune.

(0.234, 0.226) and features a strong extraction mechanism at the edge of the beam core (see Fig. 4.6, *right*). This agrees with the increase of the beam losses observed for that particular choice of tunes (Fig. 4.35).

As last measurement at 37 GeV/c we reproduced a beam-wire distance scan between 5 and 7 σ at the tune (0.3125, 0.285). From all the previous results this tune seems to be the best one in our case. The results are plotted in Fig. 4.36 (note the change of vertical scale). It is possible to observe again a significant increase of the losses while reducing the beam-wire separation. The value with no excitation is plotted to show that the noise signal is small compared the beam losses induced by the wire. We observe no perturbation at 7 σ beam-wire separation and modest losses at 6 σ , possibly dominated by the aperture restriction due to the wire. The maximum observed loss rate is $\approx 0.7\%/s$ and corresponds to the minimum separation considered (5 σ).

Rescaling the problem to the LHC (we have to consider a factor ≈ 4 due to the difference of the bunch frequency in the two machines) it would correspond to $0.2\%/s$. On one hand this value, that does not consider the other head-on and long-range interaction that will take place in the sLHC, would be still too high for a safe operation of the machine. On the other hand from the simulations (compare Fig. 4.17, *bottom* and 4.32), supported by the Sp \bar{p} S experience, we can conclude that the wire approximation together with the sum in phase of all the parasitic interactions reproduce a more severe excitation than the actual beam-beams effect.

4.2.3 Experiments at 55 GeV/c

During the excitation experiments at 55 GeV/c the cabling of the wires is changed: only half of the wires is powered. This allows, on one hand, a better control of the beam-wire separation, but on the other hand, it implies the halving of the integrated strength of the wire. In the following this factor is taken into account when we convert a given current in the wire in an equivalent number of long-range encounters.

As we can see in Fig 4.24, considering the SPS cycle a 55 GeV/c has the advantage to extend by more than a factor 3 the duration of the flat-top with respect to the 37 GeV/c cycle. This corresponds to a longer observation time, Δt , of the beam decay: in this condition we prefer to express the effect of the wire on the beam in term of beam lifetime instead of considering the beam losses (see Section 4.2.2). Nevertheless estimating a beam lifetime of the order of hours in few seconds of data acquisition implies large error bars. Therefore multiple measurements of the same experimental condition are necessary to acquire a reasonable statistics.

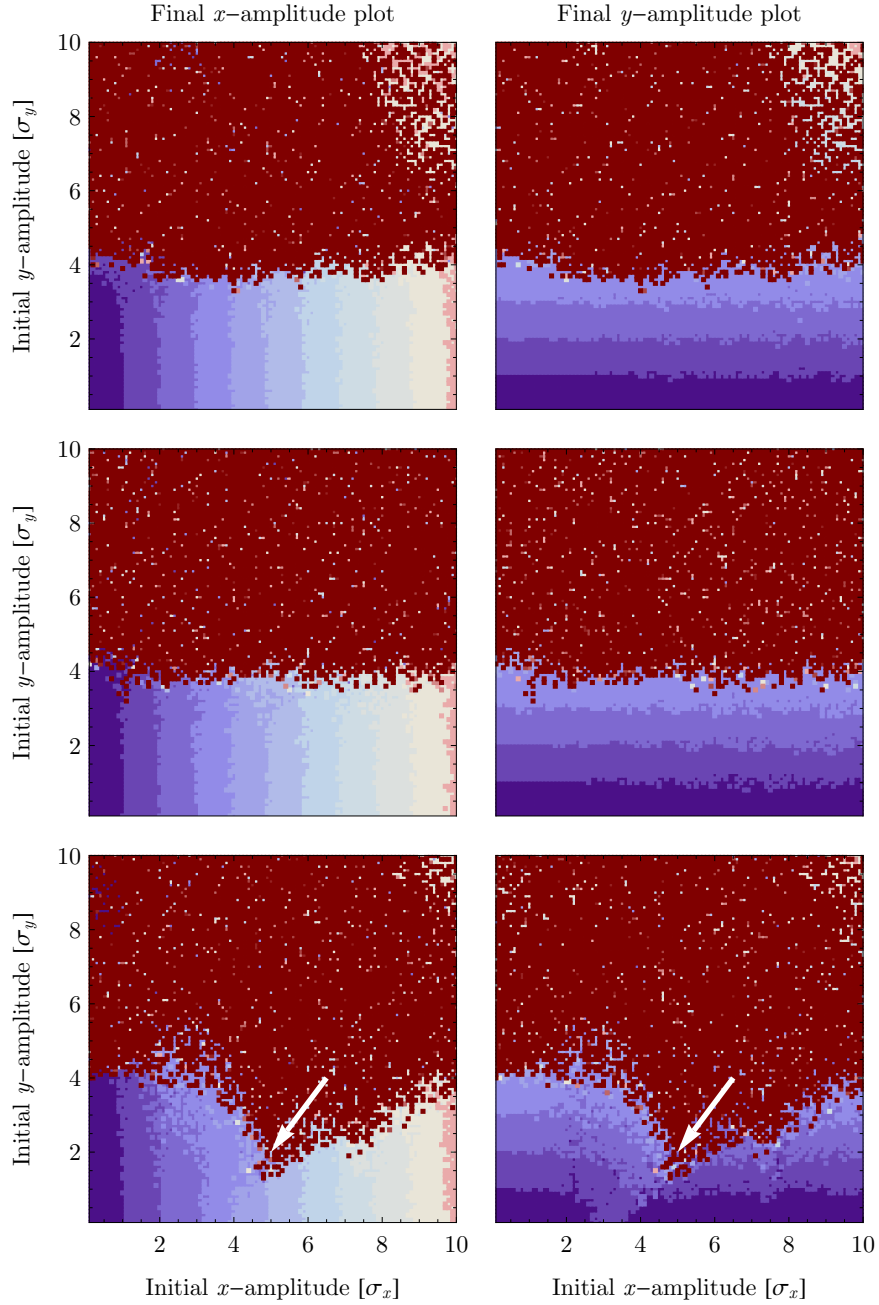


Figure 4.37: The results of the simulations of the dynamic aperture assuming a vertical wire at 5σ with an equivalent strength of 12 beam-beam long-range encounters at ultimate bunch current. The *top*, *middle*, *bottom* plots correspond, respectively, to the tunes $(0.31, 0.29)$, $(0.12, 0.16)$ and $(0.234, 0.226)$. The simulations show a similar behavior for the tune $(0.31, 0.29)$, $(0.12, 0.16)$ and a worsening of the dynamic aperture for the tune $(0.234, 0.226)$ where a strong extraction mechanism takes place, perturbing directly the core of the beam (see arrow). This is, qualitatively, in agreement with the experimental observations (see Fig. 4.35).

Distance scan experiment

In Fig. 4.38 we show a distance scan compared to the 37 GeV/c results at the tunes $(0.31, 0.28)$. In the distance scan at 55 GeV/c and 37 GeV/c, the wire current is equivalent, respectively, to ≈ 35 and 12 beam-beam encounters at ultimate LHC bunch current ($N_b = 1.7 \cdot 10^{11}$ ppb) and nominal normalized emittance ($\epsilon_n = 3.75 \mu\text{m}\cdot\text{rad}$): apart from the different beam emittance of the two experiments ($\epsilon_n \simeq 1.5 \mu\text{m}\cdot\text{rad}$ at

55 GeV/c and $\epsilon_n \simeq 6 \mu\text{m}\cdot\text{rad}$ at 37 GeV/c) and the different current on the wire ($I_1 = 200 \text{ A}$ at 55 GeV/c and $I_1 = 125 \text{ A}$ at 37 GeV/c), only half of the length of the wire is used at 55 GeV/c. The equivalent wire excitation at 55 GeV/c is therefore three times stronger than the one at 37 GeV/c (see scaling law Section 3.2.3). Due to the limit on the maximum magnetic field of the SPS orbit correctors we could not reduce the separation below 5.5σ (see Fig. 4.26).

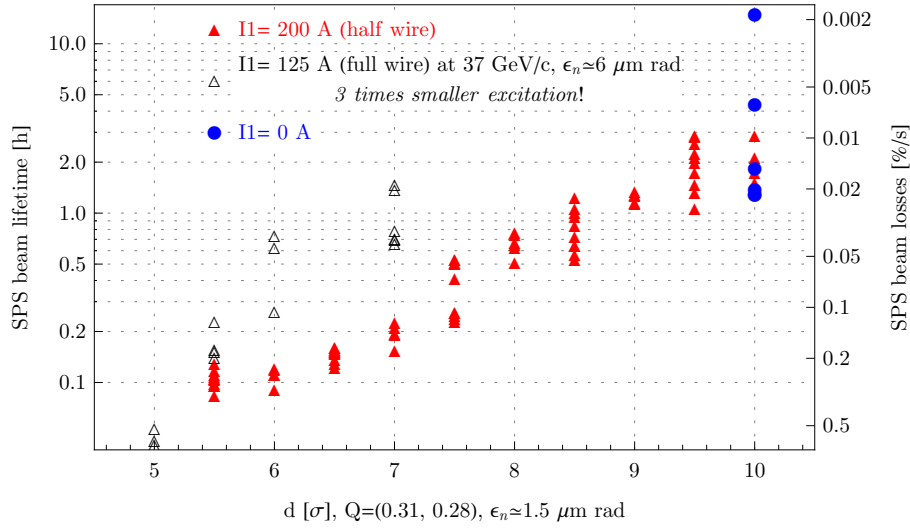


Figure 4.38: The losses induced by the wire varying the separation beam-wire with the optimized vertical tune (55 GeV/c). The $I_1=200 \text{ A}$ on half of the BBLR1 length is equivalent to ≈ 35 encounters at the ultimate bunch current (≈ 52 encounters at the nominal bunch current).

From Fig. 4.38 it is possible to observe that the beam lifetime, without wire excitation, is of the order of hours.

The fast dependence of the wire effect on the beam-wire separation is evident also at 55 GeV/c: the beam lifetime is reduced exponentially (linearly in the log-scale) in good agreement with the fitting proposed for Fig. 4.30 in Eq. 4.5.

The points at 9.5σ of Fig. 4.38 have a beam lifetime comparable to the lower range of the one with vanishing excitation: the wire current corresponds to ≈ 52 encounters at the nominal bunch charge (in fact, 35 encounters at $N_b = 1.7 \cdot 10^{11}$ ppb correspond to ≈ 52 encounters at $N_b = 1.15 \cdot 10^{11}$ ppb, i.e., the nominal LHC bunch charge), very similar to the long-range LHC excitation with the two interaction points adding in phase.

The beam losses at 55 GeV/c are, in general, larger than the ones at 37 GeV/c: this is consistent with the three time larger equivalent strength of the excitation. Nevertheless comparing the result obtained at 55 GeV/c with those at 37 GeV/c (Fig. 4.36) potential inconsistencies emerge. Considering the scaling with emittance and the fact that at 55 GeV/c only half of the length of the wire is used, the excitation at 37 GeV/c is three times weaker than the one at 55 GeV/c: only 12 equivalent parasitic encounters at the ultimate bunch charge with respect to the 35 of the experiment done at 55 GeV/c. The measurements done at the two energies tend to cross at the normalized distance of 5.5σ (Fig. 4.36), while we would expect, due to the lower excitation, to have always a better behavior at 37 GeV/c. As we will discuss later, this is probably due to the different profile of the beam and the different physical aperture of the machine in the two experiments.

Current scan experiment

In Fig. 4.39 we report the results of a current scan experiment at 55 GeV/c with tunes (0.31, 0.28). The current scan is performed with a beam-wire separation of 5 and 7 σ . For comparison we put on the plot the

losses measured for at 55 GeV/c for the same beam-wire separation (5 and 7 σ , see Fig. ref). We rescale the wire excitation passing from 37 GeV/c to 55 GeV/c: at 37 GeV/c the normalized emittance of the beam was 2 times larger than the one at 55 GeV/c but, at 55 GeV/c, we used only half of the wire length, i.e., half the integrated current. From the scaling laws, it yields that we can compare directly the results since the equivalent strength of the wire is the same. Even if the vertical tune of the measure at 37 GeV/c is 0.285 instead of 0.28 we consider negligible this difference as the tune scans at 37 GeV/c show (see Figs. 4.33 and 4.34).

In Fig. 4.39 we show, in addition, a result that qualitatively confirms the scaling law on the normalized emittance (Eq. 3.42). We make two current scans at 7 σ with two different normalized emittances (3 and 2 $\mu\text{m}\cdot\text{rad}$). Rescaling the second curve on the first one using the Eq. 3.42 gives a consistent overall behavior and confirms the scaling laws of the current with respect to the normalized emittance (Eq. 3.42).

Similarly, as we observe from simulation and from the 37 GeV/c experiments, the losses at 7 σ are always larger than the ones at 5 σ , for the same wire current and working point.

We would expect to observe the points measured at 37 GeV/c to lie on the curves measured at 55 GeV/c: this is not the case. At 5 σ beam-wire separation and at 37 GeV/c the beam losses are larger than at 55 GeV/c (same normalized separation) while, an opposite behavior takes place for the separation at 7 σ .

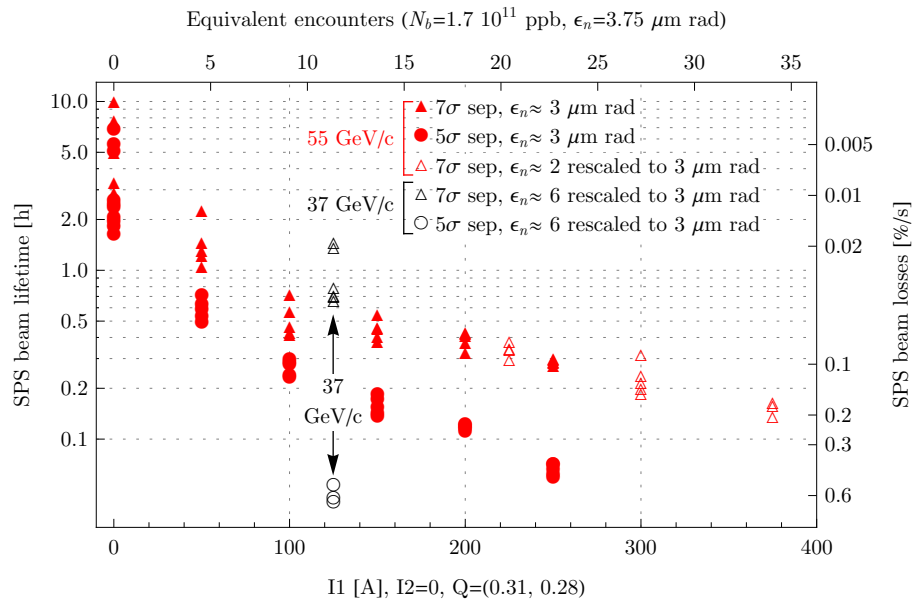


Figure 4.39: The losses induced by the wire varying the wire current for 5 and 7 σ separation with the optimized vertical tune.

These apparent inconsistencies can be explained using the following argument. The scaling laws discussed in Section 3.2.3 state that the two machines (SPS + wire at 37 GeV/c and at 55 GeV/c) are equivalent from the beam dynamics point of view neglecting the different physical aperture of the machine, the non-idealities due to the ripples in the power supply and the coupling of the wire with other non linearities of the machine. It is fundamental to observe at this point that having an equivalent beam dynamics and equal beam revolution frequency does not imply to have the same beam loss rate. In fact the beam loss rate depends both upon the beam dynamics and the beam distribution. The beam loss rate is equal for the same beam dynamics only if the beam distribution in the normalized space is the same in the two machines: this means, in practice, if the shape of beam profile is the same in the two machines for each of the two transverse directions.

We observed during the different experiments that the profile of the beam can change significantly: it depends upon the beam energy, the tunes, the emittance, the closed orbit... In Fig. 4.40, *top*, we show two examples of beam profile measurements: the Gaussian fit is not good along the tails of the beams. We quantify analytically (Fig. 4.40, *top*) the problem considering a parabolic profile (well collimated, no tails) and a bi-Gaussian profile (large tails). The Gaussian fit overestimates or underestimates the tails of 3 – 4%

(Fig. 4.40, *bottom*). The first particles to be lost due to the wire effect are the large amplitude particle that populate the tails. We expect that the beam loss rate in our observation period (1 – 5 s), short with respect to the minimum beam lifetime observed (1 min), is dominated by the particles in the tails. This will be verified during the experiment at 120 GeV/c when the time constant of the beam-beam phenomena will be investigated (see next section).

From what we said, assuming that the at 37 GeV/c the beam profile was almost parabolic (no tails, e.g., due to an aperture restriction during the ramp since the emittance is very large, $\epsilon_n = 6 \mu\text{m}\cdot\text{rad}$), this would explain the result in Fig. 4.39: with 7σ of beam-wire separation the effect is minimized since the beam core is too far and the tails are already emptied. When the separation is reduced to 5σ the sudden increase of beam losses is due to the extraction of particles in the core. A similar argument can be used for Fig. 4.38.

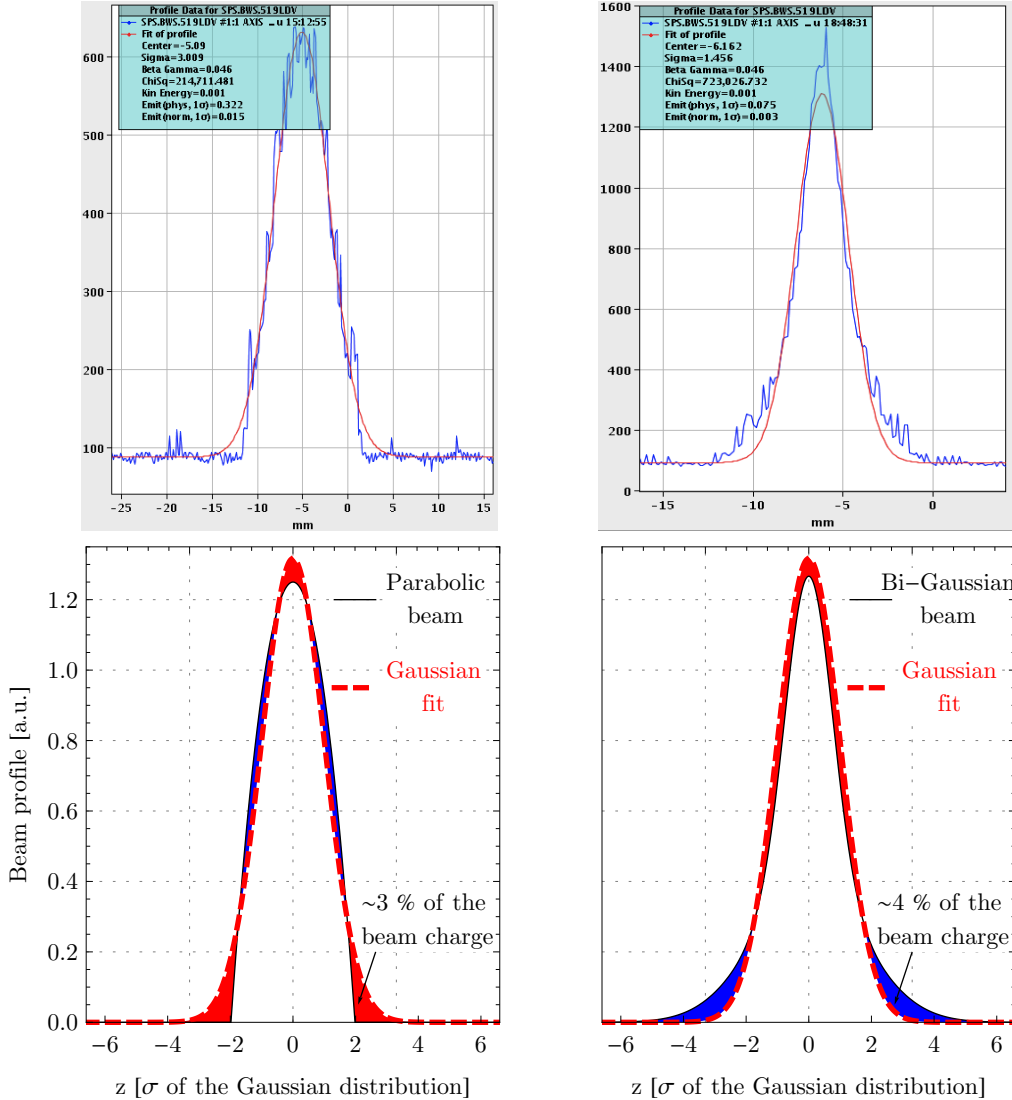


Figure 4.40: The difference in the tail of the beam profiles. The measurements of the beam profiles (*top*) are compared with a parabolic and bi-Gaussian distribution (*bottom*).

4.2.4 Experiments at 120 GeV/c

We complete the picture of the SPS wire experiments by commenting the results obtained at the beam momentum of 120 GeV/c. The 120 GeV/c cycle adopted is displayed in Fig. 4.24. Differently from the other cycles it can run in *coast*: this means that the beam current instead of being dumped at the end of the cycle is stored in the machine at the momentum of 120 GeV/c. This allows to observe the beam behavior for a

much longer time: from the 1 – 5 s long flat-top of the cycles at 37 and 55 GeV/c we go to ≈ 30 min long flat-top at 120 GeV/c. This allows to explore the different time constants of the processes involved in the beam-wire excitation. The difficulties connected with a coasting beam in SPS are two-fold:

- most part of the SPS control software has been programmed to operate only within a cycle, therefore is not available during the coast (e.g., the code that control the orbit steering or the tune correction). For this reason the tune shift and the orbit change induced by the wire are not corrected. Nevertheless, due to the large physical distance between the beam and the wire, these effects are negligible (Eq. 4.4).
- due the higher beam rigidity, we need to increase the beam emittance by a significant factor in order to reduce the normalized beam-wire separation. We manage to reach the 8σ separation between the beam and the wire with a normalized emittance of $7.5\ \mu\text{m}\cdot\text{rad}$ (in agreement with Fig. 4.26). The emittance blow-up cannot be done at the injection energy due to the limitation of the mechanical aperture of the machine. We performed it the last part of the ramp.

In Fig. 4.41 we show the beam current as function of the time during a coast at the nominal LHC tune. The beam wire separation is 8σ . In the same coast we have excitation and compensation experiments. As in the previous experiment we use the BBLR1 wires for the excitation with a current $I_1 = 250$ A and the BBLR2 equipment for the compensation but instead of powering it with $I_2 = 210$ A, as in the past experiments, we calibrate the position of its two wires to reproduce the BBLR1 tune shift obtaining the best compensation current $I_2 = 230$ A. We verified with the wire scanner measurements that the normalized emittance does not change significantly during the coast and therefore the normalized beam-wire separation stays constant.

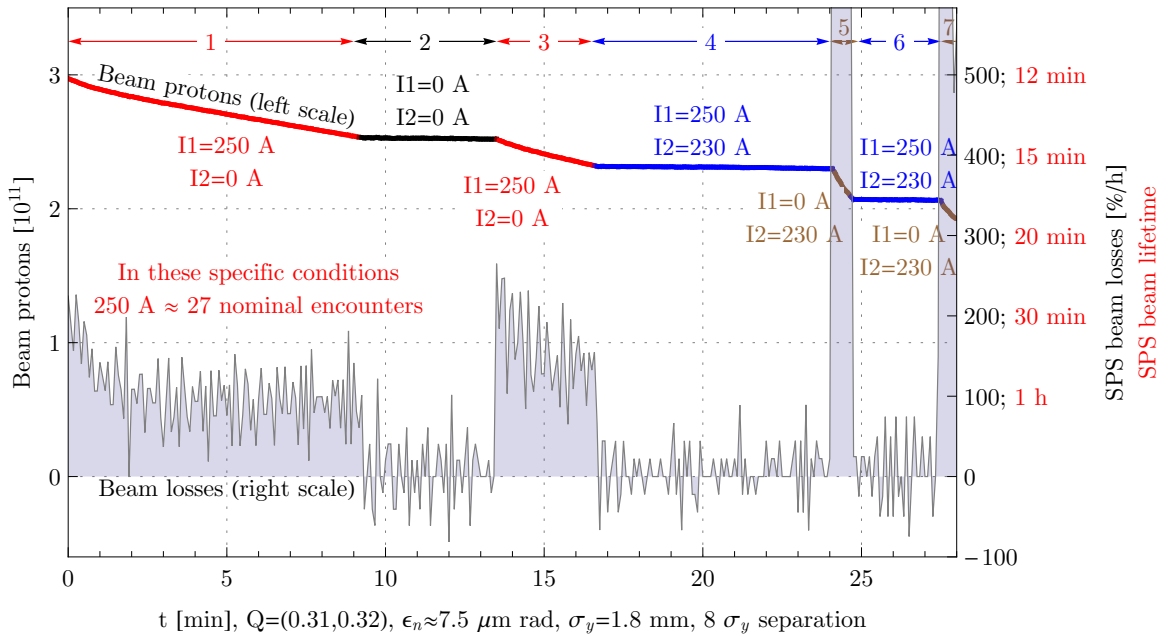


Figure 4.41: Coast at 120 GeV/c with a beam-wire separation of 8σ .

In the experiment condition, $I_1 = 250$ A corresponds to 27 beam-beam encounters at the nominal bunch population ($N_b = 1.15 \cdot 10^{11}$ ppb, $\epsilon_n = 3.75\ \mu\text{m}\cdot\text{rad}$), i.e., slightly less than the effect of a single nominal LHC insertion. Their effect is evident on the plot (Fig. 4.41, *period 1*): in ten minutes 15% of the beam is lost corresponding to a lifetime in SPS of 0.5 – 2 h (2 – 4 h in LHC). In comparison, the beam without excitation does not have visible losses on this scale. The losses are also well reproducible (see *periods 1 and 3*): this suggests that the natural diffusion of the SPS during the *period 2* populates continuously the tails. In addition of a fast emptying of the beam tails (see the peak of beam loss at the beginning of the excitation), we observe that the loss rate stays constant for minutes. This can be due the combination with the natural diffusion of the machine and the extraction of the particle due to the wire effect: after a transient of 3 – 5 minutes, the steady state losses are of the 100 %/h corresponding to a beam life time of 1 h (see Eq. 4.1, it is still valid in the approximation that the period of observation is significantly shorter than the beam lifetime,

i.e., in the steady state of the *period 1*, $7 \text{ min} \ll 1 \text{ h}$).

In Fig. 4.41 it is shown (*period 4*), how efficient the beam-beam long-range compensation can be: the beam losses, after the compensation, are reduced to the non-excited case. Furthermore the plot shows that the excitation by the BBLR2 alone (*periods 5 and 7*) is much more harmful for the beam inducing higher beam losses. We can explain it observing that, due the opposite polarity of the wires of BBLR1 and BBLR2, the induced tune shift has opposite direction in the tune plane therefore the beam can be excited by different resonances with a consequent different impact on the beam lifetime. It is worth noting that, due to the wire cabling, the BBLR2 is pushing towards the diagonal resonance: this is in agreement with the previous experimental result and with the performed simulation that show that near the diagonal some resonant mechanism takes place.

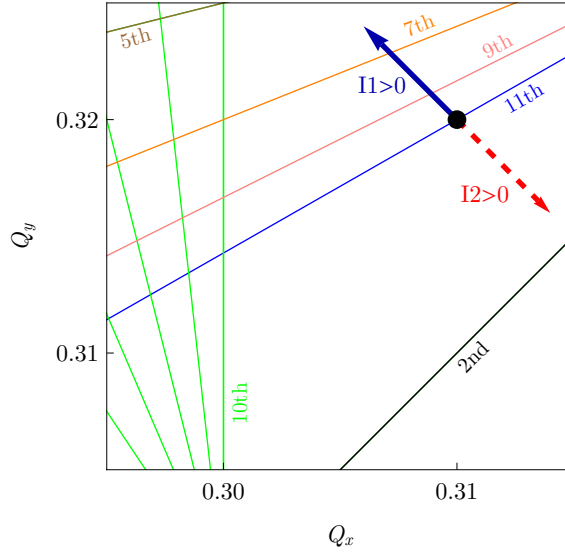
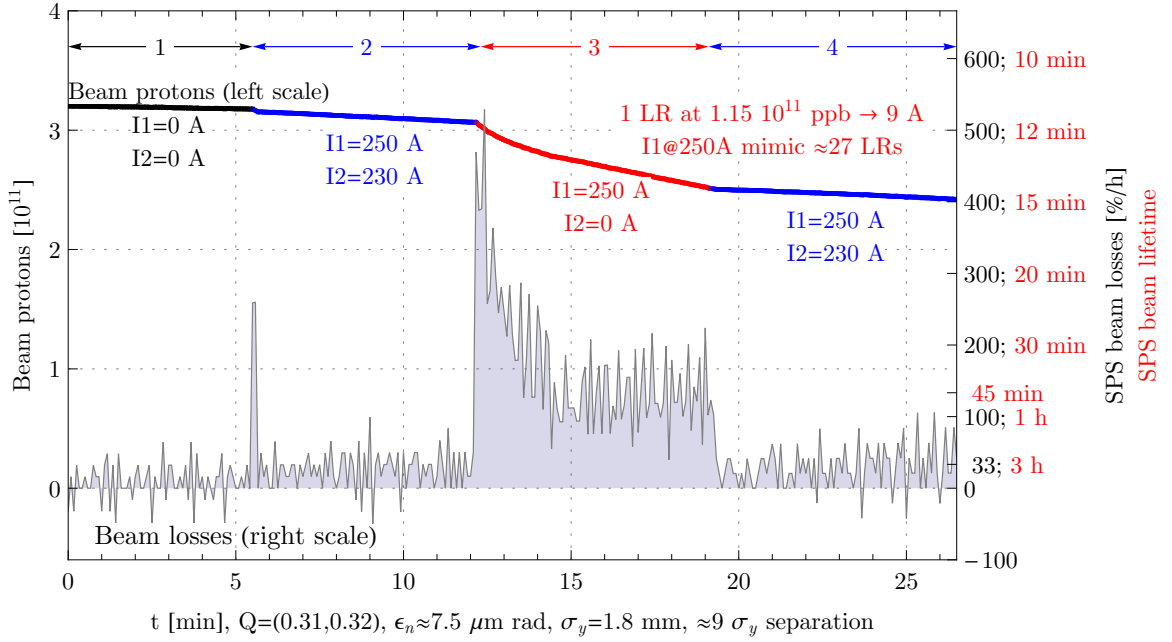


Figure 4.42: The different tune shift directions due to the BBLR1 and the BBLR2 polarity.

In Fig. 4.43 we show the results for a second experiment with same setting except for the beam-wire separation of 9σ instead of 8σ . The wire compensation in this case is less effective probably because by changing the beam closed orbit (passing from 8 to 9σ separation) would have required a new calibration of the BBLR2 wires positions that we did not do.

The beam losses at 9σ are comparable to the ones at 8σ and their effect is important. The beam losses observed in steady-state are larger than $100 \text{ \%}/\text{h}$ (*period 3*). The excitation on the wire ($I1 = 250 \text{ A}$) represents then almost all the long-range of the nominal LHC interaction. Even rescaling this loss to the LHC frequency (≈ 4 times lower) we obtain a loss greater than $25 \text{ \%}/\text{h}$ (less than 4 h LHC beam lifetime), that is incompatible with the machine operations. Increasing by about a factor 6 the beam emittance may reduce significantly the good field region of the magnets in term of beam σ , therefore the importance of the machine non-linearity might be emphasized. These non-linearities coupled with the wire excitation might reduce the applicability of the scaling laws and worsen significantly the beam lifetime. In fact, we observe a much better beam lifetime in the experiments at $55 \text{ GeV}/c$ (Fig. 4.38): almost doubling the excitation, 52 encounters ($N_b = 1.15 \cdot 10^{11} \text{ ppb}$, $\epsilon_n = 3.75 \mu\text{m}\cdot\text{rad}$) with the optimal tune of $(0.31, 0.28)$ and at 9σ wire-beam separation produce even lower beam loss rate ($\approx 0.02 \text{ \%}/\text{s}$, that is $\approx 70 \text{ \%}/\text{h}$). It is important to consider that in the experiments at $55 \text{ GeV}/c$ we observe the transient losses that, as well shown in the experiments at $120 \text{ GeV}/c$, can be significantly higher of the steady state. We think the steady state losses are more significant observables that the transient losses: while the transient losses depends upon the details of the profile of the beam tails, the steady state are related to the diffusion of the particle in the core. Even if this diffusion can be the combination of the natural diffusion of the machine and the diffusion induced by wire, we can compare and rescale with reasonable accuracy the steady state losses but not the ones related to the transient: comparing Figs. 4.41 and 4.43 we observe very different loss rates during the transient (respectively $\approx 250 \text{ \%}/\text{h}$ and $\approx 500 \text{ \%}/\text{h}$), while the steady state loss rates are similar (respectively

Figure 4.43: Coast at 120 GeV/c with a beam-wire separation of 9σ .

$\approx 100\text{ \%}/\text{h}$ and $\approx 125\text{ \%}/\text{h}$).

We summarize in the following the main considerations drawn from the experiments at 120 GeV/c:

- the measurement in coast is much more discriminant and sensitive than the ones made with much shorter observation period (in the pulsed cycle at 37 and 55 GeV/c),
- the nominal long-range beam-beam effect (in isolation from the head-on beam-beam effect) appears too drastic for operations on the nominal tunes,
- the long-range beam-beam compensation suppresses this effect in one experiment and significantly decreases it in the second, with no clear explanation for the difference,
- the Early Separation Scheme cannot be studied at 120 GeV/c for lack of strength in the orbit correctors.

4.3 Summary and interpretation of the experiments

In the first part of the chapter we described the simulations carried out to study the impact of the Early Separation Scheme on the beam dynamics of the sLHC and

- we motivated our choice to use the evolution of the particle amplitudes to study the beam dynamics problem,
- we introduced the amplitude plane, the space we use to show the results of our simulations putting in evidence its difference with the physical plane,
- we described the code we developed in CUDATM, showing its potential, its limits and the solutions we adopted to overcome them,
- we showed that the single precision tracking is adequate for our purpose, benchmarking the code with the linear machine case and with other simulations, in double precision, of non-linear machines,
- we reported the results of our Early Separation Scheme simulations considering a total of 4, 8, 12 encounters at $\Delta_{in} = 5$, $\Delta_{out} = 12$, two alternating crossings, nominal LHC collision tunes and ultimate LHC bunch current. We observed a minimum dynamic aperture of 4σ but moving the tune to (0.31, 0.28) the dynamic aperture increases to 6σ ,
- we observed that a total of 12 encounters at $\Delta_{in} = 7$, $\Delta_{out} = 12$ are almost equivalent from the beam-beam effect point of view to have the nominal crossing scheme, $\Delta_{in} = \Delta_{out} = 9.5$.

In the second part of this chapter, devoted to the results obtained during the SPS wire experiments,

- we described the experimental setup, emphasizing the limit of the orbit correction and the emittance blow-up technique,
- we confirmed with several experiments that the tune (0.31, 0.28) is better than the nominal one for the long-range beam-beam effect,
- we benchmarked our code with some experimental results observing a good agreement,
- we observed that the simulations of the wire mimicking 12 encounters at 5σ separation show a smaller dynamic aperture than the simulations of the sLHC in similar condition, concluding that the wire experimental results overestimate the losses induced by beam-beam effect at reduced separation,
- we investigated the time constants of the beam-beam interaction with the experiments in coast at 120 GeV/c,
- we showed the limitations of the experiments with short flat-tops at 37 and 55 GeV/c, dominated by transient depending on uncontrollable details of the beam tails distribution.
- we showed that the experimental results are consistent with the scaling law on the beam emittance
- we reported in details and commented the Sp \bar{p} S beam separation pattern, underlining the limits of its direct rescaling to the sLHC.

By putting all the previous results in the Early Separation Scheme perspective, we can make the following conclusions. It appears reasonable to operate the machine with 12 encounters at 7σ , $\Delta_{out} = 12$, with an appropriate choice of the tune and at the ultimate bunch population ($N_b = 1.7 \cdot 10^{11}$). The possibility to reduce the inner separation to 6σ is partially corroborated by the Sp \bar{p} S data. Sticking to the wire experiments results in SPS, it appears difficult or suspicious to reduce the inner separation to 5σ . Since we observed for this separation only transient effects and, in addition, the simulations show that the beam dynamics in the SPS experiments is worse than one expected for the sLHC, the experimental results may overestimate the losses. For all these reasons, the proposed hardware is designed for reaching $\Delta_{in} = 5$, as explained in the Chapter 5. In the same chapter, we will show that reducing the number of parasitic encounter at 5σ below 12 it is not possible if we assume the same hardware solution in the two experiments.

Chapter 5

The integration and the preliminary design of the Early Separation Scheme

Contents

5.1	The integration in the detectors of the Early Separation Scheme	101
5.2	The power deposited on the D0 dipole by the collision debris	110
5.2.1	The debris from the Interaction Point	111
5.2.2	The simulations of the power deposition on the D0 dipole	113
5.3	The magnet preliminary design	116
5.3.1	The mechanical stresses on the D0 dipole's coils	117
5.3.2	A preliminary cross-section for the D0 dipole	118

In this chapter we describe several aspects related to the implementation of the Early Separation Scheme. We discuss the different constraints settled on the positioning of the Early Separation dipoles by the ATLAS [30] and CMS [31] detectors specific layouts,. These constraints and, in addition, the integrated magnetic field that has to be provided by the magnets require the use of superconducting technology. In this situation the power deposited by the collision debris in the cryostat (dynamic heat load) becomes a potential issue: we show in Section 5.2 the approach adopted to address it and the simulation results from the FLUKA code. Finally in Section 5.3 we propose a magnet layout compatible, from the collider point of view, with the requested integrated field and with the constraints due to the detectors and to the dynamic heat load.

5.1 The integration in the detectors of the Early Separation Scheme

The Early Separation Scheme, as already discussed in Chapter 1, requires the installation of machine elements in the detectors straight section, namely one dipole for each side of the detector (the so-called D0 dipole, see Fig. 1.18). The other dipole needed for the scheme (the OC dipole) has to be installed in the tunnel and for that reason its requirements are less critical.

In the nominal LHC all the collider hardware is installed in the machine tunnel while the experimental cavern are exclusively dedicated to host the detectors. The integration of the D0 dipole in the experimental caverns is a challenging task and requires several studies and iterations between the design teams of the collider and of the detectors.

It is worth considering that the detectors' design and optimization for the Luminosity Upgrade is still under discussion and it will deeply depend on the physics emerging from the LHC. It is not clear yet if the detectors upgrade have to be optimized for a large spectrum of physics research (general purpose detectors) or if they have to be focused on more specific phenomena: the possibility to integrate the Early Separation dipoles will depend also on these decisions. Nevertheless, it is already clear that in the two experiments the inner detectors have to be rebuilt to cope with the increased proton-proton interaction rate (multiplicity). Moreover, in ATLAS for the same reason, the detector shielding has to undergo major modifications. On the contrary, the magnetic system of both detectors will not be modified. On the collider side, being aware of the complexity of the D0 dipole integration, we study and propose the less invasive positioning of the Early

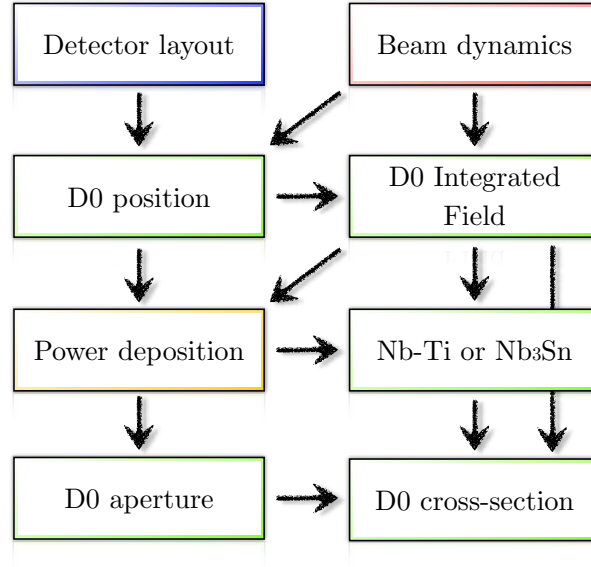


Figure 5.1: The logic flow used to dimension the Early Separation Scheme.

Separation dipoles still compatible with the aimed luminosity performance of the Phase II LHC Luminosity Upgrade (sLHC, Chapter 2) and with beam dynamics stability (Chapter 3 and 4).

In order to dimension the D0 dipole, we followed the logic flow described in Fig. 5.1. We start considering the possible D0 dipole positions given the detectors and beam dynamics constraints. After having selected the D0 dipole position, the beam dynamics constraints (namely the normalized inner and outer beam separation, Δ_{in} and Δ_{out}) set the requested D0 dipole's integrated field. The D0 dipole position and its field are used as input for computing the power deposited on the coil by the collision debris. The superconducting technology (Nb-Ti or Nb₃Sn) is chosen in relation to the peak power deposition in the coil and the magnetic field requested. Finally starting from the aperture, the field and the mechanical stress limit of the superconductors, we design a preliminary cross-section for the D0 dipole.

The constraints due to layouts of the detectors

We consider in Fig. 5.2 (not to scale) the layout of ATLAS and CMS detectors. Both the detectors present a left-right symmetry with respect to the collision point: this fits with the Early Separation symmetry and allows us to consider only one side of the detectors.

Apart from the common left-right symmetry, the two detectors are significantly different: on one hand, this has been deliberately decided to give a stronger evidence of the physics processes observed by revealing them with very different detectors. On the other hand, they are different due to their specific optimization in caverns of different sizes (larger for ATLAS than for CMS).

The magnetic system of the ATLAS detector is toroidal while in CMS is solenoidal. In ATLAS, however, a 2 T central solenoid serves the inner detector. The calorimetry of CMS is inside the bore of the solenoid while, in ATLAS, the solenoid hosts only the inner detector. The large return yoke of CMS (the barrel and the end caps elements) has, at the same time, a magnetic and shielding function while. In ATLAS, the shielding has no magnetic purpose and is mainly concentrated along the beam direction.

In Fig. 5.3, half of the longitudinal cross-section of the two experiments is shown: ATLAS in the upper part and CMS is the lower part. The shielding blocks of ATLAS detector are well visible (elements JM, JD, JT and JF). The forward calorimetry of the ATLAS detector is between the moderator shielding (JM block) and the shielding disk (JD block) in a position between 4.5 and 7 m from the Interaction Point. In the CMS detector there is no shielding cone along the beam axis and the region between the inner detector to the forward calorimetry has been designed to be as transparent as possible not to spoil the calorimetry (indeed the TOTEM detector, not shown in the picture, is installed in this region). The CMS forward calorimeter is positioned between 10.5 and 13 m from the collision point: it is much more external than the one in ATLAS and this, as explained in the following section, has a significant impact on the position of the D0 dipole.

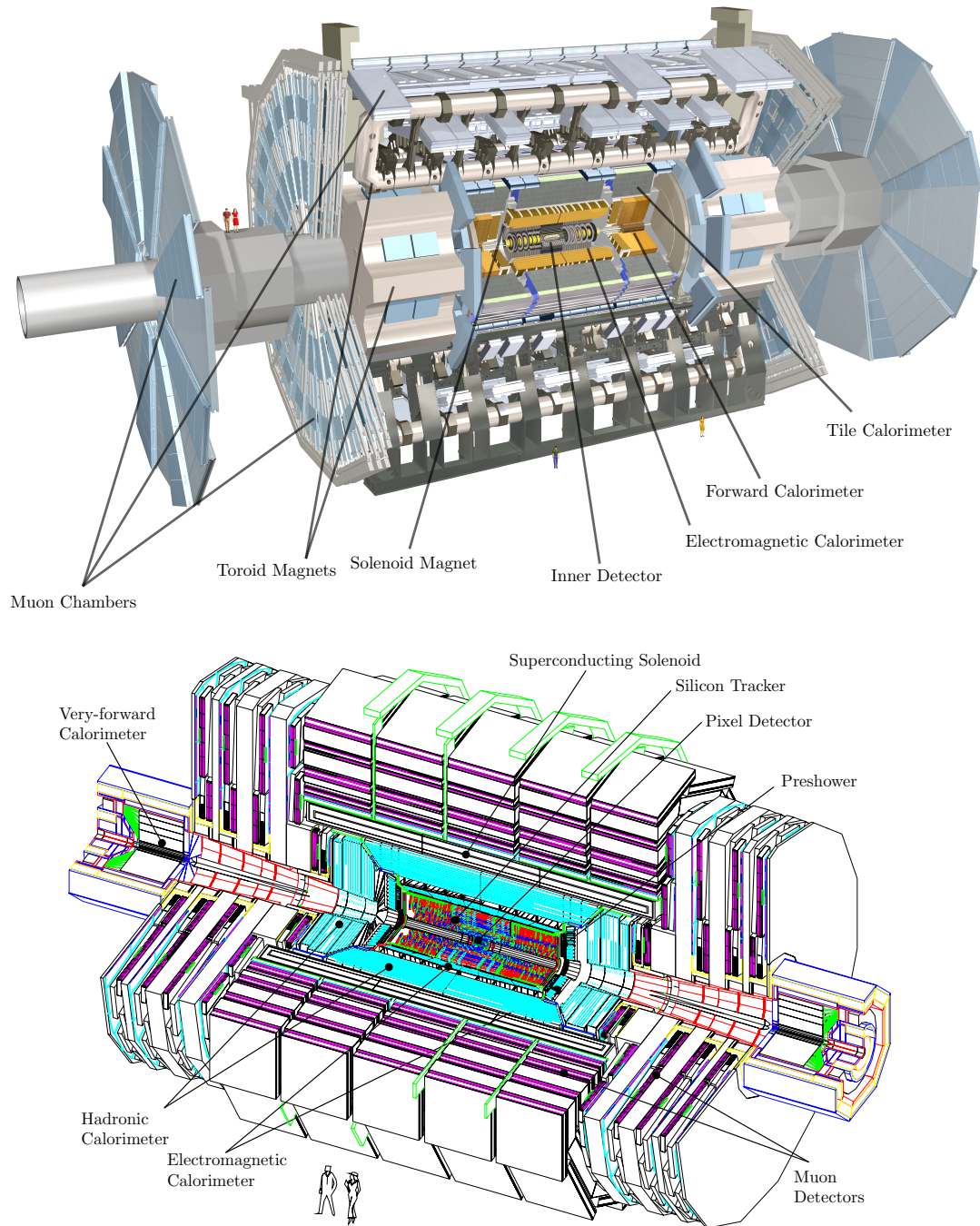


Figure 5.2: An artistic view of ATLAS, *top*, and CMS, *bottom*, detectors. Courtesy of the ATLAS and CMS collaborations.

The ATLAS shielding and the CMS forward detectors

The CARE-HHH workshops on the LHC Luminosity Upgrade have been the official framework of discussion, among several other topics, about the integration of the Early Separation Scheme in the detectors [65, 66, 67, 68, 69].

The ATLAS collaboration indicated the detector shielding blocks as potential positions for the D0 magnet [56]. The purpose of the shielding in ATLAS is to reduce the number of background particles in the Inner Detector and in the Muon Spectrometer to a manageable level and to protect staff working in or nearby

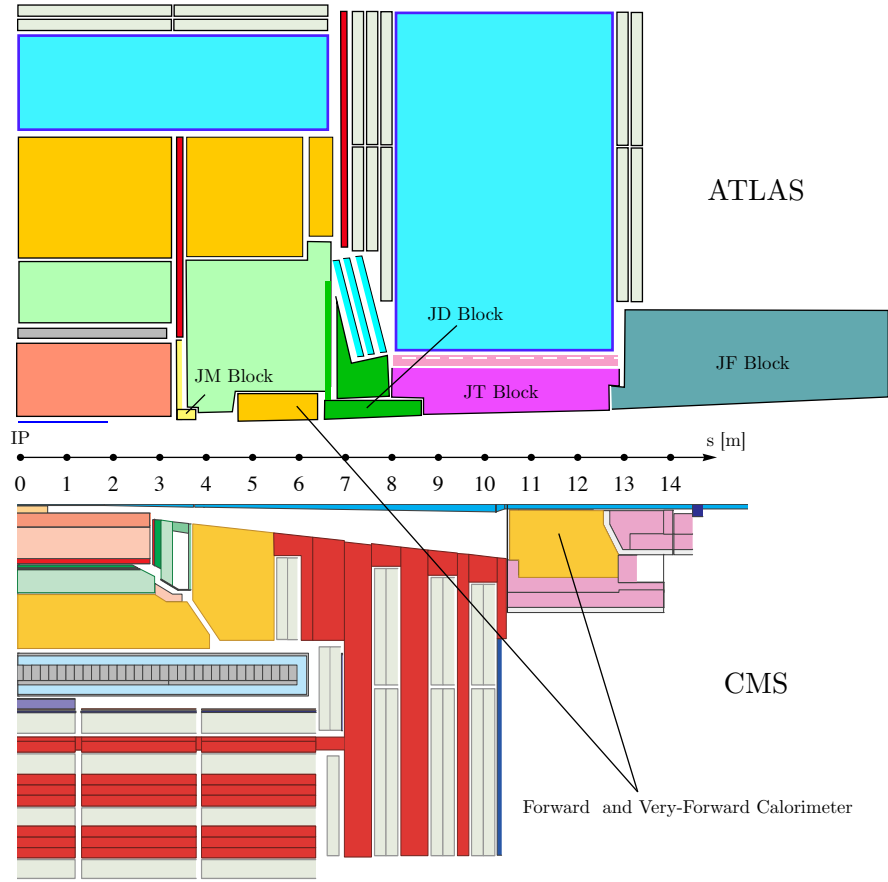


Figure 5.3: Artistic view of the longitudinal section of ATLAS (*top*) and CMS (*bottom*). It is worth noting the different positioning of the forward calorimeter in the two detectors. Courtesy of the ATLAS and CMS collaborations.

the cavern during the maintenance periods. The core of the shielding blocks are mainly made out of cast iron for the density of this material, the presence of carbon atoms in it and its cost. The function of the cast iron is to extract by means of hadronic shower the energy of the high energy impinging particles. Its carbon content works as moderator for the neutrons generated in the hadronic shower. An external shell of polyethylene around the cast iron core is used to moderate further and capture the neutrons. Finally a layer of stainless steel or lead is used to collect the photons produced during the neutron capture process.

The four slots proposed by the ATLAS collaboration for the D0 magnet are shown in the Fig. 5.4 and are reported in Table 5.1. The D0 dipole should not reduce the overall effectiveness of the shielding (i.e., by replacing shielding material with material with lower density) and should remain in the shadow of the ATLAS shielding not to produce unwanted interactions (pre-showering) with the consecutive spoiling of the detector's performance.

For each slot we defined the specific difficulties of the D0 dipole integration from the collider side [71, 72]. As an example we consider in the following the JM region: it consists of a neutron moderator. Differently from the other shielding blocks it is extremely light (168 kg of polyethylene per each side of the Interaction Point (IP) to compare with the ≈ 400 tons of the JF block) to avoid the backscattering of neutron from the calorimeter in the inner detectors. Positioning an object like the D0 in that region would increase by a large factor the neutron flux in the inner detector. We exclude the slot from 3.5 to 4.5 m because

- the anticipated strong neutron back-scattering in the inner detector,
- the anticipated difficulties in the integration of the piping and the service in the detectors,
- too small for the D0 dipole,
- the fringe field of the solenoid and the consequent difficulties in the mechanical support of the dipole (see next section).

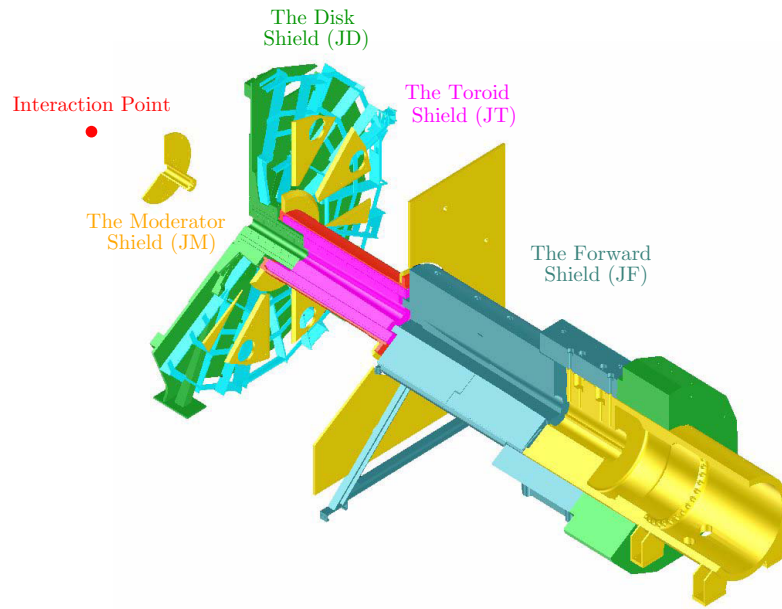


Figure 5.4: Details of the possible position for the D0 dipole in ATLAS. Courtesy of the ATLAS collaboration [70].

Table 5.1: The possible D0 dipole positions in the ATLAS shielding blocks with the maximum possible size of the cryostat.

Name	Longitudinal Position from the IP [m]	Max. radius of the D0 cryostat [mm]
JM region (slot 1)	3.49 – 4.58	180
JD region (slot 2)	6.80 – 8.66	430
JT region (slot 3)	8.69 – 12.87	870
JF region (slot 4)	12.95 – 18.60	1500

Regarding the positioning of the magnet in the blocks JD and JT, the ATLAS collaboration analyzed the impact of the D0 dipole presence on the detector performance [73]. The outcome of this study is that the D0 dipole positioned in the JD alcove increases by factor 2 – 3 the neutron flux in the inner detector. Its impact on the forward calorimeter, even if not simulated, is extrapolated from the effect on the inner detector and is expected to noticeably degrade the performance of the forward calorimetry. Positioning the D0 dipole in the JT shielding block would produce an increase of the background between 10 – 40 % depending of the system of the detector considered. *“Whether these increases are serious or not depend on many other factors associated with upgrade design, and with simulation uncertainties”* [73].

In the CMS detector the situation is dominated, as already pointed out, by the position of the forward calorimeter: on one hand, putting a dipole between the inner detector and the calorimeter, would blind a significant portion of the forward calorimetry and back-splash neutrons towards the inner detector. On the other hand, the possibility to move the forward calorimeter towards the inner detector and putting the D0 dipole behind it can be, in principle, explored. Nevertheless, as we discuss in the following section, we have to take into account the magnetic field of the solenoid too and putting the D0 dipole inside the solenoid’s bore or in the end-cap yoke of the solenoid has to be excluded.

The detector magnetic field

Another important element to consider for the D0 dipole positioning is the direction and the intensity of the magnetic field of the detectors. In Fig. 5.5 the module of the detectors \vec{B} on the machine alignment orbit is shown together with the four slots of the ATLAS shielding (shaded regions). The field, due to the cylindrical symmetry of the detectors has only longitudinal component on the detectors axis ($\vec{B} = B_s \vec{s}$). In the D0 dipole's volume, the detectors magnetic field varies only longitudinally and is almost constant along the transverse directions. The field of the CMS solenoid is 4 T in the bore and is significantly reduced only

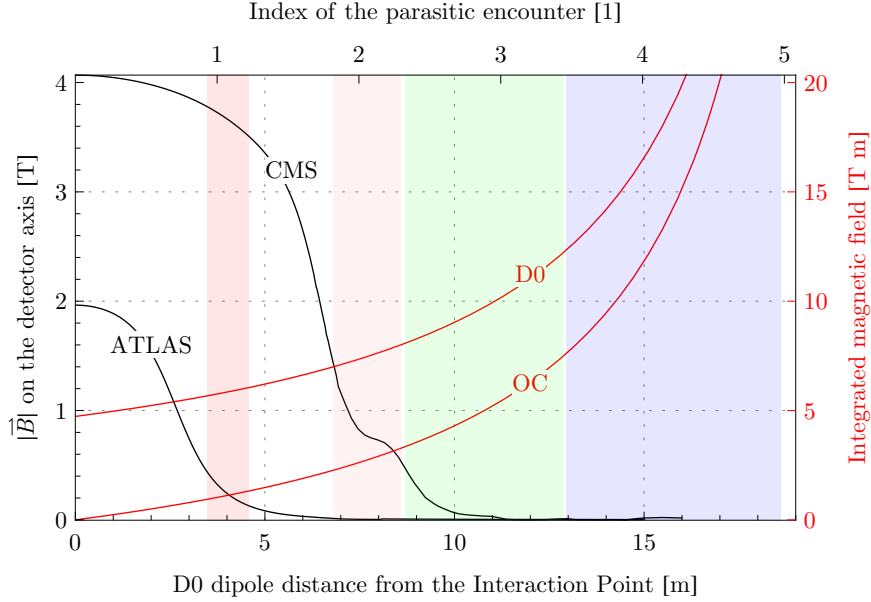


Figure 5.5: The magnetic field in ATLAS and CMS detectors.

after the end-cap iron yoke (at 10 m from the Interaction Point). The field of the ATLAS solenoid is 2 T and already at 7 m is almost vanished.

The magnetic field of the detector's solenoid can strongly interact with the D0 dipole: it induces a torque on the D0 coil that tends to rotate it in the transverse plane to align the dipole's field along the solenoidal field direction. In addition, if the dipole has a return yoke to confine its fringe field, the detector solenoid applies on the ferromagnetic material of the yoke a force that tends to pull it towards the center of the solenoid. Putting a large amount of ferromagnetic material in the detectors can change significantly the magnetic solution of the solenoid and the yoke of the dipole can be, depending on its position, totally saturated by the detector solenoid: if the yoke is saturated by the solenoid becomes useless for the D0 dipole. Moreover, the superconducting cable of the D0 dipole, working in the magnetic field of the solenoid, reduces its effective critical current. The amount of this performance loss depends on the vectorial sum of the dipole field and of the solenoidal field.

The ferromagnetic yoke of the D0 dipole can vary significantly the magnetic field of the detectors (the unperturbed detector field is shown in Fig. 5.5). In Fig. 5.6 is shown a simplified finite elements model using COMSOL [47] where we consider the ATLAS and the CMS solenoids (the CMS return yoke is not implemented and it can change considerably the situation). By putting a ferromagnetic cylinder (2 m long, 200 mm inner radius, 400 mm outer radius) at 13 m from the Interaction Point, the cylinder's material is completely saturated by the CMS solenoid and it is pulled by a force of ≈ 10 ton force toward the solenoid's center. Of course, considering the CMS yoke, and in particular the end-cap yoke, we expect to observe a significant reduction of the solenoid effect on the dipole yoke. Nevertheless all these considerations point out that, putting the dipole between the Interaction Point and the CMS end-cap, gives rise to very important forces. In the ATLAS case, on the contrary, the interaction between the ferromagnetic material and the solenoid is negligible.

The magnitude of the torque can be estimated considering the Lorentz force, F , on the coils end due to

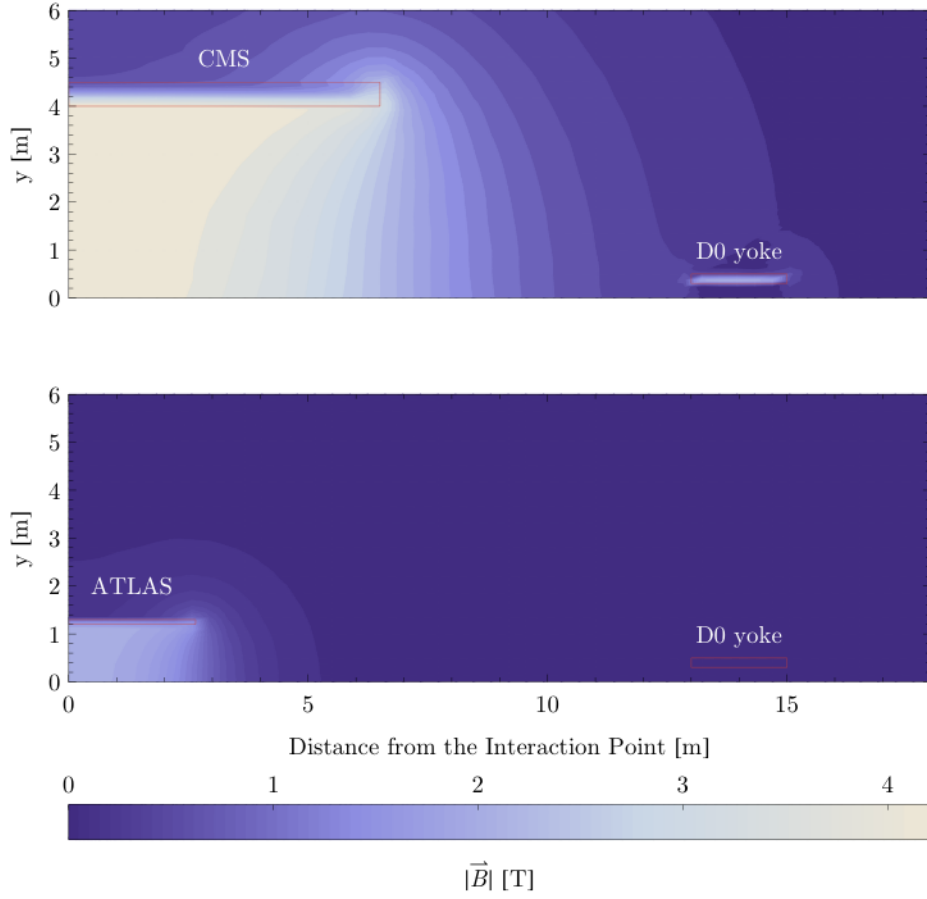


Figure 5.6: A simplified finite elements model to compute the force exerted by the ATLAS and CMS detectors on the yoke of the D0 dipole. In CMS, *top*, the solenoid's field saturates the D0 dipole iron yoke, positioned at 13 – 15 m from the Interaction Point (IP), and pull it towards the IP with a force of ≈ 10 ton force. The magnetic interaction between the iron yoke (same position) and the ATLAS solenoid is negligible, *bottom*.

the solenoidal field. Given the geometry of the problem, we can use the simplified approach $F = L I B$, where L is the transverse length of the dipole's end, B the solenoid's magnetic field and I the current flowing in the dipole cable times the number of cables in the dipole's cross-section. Considering the $L = 0.2$ m, $I = 18 \text{ kA} \times 70$ conductors and a solenoidal field of 1 T [72], it yields a force of ≈ 50 ton force on each dipole's end with a corresponding torque of $\approx 10^6$ N·m for a coil length of 2 m. We assumed that the solenoid's field is constant along the coil. These numbers are quite impressive: even if we miss a complete study, from the first iteration with the CMS team, we believe that positioning the dipole in the end-cap yoke or in the solenoidal bore of the detector requires a cantilevering structure not compatible with the detector.

The dipole position versus the integrated field requested and the beam dynamics

We put in evidence in the previous section the different issues of the integration of the D0 dipole in the ATLAS and CMS detectors. Before proposing what we consider the best trade-off for the D0 dipole position we recall the results of Chapter 1 (Eq. 1.17) relative to the integrated field in the dipoles of the Early Separation Scheme (the D0 and OC dipoles):

$$\left| \int_{D0} B dl \right| = \frac{B\rho}{2(s_{OC} - s_{D0})} \sqrt{\frac{\epsilon}{\beta^*}} s_{OC} \quad \text{and} \quad \left| \int_{OC} B dl \right| = \frac{B\rho}{2(s_{OC} - s_{D0})} \sqrt{\frac{\epsilon}{\beta^*}} s_{D0}.$$

Assuming a position of the orbit corrector (s_{OC}) at 21 m from the IP, a normalized inner separation (Δ_{in}) of 5, a normalized outer separation (Δ_{out}) of 12, a beam momentum of 7 TeV/c and an emittance (ϵ) of $5 \cdot 10^{-10}$ m-rad, the integrated fields requested in the D0 and in the OC increase with the distance of the

D0 from the IP (s_{D0}) as shown in Fig. 5.5: the D0 integrated field required by the Early Separation Scheme goes from 6 T·m at 3.5 m to 20 T·m at 16 m from the IP.

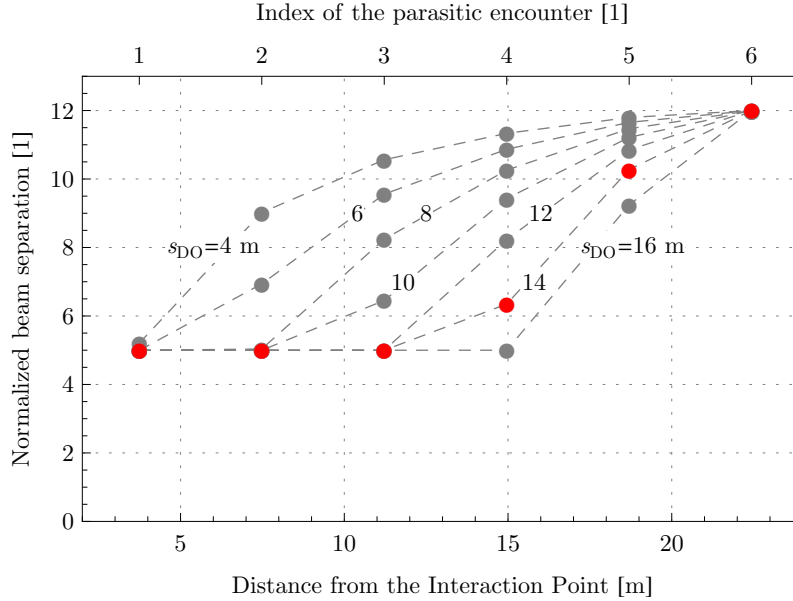


Figure 5.7: The beam normalized separation patterns for one side of the Interaction Point for different positions of the D0 dipoles. The six curves represented correspond to six different separation patterns for the D0 position, s_{D0} , at 4, 6, 8, 10, 12, 14, 16 m from the Interaction Point. The separation pattern with red markers corresponds to a D0 position at 14 m from the Interaction Point.

As already mentioned in Chapter 4 the beam-beam interaction and consequently the beam dynamics depends on the number of parasitic encounters that we have at reduced separation (i.e., 5σ separation for $\Delta_{in} = 5$) and the number of the encounters at reduced separation depend on the position of the D0. In Fig. 5.7 we represent seven different separation patterns for a D0 position ranging between 4 and 16 m from the IP and for $\Delta_{in} = 5$ and $\Delta_{in} = 12$.

Positioning the D0's center at 14 m from the IP corresponds, for $\Delta_{in} = 5$ and $\Delta_{in} = 12$, to have (Fig. 5.7, red markers) 3 encounters at 5σ and 1 at ≈ 6 per each side of each detector.

The tracking results (Chapter 4, Fig. 4.17), assuming a bunch current of $N_b = 1.7 \cdot 10^{11}$ ppb (end of the luminosity leveling for an initial bunch current of $N_b = 2.3 \cdot 10^{11}$ ppb, Fig. 2.15) shows a dynamic aperture of $\approx 6\sigma$ with the optimized tune of (0.31, 0.28). In principle this should be compatible with the machine operation since the aperture restriction of the machine, set by the primary collimators, is at 6σ .

The experimental results carried out in the SPS shows, on one hand, that few encounters at 5σ beam-wire separation has a significant impact on the beam losses, Chapter 4. On the other hand, in the experimental conditions we operated, the beam loss rate is completely dominated by the details of the tail distributions.

From the SpS case, we can observe that 7 encounters adding not in phase (Fig. 4.31) with equal bunch population in the proton beam (N_b) and similar normalized emittance in the anti-proton beam ($5\mu\text{m}\cdot\text{rad}$) are compatible with the machine operation. This fact suggests that it should be possible to reach, in LHC, at least $\Delta_{in} = 6$ (always assuming $\Delta_{out} = 12$). The condition $\Delta_{in} = 7$ and $\Delta_{out} = 12$ with the D0 at 14 m, by having a separation pattern almost equivalent to nominal separation (Fig. 4.16), should be safe.

In conclusion, with a D0's center at 14 m, a normalized outer separation of 12 with a bunch population of $1.7 \cdot 10^{11}$ at the end of the leveling we think it is possible to reach a Δ_{in} between 6 and 7 and we do not exclude the possibility to reach $\Delta_{in} = 5$. The result of the luminosity performance, with luminosity leveling starting at $\Delta_{in} = 12$, a β -function at the IP (β^*) of 0.15 m and 25 ns bunch spacing are reported in Fig. 5.8. With an initial bunch current of $2.3 \cdot 10^{11}$ and an average turn around time of 5 h it is possible to reach the target of 3000 fb^{-1} of integrated luminosity in 6.5–7 years depending on the actual Δ_{in} that can be reached. This is possible without exceeding a peak luminosity of $5.5 \cdot 10^{34}\text{ cm}^{-2}\text{s}^{-1}$ and, therefore, with less than 130 proton-proton collisions per bunch crossing. In comparison, we can observe that, for this particular choice

of the machine parameters, a normalized inner separation of 12 (i.e., without the Early Separation Scheme, $\Delta_{in} = 12$ in Fig. 5.8) takes from 2 to 3 years more to attain the same level of integrated luminosity while crab-crossing (see Section 1.2.3) would reach the integrated luminosity target saving 1 – 1.5 years of data acquisition ($\Delta_{in} = 0$ in Fig. 5.8). The magnetic field requested on the D0 is 14 T·m with the D0's center at

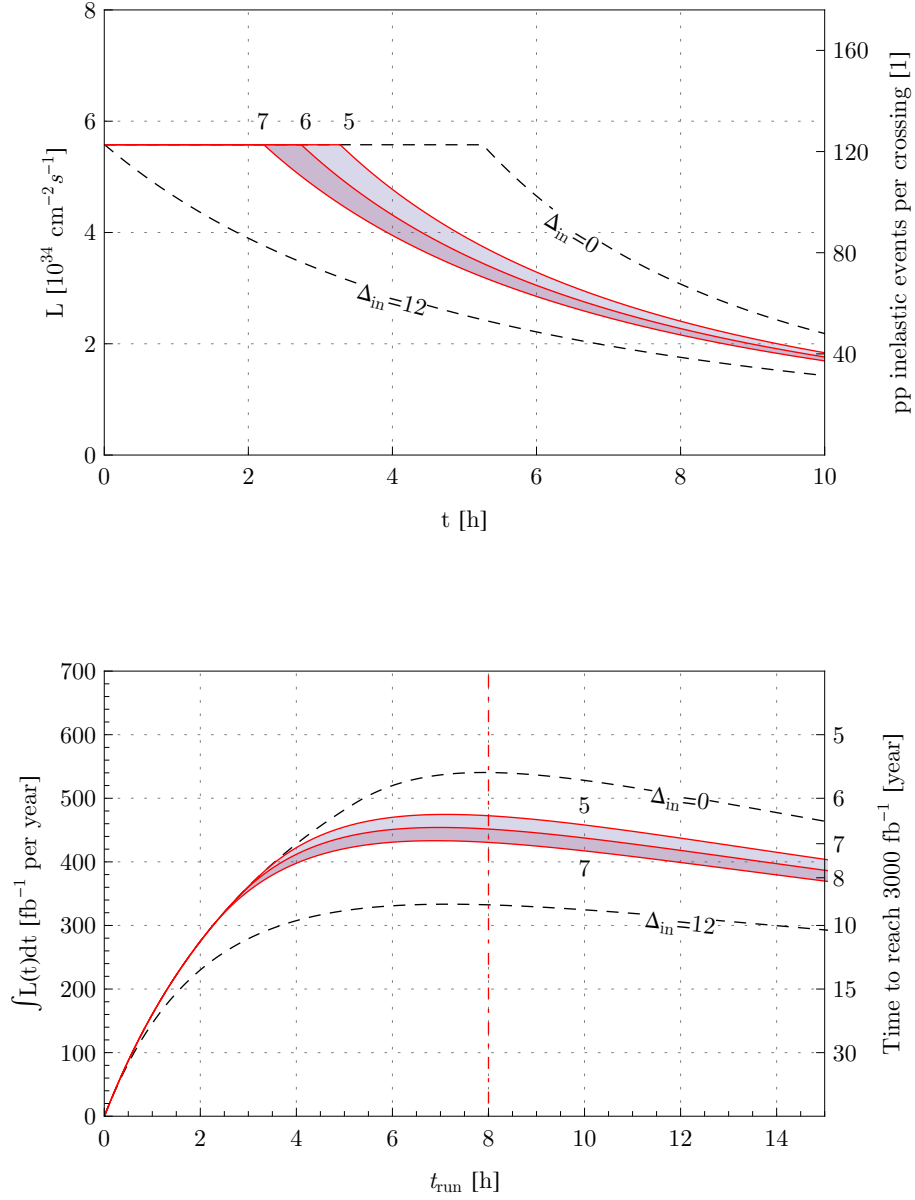


Figure 5.8: The result of the luminosity performance with the D0 dipole at 14 m from the Interaction Point. We consider a luminosity leveling starting at $\Delta_{in} = 12$, a $\beta^* = 0.15$ m, 25 ns bunch spacing, a $N_b = 2.3 \cdot 10^{11}$ ppb and an average turn around time of 5 h. It is possible to reach the target of 3000 fb^{-1} of integrated luminosity in 6.5 – 7 years depending on the actual Δ_{in} that can be reached (between 5 – 7). This is possible without exceeding a peak luminosity of $5.5 \cdot 10^{34} \text{ cm}^{-2} \text{ s}^{-1}$ and, therefore, with less than 130 proton-proton collisions per bunch crossing. For completeness we show the case without Early Separation Scheme (no luminosity leveling and $\Delta_{in} = 12$) and the case with Crab Crossing Scheme (luminosity leveling until $\Delta_{in} = 0$).

14 m from the IP and a D0 cryostat of 2 m (due to the limit of the CMS calorimeter at 13 m), as we show in the following sections seems feasible with the Nb₃Sn technology.

In this region between 13 and 15 m from the IP we are beyond the forward calorimeters of the two detectors: even if the back-splash of the hadronic shower into the inner detector, the calorimetry and the muonic spectrometer can be still a problem, the challenge is surely reduced. At this position the D0 lies beyond the end-cap yoke of the CMS solenoid, therefore we do not expect a significant interaction with the CMS magnetic field. In the ATLAS detector we could in principle consider to position the magnet between from 7 to 14 m but we concentrate on a scheme compatible with both experiments therefore, due the CMS limitation, the proposed position for the D0's center is at 14 m from the Interaction Point hosted in a cryostat of 2 m long starting at 13 m and ending at 15 m from the Interaction Point.

In Fig. 5.9 the forward shielding of ATLAS, *right*, and the shielding nose of CMS, *left*, are shown. The Interaction Point is at the left of each picture. For ATLAS, the visible cylinder corresponds to half of the forward shielding (JF block). The vacuum pipe is positioned in the center of the cylinder and the cryostat of the end-cap toroid is visible on the left: the dipole should start just after the end-cap toroid and should be embedded in the JF block. In CMS, it is possible to see partially, on the left, the forward calorimeter and, on the right, the rotating shielding of CMS. It can be opened on the horizontal plane to access the inner part of the detector (in the picture it is partially opened). The D0 dipole should be installed just after the CMS forward calorimeter, partly in the shielding block of the calorimeter and partly on the last part of the rotating shielding. The cantilevering of the dipole in the CMS appears more problematic than in the ATLAS case where, on the contrary, the shielding opens in the vertical plane (Fig. 5.9).

The solutions for a mechanical supporting structure compatible with an easy and fast maintenance of the detector and for the piping of all the dipole services (cables from the power supply, cryogenics, quench protection system...) have to be studied.

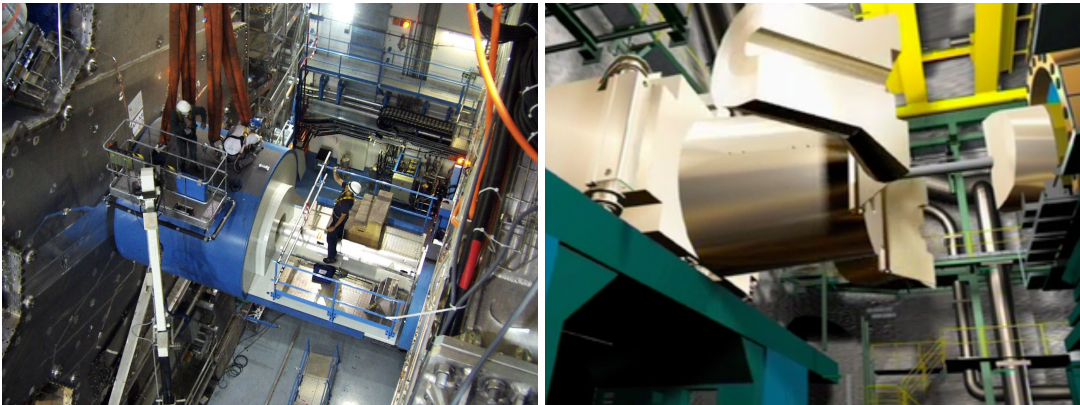


Figure 5.9: The proposed position of the D0 dipole in the experiment. The forward shielding of ATLAS, *right*, and the rotating shielding of CMS, *left*, are shown. The Interaction Point is at the left of each picture. Courtesy of the ATLAS and CMS collaborations.

5.2 The power deposited on the D0 dipole by the collision debris

The magnets of the Early Separation Scheme have to use superconducting technology because of their relative high integrated magnetic field and due to the space constraints in the detectors (for the D0) and in the machine (for the OC). In the following we consider Niobium-Titanium alloy (Nb-Ti) or Niobium-Tin compound (Nb₃Sn) superconductors: the first is extensively adopted in all superconductive collider, the latter has not yet been adopted in an accelerator but a lot of research on stand alone dipole and quadrupole prototype is on going. These superconductors implies (for our specific needs, see Section 5.3.2) the use of cryogenic temperature between 1.9 and 4.2 K.

The interaction region is an harsh environment especially for superconducting magnets since the protons interacting at the collision point (the so-called primary particles or simply primaries) produce a large quantity of secondary particles (collision debris) that deposit their energy on the components of the detectors and of the machine. This can affects the superconducting magnets in several ways:

- even a tiny quantity of power (few mW/cm³) locally deposited on the superconducting cable can cause an increase of its temperature and a consequent phase transition from the superconducting to the normal conducting state. This transition is generally referred to as *quench*,
- the total amount of power deposited on the cryostat requires an equivalent cryogenic power to keep the dipole at constant temperature,
- the debris can activate the dipole making it more difficult to be handled,
- the debris can accelerate the aging of the magnet, mainly for the radiation damage induced on its organic materials.

The first two items can be addressed studying the peak power deposited on the dipole's coils and the total power deposited in the cryostat. The latter two problems (activation and aging of the magnet) are not considered at this stage of the study and are a more general problem connected to the increase of integrated luminosity of the machine.

In the following, after some considerations on the debris composition coming from the Interaction Point (IP), we study the energy deposition on the D0 magnet using the FLUKA software [74]: a Montecarlo code to quantify the interaction between particles and matters. The case of the OC magnet is not analyzed: due to its position, that allows a more effective shielding strategy, and its magnetic field, that allows a higher temperature margin on the superconductor, it is less difficult to dimension than the D0 magnet.

5.2.1 The debris from the Interaction Point

Assuming an instantaneous luminosity, L , of $10^{35} \text{ cm}^{-2} \text{ s}^{-1}$ the total debris power coming out from the Interaction Point (IP) is

$$\text{total debris power} = \underbrace{L \sigma}_{\text{Events per second}} \times \underbrace{14 \text{ TeV}}_{\text{Energy per event}} \simeq 18 \text{ kW}$$

where we consider $\sigma = 80 \text{ mbarn}$ (non-elastic proton-proton cross-section at $\sqrt{s} = 14 \text{ TeV}$, see Fig. 1.3) since the elastic collisions have no impact on the power deposited on the machine devices under study [75]. This means that 9 kW of debris power are projected on the left and on the right of the collision point: in the nominal LHC, assuming an instantaneous luminosity of $10^{34} \text{ cm}^{-2} \text{ s}^{-1}$, it is reduced to 0.9 kW.

Before computing the power deposited on the coils we analyze the debris composition coming from the IP using the DPMJET code [76], embedded in FLUKA, for simulating the interactions between high energy particles.

From each proton-proton collision (pp collision), ≈ 110 secondary particles emerge on average. In Fig. 5.10, *top*, we show the composition of the debris with respect to the total energy contribution, i.e., out of the 14 TeV emerging from the Interaction Point for each pp collision, almost 4 TeV are carried by protons. We can observe that most part of the energy (more than the 80 % of the total) is carried by protons, neutron and pions. The neutral and charged pions will decay respectively in photons and muons. The amount of antimatter coming out is negligible (less than 3 % out of the 18 kW). The positive, neutral and negative particles corresponds to, respectively, the 45, 40 and 15 % of the total power of the debris.

In Fig. 5.10, *bottom*, we show the total energy distribution of the particles that contribute mostly to the total power of the debris, namely protons, neutrons and pions. From the figure we can, for instance, observe that almost 6 % of the total number of the protons of the debris particles have an energy around 7 TeV and more than 25 % of neutron and protons have an energy larger than 1 TeV. Pions have, in average, a smaller total energy. This means that a large fraction of the total power of the collision debris is carried by high energetic protons, with a high magnetic rigidity.

An other important information to keep in mind is shown in Fig. 5.11. In this plot we represent the power distribution with respect to the polar angle, ϕ_s with $0 \leq \phi_s \leq \pi$, that is the angle relative to the alignment orbit of the machine or, equivalently, the detector's axis (Fig. 5.12). We show on the plot (Fig. 5.11) two different curves corresponding to a full crossing angle between the beams, θ_c , of 0 and 1 mrad. We consider a statistic upon 1000 pp collisions. It is possible to observe that the power of the debris coming out from the collision point is extremely collimated: most of it is concentrated within an angle of 2 mrad from the detector's axis. This is true even for the full crossing angle of 1 mrad: in this case, as expected, an offset of 0.5 mrad of the peak of the distribution can be observed.

Assuming a normalized inner separation $\Delta_{in} = 12$, a β -function at the Interaction Point $\beta^* = 0.15 \text{ m}$ and a beam emittance $\epsilon = 5 \cdot 10^{-10} \text{ m}\cdot\text{rad}$, the corresponding θ_c is $\approx 0.7 \text{ mrad}$ (see Eq. 1.6). Then, assuming an inner radius, R_{in} , of the D0 magnet of 50 mm and the dipole's end being at 15 m from the IP, all the magnet is positioned at $\phi_s \Rightarrow 3.3 \text{ mrad}$. The conclusions that we can draw, in the approximation that during the

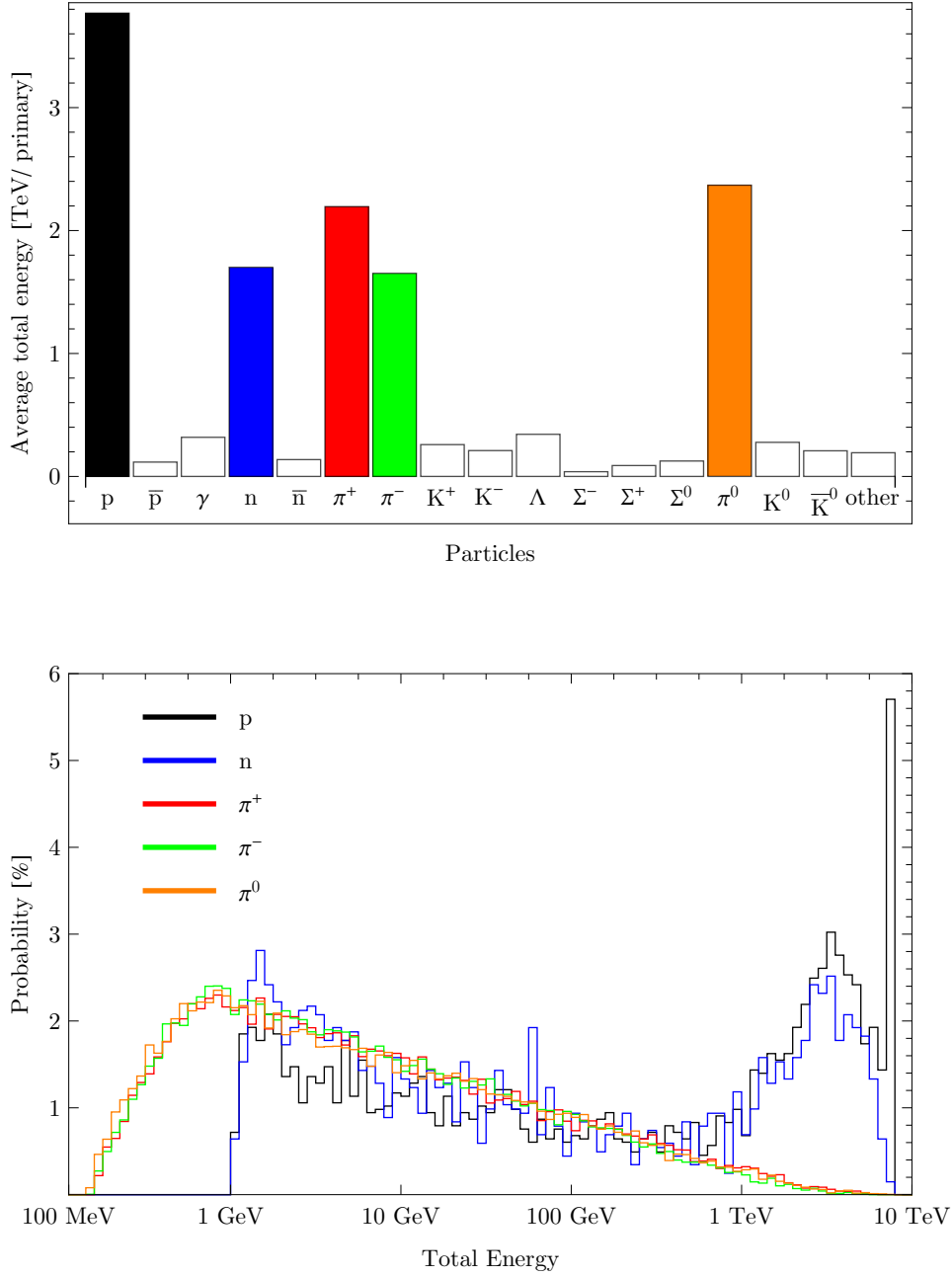


Figure 5.10: The debris particles emerging from the Interaction Point. We show, *top*, the debris particles with respect to their energy contribution, e.g., out of the 14 TeV emerging from the Interaction Point, almost 4 TeV are carried by protons. We show, *bottom*, the total energy distribution of the particles that contribute mostly on the total power of the debris, namely protons, neutrons and pions, e.g., almost 6 % of the total number of the protons of the debris particles have an energy around 7 TeV.

decays of the secondaries the energy distribution is conserved and is not affected by the D0 magnetic field, are:

- the dipole is not directly exposed to the most intense cone of the debris particles,
- the effect of the crossing angle on the power distribution for $\phi_s > 1.5$ mrad (and therefore on the D0)

is strongly reduced (see Fig. 5.11): we do not expect a large effect of the beam crossing angle on the power deposited on the D0 magnet.

In the following section we present the result of the simulations on the total and the peak power deposited on the D0 dipole.

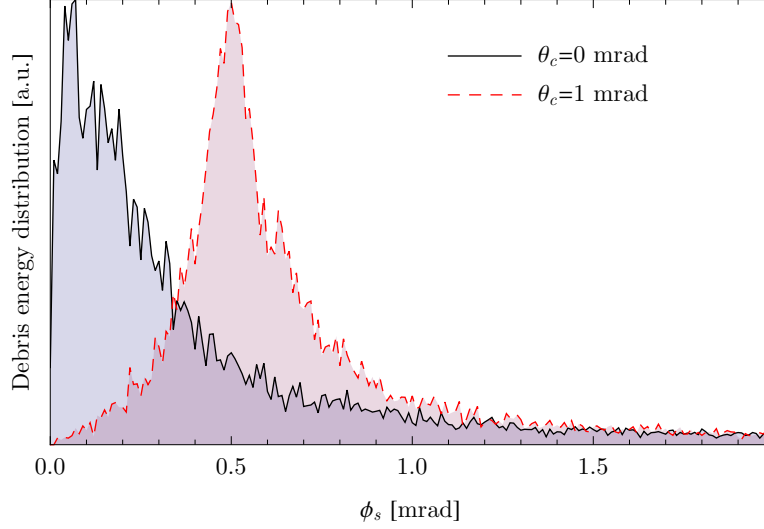


Figure 5.11: The distribution of the energy of the collision debris with respect to the polar angle with the detector axis, ϕ_s (see Fig. 5.12).

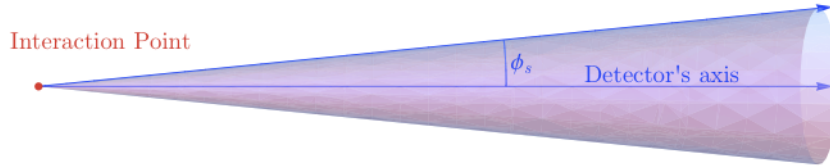


Figure 5.12: The polar angle ϕ_s .

5.2.2 The simulations of the power deposition on the D0 dipole

A power deposition study on the D0 dipole has been carried out using the FLUKA code [74] over a statistic of at least 10^4 pp collisions. We make the following assumptions and approximations

- the peak luminosity is $10^{35} \text{ cm}^{-2}\text{s}^{-1}$,
- the divergence of the primaries particles with respect to the beam closed orbit and the crossing angle is negligible,
- the detector field is negligible,
- the magnet is modeled with a 60° copper sector coil with aluminum collars (see Fig. 5.13). No other elements of the detector or of the magnet are considered in the simulation. The D0's inner radius, R_{in} , ranges from 50 to 70 mm. Its outer radius is referred to as R_{out} . The length and the field of the D0 is chosen to be compatible with the 13 m starting position of the cryostat and the 14 m D0' center assumption: this yields to a D0's coil length of ≈ 1.6 m (it starts at 13.2 m from the Interaction Point)
- the D0 field assumed for the power deposition simulations is of 10 T: an ideal dipolar field in the D0's aperture without fringe effect due to the dipole's ends.

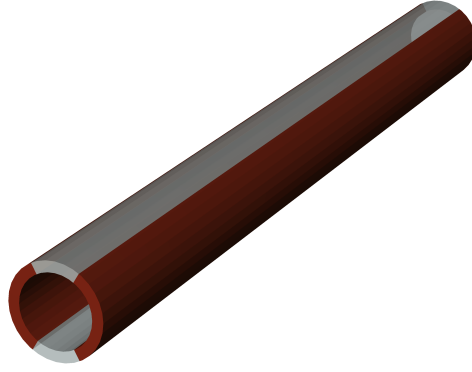


Figure 5.13: The simplified model of the D0 magnet used in the simulation.

In the following plots we consider mainly two quantities: the average power deposited and the peak power deposited.

The average power deposited or dynamic heat load (measured in W/m) is the power deposited per unit of magnet length averaged on the dipole cross-section. The maximum value that can be tolerated by the dipole depends essentially on the cryogenics serving the magnet and on the cryogenic line that can limit the power extraction (namely the cross-section of the piping and the helium pressure). As comparison, the cryogenic system of the nominal final focusing quadrupoles (triplet) has been dimensioned for a dynamic heat load of 10 W/m at 1.9 K (the triplet's operating temperature).

The peak power deposition (measured in W/cm³) represents the maximum density of the power deposited on the cross-section of the dipole in a particular longitudinal position. It can depend on the statistics and on the size of elementary volume where it is evaluated (binning size). The elementary volume that we are considering consists, along the transversal plane, of 1 deg circular sector between the inner radius and outer radius of the hollow cylinder representing the D0 (see Fig. 5.13) while the length of the elementary volume, in the longitudinal direction, is 10 mm. This volume is considered representative of region occupied by 10 mm of superconducting cable. We assume that the maximum value of the peak power deposition that can be tolerated on the superconductor are 4.3 and 12.3 mW/cm³, respectively, for the Nb-Ti [19] and for the Nb₃Sn [77]: the Nb₃Sn is able to cope with three times higher power density than the Nb-Ti. In the following plots, we represent on the same plane the average power deposition (black curves and left scale) and the peak power deposition (red curves and right scale).

In Fig. 5.14 we report the results of the average and the peak power deposited on the D0 magnet for three different cases: without shielding, with shielding, with shielding but without considering the D0 magnetic field. We assume an inner radius $R_{in} = 50$ mm and an outer radius $R_{out} = 60$ mm. We can observe that the heat load of the solution without shielding can exceed the 200 W/m and that the peak power deposition can reach, in some positions of the magnet, the 80 mW/cm³ that is far beyond the limit of the known technologies. Even if the aperture of the magnet is relative large ($R_{in} = 50$ mm to compare with 28 mm of the LHC arc dipole) a shielding is required to protect the coils from the debris particles.

We try to limit as much as possible the use of the shielding in order not to increase the background noise level in the experiments: for example we do not use shielding material around the vacuum pipe (so-called *liners*). We protect the D0 dipole using a 150 mm ring of tungsten positioned at 13 m with an inner radius of ≈ 50 mm and an outer radius equal to the D0 outer radius (60 mm). The effect of the shielding on the dynamic heat load is evident: the average power deposition stays below the 50 W/m and the maximum peak deposition is ≈ 15 mW/cm³.

To see the amplitude of the effect of the dipole magnetic field we switched it off in the simulation (see Fig. 5.14). The patterns of the average and peak power deposition are similar in the cases with and without the magnetic field only the first half of the D0 length. On the contrary, in the second half, the bending effect of the dipole is clear: the secondaries with a reduced magnetic rigidity are pushed toward the coils depositing power. This increases the overall heat load but has a minor impact on the peak energy deposition.

To evaluate the effect of the magnet aperture on the heat load, we study three different dipoles with $R_{in} = 50, 60$ and 70 mm. The dimension of the shielding ring is conveniently modified and, assuming a coil thickness of 15 mm we modified the R_{out} ($R_{out} = R_{in} + 15$ mm). The results of the peak power deposition are shown in Fig. 5.15: the Nb-Ti and Nb₃Sn limits are explicitly reported. The total power deposition decreases

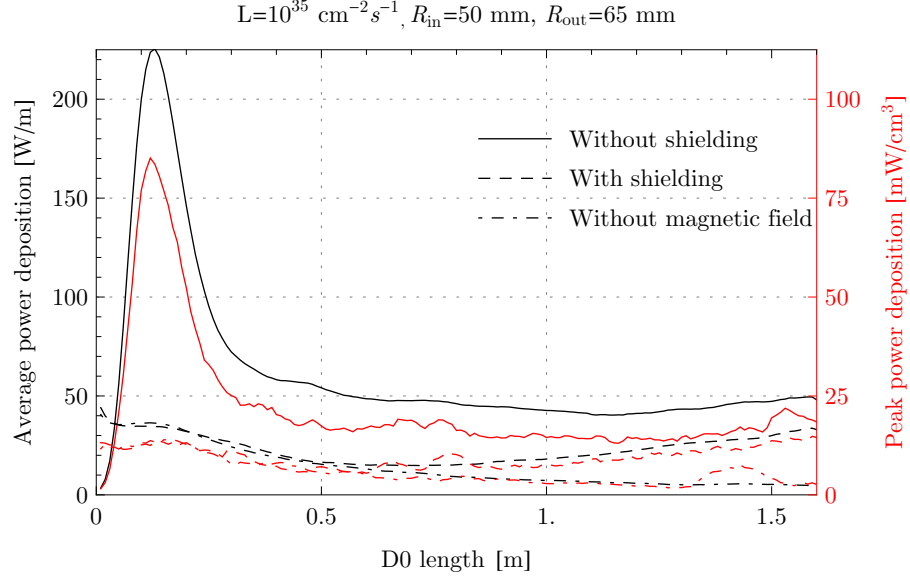


Figure 5.14: The average (black curves, *left scale*) and peak power (red curves, *right scale*) deposition along the D0 dipole. Three cases are represented: the magnet without shielding, the shielded magnet and the shielded magnet without including its magnetic field.

by increasing the magnet aperture and it is, for the previous three cases, 34, 28, and 20 W respectively.

A D0 dipole with 60 mm inner radius appears adequate: in order to cope with the peak power deposition and with the field required ($\approx 10 \text{ T}$), the Nb_3Sn superconductor is required.

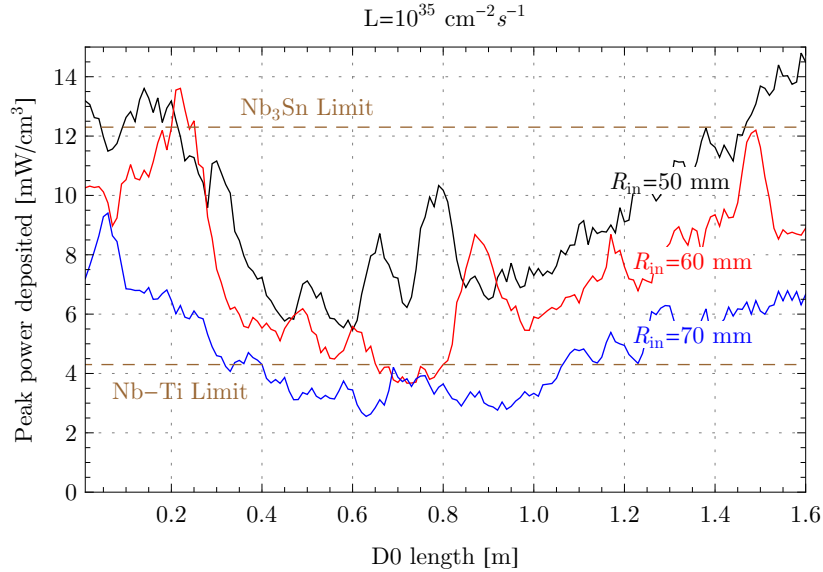


Figure 5.15: The average and peak deposition on the D0 magnet as function of its aperture. Three different inner radius are considered ($R_{\text{in}} = 50, 60$ and 70 mm).

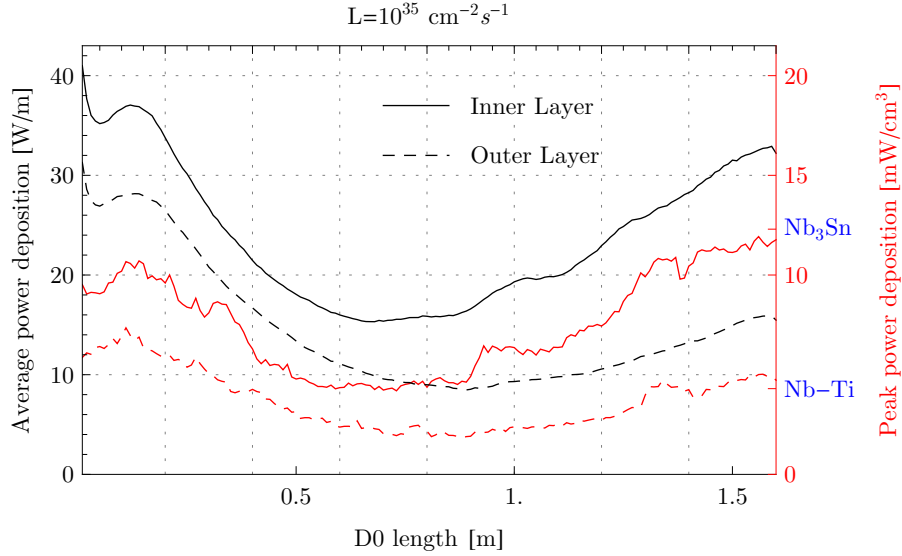


Figure 5.16: The average power deposition on the D0 dipole inner and outer layer.

To achieve the 14 T·m on a coil length of 1.6 m, we need to design 9 T magnet cross-section: as we show in the Section 5.3, due the large aperture, this field level can be reached only considering at least two layers of superconducting coil. Since, as we discuss in Section 5.3, we consider a 15 mm large superconducting cable, the two layers of the D0 dipole can be modeled with a hollow cylinder with $R_{out} = R_{in} + 2 \times 15 \text{ mm} = 90 \text{ mm}$.

The simulation results for this last case are shown in Fig. 5.16 where we present the results for the inner layer and outer layer coils on separate curves. We used a statistic of 20000 particles: it is possible to see that the noise on the peak power deposition, the quantity that requires a higher statistic, is significantly reduced passing from 10000 particle (in Fig. 5.15) to 20000 (Fig. 5.16).

The total power deposited on the D0 dipole model is $\approx 62 \text{ W}$. If we compare it with the 200 W deposited at 1.9 K, at the LHC nominal luminosity, on the four quadrupole units of the triplets, it appears significant but still within reach. In fact even if the model does not include neither the complete aluminum collar neither the iron yoke, we expect that the collar contribution is small due to the lower density of the material with respect to the superconductor. The iron yoke could be external to the cryostat (warm iron yoke): in this configuration it would have no direct impact of cryogenic power required. Furthermore, with the leveling, halving the peak luminosity of the machine, would halve the cryogenic power required too. The plot (Fig. 5.16) confirms that the Nb-Ti is not adequate for this dipole and, as we point out on the next section, a Nb₃Sn superconducting cable can achieve 9 T magnetic field target at 4.2 K, therefore depositing power at 4.2 K instead of at 1.9 K would further reduce the cryogenic requirements.

5.3 The D0 magnet preliminary design

In the previous two sections of the chapter, we developed the motivations for positioning the D0 dipole of the Early Separation Scheme in a 2 m cryostat between 13 and 15 m from the Interaction Point and we showed that, assuming an effective coil length of 1.6 m, the required field of the dipole is 9 T: a superconducting magnet is therefore required. The energy deposition from the debris particle, even if minimized enlarging the dipole aperture and considering a tungsten shielding ring, is significant. For this reason and for the high magnetic field required, the Nb₃Sn superconductor technology is considered.

The design of a superconducting magnet is a topic largely discussed in the dedicated literature [78, 79]. In this section we consider some peculiar features of the D0 dipole giving preliminary results: our aim is not to have a complete design of the dipole but to show its feasibility using Nb₃Sn superconductor.

The main feature of this dipole is the large aperture chosen due to the power deposition issue and not due to the beam dimension, as in general happens for accelerator magnets. The large aperture and the high

magnetic field induce large mechanical stresses on the superconducting coils: these stresses may significantly degrade the performance of the Nb₃Sn cable. For this reason, in order to dimension the D0 dipole, we have to consider the use of the superconductor with respect to both its magnetic and its mechanical limits, as shown in the following section.

5.3.1 The mechanical stresses on the D0 dipole's coils

In this section we study, using the approach and scaling laws developed in [79] and [80], the D0 dipole field as function of the D0's aperture and the coils width assuming a 60° sector coil design [79]: this configuration, despite its simplicity, is sufficiently representative for a large configuration of superconducting dipole based on sector coil geometry [78].

We make the following assumptions:

- the maximum stress on the superconducting coils must not exceed the 150 MPa: the actual limit of the Nb₃Sn superconductor is still controversial and might be larger,
- the fitting of the Nb₃Sn critical surface is the one proposed in [79] and corresponding to the original aim of superconducting cable developed in the framework of the LHC Accelerator Research Program and of the Next European Dipole [81]. This means a maximum current density in the superconducting material of 3700 and 3000 A/mm² at 12 T at the temperature, respectively, of 1.9 and 4.2 K.
- we are considering a total filling factor of the cable $k = 0.29$ [79]: this is due to the area occupied by the copper stabilizer, the voids between the strands and the isolation of the cable and it is the ratio between the maximum current density in the insulated cable and the maximum current density in the superconductive material of the strands. With $k = 0.29$ a current density of 3000 A/mm² on the superconducting material reduces to 870 A/mm² averaged on the insulated cable cross-section (engineering current density).

In Fig. 5.17 we show the result of the analysis for the different aperture of the D0 dipole: $R_{in} = 50$ (*top*), 60 (*middle*), 70 mm (*bottom*). In the plane we adopted, the magnetic field on the dipole's aperture is shown with respect to the coils' width of the dipole. We show:

- the limit of the superconductors with the four curves: two for the Nb₃Sn and, for comparison, two for Nb-Ti cables at the temperature of 1.9 K and 4.2 K. The curves already include a 20% margin on the maximum magnetic field,
- the limit of the mechanical stress: the shaded area represents the region where the maximum stress in the coil is below the 150 MPa.

From this plot it is possible to conclude from a quantitative point of view that using the Nb₃Sn, due to the large aperture required, the D0 is limited by the mechanical stresses. For an aperture of $2 \times R_{in} = 120$ mm and with a coils thickness of 30 mm it is possible to reach the 9 T field with a small margin with respect to the mechanical stress and with a large margin (30%) in terms of magnetic field at the temperature of 4.2 K: for a constant power deposition, working at 4.2 instead of 1.9 K, saves $\approx 60\%$ of the cooling power required by the cryogenic system. An aperture of $2 \times R_{in} = 100$ mm would be less demanding from the mechanical point of view of the dipole but would increase the energy deposition (see Fig. 5.15): we propose a D0 dipole with an aperture of 120 mm.

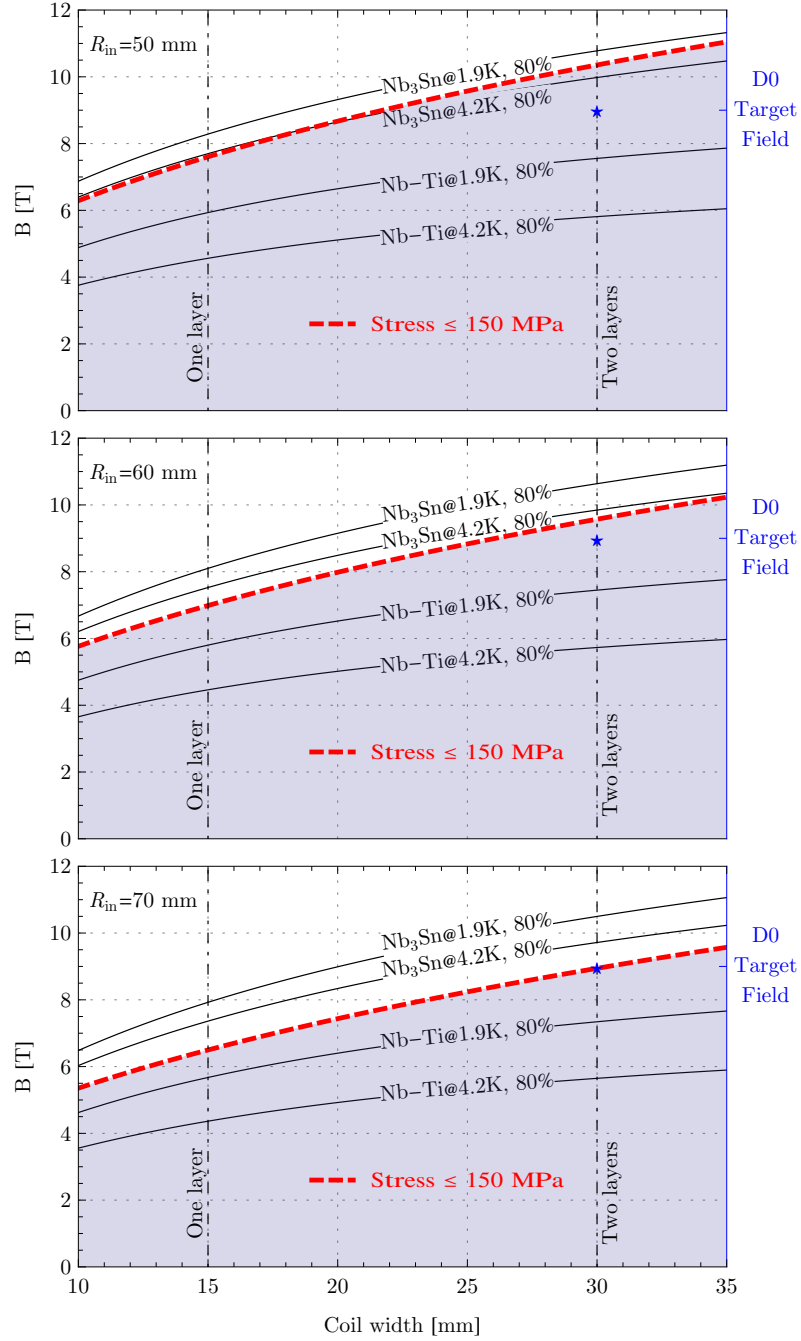


Figure 5.17: The D0 magnetic field for different coil thickness. The magnetic limit of the different technology and different temperature is shown (assuming a 20% margin, therefore at 80% of the short sample field). The shaded area represents the region in this plane where the maximum stress in the coil is below the 150 MPa.

5.3.2 A preliminary cross-section for the D0 dipole

Following the results of the previous section, for an aperture of 120 mm ($R_{in} = 60$ mm), a coil width of ≈ 30 mm is required: this implies the use of, at least, two layers of superconductors. In order to reduce the complexity of the model and, therefore, to increase its reliability, a two layers cross-section has been chosen. We assume to use the same cable for the two layers. This implies a cable width of 15 mm: we consider a Rutherford cable, with 1.27° keystone angle [78], composed by 2×15 strands of 1 mm of diameter.

The β -function at the position of the D0 dipole's end (15 m from the Interaction Point, IP) is ≈ 1500 m assuming a β -function at the collision point of 0.15 m (see Eq. 1.10). Assuming a beam separation of 12σ and allocating $2 \times 6\sigma$ for the beam halo, the beam envelope diameter is 24σ . This yields a physical radius of the beam envelope, R_{beam} , of $12\sigma = 10$ mm: in fact $\sigma \approx 0.85$ mm at 15 m from the IP (given $\epsilon = 5 \cdot 10^{-10}$ m-rad and $\beta = 1500$ m). For the D0 dipole, the ratio magnet-aperture/beam envelope is relative large ($R_{in}/R_{beam} = 60$ mm/10 mm = 6). This, together with the relative small integrated field of the D0, the reduced number of D0 dipoles in the machine and the fact that they are switched off during the injection and the acceleration phases, makes the D0 field quality less critical with respect to the one typically required in other LHC magnets (e.g., the final focusing triplets or the arc dipoles).

In Fig. 5.18 we propose a preliminary cross-section of the D0 dipole. To reach 9 T field in the aperture a 13 kA power supply is needed. No iron yoke is considered at the moment: it has still to be verified the effect of the CMS solenoidal field on it and, secondly, it is still to be decided whether to use a warm or cold iron yoke, that is if consider the yoke outside or inside the cryostat.

We propose, Fig. 5.18, an inner layer with three blocks (with 20, 10 and 9 conductors) and an outer layer consisting of a single block (42 conductors). To evaluate the quality of the magnet its multipolar content is analyzed [22][78]: in fact, a real dipolar magnet would have high multipolar components like quadrupolar, sextupolar, etc., components. The actual positioning of the superconductor cables aims to reduce as much as possible this spurious magnetic content that can badly affect the beam dynamics. For an accelerator quality magnet the unwanted multipolar components should be around 10000 weaker than the principal component of the field (i.e., the dipolar component for a dipole, the quadrupolar component for a quadrupole...). From a mathematical point of view we can express the vector components of the field in terms of multipolar expansion: for a purely transverse magnetic field ($\vec{B} = \{B_r, B_\theta, B_s = 0\}$) in a domain where $\nabla \times \vec{B} = 0$ (i.e., in the magnet aperture without beam) the B_θ can be expressed as

$$B_\theta(r, \theta) = B_{ref} \sum_{n=1}^{\infty} (b_n \cos(n\theta) + a_n \sin(n\theta)) \left(\frac{r}{R_{ref}} \right)^{n-1} \quad (5.1)$$

where B_{ref} and R_{ref} are, respectively, the reference magnetic field and the reference radius used for the multipolar expansion. For the D0 we consider $B_{ref} = 9$ T that is its dipolar field: in our specific problem, due to linearity (absence of iron yoke), the b_n and a_n coefficients do not depend on the actual value of the dipolar field. The multipolar content of the D0 is evaluated at the $R_{ref} = 2/3 R_{in} = 40$ mm. Since the layout of a dipole has, ideally, a particular symmetry and orientation, only odd normal multipoles are allowed ($b_n = 0, n \in \{2, 4, 6 \dots\}$) and the skew multipoles vanish ($a_n = 0, n \in \{1, 2, 3 \dots\}$). After a first optimization we performed using the ROXIE code [26], the allowed magnetic multipoles until b_{11} are reported in Table 5.2. The multipoles b_7 , b_9 and b_{11} are still moderately large but their final optimization can be pushed when the geometry of the iron yoke will have been defined.

Table 5.2: The multipolar content of the proposed D0 cross-section.

Multipole	Value [10^{-4}]
b_1	10^4 .
b_3	0.0014
b_5	0.0095
b_7	2.5292
b_9	-3.7235
b_{11}	1.9666

It is interesting to compare the multipolar content of the D0 with the equivalent one of a single beam-beam interaction at the nominal LHC bunch population ($N_b = 1.15 \cdot 10^{11}$ ppb). The magnetic part of the electromagnetic field of the bunch does not have a multipolar component ($\nabla \times \vec{B}_{beam} \neq 0$). Nevertheless, at sufficiently large distance from the beam center, d , (i.e., $d = 10\sigma$ of the beam, assuming round beam) we can approximate the effect of the beam electromagnetic field with the effect of the magnetic field produced by a wire (see Section 3.2.2) placed at the beam center with a length L_w and with a current I_w given by the Eq. 3.34, reported for the reader's convenience

$$I_w L_w = q c N_b.$$

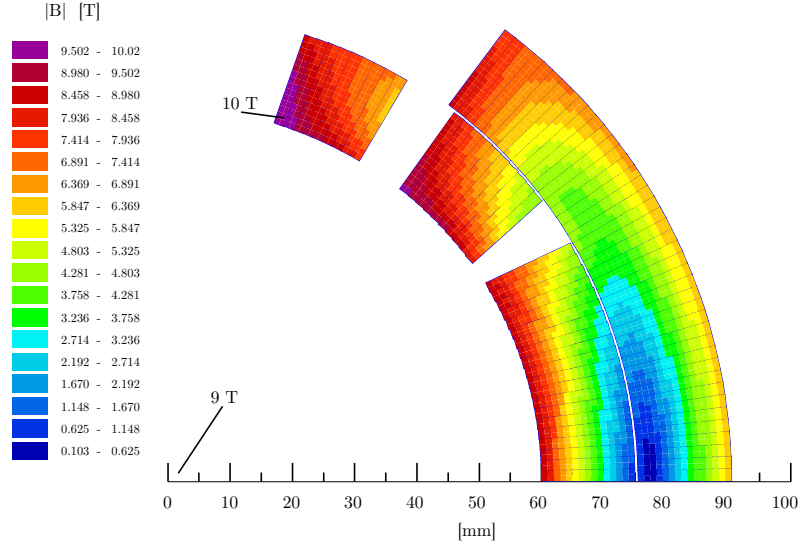


Figure 5.18: The preliminary cross-section considered. The value of the magnetic field shown corresponds to a magnetic field in the aperture of 9 T.

The multipolar expansion of the wire positioned in $\{x, y\} = \{d, 0\}$ is [51]

$$B_\theta(r, \theta) = -\frac{\mu_0 I_w}{2\pi d} \sum_{n=1}^{\infty} \cos(n\theta) \left(\frac{r}{d}\right)^{n-1}, \quad (5.2)$$

that is $b_n = 1$ and $a_n = 0$ for $n \in \{1, 2, 3, \dots\}$ considering $B_{ref} = -\frac{\mu_0 I_w}{2\pi d}$ and $R_{ref} = d$ (Eq. 5.1).

To compare the effect of the multipolar content of the D0 with that of wire, we have to compare the integrated multipolar components of the D0 with the integrated multipolar components of the wire assuming the same reference radius and considering that the D0 length is 1.6 m and the wire's length is L_w . Since the beam is not supposed to pass in the D0 center we should consider a feed down of the D0 multipolar content to the actual position of the beam. We computed it by moving the center of the multipolar expansion on the assumed beam position ($-d/2$) observing that the result we obtain does not significantly change: the beam distance from the magnetic center is small with respect to the reference radius of the magnet ($d/2 \approx 5 \text{ mm} \ll R_{ref} = 40 \text{ mm}$). Defining as K_n the ratio between the integrated multipole b_n of the D0 dipole and the wire, we have

$$K_n = \frac{L_{D0} \times B_{D0} \times b_n}{L_w \times \frac{\mu_0 I_w}{2\pi d} \times 1} \left(\frac{d}{R_{ref}}\right)^{n-1} \quad (5.3)$$

where the factor $\left(\frac{d}{R_{ref}}\right)^{n-1}$ is necessary to rescale the multipolar component of the D0 to the reference radius d of the wire (see Eq. 5.2). The numerical value of K_n are reported in Table 5.3 (for $d = 10 \sigma = 8.5 \text{ mm}$ and considering the values in Table 5.2): apart from the main component of the D0 field that is by far larger than the wire effect, we observe that even a single beam-beam encounter at nominal current has a multipolar content by far larger than the one of D0 dipole considering the proposed cross-section. The numbers in Table 5.3 confirm what emerges from the simulations, that is the beam-beam effect dominates over the non-linearities of the machine lattice.

The magnetic load line of the D0 coils is shown in Fig. 5.19. The ratio between the peak field on the coil (10 T) and the field in the aperture (9 T) is 1.11. This relatively high value is due to the small coil thickness with respect to the aperture radius: this choice is related to the power deposition issue, with a minimization of dense material, namely superconducting cable, in the cryostat.

With a central field of 9 T the energy stored in the dipole is of the order of 1 MJ (to compare with the 6 MJ of the double aperture LHC arc dipole): the dimensioning of the D0 quench protection system and D0 cryostat are not addressed in this work and have to be designed. Ideally, if compatible with the power that can be dissipated in the coil and the voltage that can be withstood by the dipoles during the quench, the Early Separation dipoles should be connected in series. This would prevent, even in case of a quench,

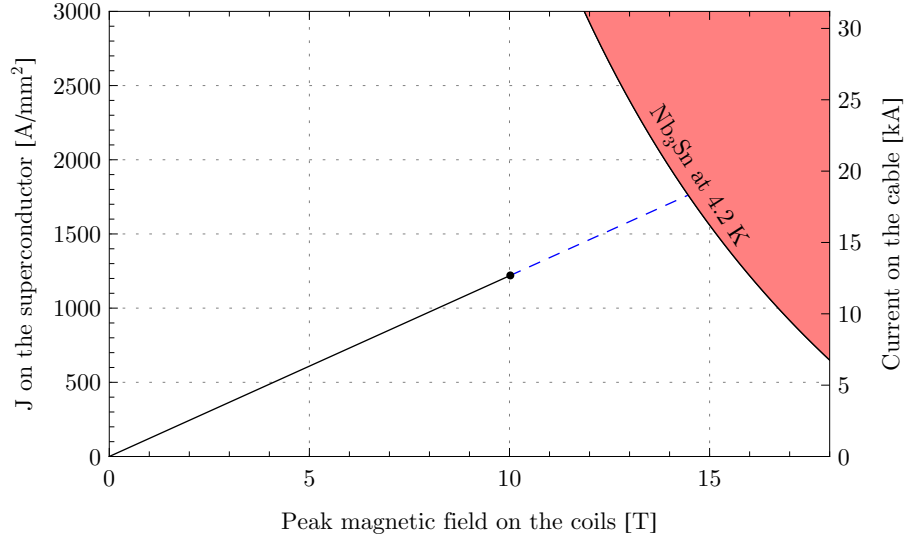


Figure 5.19: The magnetic load line of the the D0 dipole.

Table 5.3: The ratio between the integrated multipole b_n of the wire and the D0.

K_n	Value
K_1	$1.1 \cdot 10^5$
K_3	$6.9 \cdot 10^{-4}$
K_5	$2.1 \cdot 10^{-4}$
K_7	$2.6 \cdot 10^{-3}$
K_9	$-1.7 \cdot 10^{-4}$
K_{11}	$4.0 \cdot 10^{-6}$

to affect the overall closed orbit of the machine: the Early Separation bump, during the dipoles discharge, would slowly vanish remaining always closed. If the Early Separation dipoles cannot be connected in series, in case of quench we expect, due to the small amplitude of the Early Separation bump and the inductances of the magnets, that the interlock system and the collimators of the collider can easily protect the machine and the detectors. Nevertheless a quantitative study of the different quench scenarios has not been considered in this work and has still to be addressed.

Conclusions

In this thesis we evaluated the potential of the Early Separation Scheme for the Phase II of the LHC Luminosity Upgrade (sLHC) and we proposed a preliminary layout of the scheme. The ambitious target of the sLHC can be achieved by an Early Separation Scheme working in synergy with an increased beam current and with a stronger final focusing of the collider. We assumed that it is possible:

- to double the machine beam current with respect to the nominal one by keeping the same bunch separation (25 ns, 2808 bunches) and doubling the bunch charge ($N_b = 2.3 \cdot 10^{11}$ ppb). We pointed out that in sLHC, in contrast to other colliders, an increase of the beam current is, in practice, necessary in all upgrade scenarios,
- to reduce the β -function at the Interaction Point (β^*) from the nominal value, 0.55 m, to 0.15 m.

We showed that sLHC can reach the 3000 fb^{-1} in a period of 6.5 – 7 years with less than 150 proton-proton interactions per bunch crossing. This relatively low multiplicity is possible thanks to the luminosity leveling strategy we presented. Without the Early Separation Scheme, for the same beam and machine conditions (beam current, peak luminosity and machine turn-around time), 9 years of data acquisition are needed for achieving the same target, while, replacing the Early Separation Scheme with a Crab Crossing Scheme, this data acquisition time could be reduced to 5.5 years. All these figures help to compare the different solutions but convey only a partial picture. Each upgrade scenario has a different impact on the dynamics of the beam with possibly different beam lifetime; they have different complexities during the operation corresponding to different turn around times for the machine; they require a different time for commissioning and maintenance impacting differently on the overall luminosity performance.

The study of the Early Separation Scheme encompasses three major aspects:

- the beam dynamics,
- the integration of the scheme in the detectors,
- the magnet technology.

We studied the impact of the Early Separation Scheme on the beam dynamics by evaluating its linear and non-linear effects. All induced linear effects turned out to be negligible making almost straightforward the luminosity leveling. The non-linear effects, namely the beam-beam effect, are considered showing that under specific conditions it is possible to compare different non-linear machines by means of scaling laws. These are important to rescale to sLHC the beam-beam experience of other colliders and to simulate the beam-beam excitation of sLHC in other machines. Using this approach, we performed several experiments in the Super Proton Synchrotron (SPS) by using a wire carrying an electrical current to mimic a second beam in this synchrotron. We used different SPS cycles and different beam momentum (37, 55, 120 GeV/s): the global picture emerging from the experiments is that few beam-beam encounters at reduced normalized separation have a significant impact on the beam lifetime. We could observe, at the beam energy of 120 GeV, the time constants involved in the beam-wire interaction and this helped in understanding the behavior and the limits of the observation done at lower energy.

To simulate the beam-beam effect in the sLHC and the SPS experiments we use as indicator of particle stability their amplitude blow up: to have a sufficient detailed description of the beam a large number of particles is required to be tracked, therefore we wrote a high performance code running on multicore graphics cards to make tracking studies. With these simulations, we reproduced some of the SPS experimental results and we concluded that the beam-wire interaction appears much stronger than the actual beam-beam interaction: this is especially true if we consider reduced separation interactions. These sets of simulated results and measured data are compared with the past operating experience of the SpS collider where there was a significant number of beam-beam interactions at reduced separation. From all these results and in relation to the positioning proposed for the dipoles of the scheme, the possibility to reach an inner separation

between the beams of 5σ appears to be unlikely even if we cannot exclude it. Nevertheless we think that, assuming 12σ beam separation in the triplet, an inner separation between 6 and 7σ can be achieved without compromising the beam stability.

Concerning the integration of the scheme in the detectors, we analyzed the different possible positions for the more critical dipole of the scheme (the D0) in the two high luminosity experiments, ATLAS and CMS. We opted for a common solution in the two experiments: the D0 and the OC dipoles' positions we proposed are respectively at 14 and 21 m (center) from the Interaction Point. The position of the D0 has been chosen in relation to the CMS constraints, more stringent than the ATLAS ones: the forward calorimeter is much closer to the Interaction Point in ATLAS than in CMS and, in addition, the interaction between the dipole's and the solenoid's magnetic field is much stronger in CMS than in ATLAS. A D0 at 14 m would be positioned after the CMS forward calorimeter and the end-cap yoke: it would be integrated in the rotating shielding of the CMS detectors and in the forward shielding block of ATLAS.

Given the magnetic integrated field required, superconducting technology has to be adopted. We optimized the dipole aperture and its shielding with respect to the power deposition of the collision debris. We propose a D0 aperture of 120 mm and to use a 150 mm thick shielding ring of tungsten in front of the dipole: assuming a peak luminosity of $10^{35} \text{ cm}^{-2}\text{s}^{-1}$, the power deposition on the D0's cryostat is $\approx 62 \text{ W}$ while the maximum peak deposition in the coils is 12 mW/cm^3 . The Nb-Ti superconductor cannot operate with such values of power density therefore the Nb₃Sn superconductor has been chosen.

We showed that the performance of the D0 is expected to be limited by the mechanical stress on the coils and not by the magnetic performance of the superconducting cable. In this condition it is natural to use the superconductor at a temperature of 4.2 instead of 1.9 K in order to reduce the cryogenics power required to cope with the dynamic heat load of the cryostat. We proposed a preliminary cross-section using two layers of superconducting cables and we obtained a field in the aperture of 9 T with a significant operational margin. This means that the D0 can deliver the requested integrated field in a 2 m long cryostat.

We showed that the Early Separation Scheme is feasible from the technical point of view. It can contribute significantly to the LHC Luminosity Upgrade adding greater flexibility during the machine operation by making possible to optimize the beam separation pattern with respect to the beam-beam effect observed in the collider. The strong point of the Early Separation Scheme, as compared to other options, is to minimize the beam dynamics and technological challenges. Combined with the Crab Crossing Scheme, it would mitigate the higher risks of the latter and thereby improve the robustness of the LHC upgrade.

Concerning the possible future developments of the work, in our opinion it is important to increase our understanding on the beam-beam long-range effect by making additional wire experiments in SPS at 120 GeV. At this energy, as we showed, it is possible to observe the steady-state beam losses induced by the wire: for rescaling the SPS behavior to the LHC, they convey much more information than the transient beam losses. The possibilities of replacing the SPS wires with new ones is presently under investigation: the new hardware would allow to make experiments at different beam emittances and at reduced beam-wire separation. In addition, it is interesting to investigate with tracking the compensation of reduced separation beam-beam long-range encounters using an appropriate multipolar lens instead of a wire.

The physics emerging from the LHC together with the performance of the nominal detectors will clarify if the D0 dipole can be integrated in the experimental caverns: at that stage a complete technical design of the Early Separation Scheme has to be produced in collaboration with the ATLAS and the CMS teams, encompassing all aspects related to the services and the piping of the cryogenics and the powering, the machine and detector protection in the different quench/failure scenarios, the mechanical cantilevering of the dipoles and its compatibility with the detector and machine maintenance.

Acknowledgments

I want to express my sincere gratitude to my supervisors Dr. J.-P. Koutchouk and Prof. L. Rivkin for their precious presence, invaluable help and continuous inspiration all along the preparation of the thesis.

I would like to thank Dr. E. Todesco and Prof. L. Rossi who have made available their support in a number of ways during the last three years. I am particularly indebted to Dr. W. Scandale, Dr. D. Tommasini and Dr. F. Zimmermann who helped me with advices, suggestions and by continuously fostering my own curiosity with their enthusiasm.

This work would not have been possible without the support of many experts who shared with me, in the most generous way, their experience in accelerator sciences. Among others, I would like to acknowledge G. Burtin, Dr. R. Calaga, Dr. U. Dorda, Dr. W. Fischer, Dr. J.-J. Gras, Dr. E. Laface, Dr. E. Métral, Dr. B. Salvant, Dr. R. Tomàs and Dr. J. Wenninger for the most enjoyable collaboration during the preparation and the realization of the beam-wire experiments. Regarding the magnet design and the power deposition studies, I am grateful to Dr. B. Bordini, Dr. F. Borgnolutti, Dr. F. Broggi, Dr. C. Hoa, Dr. F. Regis, Dr. S. Russenschuck and Dr. E. Wildner. In the framework to the HHH-CARE workshops and thanks to the initiative of Dr. P. Limon and Dr. E. Tsesmelis, fruitful interactions with the detector experts could take place: I am grateful to Dr. M. Nesi, for the ATLAS collaboration, and Dr. J. Nash, for the CMS collaboration.

To formulate an appropriate acknowledgment to my family is an extremely difficult task: there is too much to say and spelling it out in words could convey just a small part of the gratefulness I would like to express. My family show me what is worth to love and to work for: by observing what they did and daily do I took the will and the energy to accomplish this results.

Finally, it is a true pleasure to thank all my friends who make easier and amusing each single week in the last three years: I wish to dedicate my thesis to all them. Thanks to you all.

A handwritten signature in black ink, appearing to read 'Guido', written in a cursive style.

Bibliography

- [1] O. S. Brüning *et al.*, *LHC Design Report*. Geneva: CERN, June 2004, vol. 1.
- [2] “European Organization for Nuclear Research, <http://public.web.cern.ch/public>.”
- [3] O. S. Brüning *et al.*, “LHC Luminosity and energy upgrade: A Feasibility Study,” CERN, Geneva, Tech. Rep. LHC Project Report 626, December 2002.
- [4] A. Blondel *et al.*, “Physics Opportunities with Future Proton Accelerators,” in *Finalize Orsay Symposium Contribution*. Physics Opportunities for Future Proton Accelerators, 2006.
- [5] “The Tevatron luminosity web site, <http://www.fnal.gov/pub/now/tevlum.html>.”
- [6] “The sLHC web site, <http://project-slh.web.cern.ch/project-slh>.”
- [7] R. Ostojic, “LHC Interaction Region Upgrade-Phase I: goals and conceptual design,” in *Final CARE-HHH Workshop on Scenarios for the LHC Upgrade and FAIR*, 2008.
- [8] W. Scandale and F. Zimmermann, “LHC Phase-2 Upgrade Scenarios,” in *Final CARE-HHH Workshop on Scenarios for the LHC Upgrade and FAIR*, 2008.
- [9] M. Benedikt *et al.*, “Preliminary accelerator plans for maximizing the integrated LHC luminosity,” CERN, Tech. Rep. CERN-AB-2006-018, 2006.
- [10] V. M. *et al.*, “The LINAC4 project: overview and status,” in *Final CARE-HHH Workshop on Scenarios for the LHC Upgrade and FAIR*, 2009.
- [11] E. Shaposhnikova, “SPS upgrade,” in *Final CARE-HHH Workshop on Scenarios for the LHC Upgrade and FAIR*, 2009.
- [12] “SPS upgrade website, <http://paf-spsu.web.cern.ch>.”
- [13] K. Johnsen, “CERN Intersecting Storage Ring,” *Proc Natl Acad Sci*, vol. 70, no. 2, pp. 619–626, 1973.
- [14] H. Koziol and D. Möhl, “The CERN Antiproton Collider Programme: Accelerators and Accumulation Rings,” *Phys. Rep.*, vol. 403-404, pp. 91–106, November 2004.
- [15] *Design Report Tevatron 1 Project*. Fermi National Accelerator Laboratory, Sep 1984.
- [16] “Hera: A proposal for a large electron proton colliding beam facility at desy,” DESY-HERA, Tech. Rep. 81-10, 1981.
- [17] N. P. Samios, “RHIC: the early years,” *Journal of Physics G: Nuclear and Particle Physics*, vol. 34, pp. S181–S189, 2007.
- [18] A. W. Chao and M. Tigner, *Handbook of Accelerator Physics and Engineering*. World Scientific Pub Co Inc, 1999.
- [19] N. V. Mokhov *et al.*, “Protecting LHC IP1/IP5 Components Against Radiation Resulting from Colliding Beam Interactions.” CERN, Geneva, Tech. Rep. LHC Project Report 633, April 2003.
- [20] “The Particle Data Group website, <http://pdg.lbl.gov>.”
- [21] M. A. Furman, “The Møller Luminosity Factor, <http://mafurman.lbl.gov/LBNL-53553.pdf>,” Lawrence Berkeley National Laboratory, Bldg. 71R0259 1 Cyclotron Rd. Berkeley, CA 94720-8211, Tech. Rep. LBNL-53553, CBP Note-543, September 2003.
- [22] S. Turner, Ed., *Cern Accelerator School Fifth General Accelerator Physics Course*, ser. University of Jyväskylä, Finland. CERN, 1994, vol. 1.
- [23] A. Piwinski, “Computer simulation of the beam-beam interaction at a crossing angle.” *11th IEEE Particle Accelerator Conference Proceedings*, May 1985.

- [24] “General layout 6.5, (http://edms.cern.ch/cedar/plsql/navigation.tree?top=CERN-0000010259&open=CERN-0000010259&expand_open=Y).”
- [25] N. J. Sammut *et al.*, “Measurement and Effects of the Magnetic Hysteresis on the LHC Crossing Angle and Separation Bumps,” CERN, Geneva, Tech. Rep. LHC Project Report 1107, August 2008.
- [26] “The database of ROXIE input files for LHC superconducting magnets, <http://roxie93.web.cern.ch/roxie93>.”
- [27] 4th IEEE Particle Accelerator Conference, Ed., *Hourglass effects for asymmetric colliders*, vol. LBL-30833, 1991.
- [28] R. Calaga *et al.*, “LHC Crab Cavities,” in *Final CARE-HHH Workshop on Scenarios for the LHC Upgrade and FAIR*, 2008.
- [29] R. Calaga *et al.*, “Crab Compensation for LHC Beams,” CERN, Geneva, Tech. Rep. LHC Project Report 1136, Sep 2008.
- [30] *ATLAS Detector and Physics Performance Technical Design Report*. ATLAS Collaboration, May 1999, vol. 1.
- [31] M. Della Negra *et al.*, “CMS physics Technical Design Report,” CERN, Tech. Rep. LHCC 2006-001 TDR 8.1, Feb 2006.
- [32] K. Ohmi, “Study of beam-beam interaction with a large Piwinski angle at LHC,” *BEAM’07*, 2008.
- [33] R. Garoby, “Upgrade Issues for the CERN Accelerator Complex,” CERN, Geneva, Tech. Rep. LHC Project Report 1110, Sep 2008.
- [34] W. Scandale and F. Zimmermann, “LHC phase-2 upgrade scenarios,” in *Final CARE-HHH Workshop on Scenarios for the LHC Upgrade and FAIR*, CERN, Geneva, Switzerland, 2008.
- [35] “The SimulinkTM code, <http://www.mathworks.com/products/simulink/>.”
- [36] R. Garoby, “Spl at cern,” CERN, Geneva, Tech. Rep. sLHC Project Report 15, Oct 2009.
- [37] J.-P. Koutchouk *et al.*, “A Concept for the LHC Luminosity Upgrade Based on Strong β^* Reduction combined with a Minimized Geometric Luminosity Loss Factor,” CERN, Geneva, Tech. Rep. LHC Project Report 1067, June 2007.
- [38] W. Scandale and F. Zimmermann, “Two scenarios for the LHC Luminosity Upgrade,” CERN, Tech. Rep., 2007.
- [39] “LHC MadX optics v6.5 (<http://proj-lhc-optics-web.web.cern.ch/proj-lhc-optics-web/V6.5/>).”
- [40] F. Schmidt *et al.*, “MadX manual (<http://mad.web.cern.ch/mad/uguide.html>).”
- [41] S. Ross, *A first course in probability*, 7th ed., P. Education, Ed. Prentice Hall, 2006.
- [42] K. Cornelis *et al.*, “Beam-beam effects and high luminosity operation in the SPS proton antiproton collider,” CERN, Geneva, Tech. Rep. CERN-SPS-86-14-MS, 1986.
- [43] Y. Papaphilippou and F. Zimmermann, “Estimates of Diffusion due to Long-range Beam-beam Collisions,” *Phys. Rev. Spec. Top. Accel. Beams*, vol. 5, no. 7, p. 22 p, Jul 2002.
- [44] L. R. Evans *et al.*, “Beam-beam effects in the strong-strong régime at the CERN SPS,” CERN, Geneva CERN-SPS-89-12-AMS, Mar 1989.
- [45] W. Herr, “Dynamic behaviour of nominal and PACMAN bunches for different LHC crossing scheme,” CERN, Geneva, Tech. Rep. LHC Project Report 856, June 2005.
- [46] J. D. Jackson, *Classical electrodynamics*, 3rd ed. New York, NY, USA: Wiley, 1999.
- [47] “COMSOL Mytliphysics Modelling and Simulation, <http://www.comsol.com/>.”
- [48] J.-P. Koutchouk *et al.*, “Experiments on LHC Long-Range Beam-Beam Compensation in the CERN SPS,” CERN, Geneva, Tech. Rep. LHC Project Report 777, August 2004.
- [49] W. Fischer *et al.*, “Observation of long-range beam-beam effect in RHIC and plans for compensation,” no. EPAC-06, p. 3 p, June 2006.
- [50] V. Kamerdzhiyev *et al.*, “Progress with Electron Beam System for the Tevatron Electron Lenses,” in *11th European Particle Accelerator Conference*, Genoa, Italy, Jun 2008.
- [51] J.-P. Koutchouk, “Principle of a correction of the long-range beam-beam effect in LHC using electromagnetic lenses,” CERN, Geneva, Tech. Rep. LHC-Project-Note-223, Mar 2000.
- [52] “The CUDA web site, http://www.nvidia.com/object/cuda_home.html#.”

- [53] “The CUDA programming guide, http://developer.download.nvidia.com/compute/cuda/2.21/toolkit/docs/NVIDIA_CUDA_Programming_Guide_2.2.1.pdf.” nVIDIA Graphics.
- [54] M. Salt *et al.*, “Beam dynamics using graphical processing units,” in *Proceedings of EPAC08*, Genoa, Italy, 2008.
- [55] A. Papouilis and S. U. Pillai, *Probability, Random Variables, and Stochastic Processes*, 4th ed. McGraw-Hill, 2002.
- [56] M. Nessi, “sLHC and ATLAS, initial plans.” in *Interaction Regions for the LHC Upgrade, DAFNE and SuperB*, INFN-LNF, Frascati, Italy, November 2007.
- [57] M. Nessi, “The Experiments’ (ATLAS) View on LHC Crab Cavities,” Aug 2008.
- [58] U. Dorda, “Compensation of long-range beam-beam interaction at the CERN LHC,” Ph.D. dissertation, Technical University of Vienna, 2008.
- [59] U. Dorda *et al.*, “Wire excitation experiments in the CERN SPS,” CERN, Geneva, Tech. Rep. LHC-project-Report-1102, Aug 2008.
- [60] G. Burtin, 2009, private communication.
- [61] J. Bauche, 2009, private communication.
- [62] W. Herr, “Diffusion of particles induced by transverse noise and its application to crystal extraction experiments.” CERN, Geneva, Tech. Rep. CERN-SL-92-53-AP, Nov 1992.
- [63] C. Bracco, “Commissioning Scenarios and Tests for the LHC Collimation System,” Ph.D. dissertation, École Polytechnique Fédérale de Lausanne, 2009.
- [64] K. Cornelis, “Beam-Beam effects in the SPS proton-anti proton collider,” in *Proceedings of the Workshop on Beam-Beam Effects in Large Hadron Colliders*, Apr 1999.
- [65] “LUMI-2005: Scenarios for the LHC Luminosity Upgrade, <http://care-hhh.web.cern.ch/CARE-HHH/LUMI-05/default.html>,” CERN, 2006.
- [66] “LUMI-2006: Towards a Roadmap for the Upgrade of the CERN and GSI Accelerator Complex, <http://care-hhh.web.cern.ch/CARE-HHH/LUMI-06/default.html>,” CERN, 2007.
- [67] “IR-2007: Interaction Regions for the LHC Upgrade, DAFNE and SuperB, <http://care-hhh.web.cern.ch/CARE-HHH/IR07/default.html>,” CERN, 2008.
- [68] “BEAM-2007: Finalizing the Roadmap for the Upgrade of the CERN and GSI Accelerator Complex, <http://care-hhh.web.cern.ch/CARE-HHH/BEAM07/default.html>,” CERN, 2008.
- [69] “HHH-2008: Scenarios for the LHC Upgrade and FAIR, http://care-hhh.web.cern.ch/CARE-HHH/HHH-2008/proceedings_hhh2008.htm,” 2009.
- [70] “The ATLAS shielding project website, <http://atlas.web.cern.ch/Atlas/GROUPS/Shielding>.”
- [71] G. Sterbini, “Layout VERSION 1 for the Early separation scheme in ATLAS,” CERN, Internal Note 04, 2007.
- [72] G. Sterbini and D. Tommasini, “A Feasibility Study of Superconducting Dipole for the Early Separation Scheme of SLHC,” CERN, Geneva, Tech. Rep. CERN-AT-2008-016, Aug 2008.
- [73] I. Dawson and M. Shupe, “Radiation background studies for the LHC upgrade: Impact of machine magnets inside the ATLAS experiment,” CERN, Tech. Rep. EDMS: 932316, June 2008.
- [74] G. Battistoni *et al.*, “The FLUKA code: Description and benchmarking,” *AIP Conf. Proc.*, vol. 896, no. SLAC-REPRINT-2007-184, pp. 31–49, 2007.
- [75] N. V. Mokhov, 2009, private communication.
- [76] S. Roesler *et al.*, “The Monte Carlo Event Generator DPMJET-III,” SLAC, Stanford, CA, Tech. Rep. hep-ph/0012252., Dec 2000.
- [77] I. Novitski and A. Zlobin, “Thermal Analysis of SC Quadrupoles in Accelerator Interaction Regions,” *Applied Superconductivity, IEEE Transactions on*, vol. 17, no. 2, pp. 1059–1062, June 2007.
- [78] K. H. Mess *et al.*, *Superconducting Accelerator Magnets*. World Scientific Pub Co Inc, December 1996.
- [79] E. Todesco and L. Rossi, “Electromagnetic Design of Superconducting Dipoles Based on Sector Coils,” *Phys. Rev. Spec. Top. Accel. Beams*, vol. 10, p. 112401, Dec 2007.
- [80] P. Fessia *et al.*, “Parametric analysis of forces and stresses in superconducting dipoles,” *IEEE Trans. Appl. Supercond.*, vol. 19, pp. 1203–1207, June 2009.
- [81] A. Devred *et al.*, “Overview and status of the next european dipole (ned) joint research activity.” *Supercond. Sci. Technol.*, vol. 19, no. S67-S83. 27 p, 2006.

Guido Sterbini

Curriculum Vitæ

PERSONAL INFORMATION

Name	Guido Sterbini
Date of birth	February, 3 rd 1981
Citizenship	Italian
Address	2, Rue des Champs Fusy 01630 Saint Genis Pouilly, France
E-mail	guido.sterbini@cern.ch

EDUCATION AND QUALIFICATION

Present	CERN Doctoral Student in Physics c/o TE-MSU and EPFL
Dec 08	Teaching assistant for the course of "Introduction to Particle Accelerators", EPFL
Nov 06	CERN Technical Student c/o Magnets, Cryostats and Superconductors group
May 06	M.Sc. in Electronics: Università degli Studi di Roma "La Sapienza" Final mark: 110/110 summa cum laude Thesis title: "Ottimizzazione del canale ottico per le zone di interazione del Large Hadron Collider" sponsored by CERN, Switzerland. Advisor: Full Professor L. Palumbo
Feb 04	"Accelerator Technology" : Joint Universities Accelerator School, France Final mark: A (class ranking 1/21)
Jan 04	"Accelerator Physics" : Joint Universities Accelerator School, France Final mark: A (class ranking 1/18)
Dec 03	B.Sc. in Electronics: Università degli Studi di Roma "La Sapienza" Final mark: 110/110 cum laude Thesis title: "Evaluation of multibeam antennas performances" sponsored by Alenia Spazio, Italy Advisor: Full Professor P. Lampariello
Jul 02	Scientific High School degree Final mark: 100/100 Liceo Scientifico "R. Cartesio" in Olevano, Italy.

PUBLICATIONS

Sterbini, G.	"Analysis of satellite multibeam antennas' performances", Acta Astronautica, Volume 59, Issues 1-5, Pages 166-174, July-September 2006.
Koutchouk, J. P. et al.	"An early beam separation scheme for the LHC", Proceedings of EPAC06, Edinburgh, Scotland, 26-30 Jun 2006.
Sterbini, G. et al.	"D0 and its integrability", Proceedings of LUMI 2006 CARE-HHH-APD Workshop, Valencia, Spain, 16-20 Oct 2006.
Sterbini, G. et al.	"A luminosity leveling method for LHC luminosity upgrade using an Early Separation Scheme", CERN, LHC Project Note 403.
Assmann, R. W. et al.	"A Concept for the LHC Luminosity Upgrade Based on Strong β^* Reduction Combined with a Minimized Geometrical Luminosity Loss Factor", Proceedings of PAC07, 25-29 Jun 2007, Albuquerque, New Mexico.
Cerutti, F. et al.	"Parametric Study of Heat Deposition from Collision Debris into the Insertion Superconducting Magnets for the LHC Luminosity Upgrade", Proceedings of PAC07, 25-29 Jun 2007, Albuquerque, New Mexico.

Wildner, E. et al.	“Are Large-Aperture Nb-Ti Magnets Compatible with 1e35? ”, Proceedings of the Workshop on Interaction Regions for the LHC Upgrade, DAFNE, and SuperB, 6 - 9 Nov 2007, pp.74-80, Frascati, Italy
Sterbini, G. et al.	“D0 Design and BeamBeam Effect ”, Proceedings of the Workshop on Interaction Regions for the LHC Upgrade, DAFNE, and SuperB, 6 - 9 Nov 2007, pp.46-50, Frascati, Italy
Koutchouk, J.-P. et al.	“New Results on the Early Separation Scheme ”, Proceedings of the Workshop on Interaction Regions for the LHC Upgrade, DAFNE, and SuperB, 6 - 9 Nov 2007, pp.40-42, Frascati, Italy
Koutchouk, J.-P. et al.	“Increasing the Integrated Luminosity of SLHC by Leveling via the Crossing Angle”, Proceedings of EPAC08, 11th European Particle Accelerator Conference, 23-27 June 2008, Genoa, Italy.
Sterbini, G. et al.	“A Feasibility Study of Superconducting Dipole for the Early Separation Scheme of SLHC”, Proceedings of EPAC08, 11th European Particle Accelerator Conference, 23-27 June 2008, Genoa, Italy.
Fischer, W. et al.	“Long-range and head-on beam-beam compensation studies in RHIC with lessons for the LHC ”, Proceedings of Final CARE-HHH Workshop on Scenarios for the LHC Upgrade and FAIR, 24 - 25 Nov 2008, pp.92-101, Chavannes-de-Bogis, Switzerland
Sterbini, G.	“Early separation scheme for the LHC upgrade”, Proceedings of the Final CARE-HHH Workshop on Scenarios for the LHC Upgrade and FAIR, 24 - 25 Nov 2008, pp.102-105, Chavannes-de-Bogis, Switzerland
Sterbini, G.	“Study of a less invasive LHC Early Separation Scheme”, Proceedings of PAC09, 04 - 08 May 2009, Vancouver, Canada.
Sterbini, G. et al.	“An Early Separation Scheme for the LHC Luminosity Upgrade”, Physical Review Special Topics - Accelerators and Beams, in preparation